Advanced seeding methods for generation of fully-coherent ultra-short soft x-ray pulses

Dissertation
zur Erlangung des Doktorgrades
an der Fakultät für Mathematik, Informatik und Naturwissenschaften
Fachbereich Physik
der Universität Hamburg

vorgelegt von

Vanessa Grattoni

Hamburg
2020

Gutachter der Dissertation:	Prof. Dr. rer. nat. Wolfgang Hillert Dr. rer. nat. Ralph Assmann
Zusammensetzung der Prüfungskommission:	Prof. Dr. rer. nat. Wolfgang Hillert Dr. rer. nat. Ralph Assmann Prof. Dr. rer. nat. Daniela Pfannkuche Prof. Dr. rer. nat. Markus Drescher Dr. rer. nat. Ingmar Hartl
Vorsitzende/r der Prüfungskommission:	Prof. Dr. rer. nat. Daniela Pfannkuche
Datum der Disputation:	10.08.2020
Vorsitzender Fach-Promotionsausschusses PHYSIK:	Prof. Dr. Günter Hans Walter Sigl
Leiter des Fachbereichs PHYSIK:	Prof. Dr. Wolfgang Hansen
Dekan der Fakultät MIN:	Prof. Dr. Heinrich Graener

Contents

Kurzzusammenfassung In dieser Arbeit werde ich fortgeschrittene Seeding-Techniken zur Erzeugung von Strahlung im Bereich von EUV und weicher Röntgenstrahlung sowie die Eigenschaften der erzeugten Strahlung beschreiben. Ich werde mich auf das echofähige harmonische Erzeugungsschema (EEHG) konzentrieren, das kürzlich im Bereich der weichen Röntgenstrahlung am Freie-Elektronen-Laser (FEL) von FERMI gezeigt wurde. Ich werde Simulationen unter Verwendung des EEHG-Schemas mit der derzeit installierten Hardware bei sFLASH, dem Seeding-Experiment bei FLASH und dem FEL bei DESY, Hamburg, vorstellen. Ich erwäge auch ein mögliches Schikanen-Upgrade für sFLASH und des Lasersystems, um die Vorteile exotischerer Anwendungen des EEHG-Schemas zu analysieren, z.B. durch die Verwendung zweier unterschiedlicher Seed-Laser-Wellenlängen. Das EEHG-Schema wird für eine geplante Aufrüstung bei FLASH in Betracht gezogen, um Wellenlängen bis hinunter zu 4 nm zu erreichen. Ich werde die erforderlichen Parameter der Strahlführung definieren und die Grenzen des EEHG-Schemas untersuchen.

Abstract In this thesis I am going to describe advanced seeding techniques to generate radiation in the region of EUV and soft X-ray and the properties of the generated radiation. I am going to focus on the echo-enabled harmonic generation (EEHG) scheme, recently shown in the soft X-ray region at the FERMI free-electron laser (FEL). I am going to present simulations using the EEHG scheme using the currently installed hardware at sFLASH, the seeding experiment at FLASH, the FEL at DESY, Hamburg. I also consider a possible chicane upgrade for sFLASH and of the laser system to analyze the advantaged of more exotic applications of the EEHG scheme, for example by using two different seed laser wavelengths. The EEHG scheme is considered for a planned upgrade at FLASH to achieve wavelengths down to 4 nm. I am going to define the needed beamline parameters and study the limitations of the EEHG scheme.

Introduction

Chapter 1

Introduction

The first laser was invented in 1960 by Theodore Maiman and it was delivering radiation in the optical-wavelength. The laser radiation is contained in a very narrow beam and it is characterized by coherence and monochromaticity. Coherence enables diffraction experiments and interferometry studies, which are the basis of several instruments used today for engineering and applied sciences. After the discovery of the chirped pulse amplification (CPA), it was possible to generate ultra-short lasers (few tenths of femtoseconds) with high peak powers (GW, TW) [1]. The limitation of laser sources is linked with the achievable wavelength, which depends on the separation of the energy bands of the material used as active medium. In fact, today the gas laser ArF has the shortest wavelength of 193 nm. However, complex laser systems such as laser-produced plasma (LLP) enable to achieve the extreme ultraviolet (EUV) range down to 13.5 nm [2]. These laser systems are designed for lithography applications, hence the peak power is limited to tenths of watts and the laser pulse length is of the order of the nanoseconds. These are fundamental limitations for scientists interested in the study of molecular and atomic systems, which needs wavelengths from 100 nm to the Angstrom level and high peak powers to maximize the events, ergo the statistics.

One powerful light source which can offer a spectrum from infrared to X-rays is the synchrotron. The radiation is generated by a relativistic electron beam passing through wigglers, undulators or dipoles. The synchrotron radiation is limited to

pulse duration in the nanoseconds to picoseconds ranges, the peak power is lying in the kW range and it is limited in peak brightness. Synchrotron pulse length is limiting time-resolved biological studies aiming at characterizing the progress of biochemical reactions [3].
In the seventies, Madey brought together two working principles: the laser and the mechanism of the vacuum tubes. Madey and his working group invented the free electron laser (FEL) [4]:

> [...] In the years following Maiman's invention, I was to learn that the principles embodied in Maiman's laser could also be applied to develop short wavelength amplifiers and oscillators based on the bremmstrahlung radiation emitted by beams of relativistic free electrons moving through spatially periodic transverse magnetic fields [...]

In the quoted extract from [4] is enclosed the basic working principle of a FEL. Madey describes the FEL as

> [...] new, completely tunable and highly coherent [...]

The FEL generates pulses with narrow-bandwidth at wavelengths that can go below the nanometer level depending on the machine design. FEL pulses can achieve high peak power (GW level), ultra-short duration (transformed-limited, in the order of tenths of fs) and transverse coherence. Advanced schemes like seeded FEL enable the generation of light pulses with the additional properties of temporal coherence, extreme stability from pulse to pulse in temporal and spectral domain and clean spectra, that together with polarization control, are fundamental properties to study the evolution of atomic and molecular systems in time with the coherent diffraction imaging (CDI) [5], doing interferometry experiments [6] and studying the magnetic properties of the materials [7]. The interferometry experiment presented in [6] has shown that the seeded FEL source FERMI statistically behaves as a real laser-like source according to Glauber's definition [8]: a truly coherent source of radiation should be coherent in all orders of intensity correlation functions.

1.1 The concept of brightness: Synchrotrons and FELs

The brightness quantifies the number of photons within a narrow bandwidth $d\omega/\omega$ that can be focused on the unit surface of a detector:

$$B = \frac{\dot{N}_{ph}}{4\pi^2 \Sigma_x \Sigma_{\theta_x} \Sigma_y \Sigma_{\theta_y} \frac{d\omega}{\omega}} \tag{1.1}$$

where $\dot{N}_{ph}$ is the photon flux, $\Sigma_x = \sqrt{\sigma_{x,ph}^2 + \sigma_{x,e}^2}$, $\Sigma_{\theta_x} = \sqrt{\sigma_{\theta_x,ph}^2 + \sigma_{\theta_x,e}^2}$ and Σ_y, Σ_{θ_y} are defined similarly. The peak brightness is an important parameter for nonlinear experiments or experiments where the target is destroyed by each pulse. It is also possible to quantify an average brightness, which is important for experiments where the output signal is linear in photon flux and where backgrounds are not a problem [9]. Figure 1.1 shows that the peak brightness of the FELs is several orders of magnitude greater compared to the one of synchrotrons. Hence FELs and synchrotrons offer complementary performances and one type cannot replace the other, similarly to the capabilities offered by pulsed and continuous (DC) conventional lasers respectively [10].

1.2 Importance of seeding and seeding experiments worldwide

Seeded FEL sources have unique properties as full coherence (transverse and longitudinal), narrow and Gaussian-like spectrum, pulses close to the Fourier-transform limit,... . The request for these FEL properties from the scientific community is constantly growing, as a result, the FEL community is exploring different schemes and techniques to achieve these properties and understand which are the technological challenges and the quality of the resulting FEL radiation.
We can distinguish between schemes based on external seeding and self-seeding. In the former, an external coherent source is used e.g. the direct seeding amplifies the radiation generated from a laser, or a HHG source [12] that co-propagates with the electron beam. On the other hand, self-seeding uses the spontaneous radiation generated from the electron beam in a first undulator stage to directly seed the

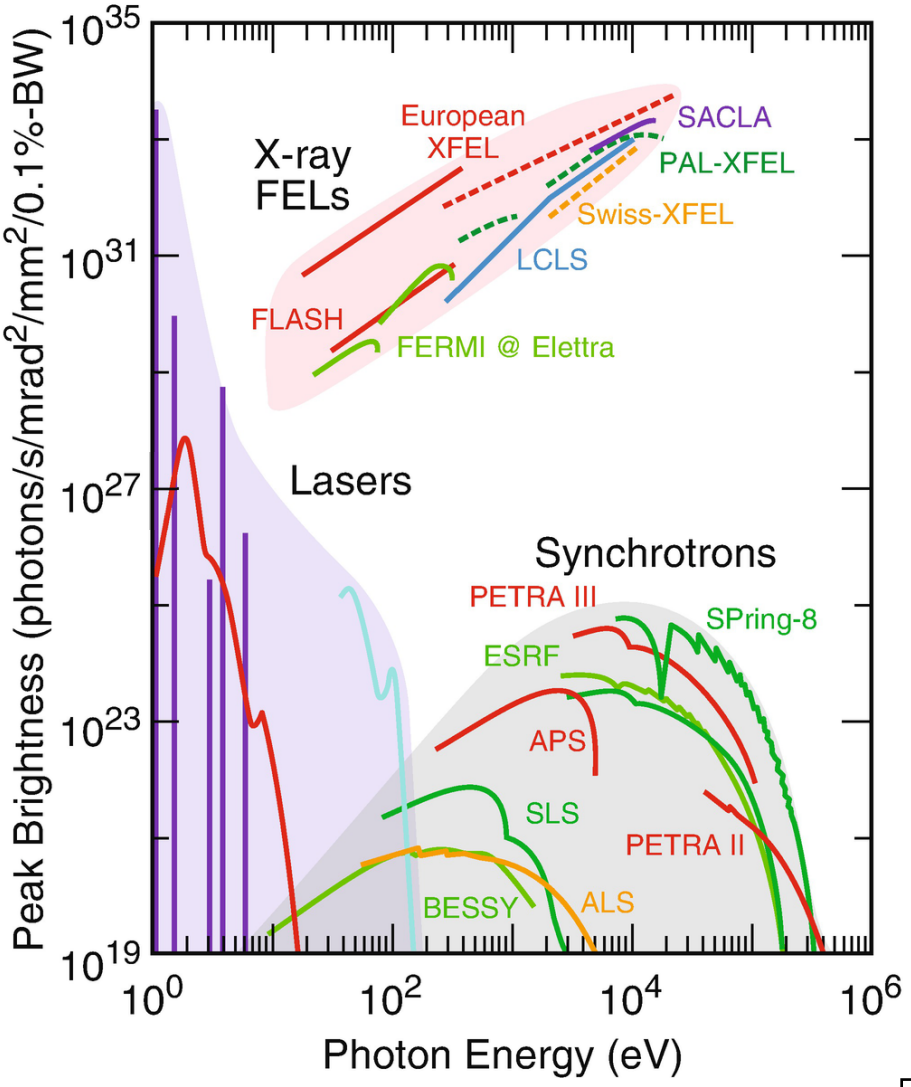

Figure (1.1) Peak brightness of lasers, Synchrotron facilities and FELs [11]

electron beam in a second undulator stage. More exotic schemes are based on the combination of external seeding with self-seeding. For example, cascaded HGHG is based on a first stage HGHG followed by a second stage HGHG. The FEL radiation produced in the first stage is used as seed for the second stage HGHG and it is overlapped in a region of the electron beam which did not participate to the first stage lasing (fresh-bunch technique). Likely, one can think to cascade HGHG stages with EEHG stages and the other way around as it is planned at the SX-FEL in Shanghai [13]. These exotic schemes are very interesting because they enable the generation of very short wavelengths ($\sim 1\,\mathrm{nm}$ and below). However, the disadvantages are the length of the setup and the high complexity of the

individual stages. At the FERMI FEL in Trieste there are two beamlines devoted to seeding available for users: FEL1 [14] and FEL2 [15]. In FEL1 is installed a HGHG seeding setup and FEL2 is dedicated to cascaded HGHG. At sFLASH at FLASH we are studying the EEHG scheme and we operate regularly the HGHG scheme. There are many FEL facilities worldwide which have implemented self-seeding: LCLS [16], SACLA [17], PAL [18] and it has been recently commissioned at the European XFEL [19]. The Swiss-FEL at PSI [20] and LCLS-II [21] are planning to implement self-seeding in the next years.

1.3 Chapter overview of this thesis

In this thesis I have investigated how to generate FEL pulses with ultra-short wavelengths with external seeding techniques.
In the second chapter we are going to give an insight into the theory necessary to understand the basics of accelerator physics and the FEL processes. In the third chapter I will focus on two seeded schemes: high-gain harmonic generation (HGHG) and echo-enabled harmonic generation (EEHG).
HGHG is the consolidated scheme working at the sFLASH experiment at FLASH. In the fourth chapter we are going to describe how the HGHG FEL radiation generated at sFLASH can be characterized and controlled through the manipulation of the seed laser. Moreover, we are going to comment on the feasibility of the EEHG experiment at sFLASH with the currently installed setup. I will also explore more exotic EEHG configurations that enable to improve the properties of the generated radiation.
In the fifth chapter, we report about the latest achievements at FERMI. Here the EEHG scheme has been implemented successfully starting from a ultraviolet (UV) source and up-converted to wavelengths in the extreme ultraviolet (EUV) range for the first time.
Given the very positive results achieved at FERMI with the EEHG scheme, at FLASH is planned an upgrade which is aiming at the installation of seeding for the user community. This project is identified with the name of FLASH2020+ and it is presented in the last chapter of this thesis. This project is very ambitious because it is planned to implement seeding at high repetition rate, exploiting the potential of the FLASH superconducting cavities. Both HGHG and EEHG

schemes are considered. The extreme sensitivity of the EEHG scheme, requires several considerations in the choices of the working points, the analysis of the performances with the chosen working point and possible degrading effects. For part of these tasks is used the latest version of the code GENESIS1.3 (version 4).

Accelerator Physics and FEL theory

Chapter 2

Accelerator Physics and FEL theory

When an accelerator is constructed, the nominal energy and trajectory of the particle beam is fixed. The reference particle has the nominal energy and goes

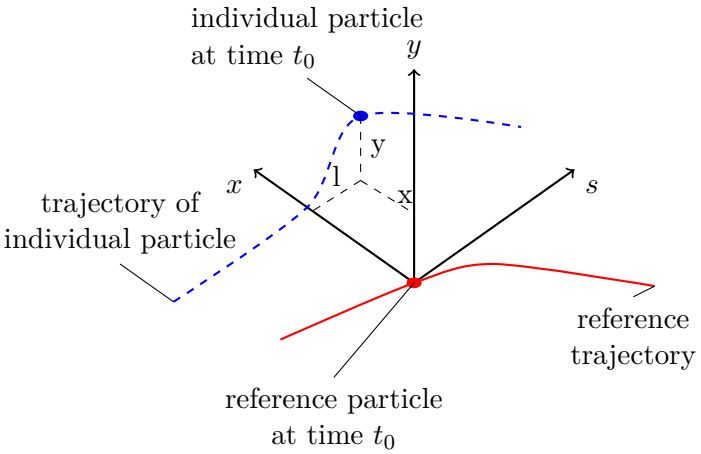

Figure (2.1) Reference system along the design orbit (red curve) and oscillations around it (blue dashed line). The $x - y - s$ coordinate system is the co-moving reference frame along the design orbit and it is centered at the position of the reference particle. The position of the an individual particle within the beam is given by the coordinates (x,y,l) respect to the reference particle.

through the designed trajectory. All the particles within the bunch have a non-zero angular divergence, spatial displacement and energy deviation with respect

to the reference particle. Therefore, the coordinates of these particles can be expressed relative to the reference particle.
To avoid particle losses, the diverging particles have to be steered to the nominal trajectory. This is done using the Lorentz force:

$$\mathbf{F} = e(\mathbf{E} + \mathbf{v} \times \mathbf{B}) = \frac{d\mathbf{p}}{dt}. \tag{2.1}$$

Commonly the steering of the beam is performed by the magnetic field of the magnets. While, accelerating the beam is performed by the electric field.

2.0.1 Transverse dynamics

Assuming that the particles are moving with constant velocity along the s-direction Fig. 2.1 with velocity $\mathbf{v} = (0, 0, v)$ and they are subject to a magnetic field $B = (B_x, B_y, 0)$ [22], hence the resulting force acting on the particle is zero and therefore the Lorentz component $F_x = -evB_y$ should cancel with the centripetal force $F_c = mv^2/R$. Where m is the particle mass and R is the curvature radius of the particle trajectory. Therefore, by setting $p = mv$:

$$\frac{1}{R(x, y, s)} = \frac{e}{p} B_y(x, y, s). \tag{2.2}$$

Because the transverse beamsize of the particle beam is much smaller then R is possible to expand the magnetic field locally around the particle trajectory [22]:

$$B_y(x) = B_{y0} + \frac{dB_y}{dx}x + \frac{1}{2!}\frac{d^2B}{dx^2}x^2 + \frac{1}{3!}\frac{d^3B}{dx^3}x^3 + ... \tag{2.3}$$

Multiplying by the elementary charge per momentum e/p enables the definition of the multipole fields:

$$\frac{e}{p}B_y(x) = \frac{1}{R} + kx + \frac{1}{2!}mx^2 + \frac{1}{3!}ox^3 + ... \tag{2.4}$$

where $1/R$ is the dipole field that is used to steer the particles. kx is the quadrupole field that is used to focus (or defocus) the beam, $1/2mx^2$ is the sexupole field that is either used for chromaticity correction or it appears as field

error, and so on.
Assuming that the steering effect of the magnetic field is only along x, the particle motion in the presented system of reference in Fig. 2.1 is described by the Hill's equations:

$$x^{''}(s) + \left(\frac{1}{R^2(s)} - k(s)\right) x(s) = \frac{1}{R(s)}\frac{\Delta p}{p} \tag{2.5}$$

$$y^{''}(s) + k(s)y(s) = 0 \tag{2.6}$$

Eq. 2.5 is inhomogeneous due to the deviation in momentum of one particle from the reference particle Δp. The dipole and quadrupole fields depend on the s-coordinate and the $''$ indicates the second derivative respect to the s-coordinate. The trajectory of a single particle - with no momentum deviation ($\Delta p/p = 0$) and with negligible quadratic contributions $1/R^2(s) = 0$ - along the beamline is described by the solution of the Hill's equation:

$$x(s) = x_0 c_x(s) + x_0' s_x(s), \tag{2.7}$$
$$y(s) = y_0 c_y(s) + y_0' s_y(s). \tag{2.8}$$

Where x_0, x_0', y_0, y_0' are the initial parameters and $c_{x,y}(s)$, $s_{x,y}(s)$ are sinusoidal functions following the initial conditions:

$$c_{x,y}(0) = 1, \quad s_{x,y}(0) = 0 \tag{2.9}$$
$$c_{x,y}'(0) = 0, \quad s_{x,y}'(0) = 1. \tag{2.10}$$

During the motion the particle is performing betatron oscillations around the design orbit. In real accelerators we never accelerate only one particle, but a bunch with millions of particles. Each particle is characterized by a six-dimensional phase space coordinate $(x, x', y, y', s, \gamma)$. The relation between angular dispersion x' and momentum p_x is given by $p_x = mc\beta\gamma x'$ where m is the particle mass, $c\beta$ is the velocity of the particle and γ is the relativistic factor. All the particles in the bunch perform betatron oscillations. Typically, one defines here an amplitude function $E(s)$ which describes the position dependent envelope of the single particle oscillation $x(s) = E(s)\cos(\Psi(s) + \phi)$, where ϕ is a constant phase

and $\Psi(s) = \int_0^s \frac{d\sigma}{\beta(\sigma)}$ is the phase advance. Another position dependent function, the beta function $\beta(s)$, is used to describe the optics of the beamline. It is only determined by the arrangements of the magnets, the *lattice*. For an ensemble of N particles, the emittance ϵ is defined as a characteristic parameter describing the properties of the particle beam. It can be defined for both the $[x, x']$ and $[y, y']$ plane. For electrons, assuming the initial positions $x_0 = y_0 = 0$,it is usually given by:

$$\epsilon_x = \sqrt{\langle x^2 \rangle \langle x'^2 \rangle - \langle x x' \rangle^2} \tag{2.11}$$

$$\epsilon_y = \sqrt{\langle y^2 \rangle \langle y'^2 \rangle - \langle y y' \rangle^2} \tag{2.12}$$

and represents the rms area of the electrons in the two-dimensional phase space normalized to π. Here $\sigma_x^2 = \langle x^2 \rangle = \frac{1}{N} \sum_{i=1}^{N} (x_i - \langle x \rangle)^2$, $\sigma_{x'}^2 = \langle x'^2 \rangle = \frac{1}{N} \sum_{i=1}^{N} (x_i' - \langle x' \rangle)^2$ and $\sigma_x \sigma_{x'} = \langle x x' \rangle = \frac{1}{N} \sum_{i=1}^{N} (x_i - \langle x \rangle)(x_i' - \langle x' \rangle)$. Here N is the total number of particles in the bunch and $\langle ... \rangle$ denotes the average value of the term in brackets.

According to the conservation of the phase space area due to the Liouville's law, the emittance is conserved under conservative forces and describes the *quality* of the beam.

The actual rms beam size and divergence are then given by:

$$\sigma_x = \sqrt{\epsilon_x \beta_x(s)} \tag{2.13}$$

$$\sigma_{x'} = \sqrt{\epsilon_x \gamma_x(s)}. \tag{2.14}$$

The contour of the area in the phase space covered by the beam is an ellipse, which can be derived from:

$$\gamma_x(s) x^2(s) + 2\alpha_x(s) x(s) x'(s) + \beta_x(s) x'^2(s) = \epsilon_x \tag{2.15}$$

with $\gamma_x(s) \equiv (1 + \alpha_x^2(s))/\beta_x(s)$ and $\alpha_x(s) \equiv -\beta_x'(s)/2$ are three of the Twiss parameters. Please note that due to the statistical definition of ϵ, there will be

particles laying outside this area.
Whenever a particle has an energy deviation $\Delta p/p \neq 0$, this effect is seen within the dipole field ($1/R \neq 0$, but $k(s) = 0$), as the kick given is energy dependent. In addition, the magnetic field direction is always vertical, so the dispersion effect is only horizontal. The solution of the Hill's equations reads:

$$x(s) = x_0 c_x(s) + x_0' s_x(s) + \frac{\Delta p}{p} d_x(s). \tag{2.16}$$

where:

$$d_x(s) = \int_0^s h(\bar{s}) G_x(s, \bar{s}) d\bar{s} \tag{2.17}$$

is the dispersion function, $h(s) = \frac{1}{R}$ and $G_x(s, \bar{s})$ is the Green function:

$$G_x(s, \bar{s}) = s_x(s) c_x(\bar{s}) - c_x(s) s_x(\bar{s}) \tag{2.18}$$

In case of dispersion, it is necessary to add a correction to the transverse emittance:

$$\frac{\sigma_x^2}{\beta_x(s)} = \frac{\sigma_x^{(0)2}}{\beta_x(0)} + \frac{D(s)^2}{\beta_x} \left(\frac{\sigma_p}{p} \right)^2 \tag{2.19}$$

where $\frac{\sigma_x^{(0)2}}{\beta_x(0)}$ is the emittance in the not-dipersive section, $\frac{\sigma_x^2}{\beta_x(s)}$ is the emittance in the dispersive section, p is the momentum of the reference particle and σ_p is the standard deviation from p. A detailed derivation of Eq. 2.19 is given in [23].

2.1 Longitudinal phase space

The particle coordinates in the co-moving reference system (Fig. 2.1) can be expressed with the vector:

$$\mathbf{X} = \begin{pmatrix} x \\ x' \\ y \\ y' \\ l \\ \delta \end{pmatrix}. \tag{2.20}$$

The first four rows of the column array describe the positions (x, y) and the angular deviations (x', y') respect to the reference particle. The evolution of these coordinates along the accelerator have been described in the previous section. These coordinates represent the transverse beam dynamics. Now, we focus on the evolution of the longitudinal coordinate and the energy deviation respect to the reference particle (l, δ) - i.e. the longitudinal phase space - along the accelerator. The longitudinal position change of a particle with respect to the reference particle is $l(0) = l_0$ at the initial position and $l(s) = l$ at the final position. The change of longitudinal position happens if there is a difference in the time of flight along the path [23]:

$$l(s) - l(0) = v_0(t_0 - t) = v_0 \left(\frac{s}{v_0} - \frac{S}{v} \right) \tag{2.21}$$

where t_0, v_0 and s are the time of flight, the velocity and the path length respectively at the starting point and t, v and S are the corresponding values at the final position. Eq. 2.21 can be simplified in linear approximation, as shown in [23]. As a final solution we get:

$$l(s) = -x_0 \int_0^s h(\bar{s}) c_x(\bar{s}) d\bar{s} + x_0' \int_0^s h(\bar{s}) s_x(\bar{s}) d\bar{s} + l(0) - \frac{\Delta p}{p} \left(\int_0^s h(\bar{s}) d_x(\bar{s}) d\bar{s} - \frac{s}{\gamma^2} \right). \tag{2.22}$$

From Eq. 2.22 we define:

$$R_{51}(s) = (l|x_0) = -\int_0^s h(\bar{s}) c_x(\bar{s}) d\bar{s} \tag{2.23}$$

$$R_{52}(s) = (l|x_0') = \int_0^s h(\bar{s}) s_x(\bar{s}) d\bar{s} \tag{2.24}$$

$$R_{55}(s) = (l|l_0) = 1 \tag{2.25}$$

$$R_{56}(s) = \left(l \middle| \frac{\Delta p}{p} \right) = -\int_0^s h(\bar{s}) d_x(\bar{s}) d\bar{s} + \frac{s}{\gamma^2} \tag{2.26}$$

The evolution of the 6D vector of Eq. 2.20 can be described by the transfer matrix $\mathbf{R}$:

$$\mathbf{R} = \begin{pmatrix} R_{11} & R_{12} & R_{13} & R_{14} & R_{15} & R_{16} \\ R_{21} & R_{22} & R_{23} & R_{24} & R_{25} & R_{26} \\ R_{31} & R_{32} & R_{33} & R_{34} & R_{35} & R_{36} \\ R_{41} & R_{42} & R_{43} & R_{44} & R_{45} & R_{46} \\ R_{51} & R_{52} & R_{53} & R_{54} & R_{55} & R_{56} \\ R_{61} & R_{62} & R_{63} & R_{64} & R_{65} & R_{66} \end{pmatrix}. \tag{2.27}$$

as follows:

$$\mathbf{X} = \mathbf{R}\mathbf{X_0} \tag{2.28}$$

where $\mathbf{X}$ is the array in Eq. 2.20 and $\mathbf{X_0}$ is the initial status of the particle coordinates. The matrix elements R_{11}, R_{12} and R_{33}, R_{34} are defined in Eqs. 2.7,2.8:

$$R_{11}(s) = c_x(s) \tag{2.29}$$
$$R_{12}(s) = s_x(s) \tag{2.30}$$
$$R_{33}(s) = c_y(s) \tag{2.31}$$
$$R_{34}(s) = s_y(s) \tag{2.32}$$

and R_{16} is defined in Eq. 2.16 and R_{26} is its derivative:

$$R_{16}(s) = d_x(s) \tag{2.33}$$
$$R_{26}(s) = d'_x(s) \tag{2.34}$$

While R_{21}, R_{22} and R_{43}, R_{44} are the respective derivatives:

$$R_{21}(s) = c'_x(s) \tag{2.35}$$
$$R_{22}(s) = s'_x(s) \tag{2.36}$$
$$R_{43}(s) = c'_y(s) \tag{2.37}$$
$$R_{44}(s) = s'_y(s) \tag{2.38}$$

If there are no couplings between the transverse components R_{13}, R_{14}, R_{23}, R_{24} and R_{31}, R_{32}, R_{41}, R_{42} are zero. If the transverse components are independent from the longitudinal position then: $R_{15} = R_{25} = R_{35} = R_{45} = 0$. Finally, if there is no horizontal dispersion it holds $R_{16} = R_{26} = 0$ and if there is no vertical dispersion $R_{36} = R_{46} = 0$. The definition of the transport matrix for the magnetic elements that inserted in an can be found in [24]. In the next paragraph we describe the transport matrix of a 4-dipole chicane, which is fundamental for the seeded FEL schemes that we are describing in the rest of the chapter.

Longitudinal dynamics in a bunch compressor In FELs, bunch compressors are used to achieve high electron beam peak currents (∼1 kA or higher) and

in general, to manipulate the longitudinal phase space distribution of the electron bunch.

In the first case, the chicane placed downstream an accelerating cavity which gives an energy chirp to the electron beam: trailing electrons have an higher energy gain respect to the electrons at the head of the beam, as showed in Fig. 2.2. As a result, leading electrons undergo through a longer trajectory in the chicane compared to the trailing electrons, due to their energy difference. At the end, the electron beam is compressed: the beam length reduces and the peak current increases. The energy at the end of the accelerating cavity reads:

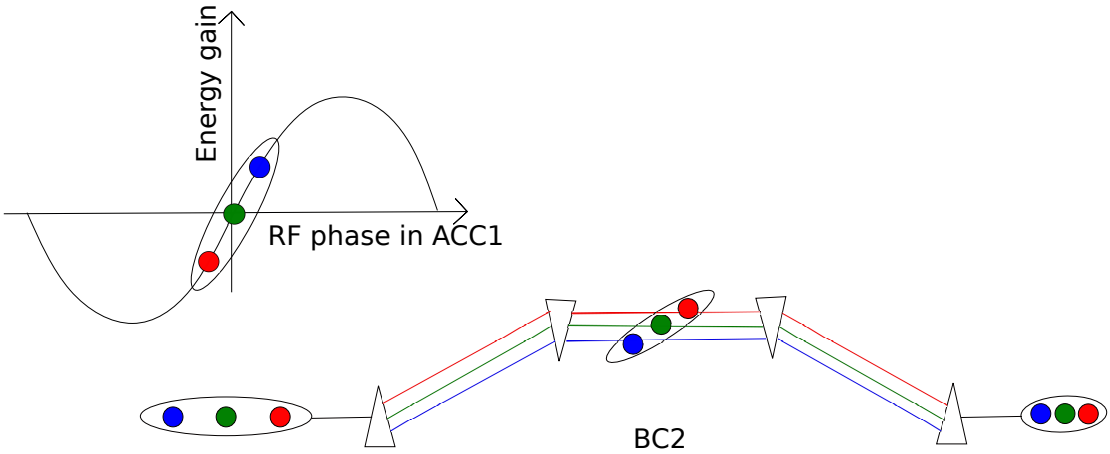

Figure (2.2) Acceleration off-crest in ACC1 and following compression in BC2. The blue electrons represent the tail and the red electrons represent the head of the electron bunch. The energy chirped electron bunch is then compressed in the bunch compressor BC2.

$$\delta(s_1) = \delta(s_0) + \frac{eV_{RF}}{E_0} \sin\left(\frac{\omega_{RF} z(s_0)}{c} + \phi_{RF}\right) \tag{2.39}$$

where e is the electron charge, V_{RF}, ω_{RF} and ϕ_{RF} are the total voltage amplitude, the RF frequency and a fixed phase offset respectively. E_0 is the reference energy and $z(s_0)$ is the longitudinal position of the electron respect to the reference particle at the entrance of the accelerating cavity, which remains the same at the exit of the cavity at s_1: $z(s_1) = z(s_0)$. At this point, the particles enter inside the bunch compressor, that has a total length of:

$$L = \frac{2L_1}{\cos\theta} + L_2 \tag{2.40}$$

where L_1 is the distance from the outer dipole to the inner dipole, L_2 is the distance from the second to the third dipole and θ is the bending angle. θ depends on the energy deviation from the energy of the reference particle:

$$\theta = \frac{\theta_0}{1+\delta} \tag{2.41}$$

Here we have neglected the length of the dipole magnet.
Upstream (s_1) and downstream (s_2) the chicane the energy remains unchanged:

$$\delta(s_2) = \delta(s_1). \tag{2.42}$$

While the longitudinal coordinate l is changed as:

$$l(s_2) = l(s_1) + 2L_1\left(\frac{1}{\cos\theta_0} - \frac{1}{\cos\theta}\right) \tag{2.43}$$

As a result, we obtain the transfer matrix for the transport of the longitudinal coordinates:

$$\begin{pmatrix} z \\ \delta \end{pmatrix}_{s=s_2} = \begin{pmatrix} 1 & R_{56} \\ 0 & 1 \end{pmatrix} \begin{pmatrix} 1 & 0 \\ R_{65} & 1 \end{pmatrix} \begin{pmatrix} z \\ \delta \end{pmatrix}_{s=s_0} \tag{2.44}$$

with

$$R_{65} = -\frac{eV_{RF}\cos\phi_{RF}}{E_0}\frac{\omega_{RF}}{c} \tag{2.45}$$

and [25]:

$$R_{56} = 2L_1\frac{\theta_0\tan\theta_0}{\cos\theta_0}. \tag{2.46}$$

A fully 6D transport matrix for the four dipole chicane is derived in [26].

2.2 Basics of FEL theory

The FEL operation is based on the energy exchange between a relativistic electron beam and a co-propagating radiation in an undulator.
The undulator is a magnetic structure which has a periodic magnetic field given

by:

$$B_x = 0 \tag{2.47}$$
$$B_y = -B_0 \cosh(k_u y) \sin(k_u z) \tag{2.48}$$
$$B_z = -B_0 \sinh(k_u y) \cos(k_u z) \tag{2.49}$$

for a planar undulator and:

$$B_x = -B_0 \cos(k_u z) \tag{2.50}$$
$$B_y = -B_0 \sin(k_u z) \tag{2.51}$$
$$B_z = 0. \tag{2.52}$$

for an helical undulator; where B_0 is the peak value of the magnetic field along the undulator longitudinal axis and $k_u = \frac{2\pi}{\lambda_u}$ with λ_u the undulator period.
In the following, we assume a planar undulator with a negligible magnetic field component along z and with simplified field [27]:

$$B_y = -B_0 \sin(k_u z). \tag{2.53}$$

2.2.1 Electron motion into the undulator

When the electron enters in the undulator it has a longitudinal velocity, which for the beginning we assume to be constant:

$$v_z = \dot{z} \approx v = \beta c = const. \tag{2.54}$$

The magnetic field of the undulator acts on the electron beam due to the Lorentz force:

$$\gamma m \dot{\mathbf{v}} = -e\mathbf{v} \times \mathbf{B}. \tag{2.55}$$

That results in two coupled equations:

$$\ddot{x} = \frac{e}{\gamma m} B_y \dot{z}, \qquad \ddot{z} = -\frac{e}{\gamma m} B_y \dot{x}. \tag{2.56}$$

As $v_x \ll v_z$ we have that $\ddot{z} \approx 0$ and from Eq. 2.54 we have that the longitudinal velocity is a constant, hence:

$$x(t) \approx \frac{Kc}{\gamma}\cos(k_u z), \qquad z(t) \approx \beta c t \tag{2.57}$$

where

$$K = \frac{eB_0\lambda_u}{2\pi mc} = 0.934 \cdot B_0[T] \cdot \lambda_u[cm] \tag{2.58}$$

is the dimensionless undulator parameter. Therefore, the velocity along the x direction is:

$$v_x(z) = \frac{Kc}{\gamma}\cos(k_u z). \tag{2.59}$$

At this point we can derive the longitudinal velocity of the electron beam as follows:

$$v_z = \sqrt{v^2 - v_x^2} = \sqrt{c^2(1 - \frac{1}{\gamma^2}) - v_x^2} \approx c\left[1 - \frac{1}{2\gamma^2}\left(1 + \gamma^2\frac{v_x^2}{c^2}\right)\right] \tag{2.60}$$

By inserting Eq. 2.59, using the trigonometric identity: $\cos^2\alpha = (1+\cos(2\alpha))/2$, we get:

$$v_z(t) = \left[1 - \frac{1}{2\gamma^2}\left(1 + \frac{K^2}{2}\right)\right]c - \frac{cK^2}{4\gamma^2}\cos(2\omega_u t) \tag{2.61}$$

where $\omega_u = \bar{\beta}ck_u \approx k_u$ and $\bar{\beta}c$ is the averaged longitudinal velocity, which is:

$$\bar{v}_z = \left[1 - \frac{1}{2\gamma^2}\left(1 + \frac{K^2}{2}\right)\right]c \equiv \bar{\beta}c \tag{2.62}$$

As a result, the exact expression for the longitudinal trajectory of the particle given in Eq. 2.57 is:

$$z(t) = \bar{v}_z t - \frac{K^2}{8\gamma^2 k_u}\sin(2\omega_u t). \tag{2.63}$$

2.2.2 Undulator radiation properties

In the system of reference moving at the average velocity (Eq. 2.62) (co-moving reference frame), the electron performs dipole oscillations along the transverse direction x, with a negligible velocity component along z [28]. The oscillating dipole is nearly at rest in the co-moving reference frame, while it is moving at a relativistic speed in the laboratory frame. The oscillating dipole emits radiation within a

cone with an angular aperture $\sim 1/\gamma$ and tangent to the electron trajectory. The maximum angle between the tangent and the longitudinal undulator axis is given by:

$$\theta_{max} \approx \left|\frac{dx}{dz}\right|_{max} \approx \frac{K}{\gamma}. \tag{2.64}$$

In the following we are going to consider only cases in which $K \approx 1$, enabling the interference between radiation cones emitted by an electron in different parts of the undulator. In the time in which the electron moves along an undulator period, from A to B in Fig. 2.3, $\lambda_u/(\bar{\beta}c)$, the radiation from A advance a distance $\lambda_u/\bar{\beta}$. The radiation emitted in A is in front of the radiation emitted in B by a distance:

$$d = \frac{\lambda_u}{\bar{\beta}} - \lambda_u \cos(\theta). \tag{2.65}$$

Constructive interference happens when:

$$d = n\lambda \tag{2.66}$$

where λ is the radiation wavelength and n is an integer number. By inserting the

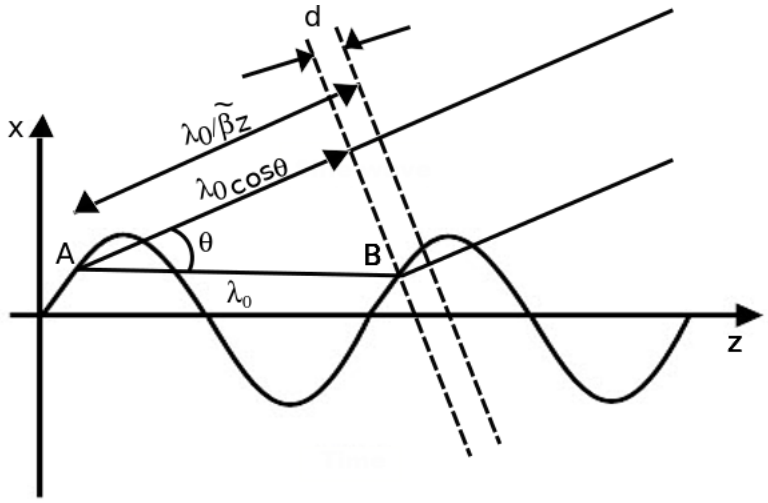

Figure (2.3) Interference in an undulator [29].

average electron velocity from Eq. 2.62 we obtain the interference condition:

$$\lambda = \frac{\lambda_u}{2\gamma^2}\frac{1}{n}\left(1 + \frac{K^2}{2} + \gamma^2\theta^2\right), \qquad n = 1, 2, 3, ... \tag{2.67}$$

where n is the harmonic number [29]. One can observe the odd harmonics at $\theta \sim 0$ and the even harmonics off from the undulator axis.

By looking only at the forward direction ($\theta \sim 0$), the undulator radiation electric field of the fundamental harmonic is given by:

$$E_l(t) = \begin{cases} E_0 \exp(-i\omega_l t) \text{ if } -T/2 < t < T/2, \\ 0 \text{ otherwise.} \end{cases} \tag{2.68}$$

This system describes a wave train with a number of oscillations equal to the number of undulator periods N_u and a time duration $T = N_u\lambda_1/c$. The Fourier transform of $E_l(t)$ gives the spectral distribution:

$$A(\omega) = 2E_0 \frac{\sin(\omega_l - \omega)T/2}{\omega_l - \omega} \tag{2.69}$$

from which we can derive the spectral intensity:

$$I(\omega) \propto |A(\omega)|^2 \propto \left(\frac{\sin(\xi)}{\xi}\right)^2 \tag{2.70}$$

where $\xi = \pi N_u \frac{\omega_l - \omega}{\omega_l}$. Eq. 2.70 shows that the undulator radiation has a maximum at the frequency $\omega = \omega_l$ and it has a characteristic width:

$$\Delta\omega \approx \frac{\omega_l}{N_u}. \tag{2.71}$$

The angular width of the first harmonic around $\theta = 0$ is given by:

$$\sigma_\theta \approx \frac{1}{\gamma\sqrt{N_u}}. \tag{2.72}$$

The fractional bandwidth for the odd harmonics is reduced by *m=2n-1* respect to Eq. 2.71 and the angular width is given by $\sigma_{\theta,m} \approx \sigma_\theta/\sqrt{m}$.
The total undulator radiation power emitted by the electron is a relativistic invariant and is given by the Larmor formula [28]:

$$P_{rad} = \frac{e^2 c\gamma^2 K^2 k_u}{12\pi\epsilon_0}. \tag{2.73}$$

FEL operation principle

The FEL is based on the interaction of a relativistic electron beam with the magnetic field of an undulator Fig. 2.4. The electron subject to the magnetic field

of the undulator begins a sinusoidal trajectory which adds a transverse component to the electron motion. Due to relativity, the electron travelling along a curved trajectory starts to emit synhrotron radiation. The transverse velocity component of the electron couples with the electric field of the emitted radiation. Depending on the phase of the electron respect to the radiation electric field there is an energy exchange from the electron to the radiation or the other way around.
It is also possible that the electron beam enters the undulator together with a coherent radiation source, which then is amplified within the radiator based on the same process. Depending on the rate of energy transfer between electrons and

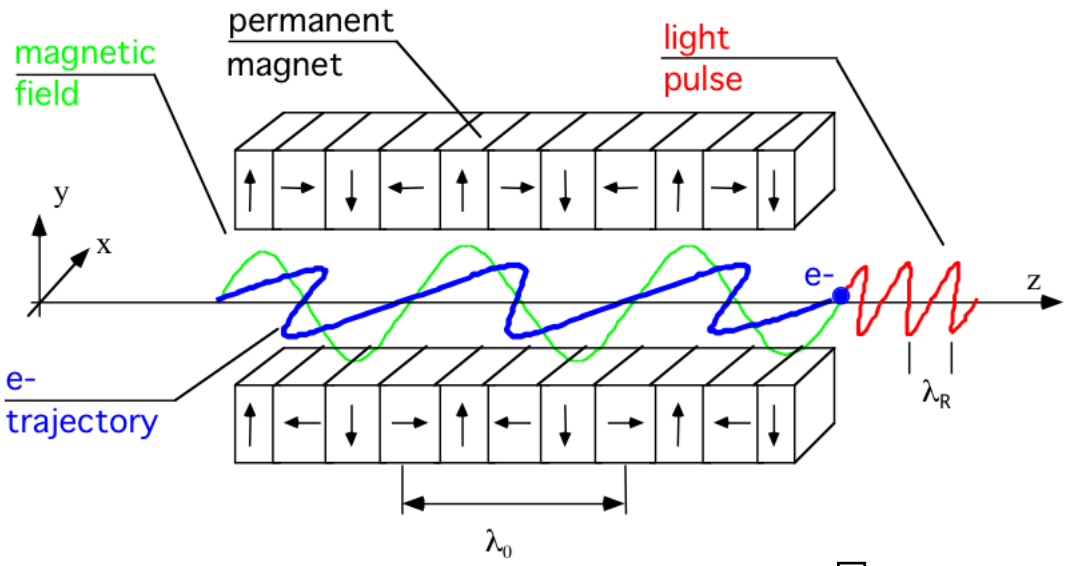

Figure (2.4) Working principle of a free-electron laser [30].

radiation, one could distinguish between low gain or high gain FEL.

Low gain FEL

We consider a circulating electron beam, either from a storage ring or from an energy recovery linac (ERL), which every pass passes through an undulator. This undulator is placed in a cavity made by two mirrors. A seed laser co-propagates together with the electron beam along the undulator. The laser radiation and the eventually generated radiation are oscillating within the optical cavity. The laser is described by a plane electromagnetic wave:

$$E_x(z,t) = E_0 \cos\left(k_l z - \omega_l z + \psi_0\right) \tag{2.74}$$

where $k_l = \omega_l/c = 2\pi/\lambda_l$ and λ_l is the seed laser wavelength. The electron is subject to the Lorentz force caused by the electric field of the laser $\mathbf{F} = -e\mathbf{E}$, which leads to an energy exchange:

$$\frac{d\gamma mc^2}{dt} = -\mathbf{v}\cdot\mathbf{F} = -ev_x(t)E_x(t) \tag{2.75}$$

where $v_x(t)$ is the electron transverse velocity component arising from the dynamics into the undulator. If Eq. 2.74 is inserted in Eq. 2.75 we get:

$$\frac{d\gamma mc^2}{dt} = -\frac{ecKE_0}{2\gamma}(cos\psi - cos\chi) \tag{2.76}$$

where ψ is the ponderomotive phase:

$$\psi = (k_l + k_u)z(t) - \omega_l t + \psi_0 \tag{2.77}$$

and χ:

$$\chi = (k_l - k_u)z(t) - \omega_l t + \psi_0 \tag{2.78}$$

where ψ_0 the phase shift of the light wave respect to the sinusoidal trajectory of the electron and $z(t) = \bar{v}_z t$.
If the ponderomotive phase is constant, the electron beam sees the same phase of the radiation every period of the undulator, meaning a continuous energy exchange:

$$\psi = \text{const} \iff \frac{d\psi}{dt} = 0 \tag{2.79}$$

which gives the result:

$$\lambda_l = \frac{\lambda_u}{2\gamma^2}\left(1 + \frac{K^2}{2}\right). \tag{2.80}$$

This wavelength is equivalent to the spontaneous undulator wavelength that can be observed for $\theta = 0$ as shown in Eq. 2.67.
Moreover, if $\psi > 0$, the electrons transfer energy to the light wave. On the other side, requesting χ to be constant, results in a condition that cannot be realized [28].
To satisfy the condition given in Eq. 2.80, the electrons have to enter the undulator at the resonance energy:

$$\gamma_r = \sqrt{\frac{\lambda_u}{2\lambda_l}\left(1 + \frac{K^2}{2}\right)}. \tag{2.81}$$

However, electrons in a bunch might have slight energy deviations, hence it is convenient to define the relative energy deviation:

$$\eta = \frac{\gamma - \gamma_r}{\gamma_r}. \tag{2.82}$$

Energy deviations from γ_r gives a non-zero derivative of the ponderomotive phase:

$$\frac{d\psi}{dt} = 2k_u c\eta. \tag{2.83}$$

From Eq. 2.76 we derive the variation of η:

$$\frac{d\eta}{dt} = -\frac{eE_0K}{2mc\gamma_r^2}\cos\psi. \tag{2.84}$$

Eq. 2.83 together with Eq. 2.84 describe the motion of the electron in the longitudinal phase space during the FEL process.
The radiation growth from pass to pass is quantified by the FEL gain function:

$$G = \frac{\Delta I_l}{I_l} \tag{2.85}$$

with $I_l = c\frac{\epsilon_0}{2}E_0^2$. For low-gain FELs the gain function is described by:

$$G(\omega) = -\frac{\pi e^2 \hat{K}^2 N_u^3 \lambda_u^2 n_e}{4\epsilon_0 mc^2\gamma_r^3} \cdot \frac{d}{d\xi}\left(\frac{\sin\xi^2}{\xi^2}\right) \tag{2.86}$$

where $\xi = \xi(\eta) = 2\pi N_u \eta$, $\hat{K} \equiv K \cdot JJ$, with

$$JJ = \begin{cases} J_0\left(\frac{K^2}{4+2K^2}\right) - J_1\left(\frac{K^2}{4+2K^2}\right) & \text{for a planar undulator} \\ 1 & \text{for a helical undulator} \end{cases} \tag{2.87}$$

with $K = \sqrt{2}a_w$ for a planar undulator and $K = a_w$ for a helical undulator and n_e is the density of electrons.

High gain FEL

Low-gain FELs are limited to the generation of wavelengths $\geq 100\,\text{nm}$ due to the existing mirror technology, in addition they are not competitive with the standard lasers. The X-ray free-electron laser oscillator (XFELO) is a proposed

scheme based on the low-gain FEL which overcomes the mirror limitation by exploiting narrow bandwidth diamond Bragg crystals [31]. The XFELO enables the generation of fully coherent X-ray radiation, however it is not experimentally demonstrated yet.

An experimentally demonstrated way to achieve shorter wavelengths, is based on radiation amplification in a single pass through an undulator. As a consequence, for this scheme we use a longer undulator and much more brighter electron beams compared to the low-gain FEL. There are two possible modes of operation for a high-gain FEL: self-amplified spontaneous emission (SASE) and seeding, which requires the use of an external coherent source. In the SASE process, initially the electrons emit spontaneous undulator radiation, that is used as seeding radiation for the remaining length of the undulator.

In high-gain FELs, the co-propagating radiation gains energy from the electrons due to the low-gain FEL process, as a result the electrons are energy modulated. As the electrons are going through the periodic trajectory within the undulator, electrons with higher energy are going through a shorter trajectory compared to low-energy electrons. In this way, the electrons form microbunches within the electron bunch at the distance of one radiation wavelength. This coherent distribution enhance the radiation growth, leading to an exponential growth.

In the following, we present a 1D treatment of the high-gain FEL based on the derivations presented in [27]. In this approximation we neglect the transverse electromagnetic field components and the transverse structures of the electron bunches and we assume that the electron bunches are infinitely long.

The high-gain FEL process can be described by a set of four coupled equations:

$$\frac{d\psi_n}{dz} = 2k_u\eta_n, \qquad n = 1, \ldots, N \tag{2.88a}$$

$$\frac{d\eta_n}{dz} = -\frac{e}{mc^2\gamma_r} Re\left[\left(\frac{\hat{K}\tilde{E}_x}{2\gamma_r} - \frac{i\mu_0 c^2}{\omega_l}\cdot\tilde{j}_1\right)e^{i\psi_n}\right] \tag{2.88b}$$

$$\tilde{j}_1 = j_0\frac{2}{N}\sum_{n=1}^{N} e^{-i\psi_n} \tag{2.88c}$$

$$\frac{d\tilde{E}_x}{dz} = -\frac{\mu_0 c\hat{K}}{4\gamma_r}\cdot\tilde{j}_1. \tag{2.88d}$$

The $\tilde{\cdot}$ indicates complex quantities and the index n identify the n-th electron in one slice of the bunch with a total of N electrons. Eqs. 2.88a and 2.88b correspond to the motion of the electrons in the longitudinal phase space that was already described in Eqs. 2.83 and 2.84. The second term in Eq. 2.88b arises from the amplitude of the current density modulation: $j(\tilde{\psi}, z) = j_0 + \tilde{j}_1(z)e^{i\psi}$ where the term $\tilde{j}_1(z)$ is described in Eq. 2.88c and it depends on the number of electrons per bunch slice N and on the continuous current density j_0.
Finally, Eq. 2.88d describes the derivative of the horizontal wave amplitude $\tilde{E}_x$ respect to the longitudinal position, which in the following will be indicated as: $\tilde{E}'_x$. Here we see that the current density modulation $\tilde{j}_1$ causes the growth of the light intensity in a high-gain FEL.
The coupled equations 2.88 do not have an analytical solution, but assuming that the periodic density modulation remains small, it is possible to eliminate the quantities ψ_n and η_n. In this way, it is derived an expression for the solely electric field amplitude $\tilde{E}_x(z)$, that can be solved analytically:

$$\frac{\tilde{E}'''_x}{\Gamma^3} + 2i\frac{\eta}{\rho}\frac{\tilde{E}''_x}{\Gamma^2} + \left[\frac{k_p^2}{\Gamma^2} - \left(\frac{\eta}{\rho}\right)^2\right]\frac{\tilde{E}'_x}{\Gamma} - i\tilde{E}_x = 0. \tag{2.89}$$

Here Γ is the gain parameter:

$$\Gamma = \frac{(\hat{K}e)^{2/3}}{\gamma_r}\left(\frac{\mu_0 k_u n_e}{4m}\right)^{1/3} \tag{2.90}$$

where $\hat{K}$ is the modified undulator parameter, μ_0 is the vacuum permeability, n_e is the electron density in the bunch slices, $k_u = 2\pi/\lambda_u$ where λ_u is the undulator period, γ_r is the resonant energy and m is the electron mass. In Eq. 2.89 it has been introduced the space charge parameter:

$$k_p = \sqrt{\frac{2\lambda_l}{\lambda_u}} \cdot \frac{\omega_p *}{c} \tag{2.91}$$

that depends on the plasma frequency:

$$\omega_p * = \sqrt{\frac{n_e e^2}{\gamma_r \epsilon_0 m}} \tag{2.92}$$

where ϵ_0 is the vacuum permittivity. Finally, ρ is the fundamental FEL parameter and it is adimensional:

$$\rho = \frac{\Gamma}{2k_u} \tag{2.93}$$

An equivalent definition of the FEL parameter is given from [32]:

$$\rho = \frac{1}{2\gamma}\left(\frac{I}{I_A}\right)^{1/3}\left(\frac{\lambda_u JJ}{2\pi\sigma_e}\frac{K}{\sqrt{2}}\right)^{2/3} \tag{2.94}$$

where γ is the electron beam energy, I is the electron beam current, $I_A = 17\,\mathrm{kA}$ is the Alfven current, JJ is the undulator coupling factor, which was defined in Eq. 2.87 and σ_e is the electron RMS transverse beamsize. This definition is very useful for practical calculation.
Now, we are going to solve Eq. 2.89 with the ansatz: $\tilde{E}_x(z) = Ae^{\alpha z}$. For $z \gg 1$ one gets [28]:

$$P(z) = \frac{P_0}{9}e^{\sqrt{3}\Gamma z} \equiv \frac{P_0}{9}e^{z/L_{G0}} \tag{2.95}$$

where L_{G0} is the gain length in the 1D approximation, which is defined as:

$$L_{G0} = \frac{1}{\sqrt{3}\Gamma} = \frac{\lambda_u}{4\pi\sqrt{3}\rho}, \tag{2.96}$$

and

$$P_0 = \frac{1}{8\pi}|\tilde{a}(0)|^2 P_s \tag{2.97}$$

where $\tilde{a}(0)$ is the normalized vector potential defined as $\tilde{a}_0 \equiv \frac{e\lambda\tilde{E}_0}{2\pi mc^2}$ and P_s is the saturation power [33]:

$$P_s \approx \rho P_{beam} \tag{2.98}$$

where $P_{beam} = \gamma_r mc^2 I_0/e$ is the beam power, where I_0 is the peak current. The FEL power profile $P(t)$ emitted from the electron beam at a certain location within the undulator can be integrated to get the FEL energy:

$$\varepsilon = \int P(t)dt \tag{2.99}$$

In Figure 6.12 is shown the whole evolution of the FEL power and the FEL energy along an undulator obtained with GENESIS1.3 version 4 [34] (see also appendix A), which is the code that is exploited for the simulation presented in the next chapters. The undulator exploited for this simulation has twelve sections, each section has a number of periods $N_u = 72$ and a period length

$\lambda_u = 33\,\text{mm}$. Here it is possible to identify an initial lethargy regime followed by the exponential growth expected from Eq. 2.95 and a final non-linear saturation region. The initial lethargy stage is the region where the three modes of the linear analysis interfere, until the divergent mode prevails. This region lasts longer if the initial condition are close to the equilibrium of the system. In Figure 2.6 it is shown the corresponding evolution of two buckets of the electron beam at the end of each undulator section. Until the fourth undulator there is almost no effect on the electron beam. From the fifth to the eighth undulator the electron beam is energy modulated, due to the energy exchange with the radiation. In the tenth undulator the electron bunch achieves the maximum bunching. In the two final undulator sections it happens the over-bunching. As a consequence the electron beam cannot transfer energy to the generated radiation anymore.

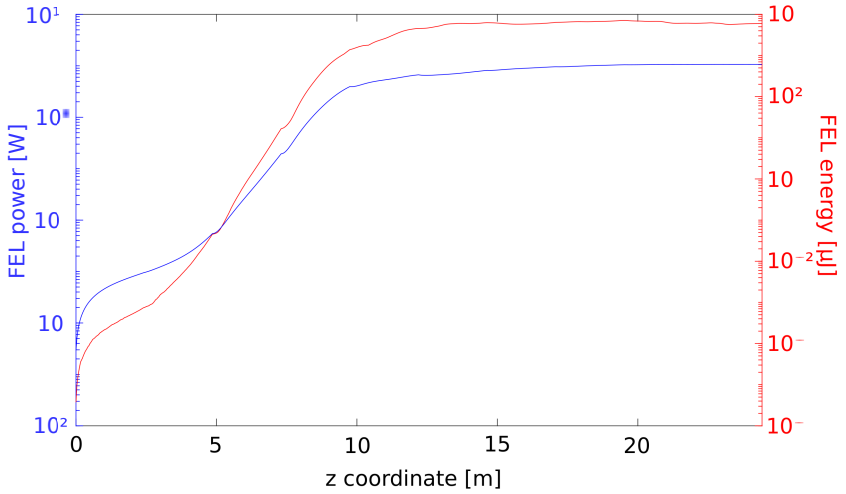

Figure (2.5) Gain curve of a FEL that starts from an electron beam without co-propagating radiation: In this plot it is possible to follow the characteristic evolution of the FEL: lethargy regime (up to 5 m), exponential growth (up to $\sim 12\,\text{m}$) and non-linear saturation (from $\sim 12\,\text{m}$ till the undulator end).

Undulator tapering In the high gain FEL the electrons loose a significant amount of energy along the long undulator due to the energy exchange with the generated radiation. As a result, to keep the FEL resonance condition 2.80 we can adjust the undulator strength: this procedure is called undulator tapering and was first proposed in [35]. Undulator tapering can also be exploited to compensate the energy chirp arising on the electron beam due to longitudinal space charge effects or to velocity bunching [36, 37].

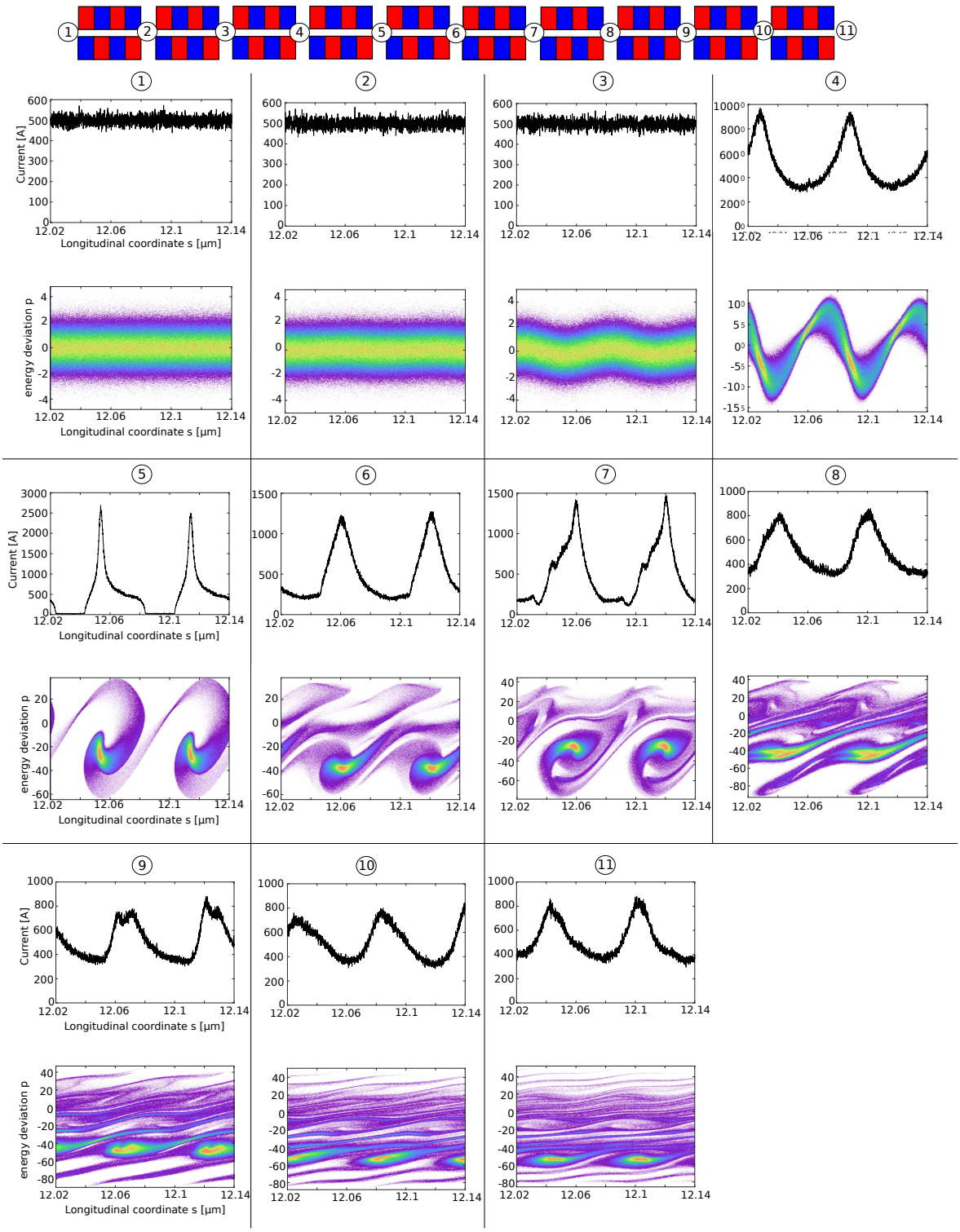

Figure (2.6) The top of this figure shows a scheme of the undulator and the numbers identify the position at which we have taken a 'photograph' of the electron beam. Below the undulator scheme, the top of each subplot shows the current profile of two buckets of the electron beam, the bottom subplot represents the longitudinal phase space distribution. With this figure it is possible to follow the movement of the electrons within the longitudinal phase space along the undulator.

Start-up with pre-bunched beam In this paragraph we describe the FEL startup process from an electron beam with a periodic charge density modulation described by:

$$j_z = j_0 + \tilde{j_1}(z)\exp(i\psi) \tag{2.100}$$

where ψ is the ponderomotive phase variable. In this case, we do not have radiation at the beginning of the undulator, so $E_0 \equiv \tilde{E}_x(0) = 0$, while the first derivative of the transverse electric field is non-zero:

$$E_0' \equiv \frac{d\tilde{E}_x}{dz}(0) = -\frac{\mu_0 c\hat{K}}{4\gamma_r}\cdot\tilde{j}_1(0) \tag{2.101}$$

and the second derivative reads:

$$E_0'' = -\frac{\mu_0 c\hat{K}}{4\gamma_r}\cdot\tilde{j}_1'(0). \tag{2.102}$$

The calculation of the first derivative of the charge density $\tilde{j}_1'(0)$ is given in [38], from which we get the second derivative of the electric field:

$$E_0'' = i2k_u\eta\frac{\mu_0 c\hat{K}}{4\gamma_r}\cdot\tilde{j}_1(0). \tag{2.103}$$

By solving Eq. 2.89 with these initial conditions we can derive again an exponential behavior as the one in Eq. 2.95. The field in Colson's dimensionless units is given by [33]:

$$a(\tau) = -2\pi g_0 b_1\frac{1-e^{-i\nu_0\tau}}{\nu_0} \tag{2.104}$$

where $g_0 = \frac{(k_u N_u\Gamma)^3}{\pi}$ is related with the gain parameter Γ, b_1 is the first term $n=1$ of the Fourier transform of the normalized electron beam current density ρ_e:

$$b_n = \frac{1}{\lambda_0}\int_0^{\lambda_0}\rho_e(\zeta)\exp(-i2\pi n\zeta/\lambda_0)d\zeta \tag{2.105}$$

where λ_0 is the resonant wavelength; $\tau = \frac{z}{N_u\lambda_u}$ and ν_0 is the detuning parameter $\nu_0 = 2\pi N_u(\omega_0-\omega)/\omega_0$. If we assume a system tuned at resonance: $\nu_0 = 0$, the FEL power evolution is given by:

$$P_{coh}(z) = \frac{1}{3}\rho_{FEL}|b_1|^2 P_{beam}\left(\frac{z}{L_G}\right)^2 \tag{2.106}$$

where $P_{beam} = mc^2\gamma I_{peak}/e$ is the power carried by the electron beam with relativistic factor γ. Equation 2.106 shows that the FEL power grows quadratic if the process is initiated by a pre-bunched beam, without co-propagating radiation.
In FEL seeding scheme we usually start from a pre-bunched beam, which is followed by a transition to the FEL growth due to the newly generated co-propagating radiation. The transition happens when the term from Eq. 2.106 is surpassed by the exponential term from Eq. 2.95, at a length within the undulator corresponding to $z_{th} = \sqrt{3}L_G$
[33]. The FEL power at the transition is:

$$P_{th} = \rho_{FEL}|b_1|^2 P_{beam}. \tag{2.107}$$

The function describing the evolution of the FEL power growth initiated by a pre-bunched beam is given by an initial quadratic growth up to z_{th} and followed by the exponential growth. An expression is derived in [33]:

$$P(z) = P_{th}\left[\frac{\frac{1}{3}\left(\frac{z}{L_G}\right)^2}{1+\frac{1}{3}\left(\frac{z}{L_G}\right)^2} + \frac{\frac{1}{2}\exp\left[\frac{z}{L_G}-\sqrt{3}\right]}{1+\frac{P_{th}}{2P_{F*}}\exp\left[\frac{z}{L_G}-\sqrt{3}\right]}\right] \tag{2.108}$$

where L_G is the gain length and $P_{F*} = P_F - P_{th}$ where $P_F \sim 1.6\rho_{FEL}P_{beam}$.
The equivalent beam shot-noise input power is obtained by solving the equation which matches the power given in Eq. 2.95 to the threshold power Eq. 2.107:

$$\frac{P_{eq}}{9}e^{\sqrt{3}} = \rho_{FEL}|b_1|^2 P_{beam} \tag{2.109}$$

so $P_{eq} \sim 1.6\rho_{FEL}|b_1|^2 P_{beam}$. The bunching coefficient for a randomly distributed electron beam is [33]:

$$b_1 \simeq \frac{1}{\sqrt{N}} \tag{2.110}$$

where N is the number of the electrons in one coherence length (Eq. 2.111).

2.3 SASE

So far it was discussed the static evolution of the FEL. Now, with the help of the GENESIS simulation code, it is possible to observe the dynamic evolution

of the FEL. The temporal profile of the radiation is shown in Fig. 2.7 together with its spectrum in correspondence of the end of the exponential gain region at 25 m of Fig. 2.5. The FEL power profile has several spikes all along the electron beam length and its spectrum is spiky as well. This behavior is typical of the self-amplified spontaneous emission (SASE) and it manifests because the radiation starts from the shot noise of the initially randomly distributed electron beam.
The radiation emitted is amplified coherently only along the coherence length L_C:

$$L_C = \sqrt{3} L_{G0} \left(\frac{\lambda}{\lambda_u} \right) \tag{2.111}$$

which is the slippage per gain length. Therefore, the FEL pulse shows a number of spikes equivalent to the number of L_C contained in the electron beam. If the electron beam length corresponds to the coherence length, the FEL pulse has only one spike that is Fourier-transformed limited. The spectrum is the Fourier transform of the radiation pulse. The overall bandwidth of the spectrum is $\Delta\omega/\omega \sim \rho$. For the SASE process the ρ-parameter defines the saturation length: $L_S \approx \lambda_u/\rho$ and the saturation power [32]:

$$P_S \sim 1.6 \rho P_{beam} \tag{2.112}$$

where $P_{beam} = mc^2 \gamma I_{peak}/e$ and I_{peak} is the peak current of the electron beam.

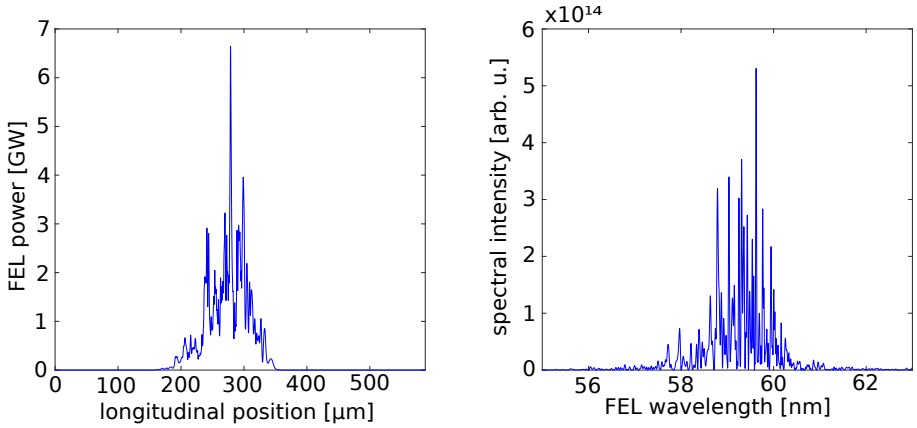

Figure (2.7) Left plot: power profile of the FEL pulse at 25 m dowstream the undulator (see Fig. 2.5). Right plot: corresponding spectrum of the FEL pulse from the right picture.

2.3.1 Ming-Xie model for FELs

Considering that the electron beam arrives from the linear accelerator with a finite energy spread, the FEL resonance condition 2.80 broadens. The resonance condition depends on the transverse beamsize of the electron beam as well. In addition, it is necessary to consider that the generated radiation naturally diffracts along the undulator.
Considering all these effects, the FEL performance degrades respect to the 1-D limit presented so far. Ming Xie has proposed correction factors for the estimation of the realistic gain length and the saturation power [39]:

$$\tilde{L}_G = \frac{L_{G0}}{\chi} \tag{2.113}$$

$$\tilde{P}_S = \chi^2 P_S. \tag{2.114}$$

The function χ depends on three parameters:

$$\eta_d = \frac{L_{G0}}{z_R}, \quad \eta_{epsilon} = \frac{L_{G0}}{\beta}\frac{4\pi\epsilon}{\lambda} \quad \eta_\gamma = 4\pi\frac{L_{G0}}{\lambda_u}\frac{\sigma_\gamma}{\gamma} \tag{2.115}$$

where $z_R = 4\pi\sigma_x^2/\lambda$ is the Rayleigh length of a radiation beam of wavelength λ and r.m.s. size euql to the projected electron beam r.m.s. transverse size σ_x, ϵ is the beam emittance and β the transverse Twiss coefficient. η_d, η_ϵ and η_γ quantifies the contribution due to respectively the diffraction effect of the radiation, the finite emittance and the non zero energy spread of the electron beam. The function χ is given by:

$$\chi(\eta_d, \eta_e, \eta_\gamma) = \frac{1}{1 + \sum a_n \eta_d^{\alpha_n} \eta_e^{\beta_n} \eta_\gamma^{\delta_n}} \tag{2.116}$$

The parameters are reported in table 2.1.

n	1	2	3	4	5	6	7
a_n	0.45	0.55	3	0.35	51	5.4	1140
α_n	0.57	0	0	0	0.95	0.7	2.2
β_n	0	1.6	0	2.9	0	1.9	2.9
δ_n	0	0	2	2.4	3	0	3.2

Table (2.1) Ming-Xie parameters.

2.3.2 Superradiance

Superradiance was showed analitically from Bonifacio [40] and was also observed experimentally [41]. Superradiance is a phenomena which arises once FEL saturation is achieved. It consists in the apparition of spikes at the extremities of the radiation pulse and it is determined from the relative slippage of the radiation and electron beams.

Superradiance happens when the electron bunch is longer respect to the region which was initially excited for radiation emission. The electrons outside the excited region have not been bunched and their energy spread was not heated from the FEL process. If the initial emitted radiation pulse is longer than the coherence length L_C, the superradiant spikes are observed at both the trailing and leading slippage regions of the pulse. While for a radiation pulse length shorter than L_C only one superradiant spike is observed.

The superradiant spike emitted from the trailing edge of the electron beam is identified as *weak superradiant pulse*. As the electrons in this region can only emit radiation, but cannot amplify it as the radiation is slipping in the forward direction. While the superradiant spike where the leading electrons are contributing is named as *strong superradiant pulse* as they are amplifying the pulse that was generated from the central region of the bunch.

The superradiance is an interesting phenomena which might be exploited for the generation of ultra-short pulses as the superradiant pulses narrow as the peak of the intensity increases [42].

is the saturation power [*The seeding techniques HGHG and EEHG*

Chapter 3

The seeding techniques: HGHG and EEHG

Besides using electron bunches as long as a coherence length, it is possible to obtain longitudinally coherent pulses also by initiating the FEL process with a coherent source, like a laser pulse. The electron beam interacts with the external seed laser and gets energy modulated. As a consequence, the dispersion in the undulator or a dedicated dispersion section converts the energy modulation into density modulation (bunching). At this point the electron beam emits fully coherent radiation at the wavelength of the coherent source and, respect to SASE the saturation length shortens. This scheme is named direct seeding. Its limitation is related to the minimum wavelength achievable by the available lasers with suitable power. The limit lies in the Ultraviolet (UV) range and the most common laser source used for this application is the third harmonic generation (THG) of the Titanium-Sapphire laser which have wavelengths between 235-330 nm. Alternative respect to using lasers it is to use high-harmonics generated in gas (HHG) [43], which was shown down to 38 nm and its second harmonic at 19 nm [44], however for the shorter wavelength the contrast with the SASE was only one order of magnitude. Direct seeding with HHG sources is currently limited for wavelengths below 10 nm due to the low peak power achievable with the HHG source. The transport and the focusing of the HHG radiation at this short wavelengths results to be extremely challenging from the technological point of view. In addition, to have a reliable seeded FEL with an HHG source it will be needed to find a method

to increase the signal to noise ratio between seeded signal and SASE [45].
The scientists are aiming at the study of molecular and atomic systems; consequently, it is needed radiation in the wavelength range between 100 nm and 1 Å. In order to overcome the mentioned limitations of direct seeding, many other seeding schemes have been proposed. In this thesis, the schemes that are going to be explained in detail are High-Gain Harmonic Generation (HGHG) and Echo-Enabled Harmonic Generation (EEHG).

3.1 HGHG

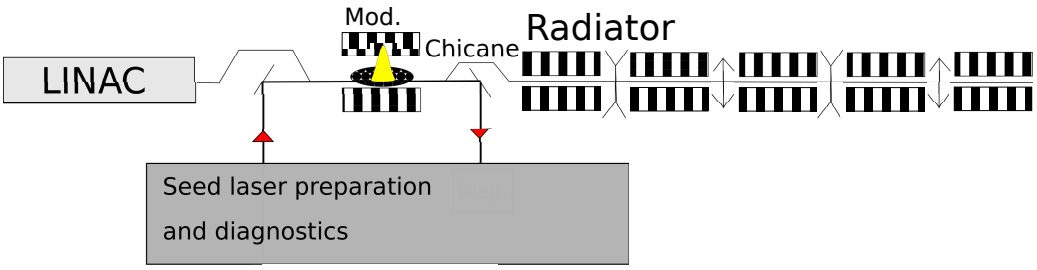

Figure (3.1) Setup for the HGHG scheme.

L. H. Yu [46] was the first to propose and demonstrate the High-Gain Harmonic Generation scheme (HGHG). The setup used for HGHG consists of an undulator, called modulator, where the electron beam interacts with a seed laser. Then a magnetic four-dipole chicane, which gives the dispersion needed to convert the energy modulation on the electron beam into density modulation. The bunching chicane is followed by a final undulator section called radiator where the manipulated electron beam radiates FEL radiation. Figure 3.1 shows the layout of the HGHG scheme.
The electron beam meets this setup after acceleration in a LINAC and proper preparation in terms of energy, current and beam size. Upstream the modulator, we assume that the electron beam has a uniform current profile and a Gaussian energy distribution. The energy standard variation is σ_E, and we define the energy through the parameter

$$p = (E - E_0)/\sigma_E \tag{3.1}$$

so that the initial distribution function of the beam is

$$f(p) = \frac{N_0}{\sqrt{2\pi}} e^{-p^2/2} \tag{3.2}$$

where N_0 is the number of particles per unit length of the beam. The beam overlaps in time and space with a seed laser of wavelength $\lambda_1 = 2\pi/k_1 = 2\pi c/\omega_1$ while it passes through the modulator, where c is the speed of light. As the modulator is tuned to be resonant at λ_1 the electron beam is energy modulated by the seed laser with periodicity λ_1. The energy modulation imprinted by the seed laser on the electron beam is ΔE.

The energy modulation ΔE is one of the two parameters that determine the bunching factor at a certain harmonic 3.13. Hence, it is fundamental to control this parameter carefully. An estimate is derived by solving Eq. 2.75. An approximated solution is given [47]:

$$\Delta E = mc^2 \sqrt{\frac{P_L}{P_0}} \frac{2KL_u JJ}{\gamma w_0} \cos(k_1 s) \tag{3.3}$$

where P_L is the seed laser power, $P_0 = I_A mc^2/e \approx 8.7\,\mathrm{GW}$ with $I_A = mc^3/e \approx 17\,\mathrm{kA}$, K is the undulator strength, $L_u = N_u \lambda_u$ is the total undulator length, JJ was defined in Eq. 2.87 and w_0 is the laser beam waist. The s variable represents the longitudinal coordinate along the electron beam. Equation 3.3 assumes a 1-D approximation where the seed laser is a planar wave. Besides the following assumptions are taken: the Rayleigh length z_R of the seed laser is longer than L_w, the seed laser waist is bigger than the electron transverse beam size, and the RMS duration of the seed laser is longer than the total slippage into the modulator.

The overall electron beam energy will transform after the modulator as follows:

$$p' = p + A\sin(\zeta) \tag{3.4}$$

where

$$A = \frac{\max[\Delta E(\zeta)]}{\sigma_E} \tag{3.5}$$

and

$$\zeta = k_1 z \tag{3.6}$$

is the dimensionless longitudinal coordinate of the beam. So, the distribution function will transform as:

$$f(\zeta, p) = \frac{N_0}{\sqrt{2\pi}} \exp\{-\left[\frac{(p - A\sin\zeta)^2\}}{2}\right] \tag{3.7}$$

in this equation we have renamed $p' \longleftarrow p$ for simplification. Then the electron

beam is sent to the chicane with strength R_{56} and the longitudinal coordinate becomes:

$$\zeta' = \zeta + R_{56} p k_1 \frac{\sigma_E}{E_0} \tag{3.8}$$

and the distribution function becomes:

$$f(\zeta, p) = \frac{N_0}{\sqrt{2\pi}} \exp\left[-\frac{1}{2}[p - A\sin(\zeta - Bp)]^2\right] \tag{3.9}$$

where

$$B = \frac{R_{56} k_1 \sigma_E}{E_0}. \tag{3.10}$$

The distribution of the particle beam density can be calculated with:

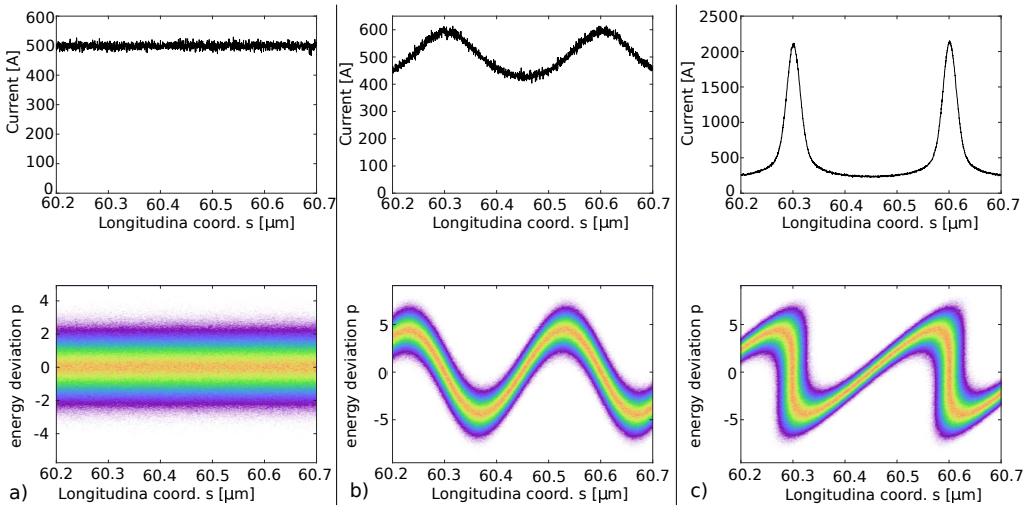

Figure (3.2) Evolution of the electron beam current profile (top) and longitudinal phase space distribution during the HGHG process. Here we focus to a small subset of the electron beam corresponding to a length of $2\lambda_1$. In a) is shown the status upstream the modulator (see Fig. 3.1). b) shows the electron beam after the interaction with the seed laser in the modulator. c) presents the electron beam downstream the magnetic chicane. These final current peaks are rich in harmonic content.

$$N(\zeta) = \int_{-\infty}^{+\infty} dp f(\zeta, p) \tag{3.11}$$

$N(\zeta)$ is a periodic function, therefore it is possible to expand it into Fourier series:

$$\frac{N(\zeta)}{N_0} = 1 + \sum_{n=1}^{+\infty} b_n \cos(n\zeta + \psi_n) \tag{3.12}$$

where b_n is the bunching factor of the harmonic n. The analytical expression for b_n [46]:

$$|b_n| = e^{-(1/2)B^2n^2}|J_n(ABn)| \tag{3.13}$$

where J_n is the Bessel function of order n. The dependence of the bunching factor respect to the two parameters ΔE and R_{56} is shown in Fig. 3.3. This Figure shows a typical plot called bunching map, which is a useful tool to determine the optimal working point for the HGHG FEL. During the decision process, it should be considered that the total energy spread on the electron beam should obey the condition:

$$\frac{\sigma_{E,tot}}{E_0} < \rho \tag{3.14}$$

where $\sigma_{E,tot} = \sqrt{\sigma_E^2 + \Delta E^2/2}$. Equation 3.14 tells that the energy spread must be smaller than the normalized bandwidth of the FEL gain [27]. The optimal FEL performances are achieved when the A and B parameters are chosen such that they satisfy the condition [48]

$$BA \approx 1 + 0.81n^{-2/3}. \tag{3.15}$$

Equation 3.13 shows that the bunching at the n harmonic is controlled by the dimensionless parameters A and B. From the physics point of view A is determined by the energy modulation on the electron beam, as shown in Eq. 3.5. While B is defined by the chicane dispersion R_{56} (Eq. 3.10). It is interesting to notice that, in the bunching factor defined in Eq. 3.13, the Bessel function argument ABn is uncorrelated energy spread independent, while the exponential factor is not. As a result, operating with a low-uncorrelated energy spread beam is advantageous because the exponential suppression contribution reduces.

The bunched beam injected into the forthcoming radiator tuned to one of the harmonics of the seed allow generation of coherent radiation that is amplified through the FEL process. While calculation of the bunching can be modelled by the prevoius Eq. 3.13; the FEL evolution in the radiator needs to be studies using suitable simuation codes such as Genesis. In Figure 3.4 is shown the typical HGHG FEL pulse predicted by simulations for the FEL operated at the fifth harmonic and before saturation. Both the power profile and the spectrum have Gaussian-like shapes close to the Fourier-limit. The trailing peak present in the power profile appears due to strong superradiance effects [49]. The longitudinal coherence driven by the coherent bunching that is starting up the process cleans

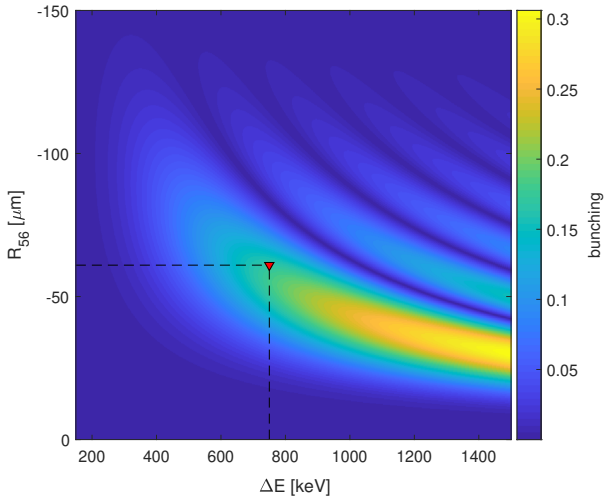

Figure (3.3) HGHG bunching factor in color-scale as a function of induced energy modulation ΔE and dispersion strength R_{56}. The highlighted red triangle is the working point chosen for the simulation that gave the phase space presented in Fig. 3.2. The target for the simulation was the fifth harmonic of a 300 nm seed laser. Using an electron beam with an energy of 750 MeV and an energy spread $\sigma_E = 150$ keV. The setup exploited in this simulation is going to be described in the chapter dedicated to the FLASH upgrade studies.

out the spiky structures of the SASE process 2.7. Generally, the exponential factor in Eq. 3.13 is a limiting factor for high harmonics. In order to minimize its effect, it would be necessary to select $B \sim 1/n$, and this implies that $A \sim n$ as the Bessel function is peaked when its argument is $\sim n$. On the other side, FEL lasing is guaranteed if the energy spread is of the order of the Pierce parameter: $\sigma_E/E \sim \rho$. For this reason, the HGHG scheme is limited to the generation of harmonics up to the thirteenth [14]. Hence, starting with a UV seed laser with a wavelength of 264 nm, the minimum wavelength achievable with the HGHG scheme is 20.3 nm. One, besides others, a possible scheme that enables to overcome this limitation is the Echo-Enabled Harmonic Generation.

3.1.1 Bunching for finite duration seed laser

The HGHG bunching factor in Eq. 3.13 is derived for a seed laser with an infinite duration and an electron beam with uniform longitudinal distribution, therefore a flat current profile. In this subsection, in the first place, we are going to derive

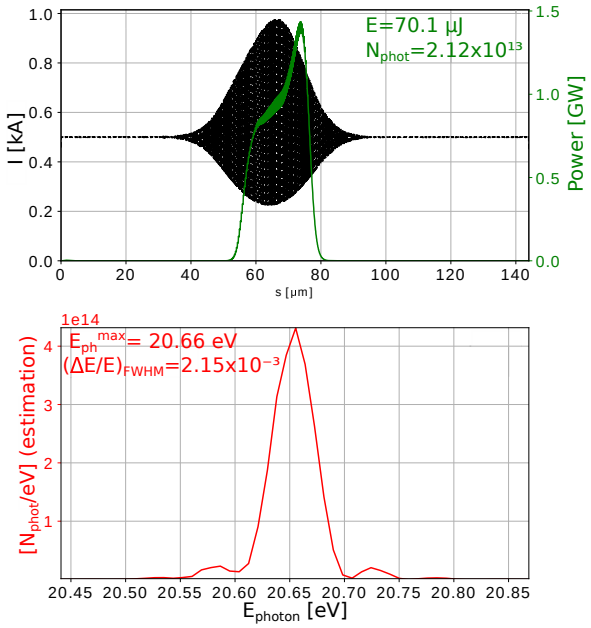

Figure (3.4) Top: current profile of the electron beam including fast current oscillations with FEL wavelength periodicity and emitted FEL power profile after 4 m into the undulator. The trailing peak in the power profile is due to the strong superradiance effect [49]. In the subplot is also given the energy of the FEL pulse **E** and the number of photons carried by the pulse N_{phot} Bottom: Spectrum of the corresponding FEL pulse. In the subplot we also give the peak photon energy E_{ph}^{max} and the relative bandwidth of the spectrum in FWHM $(\Delta E/E)_{FWHM}$

a more realistic bunching factor for a finite seed laser pulse, with a Gaussian temporal distribution. Afterwards, we see the effect of having a chirped seed laser phase on the bunching factor analytically and then prove it with simulations. The theoretical derivations are based on [48]

Spectral distribution from bunching The general definition for the dimensionless bunching factor at a given wavenumber k is defined as:

$$b(k) = \frac{1}{N_0}\langle e^{ikz} N(z)\rangle = \frac{1}{N_0 L}\int_0^L dz e^{ikz} N(z) \tag{3.16}$$

where N(z) is the 1D distribution of the beam density, N_0 is the averaged density and L is the length of the beam, so $N_0 L$ is the total number of particles in the bunch. This definition is very useful when dealing with infinite length of electron

and seed laser beams. As we want to analyse the effects of a finite duration seed laser, is more convenient to redefine the bunching as:

$$b(k) = \frac{1}{N_0}\int_0^L dz e^{ikz}\delta N(z) \tag{3.17}$$

where N of Eq. 3.16 is replaced by the density perturbation δN and the term $1/L$ is dropped. Now the bunching has a dimension of a length and it become dimensionless if multiplied by the laser wavenumber k_l.
Assuming that δN is a localized function, we extend the integration in Eq. 3.17 from $-\infty$ to $+\infty$, and the integral becomes the Fourier transformation:

$$b(k) = \frac{2\pi}{N_0}\delta\hat{N}(k) \tag{3.18}$$

where $\delta\hat{N}(k) = (2\pi)^{-1}\int_{-\infty}^{+\infty} dz e^{ikz}\delta N(z)$. This bunching definition has a relevant importance, in fact if we send an electron beam with the bunching factor $b(k)$ through a radiator in which a single electron radiates the spectrum $W(\omega)$, then the spectrum of the beam radiation is [48]:

$$W(\omega)N_0^2|b\left(\frac{\omega}{c}\right)|^2 \tag{3.19}$$

and the radiated energy is obtained by integration of this quantity over the frequency.

Variation of the laser amplitude in HGHG Typically the seed laser pulse is sitting on an electron beam that is longer, so we can assume that in the region where the laser is sitting the electron beam is still uniformly distributed as given in Eq. 3.2.
While the electron beam is passing through the modulator tuned to the seed laser central wavelength, it experiences an energy modulation. As the seed laser pulse has a power profile modelled by a Gaussian, the energy that is transferred to the electron beam will be Gaussian as well and can be described by:

$$A(\zeta) = A_0 e^{-\zeta^2/2\sigma_\zeta^2}. \tag{3.20}$$

Here $A(\zeta) = \Delta E(\zeta)/\sigma_E$, where $\Delta E(\zeta)$ is the local energy modulation transferred by the seed laser action, ζ is the longitudinal coordinate defined in Eq. 3.6, finally

σ_ζ is the dimensionless RMS length of the envelope of the electric field and is linked to the RMS length of the laser power σ_t as $\sigma_\zeta = \sqrt{2}ck_1\sigma_t$. The longitudinal coordinate after passing through the modulator and chicane transforms as:

$$\zeta^{'} = \zeta + Bp + BA(\zeta)\sin\zeta \tag{3.21}$$

where B was defined in Eq. 3.10.
The amount of bunching at the wavelength $\lambda = 2\pi/k$ is calculated by Fourier-transforming Eq. 3.11:

$$b(\kappa) = \frac{1}{k_1 N_0}\int_{-\infty}^{+\infty} dp f(p) \int_{-\infty}^{+\infty} d\zeta \left(e^{-i\kappa\zeta^{'}(\zeta,p)} - e^{-i\kappa\zeta}\right) \tag{3.22}$$

where $\kappa = k/k_1$ and $f(p)$ is defined in 3.2. The second exponential represents the initial distribution of the electron beam and can be neglected since it gives null contribution to the bunching.
By inserting 3.21 in 3.22 we get:

$$k_1 b(\kappa) = \frac{1}{N_0}\int_{-\infty}^{+\infty} dp f(p) \int_{-\infty}^{+\infty} d\zeta e^{-i\kappa\zeta} e^{-i\kappa Bp} e^{-i\kappa BA(\zeta)\sin\zeta} \tag{3.23}$$

Inserting $f_0(p)$ which was defined in 3.2:

$$k_1 b(\kappa) = \frac{1}{N_0}\frac{N_0}{\sqrt{2\pi}}\int_{-\infty}^{+\infty} dp e^{-p^2/2} e^{-i\kappa Bp} \int_{-\infty}^{+\infty} d\zeta e^{-i\kappa\zeta} e^{-i\kappa BA(\zeta)\sin\zeta} \tag{3.24}$$

solving then the first integral:

$$k_1 b(\kappa) = e^{-\kappa^2 B^2/2}\int_{-\infty}^{+\infty} d\zeta e^{-i\kappa\zeta} e^{-i\kappa BA(\zeta)\sin\zeta} \tag{3.25}$$

using the Jacobi-Anger expansion: $e^{iz\sin\phi} = \sum_{n=-\infty}^{+\infty} J_n(z)e^{in\phi}$

$$k_1 b(\kappa) = e^{-\kappa^2 B^2/2}\sum_{n=-\infty}^{+\infty}\int_{-\infty}^{+\infty} d\zeta J_n(-\kappa BA(\zeta)) e^{-i(\kappa-n)\zeta} \tag{3.26}$$

setting $\Delta\kappa = \kappa - n$ we can find the bunching near the harmonic n, by considering only the n component of the series:

$$k_1 b_n(\Delta\kappa) = e^{-\kappa^2 B^2/2}\int_{-\infty}^{+\infty} d\zeta J_n(-\kappa BA(\zeta)) e^{-i\Delta\kappa\zeta} \tag{3.27}$$

Assuming $\Delta\kappa \ll n$ we have that $n \approx \kappa$ and introducing $A(\zeta)$ form 3.20 we get:

$$k_1 b_n \approx e^{-n^2B^2/2} \int_{-\infty}^{+\infty} d\zeta J_n(-nBA_0 e^{-\zeta^2/2\sigma_\zeta^2}) e^{-i\Delta\kappa\zeta} \tag{3.28}$$

using the following variable substitution $\xi = \zeta/\sigma_\zeta$ we get:

$$k_1 b_n(\Delta\kappa) = \sigma_\zeta e^{-n^2B^2/2} \int_{-\infty}^{+\infty} J_n(-nBA_0 e^{-\xi^2/2}) e^{-i\Delta\kappa\sigma_\zeta\xi} \tag{3.29}$$

At this point we assume that $n \gg 1$. We showed in Eq. 3.15 that for a seed laser with infinite duration the parameters maximizing the bunching are given by $BA \approx 1 + 0.81n^{-2/3}$. Now we assume that with a finite seed pulse duration the performance will be partially deteriorated, so a corrector factor r is introduced as ansatz:

$$BA_0 \approx r(1 + 0.81n^{-2/3}) \tag{3.30}$$

inserting it in the bunching formula and changing the sign of the bessel function using $J_n(-x) = (-1)^n J_n(x)$ we get:

$$b_n(\Delta\kappa) \approx (-1)^n \sigma_z e^{-n^2r^2(1+0.81n^{-2/3})/2A_0^2} F_n(\Delta\kappa\sigma_\zeta, r) \tag{3.31}$$

where $\sigma_z = \sigma_\zeta/k_1$ and

$$F_n(x, r) = \int_{-\infty}^{+\infty} d\xi J_n(r(n + 0.81^{1/3}) e^{-\xi^2/2}) e^{-ix\xi} \tag{3.32}$$

When $A_0 \gg 1$ we can approximate the exponential to 1 and we get the following estimation for the bunching factor [48]:

$$|b_n(\Delta\kappa)| \approx \sigma_z |F_n(\Delta\kappa\sigma_\zeta, r)| \tag{3.33}$$

Analytically it is possible to observe that the bunching spectral profile width increases as the harmonic number grows, therefore the temporal bunching profile pulse length [48] is shorter at high harmonics respect to low harmonics. Also, by increasing the r parameter the bunching peak increases.
Taking into consideration the sFLASH setup, that is going to be presented in the next chapter, this bunching behaviour has been verified with GENESIS v.4 simulations. We optimized the setup for the fifth and the tenth harmonic of the 267 nm seed laser. The seed laser duration assumed for these simulations is

$\sigma_t = 31.7\,\text{fs}$ RMS. The seed laser pulse length at sFLASH is typically $> 148\,\text{fs}$, but here we assume a shorter pulse to reduce the computational time needed for the simulations. In fact, the seed laser should overlap longitudinally to the electron beam, so, if the laser pulse is shorter also the electron beam bunch length can be reduced. As a result the needed simulation window also reduces.
The HGHG optimization is performed by setting the maximum A parameter close to the harmonic number, in this case, $A_5 = 4.8$ and $A_{10} = 10$. Then, the chicane strength is scanned until the value maximizing the bunching is found. Once the chicane dispersion ($B \propto R_{56}$) is set, we extract the effective value of the r parameter presented in Eq. 3.30. Indicating r_n the parameter for the n-th harmonic, based on the parameters exploited in the Genesis simulation, we have found using Eq. 3.30:

$$r_5 = 0.87, \qquad r_{10} = 0.82. \tag{3.34}$$

The Fourier-transform of the bunching after the chicane is shown in Fig. 3.5a for harmonic 5 and 10 and is compared to the spectrum of the seed laser, normalized by 1. We notice that the width of the spectral bunching increases with the harmonic number. Figure 3.5b shows the RMS width of the bunching spectra for harmonic 5 and 10 and the width of the seed laser spectrum. The increment in duration confirms that higher harmonics are more sensitive to the deviation from the optimization condition Eq. 3.30, as it was observed already from the estimated r-s in Eq. 3.34. If the bunching is transformed back to the time variable, the pulse length decreases as the harmonic number increases. As a consequence, we expect to have shorter pulses for higher harmonics. In the following, we analyse the evolution of the FEL pulses along the radiator, generated from the bunched beam at the fifth and tenth harmonic. In [50] it is described the evolution of the FEL pulse along the radiator. Here it is given an estimate of the FEL RMS duration when the bunching is maximized $b = b_{max}$:

$$\sigma_{FEL}(n, b_{max}) \sim \frac{7}{6}\frac{\sigma_t}{n^{1/3}} \tag{3.35}$$

when instead we are far from the maximum bunching, the minimum duration of the FEL pulse that we can expect is

$$\sigma_{FEL}(n, b) \sim \frac{\sigma_t}{\sqrt{n}} \tag{3.36}$$

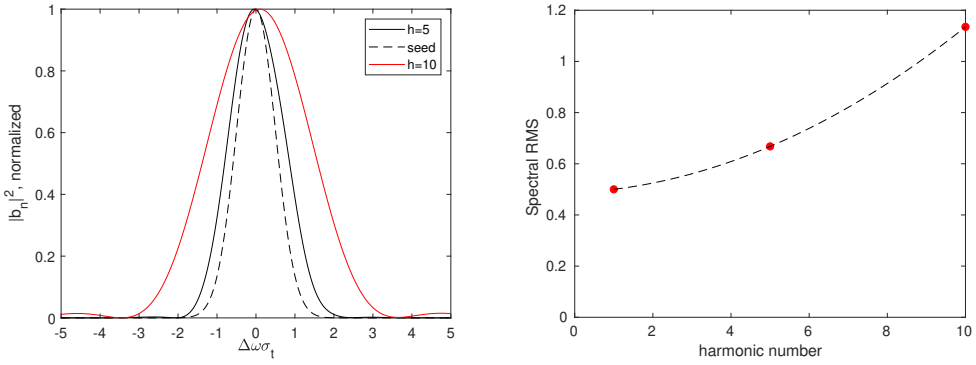

(a) (b)

Figure (3.5) a) Spectral bunching factor for harmonics 5, 10 and, in dashed-black line, seed laser spectral profile normalized to 1. The bandwidth increases for higher harmonics as expected from theory. b) The point corresponding to the first harmonic represents the RMS bandwidth of the normalized seed laser spectrum. The two other points are the RMS bandwidth of the spectral bunching profiles from Fig. 3.5a. The RMS is with no dimensions as it is calculated respect to $\Delta\omega\sigma_t$.

as demonstrated in [50]. For the fifth and the tenth harmonic it results:

$$\sigma_{FEL}(5, b_{max}) = 21.6\,\text{fs}, \qquad \sigma_{FEL}(10, b_{max}) = 17.2\,\text{fs}. \tag{3.37}$$

In Fig. 3.6 and in Fig 3.7 are shown three plots for each figure: the top left plot is the evolution of the FEL power along with the radiator, the bottom left plot shows the evolution of the RMS duration of the FEL pulse along with the radiator and the plot on the right shows the FEL profile at the end of the radiator and at the location where is achieved the RMS value is foreseen from Eq. 3.35. For both cases, we have used tapering in the radiator, and an electron beam matched to a FODO lattice.

The red dashed line in the bottom left plot of Figs. 3.6 and 3.7 remark the value of the FEL duration estimated from Eq. 3.35. For the fifth harmonic (Fig. 3.6) the $\sigma_{FEL}(5, b_{max}) = 21.6\,\text{fs}$ is achieved already after $\sim 5\,\text{m}$ within the radiator. After this point, the saturation regime starts. The saturation regime is characterized by the suppression of the exponential growth at the pulse peak position, while it continues on the leading and trailing edge of the pulse [50]. As a consequence, there is a visible increase of the pulse length, spectral broadening and appearance of structures in the spectrum as can be seen in the spectrum in the left plot of Fig. 3.8. The calculated RMS duration at the end of the radiator is $\sigma_{FEL}(5) =$

44 fs.

The evolution of the FEL tuned at the tenth harmonic is shown in Fig. 3.7. Here $\sigma_{FEL}(10, b_{max})$ is achieved almost at the end of the radiator. Therefore we do not see significant saturation effects in this case. As we can also notice from the spectra at the end of the radiator in Fig. 3.8. The duration of the FEL at the very end of the radiator is $\sigma_{FEL}(10) = 19\,\text{fs}$. In Fig. 3.8 the FEL spectra are

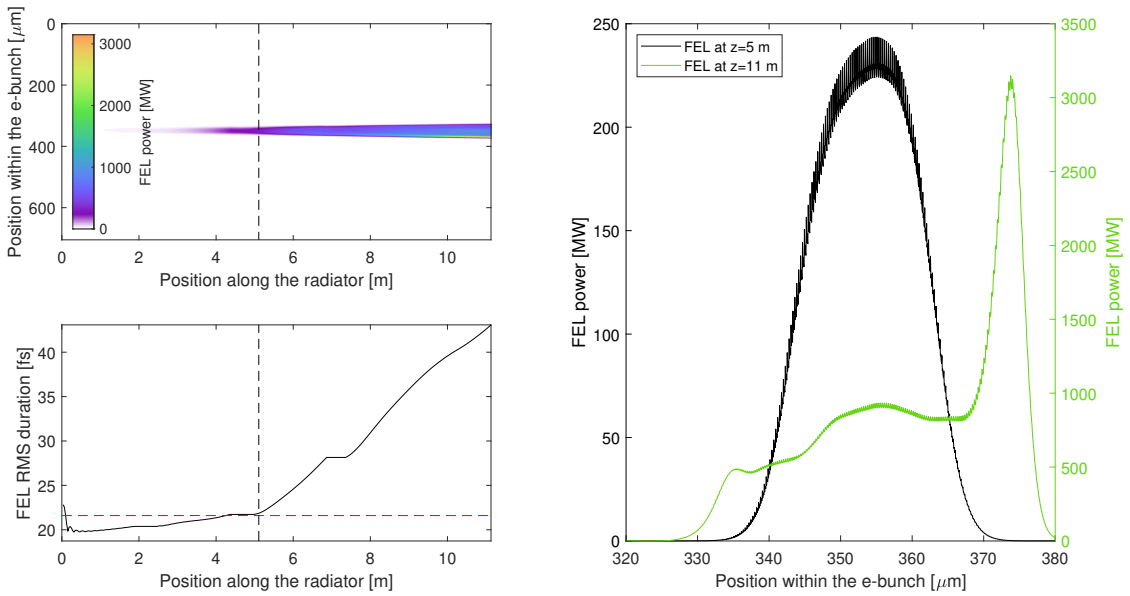

Figure (3.6) HGHG at the 5^{th} harmonic. In the plots on the left: the upper one shows the evolution of the FEL power profile, while the bottom one shows the evolution of the FEL RMS pulse length along the radiator. In the bottom left plot the red-dashed line indicates the the value of the FEL RMS pulse length estimated with Eq. 3.35. On the right plot, we show the FEL pulse at the end of the radiator and at the position where the FEL achieves the RMS pulse length foreseen from theory, in this case after 5 m within the radiator section.

shown for the fifth and tenth harmonic at the end of the radiator.

3.1.2 Bunching for a finite duration seed laser with a frequency chirp

It might happen that the laser has a frequency chirp in its phase, in this case we can reformulate the bunching factor accordingly.

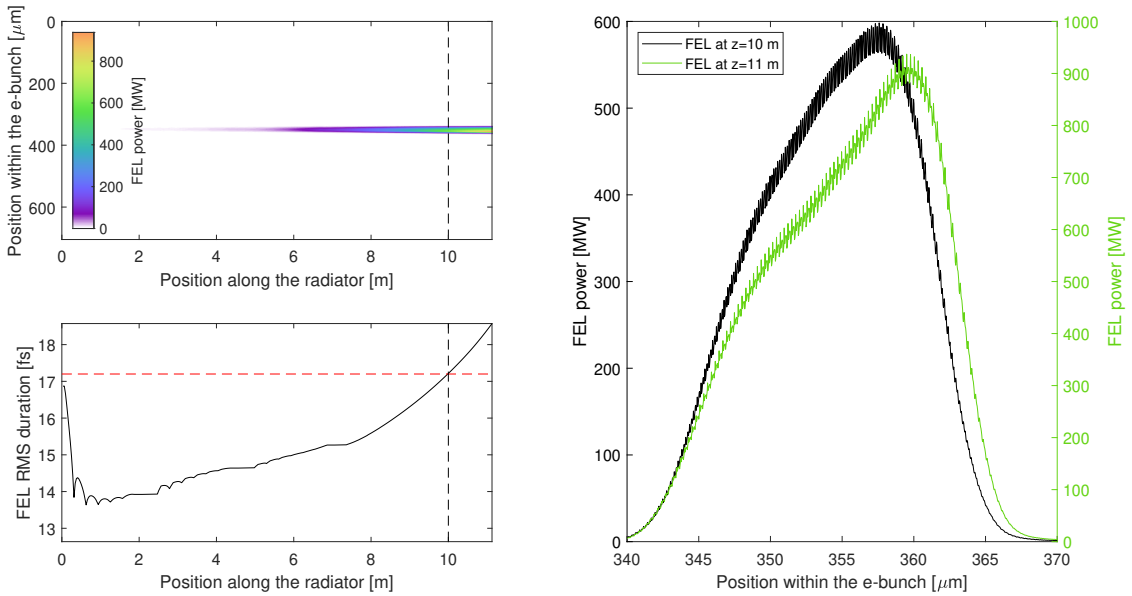

Figure (3.7) HGHG at the 10^{th} harmonic. In the plots on the left: the upper one shows the evolution of the FEL power profile, while the bottom one shows the evolution of the FEL RMS pulse length along the radiator. In the bottom left plot the red-dashed line indicates the the value of the FEL RMS pulse length estimated with Eq. 3.35. On the right plot, we show the FEL pulse at the end of the radiator and at the position where the FEL achieves the RMS pulse length foreseen from theory, in this case after 10 m within the radiator section.

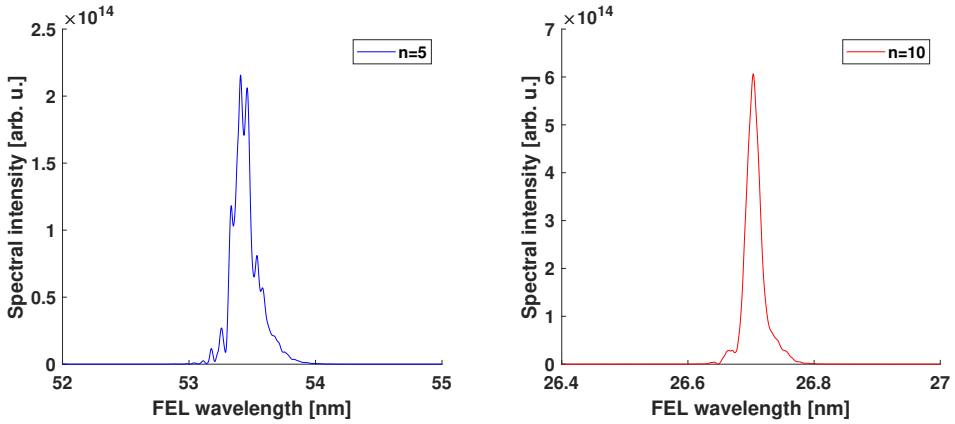

Figure (3.8) FEL spectra at the end of the sFLASH radiator for harmonics 5 and 10. We can observe a shortening of the bandwidth from the fifth to the tenth harmonic.

How is defined the frequency chirp The propagation of a light pulse in vacuum can be described by the Maxwell equations:

$$\nabla \cdot \mathbf{E} = \frac{\rho}{\epsilon_0} \tag{3.38}$$

$$\nabla \cdot \mathbf{B} = 0 \tag{3.39}$$

$$\nabla \times \mathbf{E} = -\frac{\partial \mathbf{B}}{\partial t} \tag{3.40}$$

$$\nabla \times \mathbf{B} = \mu_0 \mathbf{J} + \frac{1}{c^2}\frac{\partial \mathbf{E}}{\partial t} \tag{3.41}$$

To describe the light propagation in vacuum, where $\rho = 0$ and $\mathbf{J} = \mathbf{0}$, by taking the partial temporal derivative of 3.41 and using 3.40 we obtain the wave equation for the electric field of the light pulse [51]:

$$\nabla^2 E = \frac{1}{c^2}\frac{\partial^2 E}{\partial t^2} \tag{3.42}$$

with $c = 1/\sqrt{\epsilon_0 \mu_0}$. The solution of the wave equation for a finite light pulse is given by:

$$E(t) = E_0 e^{(-\Gamma t^2 + i\omega_0 t)} \tag{3.43}$$

where $\Gamma = 1/2\sigma_{tE}^2 = 1/4\sigma_{tI}^2$, σ_{tE} is the RMS duration of the electric field and σ_{tI} is the RMS duration of the intensity ($I(t) = |E(t)|^2$) of the light pulse and ω_0 is the central frequency. The complex argument represents the phase Φ of the electric field and this information is completely lost when the intensity of the pulse is measured. In general, once the temporal distribution of the electric field is known is possible to derive the expression for the spectral distribution applying the Fourier-Transform [51]:

$$E(\omega) = \int_{-\infty}^{+\infty} E(t) e^{i\omega t} dt \tag{3.44}$$

and vice-versa:

$$E(t) = \frac{1}{2\pi}\int_{-\infty}^{+\infty} E(\omega) e^{-i\omega t} d\omega \tag{3.45}$$

The Fourier-Transform of the 3.43 gives:

$$E_0(\omega) = \exp\left[\frac{-(\omega-\omega_0)^2}{4\Gamma}\right] \tag{3.46}$$

this result shows that the duration of the light pulse and its bandwidth are related, as the Γ parameter appears in 3.46. The particular relation between Gaussian pulses for FWHM duration of the intensity profile $\Delta t_I = 2\sqrt{2\log 2}\sigma_{tI}$ and bandwidth $\Delta\omega$ is

$$\Delta t_I \Delta\omega \geq 2\pi \cdot 0.441. \tag{3.47}$$

Equation 3.47 is called time-bandwidth product (TBP) and it states that given a fix bandwidth, there is always a minimum duration of a light pulse that cannot be decreased [51]. The same product can be given with the root mean square quantities of the intensity profile:

$$\sigma_{tI}\sigma_\omega \geq \frac{1}{2} \tag{3.48}$$

if the equality is valid, the pulse is said to be Fourier-transform-limited.
Equation 3.43 describes a Fourier-transformed limited pulse, because the angular frequency $\omega(t) = \partial\Phi/\partial t = \omega_0$ is a constant of time. If this is not the case, the pulse is said to be **chirped**. This may happen when the phase of the light pulse develops a quadratic dependence for example:

$$E(t) = \Re\left[E_0 e^{[-\Gamma t^2 + i(\omega_0 t + \alpha t^2)]}\right] \tag{3.49}$$

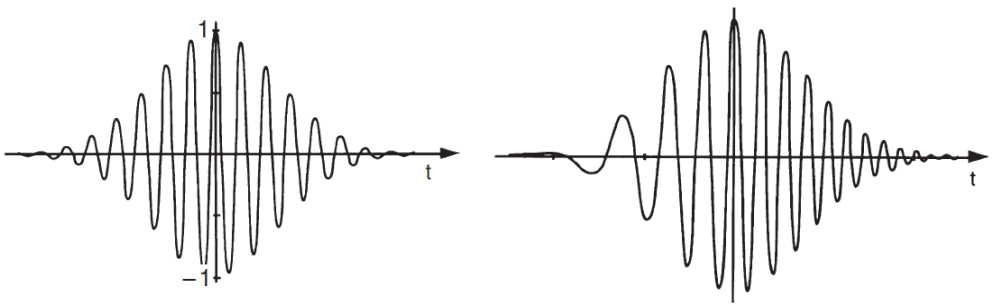

(a) (b)

Figure (3.9) a) Electric field of a laser pulse with no frequency chirp. b)Electric field of a laser pulse with a linear positive chirp in frequency: red comes earlier and blue follows. Figures from [51].

with $\alpha > 0$ so the angular frequency varies linearly $\omega(t) = \partial\Phi/\partial t = \omega_0 +$

αt [51]. This means that the trailing part of the pulse is more blue and the leading part of the pulse is more red.
When the laser pulse is chirped, the identity of Eq 3.48 is not valid and the product is greater then $\frac{1}{2}$. In the next paragraph, we are going to quantify how much greater then $\frac{1}{2}$ is the TBP.

How can a laser develop a chirp When a laser propagates through a transparent medium, it undergoes a phase distortion inducing an increase of its duration, because of its wide spectral width and group velocity dispersion [51]. To see what happens in the transparent medium, it is easier to observe the effect on the Fourier transform of the Gaussian pulse, that was given in Eq. 3.46. After the pulse propagates for a distance x, the spectrum looks:

$$E(\omega, x) = E_0(\omega) \exp\left[-ik(\omega)x\right] \tag{3.50}$$

where $k(\omega) = n\omega/c$ is a frequency dependent propagation factor. Assuming $\Delta\omega \ll \omega_0$ we can Taylor expand the propagation factor $k(\omega)$:

$$k(\omega) = k(\omega_0) + k'(\omega - \omega_0) + \frac{1}{2}k''(\omega - \omega_0)^2 + \dots \tag{3.51}$$

where:

$$k' = \left(\frac{dk(\omega)}{d\omega}\right)_{\omega_0} \tag{3.52}$$

and

$$k'' = \left(\frac{d^2k(\omega)}{d\omega^2}\right)_{\omega_0}. \tag{3.53}$$

the term in Eq. 3.53 is the **group velocity dispersion** (GVD). Inserting Eq. 3.51 in Eq. 3.50 and explicating $E_0(\omega)$ the pulse spectrum becomes:

$$E(\omega, x) = \exp\left[-ik(\omega_0)x - ik'x(\omega - \omega_0) - \left(\frac{1}{4\Gamma} + \frac{i}{2}k''x\right)(\omega - \omega_0)^2\right]. \tag{3.54}$$

This equation can be expressed as:

$$E(\omega, x) = E_0(\omega) \exp\left(-i\phi(\omega)\right) \tag{3.55}$$

where $E_0(\omega)$ is defined in Eq. 3.46 and

$$\phi(\omega) = \phi_0 + \tau_d(\omega - \omega_0) + \frac{1}{2}\beta(\omega - \omega_0)^2 \tag{3.56}$$

with

$$\tau_d = \left.\frac{\partial\phi}{\partial\omega}\right|_{\omega_0} = k'x \tag{3.57}$$

describing the **group delay** and

$$\beta = \left.\frac{\partial^2\phi}{\partial\omega^2}\right|_{\omega_0} = k''x \tag{3.58}$$

the **group delay dispersion** (GDD) [52].
The Fourier transform of Eq. 3.54 gives the time evolution of the electric field:

$$E(t,x) = \sqrt{\frac{\Gamma(x)}{\pi}}\exp\left[i\omega_0\left(t - \frac{x}{v_\phi(\omega_0)}\right)\right] \times \exp\left[-\Gamma(x)\left(t - \frac{x}{v_g(\omega_0)}\right)^2\right]. \tag{3.59}$$

The first exponential of Eq. 3.59 shows that the phase of the central phase ω_0 is delayed by the term x/v_ϕ where

$$v_\phi(\omega_0) = \left(\frac{\omega}{k}\right)_{\omega_0} \tag{3.60}$$

is the phase velocity, which is the speed of the plane-wave components of the pulse in the medium. The second exponential of Eq. 3.59 shows that after propagation along a distance x the pulse still has a Gaussian envelope. However this envelope is delayed by x/v_g, where

$$v_g = \left(\frac{d\omega}{dk}\right)_{\omega_0} \tag{3.61}$$

is the group velocity and it corresponds to $v_g = 1/k'$, where k' was defined in Eq. 3.52. In addition, the pulse envelope is distorted during the propagation along the transparent medium by $\Gamma(x)$:

$$\frac{1}{\Gamma(x)} = \frac{1}{\Gamma} + 2ik''x. \tag{3.62}$$

This term is the source of the duration broadening [51]. Now, we want to isolate all the complex terms in only one exponential, so we rewrite Eq. 3.62 as:

$$\Gamma(x) = \frac{\Gamma}{1+\eta^2x^2} - i\frac{\Gamma\eta x}{1+\eta^2x^2} \tag{3.63}$$

where $\eta = 2\Gamma k''$ and we introduce it in Eq. 3.59, and we get an exponential with complex argument:

$$\exp\left\{ i\left[\omega_0 \left(t - \frac{x}{v_\phi(\omega_0)} \right) + \frac{\Gamma \eta x}{1+\eta^2 x^2} \left(t - \frac{x}{v_g(\omega_0)} \right)^2 \right] \right\} \tag{3.64}$$

here we can define the argument of this exponential as:

$$\phi(t) = \phi_0 + \omega_0 \left(t - \frac{x}{v_\phi(\omega_0)} \right) + \frac{1}{2}\alpha \left(t - \frac{x}{v_g(\omega_0)} \right)^2 \tag{3.65}$$

where the angular frequency is:

$$\omega(t) = \omega_0 \left(t - \frac{x}{v_\phi(\omega_0)} \right) + \frac{1}{2}\alpha \left(t - \frac{x}{v_g(\omega_0)} \right)^2 \tag{3.66}$$

and

$$\alpha = 2\frac{\Gamma \eta x}{1+\eta^2 x^2} = \frac{\partial^2 \phi}{\partial t^2}\Big|_{\omega_0} \tag{3.67}$$

is the **chirp** parameter [52]. If we express α as a function of σ_{tI} and $GDD = k''x$ we get:

$$\alpha = \frac{GDD}{(2\sigma_{tI}^2)^2 + GDD^2} \tag{3.68}$$

that it is a useful equation when we want to determine the chirp of the pulse, when we know the GDD. We have a positive chirp $\alpha > 0$ when the angular frequency $\omega(t)$ grows linearly with time along the pulse. While we have a negative chirp $\alpha < 0$ when $\omega(t)$ decreases linearly with time within the pulse.
The exponential with real argument results:

$$\exp\left[-\frac{\Gamma}{1+\eta^2 x^2} \left(t - \frac{x}{v_g(\omega_0)} \right)^2 \right]. \tag{3.69}$$

Here we notice that, if we start with an unchirped laser pulse with intensity RMS duration σ_{tI}, from Eq. 3.49 we have $\Gamma = \frac{1}{4\sigma_{tI}^2}$. After passing through a transparent medium, the RMS duration increases by:

$$\sigma_{tcI}^2 = (1+\eta^2 x^2)\sigma_{tI}^2 \tag{3.70}$$

as we can derive from Eq. 3.69. The same equation can be expressed in a form which is useful while studying experimental and simulation results:

$$\sigma_{tcI}^2 = \sigma_{tI}^2 \left(1 + \frac{GDD^2}{(2\sigma_{tI}^2)^2}\right) \tag{3.71}$$

Recalling that $\eta = 2\Gamma k''$, we have that Γ is a positive quantity and the sign of k'' is determined by the dependence of the refraction index of the material respect to the frequency. k'' is positive when the index of refraction diminishes as the wavelength increases, otherwise is negative. It is possible to build up gratings systems with the desired sign of k'' [51].

When a chirped pulse with GDD_1 pass through a material with dispersion with length l and group velocity dispersion GVD, the material adds to the pulse the group delay dispersion $GDD_2 = GVD \cdot l$. Therefore the GDD of the out coming pulse is given by: $GDD_f = GDD_1 + GDD_2$.

At this point, we can express the time bandwidth product for a chirped laser pulse as:

$$\sigma_{tcI}\sigma_\omega \geq \frac{1}{2} \tag{3.72}$$

using Eq. 3.48 and Eq. 3.71 we can derive the equality:

$$\sigma_{tcI}\sigma_\omega = \frac{1}{2}\sqrt{1+a^2} \tag{3.73}$$

where

$$a = \frac{GDD}{2\sigma_{tI}^2}. \tag{3.74}$$

This relation is very useful, because when we have a pulse we can measure its spectral bandwith, that can be used to get the duration of the transform limited pulse σ_{tI} using Eq. 3.73 with $a = 0$. Afterwards, we can measure the duration of the pulse σ_{tcI} and together with the measured spectral bandwidth, we calculate the TBP from which is possible to extract a and consequently, from Eq. 3.74 the GDD. Finally, exploiting Eq 3.68 the chirp of the seed laser is quantified.

Reformulation of the bunching factor If we consider the Gaussian seed laser pulse from Eq. 3.59, which phase is described by Eq. 3.65, it holds an angular frequency given by:

$$\omega = \omega_0 + \alpha\left(t - \frac{x}{v_g(\omega_0)}\right). \tag{3.75}$$

The accumulated phase error is defined by $\Phi = \frac{\alpha}{2}\Delta t^2$ [48], where Δt is the FWHM duration of the seed laser pulse. Assuming $\Phi \ll 1$, the electron beam longitudinal coordinate at the end of the HGHG setup that uses the presented seed laser transforms as:

$$\zeta' = \zeta + Bp + BA(\zeta)\sin(\zeta + \iota\zeta^2) \tag{3.76}$$

where $\zeta = \omega_0 t$ and $\iota = \frac{\alpha}{2\omega_0^2}$. Having this coordinate transformation, now Eq. 3.26 results:

$$k_l b(\kappa) = e^{-k^2B^2/2} \sum_{n=-\infty}^{+\infty} \int_{-\infty}^{+\infty} d\zeta J_n(-kBA(\zeta)) e^{-i(\kappa-n)\zeta + in\iota\zeta^2} \tag{3.77}$$

using Eq. 3.30 we get [48]:

$$k_l b_n(\Delta\kappa) = (-1)^n \sigma_\zeta e^{-n^2r^2(1+0.81n^{-2/3})^2/2A_0^2} G_n(\Delta\kappa\sigma_\zeta, n\iota\sigma_\zeta^2, r) \tag{3.78}$$

with

$$G_n(x, y, r) = \int_{-\infty}^{+\infty} d\xi J_n(r(n + 0.81n^{1/3}) e^{-xi^2/2}) e^{-ix\xi + iy\xi^2} \tag{3.79}$$

here the y variable is responsible for the laser phase error:

$$y = n\iota\sigma_\zeta^2 = (\sqrt{2}/2.35)^2 n\Phi = 0.36n\Phi. \tag{3.80}$$

In order to better understand the FEL performances in presence of a quadratic chirp in the seed laser, we have performed a set of simulations. We have considered the harmonics: $n = 5$ and $n = 10$ of the 267 nm seed laser. For each wavelength, we have introduced a chirp in the seed laser by letting it passing through a variable amount of silica glass before the interaction with the electron beam. The passage of the seed laser radiation field through the material has been simulated using the OCELOT module *dfl_disperse* [53]. The cases that have been studied for the two harmonics are presented in table 3.1, where we show the amount of silica crossed by the seed laser (silica width), the equivalent GDD, the chirp α (defined in Eq. 3.75) and the RMS duration of the seed after the silica $\sigma_{t,seed}$. The seed laser downstream the material has a duration of $\sigma_{t=0,seed} = 31.6$ fs and a variable peak power, that is set in order to have $P_{seed} = 90$ MW for the fifth harmonic and $P_{seed} = 300$ MW for the tenth harmonic, both after the silica glass. Figure 3.10 shows the needed power of the seed laser upstream the silica glass to achieve the

Table (3.1) For the different amount of Silica we give the properties of the seed laser after the passage through them: GDD, quadratic chirp α and RMS duration

silica width [cm]	0.1	0.5	1	2	3	4	5
GDD $[fs^2]$	195.96	979.8	1959.6	3919.2	5878.8	7838.4	9798
$\alpha[rad \cdot \frac{THz}{ps}]$	24.06	98.11	124.44	101.04	76.16	59.86	48.97
$\sigma_{t,seed}$ after silica [fs]	31.9	35.3	44.4	69.8	98.3	128	158

wished power P_{seed} for both the simulated harmonics. We see that the needed power increases as the amount of silica becomes more wide. Using the field from

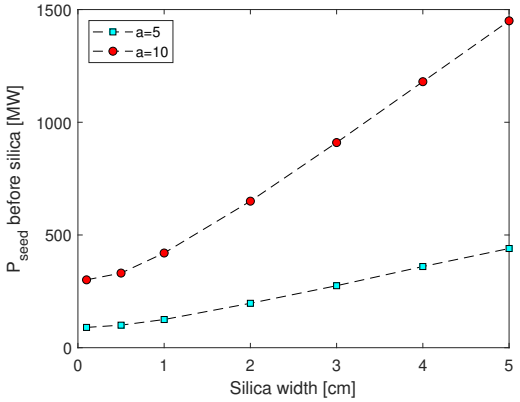

Figure (3.10) Seed laser power upstream the amount of silica glass indicated in the abscissa of the plot for harmonic 5 and 10. The needed power grows linearly as the amount of silica increase.

OCELOT, we run a Genesis1.3 (see appendix v.4 A) simulation of the HGHG process, assuming the sFLASH setup that is going to be explained in the next chapter. We observe that for both harmonics as the temporal seed laser phase chirp, so $n\phi$, increases, the width of the bunching observed in the simulations increases, as shown in Fig. 3.11. The FEL RMS duration, also shown in the figure, follows the trend of the bunching. However, the FEL duration is higher due to the slippage effect within the radiator. The duration of the FEL becomes closer to the bunching width as the amount of silica is increased, so the chirp on the seed laser increases, this is clearly evident at the tenth harmonic.

Figure 3.12 shows on the left the power and on the right the spectra at the end of the radiator for three different amount of silica: 0.5 cm ($n\phi = 2.95$), 2 cm ($n\phi = 11.8$) and 4 cm ($n\phi = 23.6$). Here it is visible the increase in temporal width of the FEL pulse. In addition, for increasing chirp in the seed laser ($n\phi \geq 11.8$), the right region of the electron beam is suppressed from lasing. A tuning of the

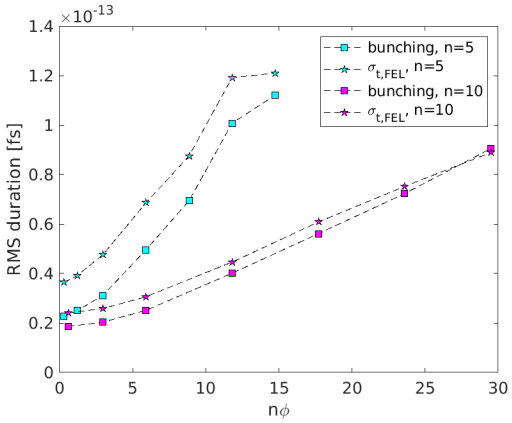

Figure (3.11) RMS width of the bunching profile upstream the radiator and the FEL pulse at the end of the radiator for both harmonics $n = 5$ and $n = 10$.

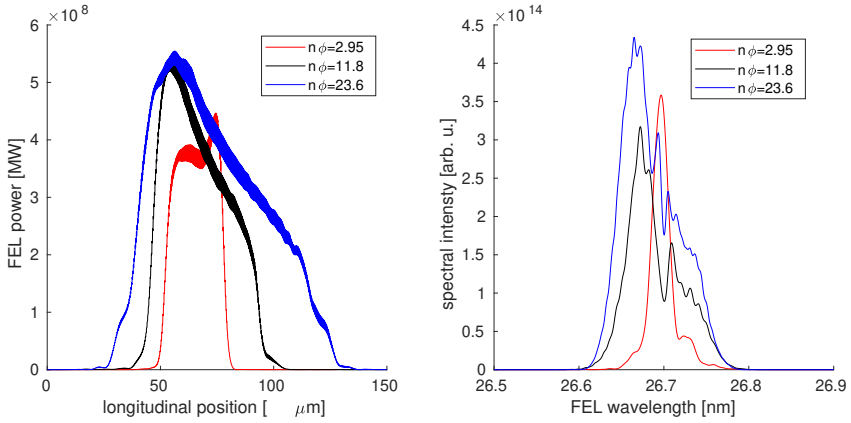

Figure (3.12) FEL power profiles and spectra for the tenth harmonic of the 267 nm seed laser.

radiator might compensate the observed suppression from lasing of the head of the electron beam for increasing chirps. On the right, the spectra shows a single peak for $n\phi = 2.95$. As $n\phi$ grows, the spectrum starts to degrade and the main peak drifts to shorter wavelengths.

Figure 3.13 shows the FEL pulses and the corresponding spectral profiles for the fifth harmonic beyond saturation. Here we present the simulation cases using: 1 cm of silica, corresponding to $n\phi = 2.95$, 4 cm ($n\phi = 11.8$) and 5 cm ($n\phi = 14.7$). Again, for $n\phi \geq 11.8$ the FEL pulse gets longer and lasing is suppressed on the right part of the electron beam. The spectral peak is drifting to lower wavelengths and the spectral quality degrades for increasing $n\phi$. The situation before saturation, earlier in the radiator, is shown in Fig. 3.14 for the same cases. Here the FEL pulses are Gaussian like and in the spectra profile we can already see a drift

of the peak to shorter wavelengths, but the spectrum is not as degraded as in the deep saturation regime seen before.

The time bandwidth product (TBP) for the two harmonics is calculated by ex-

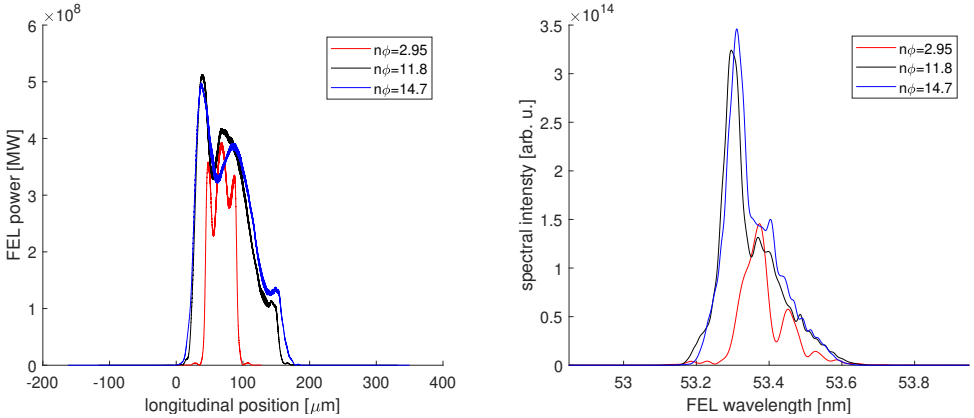

Figure (3.13) FEL power profiles and spectra for the fifth harmonic of the 267 nm seed laser.

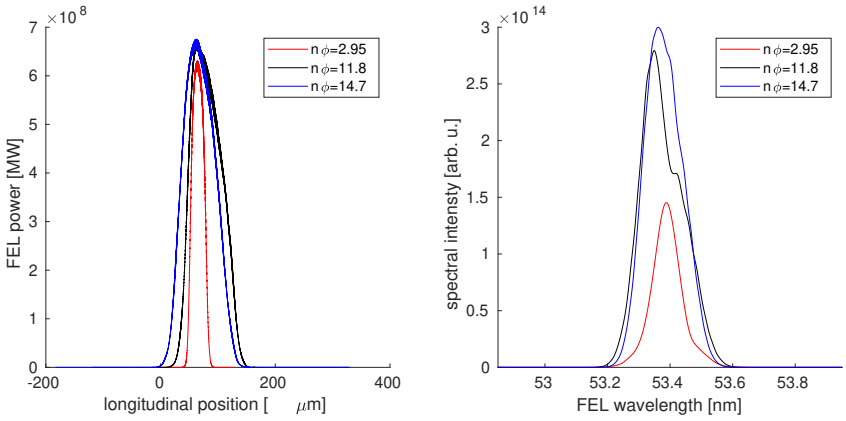

Figure (3.14) FEL power profiles and spectra for the fifth harmonic of the 267 nm seed laser before saturation.

tracting the RMS duration of the bunching profile of the electron beam upstream the radiator $\sigma_{t,bcn}$. By doing the Fourier transform of the bunching temporal profile we obtain the bunching spectral profile from which we can calculate the RMS width $\sigma_{\lambda,bcn}$. From $\sigma_{\lambda,bcn}$ we can calculate $\sigma_{\omega,bcn} = \frac{2\pi c}{\lambda^2}\sigma_{\lambda,bcn}$. Finally: $TBP = \sigma_{t,bcn} \cdot \sigma_{\omega,bcn}$. The resulting TBP is shown in Fig. 3.15. The TBP is higher for the fifth harmonic with respect to the tenth harmonic. This is not in agreement with the results given in [54] because here each harmonic has been optimized in order to give a bunching value which enables to achieve saturation at the end of the radiator. So the bunching is calculated from two different elec-

tron beams, in terms of energy modulation and added dispersion. However, the

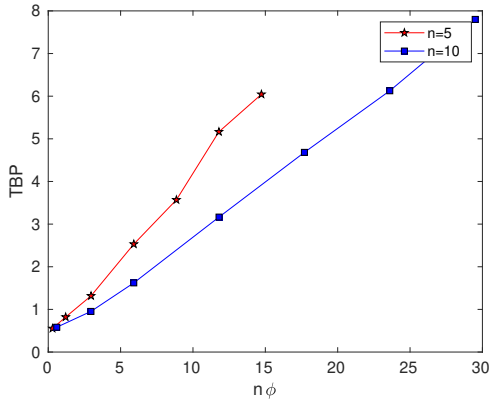

Figure (3.15) Time bandwidth product for the two cases presented.

bunching from the same beam, at the fifth and at the tenth harmonic, gives a time bandwidth product, accordingly to [54]. Figure 3.16 shows the TBP calculated from the bunching: the tenth harmonic TBP is higher compared from the fifth harmonic.

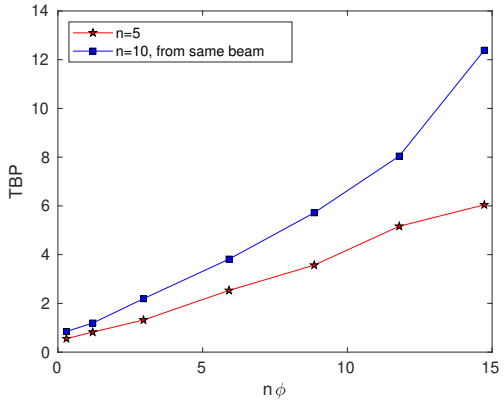

Figure (3.16) Time bandwidth product of the bunching for the fifth and tenth harmonic from the same beam. The beam is optimized for lasing at the fifth harmonic.

FEL properties

The relations derived in Eq. 3.71 and in 3.68 enable the characterization of the FEL pulses resulting from the simulation. By calculating the RMS duration of the FEL pulses and the RMS bandwidth of the spectrum we can extract the amount of chirp α and GDD holded by the pulse. In Figure 3.17 we present the chirp and

the GDD of the seeded FEL for the simulations performed at the fifth harmonic, while in Fig. 3.18 we present the results obtained for the tenth harmonic. For both plots the legend describes the amount of silica that was used to introduce dispersion in the seed laser. We observe that at the fifth harmonic is valid that

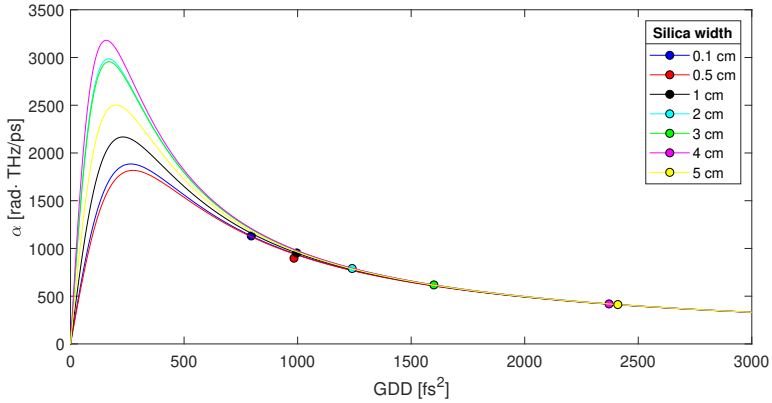

Figure (3.17) Chirp of the FEL at the fifth harmonic plotted respect to the GDD.

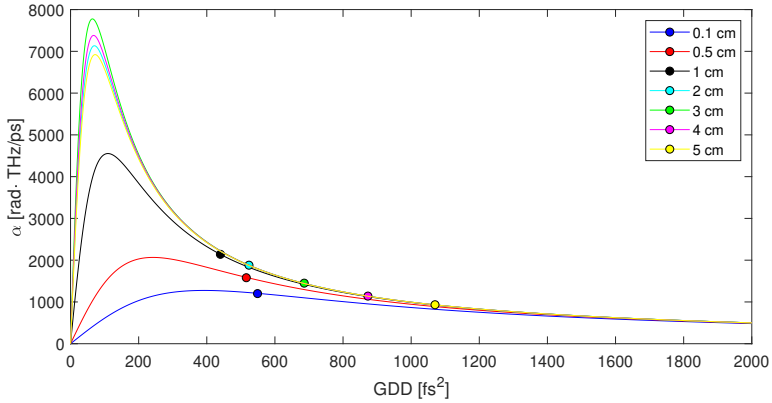

Figure (3.18) Chirp of the FEL at the tenth harmonic plotted respect to the GDD.

the GDD of the FEL grows as the seed laser GDD is increased (increase in the amount of silica), if we exclude the points for an amount of silica equal to 0.1 cm and 0.5 cm, the behavior is the same also at the tenth harmonic. Moreover, at the fifth harmonic, the GDD of the seeded FEL grows faster compared to the GDD of the FEL at the tenth harmonic for the same amount of silica. As a result, it is possible to keep a low GDD if we operate at higher harmonics.

Another remarkable point is that the transform limited pulse duration is shorter at the tenth harmonic $\sigma_{tI,FEL} \simeq 6$ fs compared to the duration at the fifth harmonic

$\sigma_{tI,FEL} \simeq 10\,\text{fs}$, so by means of chirped pulse amplification (CPA) [11], we can get shorter pulses at higher harmonics [55].

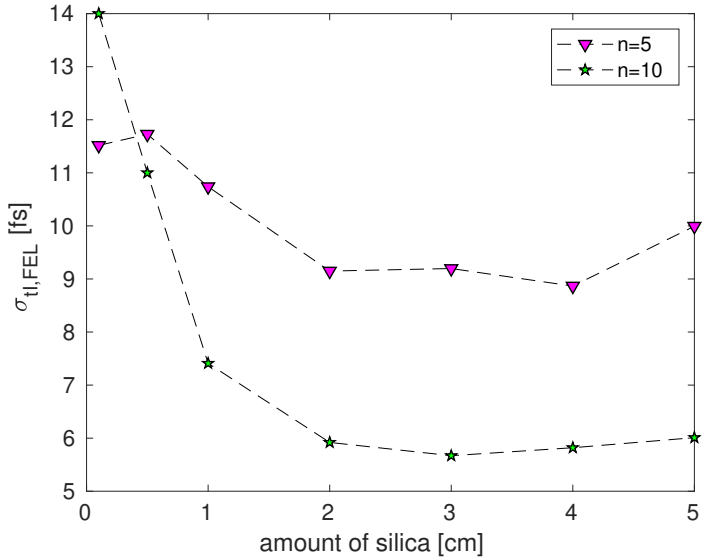

Figure (3.19) RMS duration of the transform-limited seeded FEL pulse for the different amount of silica used to introduce dispersion in the seed laser. We report the results for both the fifth and the tenth harmonic (see legend).

3.1.3 Effects of an electron beam energy chirp on HGHG

The compression of the electron bunch taking place in the bunch compressors along the linac requires that the electrons in the bunch have a linear correlation between energy and their longitudinal position. This is realized by placing the electron beam off-crest respect to the accelerating voltage of the cavities. Due to the curvature of the sinusoidal behavior of the accelerating structure, it is possible that the electron beam is left with a quadratic energy chirp as well. It is possible to correct the quadratic chirp by means of a higher harmonic cavity, respect to the cavities used for acceleration, used in decelerating mode [56]. However, having either linear or quadratic chirp in the electron beam energy profile during the seeding operation might be useful to compensate the possible imperfections present in the seed laser, hence improve the control on the properties of the generated seeded FEL.

The relative energy offset of the electron beam at the linac end $\delta = \frac{E-E_0}{E_0}$ can be described by a Taylor expansion:

$$\delta = \delta_0 + hs_i + h's_i^2 + \mathcal{O}(s^3) \tag{3.81}$$

where δ_0 is the initial uncorrelated energy offset, s_i is the particle longitudinal coordinate relative to the bunch center,

$$h = \frac{dE}{ds}\frac{1}{E} \tag{3.82}$$

is the linear chirp with dimensions of m^{-1} and $h' = \frac{d^2E}{ds^2}\frac{1}{E}$ is the quadratic chirp with dimensions of m^{-2}.
In the following subsubsection we describe the effect on HGHG when the electron beam has either a linear chirp or a quadratic chirp. For these descriptions it is useful to define a dimensionless energy chirp. The dimensionless linear energy chirp is defined by:

$$\tilde{h} = \frac{dp}{d\zeta} = \frac{d\delta}{ds}\frac{1}{k_1}\frac{E_0}{\sigma_E} = \frac{h}{k_1}\cdot\frac{E_0}{\sigma_E} \tag{3.83}$$

where we remind that $\zeta = k_1 s$.

Linear chirp

An electron beam with a linear energy chirp arriving at the entrance of the HGHG modulator has a distribution function given by:

$$f_0(p,\zeta) = \frac{N_0}{\sqrt{2\pi}} e^{-\frac{(p-\tilde{h}\zeta)^2}{2}} \tag{3.84}$$

where N_0 is the number of electrons per unit length, $p = (E - E_0)/\sigma_E$, E_0 is the beam central energy, σ_E is the initial uncorrelated energy spread, $\zeta = k_1 s$ and the linear chirp is defined by Eq. 3.83 In this case the longitudinal coordinate of the electrons in the beam transforms downstream the HGHG bunching chicane with longitudinal dispersion R_{56} as:

$$s_f = s_i + R_{56}\delta = s_i(1 + \tilde{h}R_{56}) + R_{56}\delta_0. \tag{3.85}$$

We define the linear compression factor as:

$$C = \frac{\sigma_{out}}{\sigma_{in}} = \frac{1}{1 + \tilde{h} \cdot R_{56}}. \tag{3.86}$$

where σ_{out} and σ_{in} are the RMS length of the electron beam downstream and upstream the bunching chicane respectively. When the electron beam is linearly chirped, the periodicity of the microbunches generated downstream the bunching chicane are also affected by the linear compression factor defined in Eq. 3.86 and the wavelength of the FEL radiation is shifted by:

$$\lambda' = \frac{\lambda}{C} \tag{3.87}$$

[57, 58]. Figure 3.20 shows the compression of the microbunches along the HGHG setup. The seeded FEL radiation wavelength is shifted by the factor defined in

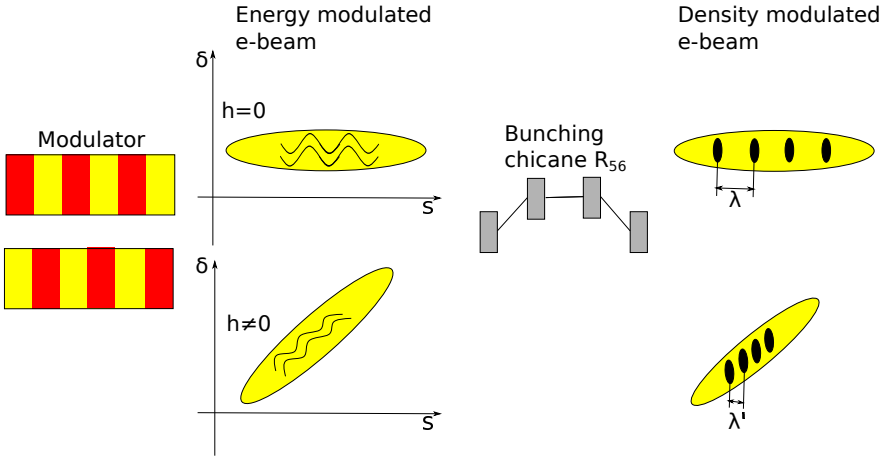

Figure (3.20) This diagram shows that after interaction with the seed laser in the modulator, the electron beam is energy modulated. Then the electron beam passes through the HGHG bunching chicane with dispersion strength R_{56}, if the electron beam has a chirp $h = 0$, the microbunches are spaced by a seed laser wavelength λ, while if the electron beam has a linear energy chirp, the spacing of the microbunches is shorter by a factor $\frac{1}{1+h \cdot R_{56}}$. For this figure I took inspiration from [59].

Eq. 3.87. In [59] it was shown that having a negative energy chirp $h < 0$ leads to shorter wavelengths $\lambda' < \lambda$, while having a positive chirp $h > 0$ leads to higher wavelengths $\lambda' > \lambda$. However, the FEL bandwidth is not affected from a linear chirp in the electron beam.

Quadratic chirp

The electron beam arriving at the HGHG modulator having a quadratic chirp, can be described with the distribution function:

$$f_0(p,\zeta) = \frac{N_0}{\sqrt{2\pi}} e^{-\frac{(p+c\zeta^2)^2}{2}} \tag{3.88}$$

where $c > 0$ when the beam is accelerated on-crest. The effect of a electron beam quadratic energy chirp on the performances of the HGHG FEL can be found by calculating the bunching factor, similarly to how we have proceed for HGHG with a chirped seed laser [48]. Therefore, we insert the electron beam initial distribution function in Eq. 3.88 in the bunching definition given in Eq. 3.22 and we get:

$$k_l b(\kappa) = \frac{1}{\sqrt{2\pi}} \int_{-\infty}^{+\infty} e^{-\frac{(p+a\zeta^2)^2}{2}} dp \int_{-\infty}^{+\infty} e^{-i\kappa Bp} e^{-i\kappa\zeta - i\kappa BA(\zeta)\sin\zeta} d\zeta \tag{3.89}$$

We can solve the integral in the momentum:

$$\int_{-\infty}^{+\infty} e^{-\frac{(p+c\zeta^2)^2}{2}} e^{-i\kappa Bp} dp = \sqrt{2\pi} e^{\frac{\kappa^2 B^2}{2}} e^{i\kappa Bc\zeta^2} \tag{3.90}$$

so the bunching becomes:

$$k_l b(\kappa) = e^{-\frac{\kappa^2 B^2}{2}} \int_{-\infty}^{+\infty} d\zeta e^{-i\kappa\zeta - i\kappa BA(\zeta)\sin\zeta} e^{-i\kappa Bc\zeta^2} \tag{3.91}$$

$$\approx e^{-\frac{\kappa^2 B^2}{2}} \sum_{n=-\infty}^{+\infty} \int_{-\infty}^{+\infty} d\zeta J_n(-\kappa BA(\zeta)) e^{-i(\kappa-n)\zeta + inBc\zeta^2} \tag{3.92}$$

This expression is the same as Eq. 3.77, where ι is replaced by Bc hence the behavior of the FEL when the electron beam has a quadratic energy chirp is the same as when there is a quadratic chirp in the seed laser phase. In [57] it was observed that there was a significant FEL bandwidth increase in the seeded FEL when an electron beam with a residual quadratic energy chirp from the linac was exploited.

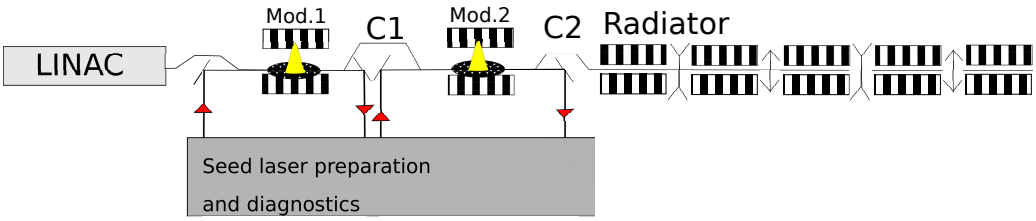

Figure (3.21) EEHG schematic setup. For EEHG we need two undulators called modulators where it happens the electron-seed laser interaction and two chicanes C1 and C2. C1 is a high dispersion chicane and C2 is the bunching chicane.

3.2 EEHG

There are three facilities world-wide that has been investigating EEHG within the last twenty years. The scheme has been tested in NLCTA at SLAC, where there has been four experiments. The first in 2010 produced the third and the fourth harmonic of a 1600 nm laser. One year later it was achieved the seventh harmonic of the same laser wavelength. In 2014 it was achieved the fifteenth harmonic and finally in 2016 the 75^{th} harmonic. This showed the robustness of the EEHG scheme against HGHG in terms of stability to electron beam imperfections and production of higher harmonics.

EEHG is superior (in terms of achievable harmonics) compared to HGHG because the harmonic content is not determined anymore by the energy modulation alone, but from the final complex density distribution resulting from the process. Also, at SDUV-FEL in Shanghai, China a seed laser with a wavelength of 1047 nm was used to generate EEHG at its third harmonic. The latest result was achieved at the FERMI (Free Electron laser Radiation for Multidisciplinary Investigations) FEL, where for the first time it has been shown high gain with the EEHG scheme in the XUV range [60] and the experimental setup, parameters and analysis of the gain curve are going to be presented in the next chapters.

Finally, also DESY in Hamburg is interested in the EEHG scheme to produce radiation in the XUV range, therefore we are optimizing the existing seeding experiment at FLASH (sFLASH) to show the feasibility of EEHG, as it will be presented in the next chapters. Moreover the future upgrade FLASH2020+ is considering to dedicate a beamline to seeding and part of the operation is going to be conducted with EEHG, as it is going to be presented in the last chapter of this thesis.

The setup used for EEHG consists of two modulator followed by two dispersive chicanes. Typically the strength of the first chicane $R_{56}^{(1)}$ is higher than the second one $R_{56}^{(2)}$, in fact it holds the relation [60]

$$R_{56}^{(2)} \approx \frac{|n|}{a} R_{56}^{(1)} \tag{3.93}$$

where a is the target harmonic and n is an integer number, usually negative and its modulus is preferably below 4 as we are going to explain further on in this chapter. The electron beam interacts with a seed laser in each modulator. Is not necessary that these two seeds have the same wavelength.
Starting from a beam with the distribution function presented in the previous subsection in Eq. 3.2, the process illustrated up to Eq. 3.10 repeats twice. The first modulator is tuned to resonance to the wavelength of the first laser λ_1, so we define the wavenumber as $k_1 = 2\pi/\lambda_1$. Here the electron beam receives an energy modulation $A_1 = \Delta E_1/\sigma_E$. Within the first modulator the energy of the electron beam changes as:

$$p' = p + A_1 \sin\zeta \tag{3.94}$$

where p is the initial electron beam normalized energy defined in Eq. 3.1 and $\zeta = k_1 z$. At this point, the distribution function corresponds to the one in Eq. 3.9, where $A = A_1$:

$$f(\zeta, p) = \frac{N_0}{\sqrt{2\pi}} \exp - \left[\frac{(p - A_1 \sin\zeta)^2}{2} \right]. \tag{3.95}$$

The electron beam encounters a high dispersion chicane upstream the modulator, the dispersive strength is quantified by the dimensionless quantity:

$$B_1 = R_{56}^{(1)} k_1 \sigma_E / E_0 \tag{3.96}$$

which transforms the longitudinal coordinate as:

$$\zeta' = \zeta + B_1 p'. \tag{3.97}$$

Upstream the chicane the distribution function transforms as:

$$f(\zeta, p) = \frac{N_0}{\sqrt{2\pi}} \exp \left[-\frac{1}{2} [p - A_1 \sin(\zeta - B_1 p)]^2 \right] \tag{3.98}$$

which has the same form as the HGHG final distribution function Eq. 3.9. However, compared to HGHG there is a fundamental difference arising from the use

of a higher R_{56} for the first chicane. In fact, looking the function in Eq. 3.98 at the center of the bunch $z = \zeta = 0$, the energy distribution changes for different values of the parameter $R_{56}\Delta E/E$, as shown in Fig. 3.22. This parameter quantifies the longitudinal effect of the chicane on energy modulated electrons. The optimal value of this parameter for HGHG, where there is only one laser with wavelength λ, is $R_{56}\Delta E/E = \lambda/4$ which gives only one energy peak. While for EEHG it is used a higher R_{56}, for the first chicane, that leads to the popping up of several energy bands. These undergo to another modulation in the second modulator and they are finally converted into density bands from the last chicane, which can potentially give high harmonic content at very high harmonics. In

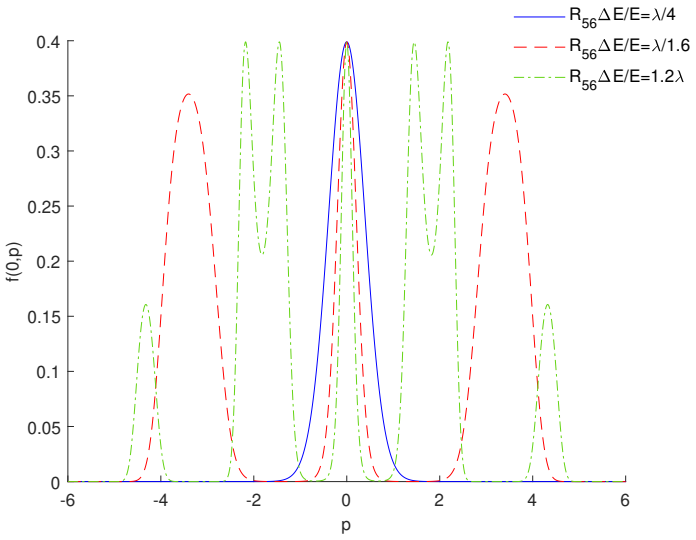

Figure (3.22) Distribution function upstream the first EEHG chicane at $z = \xi = 0$ respect to the relative energy p. For this result $A_1 = 3$, the seed laser wavelength was $\lambda = 300\,\text{nm}$, the electron energy $E_0 = 1.3\,\text{GeV}$ and its energy spread $\sigma_E = 150\,\text{keV}$. The blue curve represent the case of HGHG and $B_1 = 0.5$ ($R_{56} = 216\,\mu\text{m}$), the red dashed curve and the green dash-dotted curves are compatible with the EEHG scheme and in this case $B_1 = 1.3$ ($R_{56} = 542\,\mu\text{m}$) and $B_1 = 2.5$ ($R_{56} = 1\,\text{mm}$) respectively.

the second modulator the imprinted energy modulation on the electron beam is $A_2 = \Delta E_2/\sigma_E$. In this modulator the electron beam energy changes as:

$$p'' = p' + A_2 \sin(k_2 z + \phi) \tag{3.99}$$

where $k_2 = 2\pi/\lambda_2$, with λ_2 the wavelength of the second seed laser and ϕ is the phase of the second laser beam.

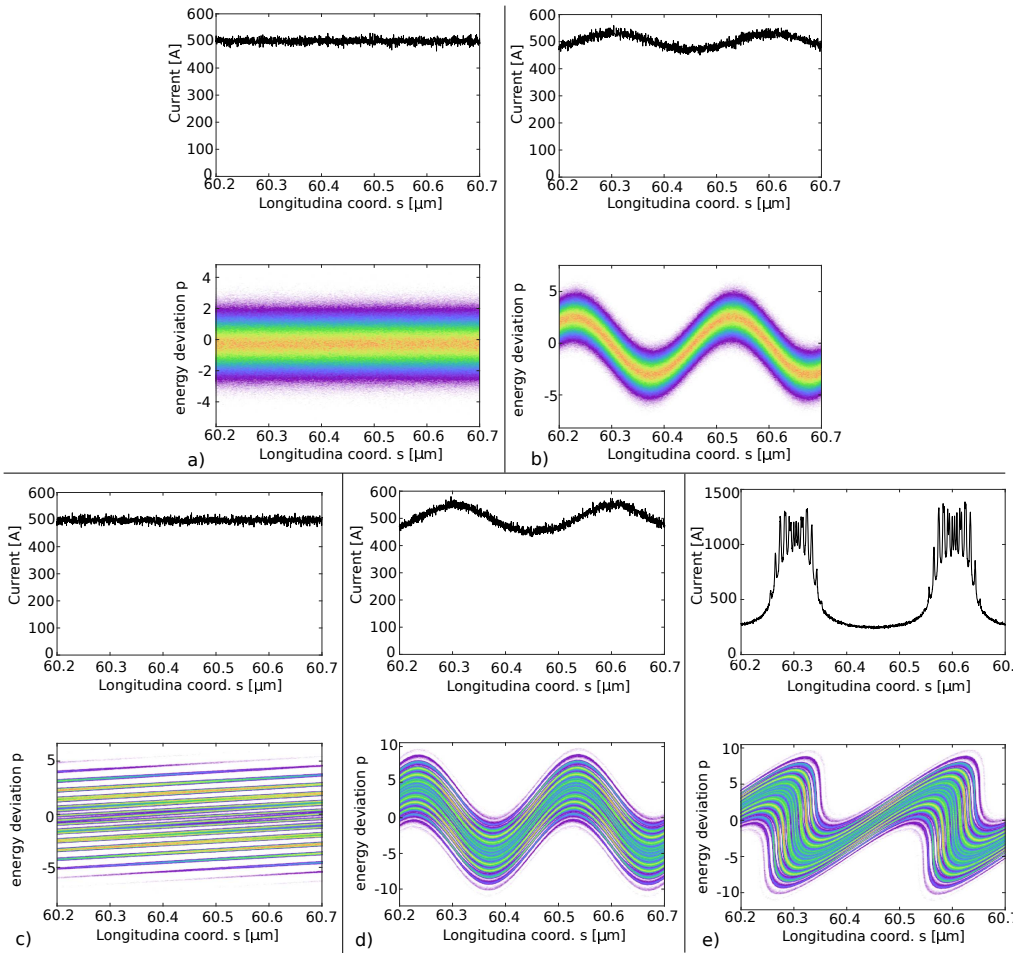

Figure (3.23) Evolution of the current profiles (top) and longitudinal phase space distribution (bottom) of two slices of the electron beam along the EEHG scheme. The status of the electron beam downstream the first modulator is shown in the two plots in a) and upstream the first modulator in b). Then subplots in c) show the status upstream the first chicane with the expected energy bands. d) Shows the electron beam upstream the second modulator and e) upstream the second chicane. Here the current profile has several spikes which are rich in harmonic content.

The second chicane strength reads: $B_2 = R_{56}^{(2)} k_1 \sigma_E / E_0$, and the longitudinal coordinate is transformed in:

$$\zeta'' = \zeta' + B_2 p''. \tag{3.100}$$

As a result, the initial electron beam coordinates (ζ, p) are transformed to:

$$\zeta'' = \zeta + (B_1 + B_2)p + A_1(B_1 + B_2)\sin\zeta + A_2 B_2 \sin\left(K\zeta + KB_1 p + KA_1 \sin\zeta + \phi\right) \tag{3.101}$$

As a result, the final distribution function results:

$$f_f(\xi, p) = \frac{N_0}{\sqrt{2\pi}} e^{\left[-\frac{1}{2}\{p - A_2 \sin(K\xi - KB_2 p + \phi) - A_1 \sin[\xi - (B_1+B_2)p + A_2 B_1 \sin(K\xi - KB_2 p + \phi)]\}^2\right]} \tag{3.102}$$

where $K = k_2/k_1$. At the same way of Eq. 3.11 it is defined the beam density. Here the bunching factor is defined as:

$$b = \frac{1}{N_0} | < e^{-ia\xi} N(\xi) > | \tag{3.103}$$

where this expression is different from zero only for

$$a = n + Km \tag{3.104}$$

where n and m are integers and a represent the harmonic number. In fact, $k_E \equiv ak_1 = nk_1 + mk_2$ where $k_E = 2\pi/\lambda_E$, which is the wavenumber of the EEHG radiation. In order to have the same signs for $B_{1,2}$ it is necessary to have the m and n indexes with opposite sign. The configuration studied in this thesis is for m positive and n negative. The maximum bunching is achieved when $n = -1$.
From [61] it is derived the EEHG bunching factor:

$$b_{n,m} = |e^{-\frac{1}{2}[nB_1 + (Km+n)B_2]^2} J_m[-(Km+n)A_2 B_2] J_n\{-A_1[nB_1 + (Km+n)B_2]\}|. \tag{3.105}$$

In this equation $J_{n,m}$ are Bessel functions of the first kind. This expression for the bunching is valid in the case $A_1 B_1 \gg 1$ [62]. When this condition is not satisfied, for example when the setup is characterized by a chicane with limited dispersion strength, it comes into play the phase ϕ, and the EEHG bunching reads:

$$b_a = \sum_{\substack{n,m \\ a=n+Km}} e^{im\phi} b_{n,m}. \tag{3.106}$$

Hence, there are more than only one bunching factor $\{n, m\}$ contributing to the final bunching at the harmonic of interest a. In this case the working point can be chosen by averaging respect to ϕ.
The knowledge of the parameters maximizing the bunching value in Eq. 3.105

at a chosen harmonic is fundamental to have a reliable starting point to set up simulations and experiments. The term $J_m[-(Km+n)A_2B_2]$ is maximized when its argument is equal to $j'_{m,1} \approx m + 0.81m^{1/3}$ (first root of the derivative of the Bessel function J_m), so it holds:

$$B_2 = \frac{j'_{m,1}}{(Km+n)A_2}. \tag{3.107}$$

For the remaining term $e^{-1/2[nB_1+(Km+n)B_2]^2} J_n\{-A_1[nB_1+(Km+n)B_2]\}$ it is introduced the EEHG scaling factor:

$$\xi = nB_1 + (Km+n)B_2, \tag{3.108}$$

so the term reduces to:

$$e^{\xi^2/2} J_n[A_1\xi]. \tag{3.109}$$

The plot in Fig 3.24 represents Eq. 3.109 as a function of A_1. Fig 3.24 shows that the function has an asymptotic behavior, converging at infinite to 0.58, which is also the maximum value. As a consequence, setting $A_1 \geq 5$ has no significant advantage, because the value of Eq. 3.109 is close to the value of the asymptote. This is also a significant aspect differentiating the EEHG scheme from HGHG. Once A_1 is fixed, is possible to find the value of ξ by finding the maximum of

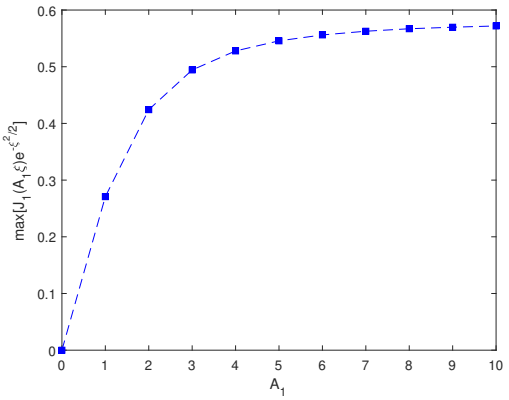

Figure (3.24) Maximal value of $J_1(A_1\xi)e^{-\xi^2/2}$

Eq. 3.109, which results approximately:

$$\xi \simeq \frac{j'_{n,1}}{A_1}\left[1 + \frac{1}{A_1^2}\frac{1}{1-(n/j'_{n,1})}\right]^{-1} \tag{3.110}$$

where $j'_{n,1} \approx |n| + 0.81|n|^{1/3}$ is the first root of the derivative of the Bessel function J_n [63].
From the definition of ξ in Eq. 3.108 and the optimized B_2 from Eq. 3.107 it is derived the optimal value for B_1:

$$B_1 = \frac{\xi - (Km + n)B_2}{n}. \tag{3.111}$$

In Figure 3.25 is shown the typical bunching map for EEHG at the harmonic *a=30*. Here there are represented all the $b_{n,m}$ from Eq. 3.105 with $n \in [-1, -9]$ that are satisfying the condition $a = n + Km$. It is highlighted with a dash-dotted line the region where the bunching goes to zero:

$$B_2 = -\frac{n}{Km + n} B_1. \tag{3.112}$$

This region is lying between two lobes of the same n, m working point. As a consequence, in the EEHG experiment, when the setup parameters are close to the chosen working point, it is always advisable to scan the chicane strengths to ensure that the working point is lying on the maximum of the lobe.
If the EEHG setup allows to operate at high first chicane dispersion (high B_1), it is convenient to operate at the $n = -1$ point or sitting on the right lobe of the $n = -2$, as the bunching b_a has the only contribution coming from the bunching factor $b_{n=-1,m=31}$ and $b_{n=-2,m=32}$ respectively. While is more challenging to operate at working points with $B_1 \leq 4$ where there are different $b_{n,m}$ which are contributing to the bunching b_a and therefore it is necessary to consider the effect of the phase ϕ as well. In this case the bunching should be estimated from Eq. 3.106. In the setting up of an EEHG experiment, it is common to set before the chicane strengths to a determinate value, while scanning the laser strength and so the consequent energy modulation on the electron beam. In Fig. 3.26 the tolerances on A_1 and A_2 are shown. The chosen working point is the right lobe of the $n = -1$ blobs of Fig. 3.25. It is evident the presence of a threshold value for A_2. Therefore, it is necessary to make sure to have enough energy in the second seed laser to achieve the needed energy modulation. While the tolerances are not so strict for the first seed laser. Also in this case there are observable regions between the lobes where the bunching goes to zero.

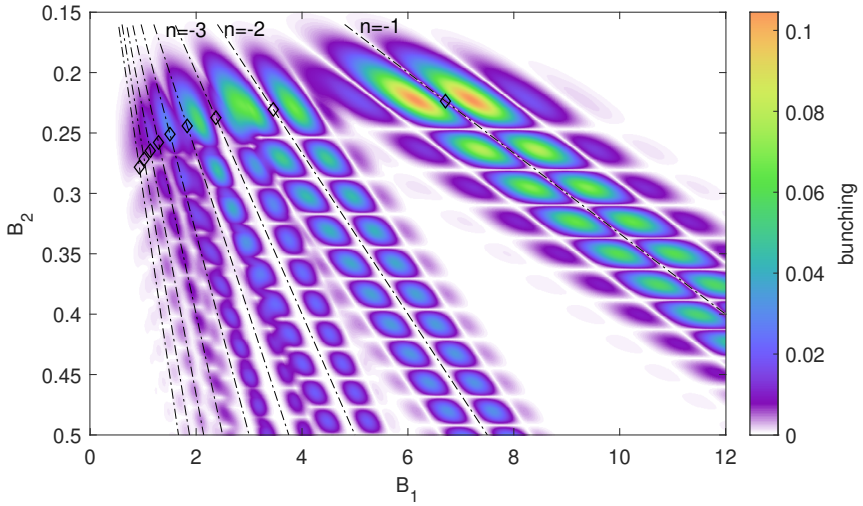

Figure (3.25) Bunching map for the harmonic 30, both seed lasers have the same wavelength of 300 nm, the electron beam energy is 1.35 GeV. $A_1 = 3$ and $A_2 = 5$. The dash-dotted curves show the region where the bunching goes to zero for a fixed n

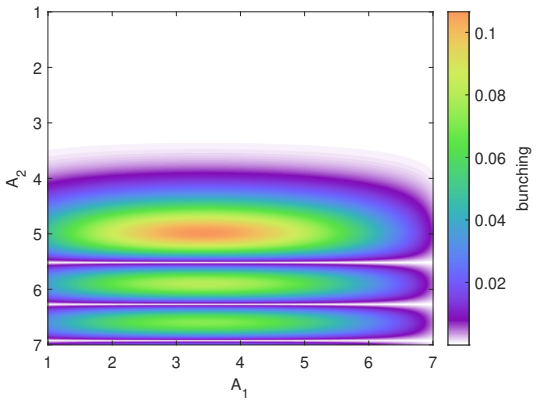

Figure (3.26) Bunching map for the harmonic 30. The parameters used are the same as Fig. 3.25. But here it is represented only the working point $n = -1$ and the B parameters are set to the maximum: $B_1 = 7.2$ and $B_2 = 0.2$. While A_1 and A_2 are scanned in order to see the tolerances.

3.2.1 Finite Laser pulse and frequency chirp in EEHG

In this section we calculate how the EEHG bunching formula from Eq. 3.105 is affected if we assume the laser pulse given in Eq. 3.20 and a laser frequency chirp Eq. 3.75 for the second seed laser only. While for the first seed laser we assume that it is long enough so we can neglect variation of the laser amplitude along the

electron bunch and we don't consider any chirp in the phase as it does not affect the EEHG process significantly [48]. Considering these assumptions, the final longitudinal coordinate of the electron beam presented in Eq. 3.101 is modified as:

$$\zeta'' = \zeta + (B_1+B_2)p + A_1(B_1+B_2)\sin\zeta + A_2(\zeta)B_2\sin\left(K\zeta + KB_1p + KA_1B_1\sin\zeta + \beta\zeta^2 + \psi\right) \tag{3.113}$$

where we have substituted A_2 with $A_2(\zeta)$ from Eq. 3.20 and β from Eq. 3.76 is related to the laser linear frequency chirp and ψ is the phase of the second seed laser.
Introducing Eq. 3.113 into Eq. 3.18 we derive:

$$k_l b(\kappa) = \frac{1}{N_0}\int_{-\infty}^{+\infty} dp e^{-i\kappa p(B_1+B_2)} f_0(p)\times \tag{3.114}$$

$$\int_{-\infty}^{+\infty} d\zeta e^{i\kappa\zeta} e^{-i\kappa A_1(B_1+B_2)\sin\zeta} e^{-i\kappa A_2(\zeta)B_2\sin\{K\zeta+KB_1p+KA_1B_1\sin\zeta+\beta\zeta^2+\psi\}}. \tag{3.115}$$

The two exponential factors in this equation can be expanded in series:

$$e^{-i\kappa A_1(B_1+B_2)\sin\zeta} = \sum_{q=-\infty}^{+\infty} e^{iq\zeta} J_q(-\kappa A_1(B_1+B_2)), \tag{3.116}$$

and

$$e^{-i\kappa A_2(\zeta)B_2\sin\{K\zeta+KB_1p+KA_1B_1\sin\zeta+\beta\zeta^2+\psi\}} = \tag{3.117}$$

$$= \sum_{m=-\infty}^{+\infty} e^{im(K\zeta+KB_1p+KA_1B_1\sin\zeta+\beta\zeta^2+\psi)} J_m(-\kappa A_2(\zeta)B_2) \tag{3.118}$$

finally the factor $e^{imKA_1B_1\sin\zeta}$ can also be expanded:

$$e^{imKA_1B_1\sin\zeta} = \sum_{l=-\infty}^{+\infty} e^{il\zeta} J_l(A_1B_1Km). \tag{3.119}$$

If we set $\beta = 0$ (no chirp in the seed laser phase) and A_2 does not depend on ζ, we obtain the condition presented in Eq. 3.104. In fact, in this limit all the terms

that depend on ζ in Eq. 3.114 combine into:

$$e^{i(q+l+mK-\kappa)}. \tag{3.120}$$

In this limit the integral does not vanish only if:

$$\kappa = n + mK \tag{3.121}$$

where $n = q + l$, which resemble Eq 3.114, so the FEL wavenumber is defined by:

$$k = k_{n,m} = nk_1 + mk_2. \tag{3.122}$$

From this we can derive that

$$\kappa = \frac{k_{n,m}}{k_1}. \tag{3.123}$$

When $\beta \neq 0$ and A_2 depends on ζ, the FEL wavelength is shifted from the original $k_{n,m}$:

$$k = k_{n,m} + \Delta k \tag{3.124}$$

and if we divide by k_1 this relation we get:

$$\kappa = \frac{k_{n,m}}{k_1} + \Delta\kappa \tag{3.125}$$

where $\Delta\kappa = \Delta k/k_1$.
Now inserting Eqs. (3.116), (3.117) and (3.119) in Eq. 3.114 we can show that:

$$b_{n,m}(\Delta\kappa) = e^{\frac{1}{2}[nB_1+(Km+n)B_2]^2} j_n(-A_1(nB_1 + (Km+n)B_2)) \tag{3.126}$$

$$\times \int_{-\infty}^{+\infty} d\zeta e^{-i\Delta\kappa\zeta + im\beta\zeta^2 + im\psi} J_m(-(Km+n)A_2(\zeta)B_2) \tag{3.127}$$

a full derivation of this expression can be found in [48].

EEHG simulations with finite seed laser pulse length and quadratic phase chirp

In order to have a better insight into the theory, in this paragraph we present the EEHG performances achieved using the sFLASH setup tuned for EEHG at the tenth harmonic.

For this EEHG working point we have chosen a peak power for the first seed $P_1 = 78\,\mathrm{MW}$ which imprints an energy modulation on the electron beam of $A_1 = 4.65$ and for the second seed laser $P_2 = 90\,\mathrm{MW}$ corresponding to an energy modulation $A_2 = 5.4$. The first chicane has a dispersion strength of $R_{56}^{(1)} = 703\,\mu\mathrm{m}$ and for the second chicane $R_{56}^{(2)} = 76\,\mu\mathrm{m}$. For an electron beam energy of 700 MeV and an uncorrelated energy spread of 70 keV we get the EEHG chicane parameters: $B_1 = 1.6543$ and $B_2 = 0.1788$.

We start from the case in which the first seed laser and the second seed laser have finite pulse length. In addition, the second seed laser holds a quadratic chirp in the phase. The chirp in the field of the second seed laser is introduced by letting it pass trough a dispersive material (silica glass) with OCELOT, in the same way as it was done for the HGHG studies with chirped seed laser. We start from a seed laser with RMS pulse length of 31.7 fs, and the needed power downstream the silica, to get after it a peak power $P_2 = 90\,\mathrm{MW}$, is shown in Fig. 3.10. The different amounts of silica chosen for this set of EEHG simulations are the same as the ones used for chirping the seed laser for the HGHG studies and are presented in table 3.1. From the same table, we learn the seed laser pulse length upstream the silica $\sigma_{t,seed}$. In the simulation we saw that, in order to have a reasonable bunching, it is better to set the pulse length of the first seed laser longer compared to $\sigma_{t,seed}$ of the second seed laser.

The resulting bunching profile of the electron beam upstream the second chicane is characterized by measuring its RMS pulse length, and this is compared to the RMS pulse length of the FEL pulse achieved at the end of the radiator section. The results are reported in Fig. 3.27 and they are compared to the corresponding parameters that were achieved for HGHG at the tenth harmonic. The EEHG FEL pulse length is shorter compared to the HGHG pulse length at the same length. Similarly to HGHG, for EEHG the bunching pulse length is shorter compared to the FEL pulse length, apart from the larger dispersion case ($n\phi \sim 29$, corresponding to 5 cm silica). At $n\phi = 11.8$ and $n\phi \sim 18$, the bunching pulse duration exactly foresees the FEL pulse length. Figure 3.28 shows the final FEL pulses in power (left) and the corresponding spectrum (right) for three different amounts of silica used to chirp the seed laser: 0.5 cm ($n\phi = 2.95$), 2 cm ($n\phi = 11.8$) and 4 cm ($n\phi = 23.6$). The shorter FEL pulse with $n\phi = 2.95$ has a clear superradiant peak at the head of the electron beam and it has a Gaussian-like spectrum centered at 26.7 nm. The pulse with $n\phi = 11.8$ shows a residual superradiant behavior at the head, which looks heavily suppressed respect to the previous case. It seems

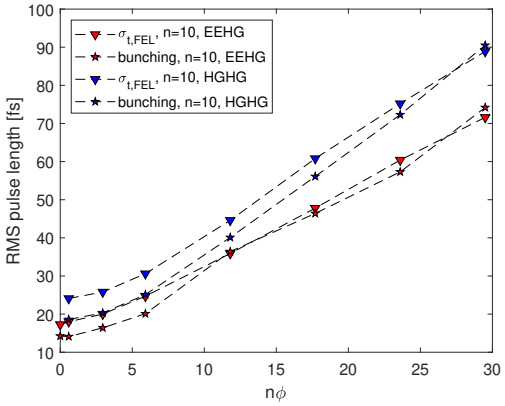

Figure (3.27) RMS pulse length of the bunching profile downstream the radiator and of the FEL pulse at the end of the radiator. The EEHG results at the tenth harmonic are compared with the HGHG results at the same harmonic.

that the tail of the electron beam is lasing more. The superradiant peak at the head is completely suppressed at $n\phi = 23.6$, here instead we have an intense lasing at the tail of the electron beam. Regarding the spectra, in this case it is not Gaussian-like anymore, but it has developed additional structures beside the main peak, in addition, the main peak is slightly shifted to lower wavelengths. From the FEL pulses and spectra, we have calculated the RMS pulse lengths re-

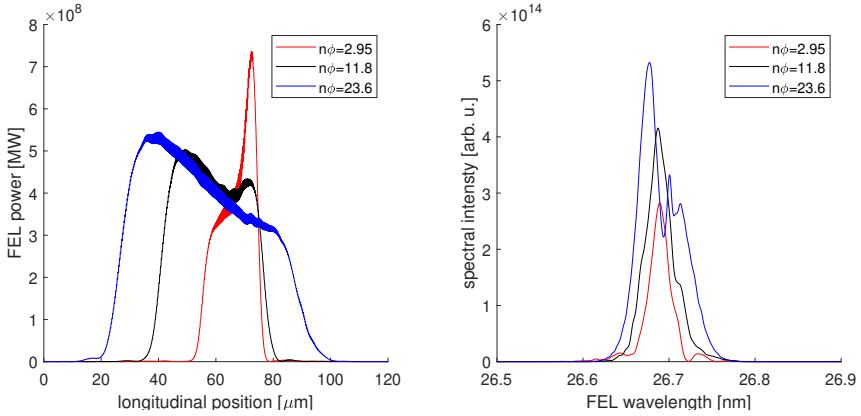

Figure (3.28) FEL power profiles and spectra for the tenth harmonic generated with EEHG exploiting as second seed a laser pulse with a quadratic chirp in the phase.

spectively: $\sigma_{t,FEL}$ and $\sigma_{\omega,FEL} = \frac{2\pi c}{\lambda^2}\sigma_{\lambda,FEL}$ and from these we have derived the time-bandwidth product: $TBP = \sigma_{t,FEL} \cdot \sigma_{\omega,FEL}$. Figure 3.29 shows the trend of the TBP for EEHG lasing at the tenth harmonic, and this is compared to the TBP that was calculated for the HGHG case at the tenth harmonic in the previous sec-

tion. The TBP achieved with EEHG is complexly smaller compared the one for HGHG, this is telling us that the EEHG pulses are closer to the transform limit despite the chirp in the second seed laser. Assuming Gaussian pulses, we have

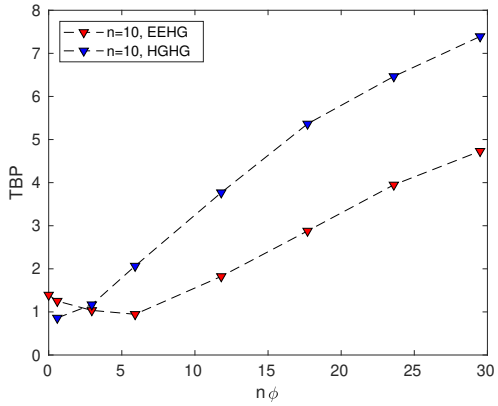

Figure (3.29) Time bandwidth product (TBP) calculated for the EEHG pulses at the end of the sFLASH radiator. These are compared with the TBP that was calculated for the HGHG at the tenth harmonic.

estimated the a parameter defined in Eq. 3.73 and from this we have obtained the chirp of the FEL α. Exploiting Eq. 3.74, GDD can be derived. Figure 3.30 is showing the relation between the chirp α and GDD. The maximum GDD of the final FEL pulse is achieved when the seed with the higher dispersion is exploited, and the resulting GDD is comparable to the maximum GDD achieved for HGHG at the tenth harmonic, as we showed in Fig. 3.18. For the EEHG case, we observe that the minimum GDD is pushed below the $500\,\mathrm{fs}^2$, as a consequence the chirp α for amounts of silica below 1 cm is significantly high, this was not the case for HGHG at the tenth harmonic (Fig. 3.18). The RMS pulse length estimated for the transform limited pulse for EEHG at the tenth harmonic and HGHG at the tenth harmonic are compared in Fig. 3.31. When the added seed laser dispersion comes from amounts of silica below the 1 cm width, the EEHG $\sigma_{tI,FEL}$ is shoter compared to the one of HGHG, while for greater amounts of silica, the $\sigma_{tI,FEL}$ is shorter for the HGHG case. In the senario of a CPA experiment [1], where the aim is to get ultra-short pulses with high peak power, it is possible to achieve pulse lengths in a range between 6 and 13 fs depending on the chirp of the seed laser and on its GDD.

We have also performed a set of simulations where the first seed laser was chirped and we have observed that even for the highest silica width used for adding dispersion in the seed laser, the bunching was not perturbed. In these simulations we

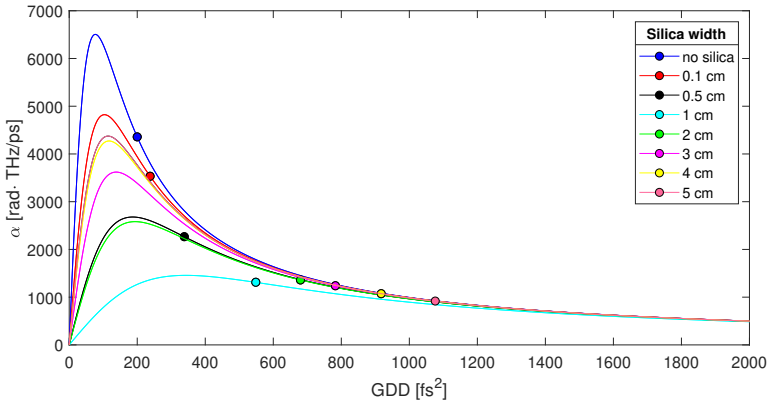

Figure (3.30) Chirp of the EEHG-seeded FEL α plotted respect to the group delay dispersion (GDD).

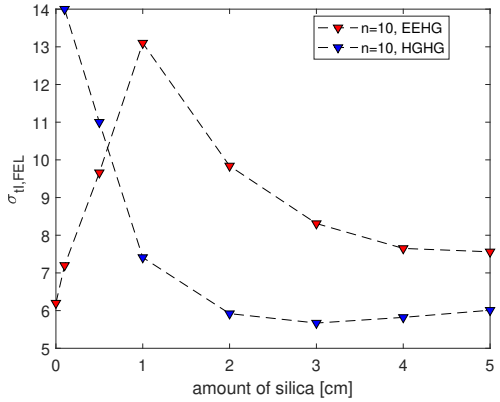

Figure (3.31) FEL RMS pulse length of the transform limited pulse having the spectrum resulting from the simulation. The EEHG at the tenth harmonic results are compared with the resuts achieved for HGHG at the tenth harmonic.

have kept the second seed laser with a RMS pulse length of 31.7 fs, demonstrating that this laser is determining the bunching and the FEL properties and not the first seed.

3.2.2 Effects of an electron beam energy chirp on EEHG

Linear chirp

The distribution function of a linearly chirped electron beam was given in Eq. 3.84. Using this function we can estimate how the EEHG bunching factor is modified

in this case. We start from the definition for the bunching factor that was given in [64]:

$$b = \frac{1}{N_0}\left| \int_{-\infty}^{+\infty} dp e^{-iapB} f_0(p,\zeta) \langle e^{-ia\zeta} \right. \tag{3.128}$$

$$\left. \times\, e^{-iaA_1 B \sin\zeta} e^{-iaA_2 B_2 \sin(K\zeta + KB_1 p + KA_1 B_1 \sin(\zeta+\phi))} \rangle \right| \tag{3.129}$$

where N_0 is the number of electrons per unit length, $B = B_1 + B_2$ with B_1 defined in Eq. 3.96 and B_2 is defined as B_1, but $R_{56}^{(1)}$ is replaced by $R_{56}^{(2)}$, a is the harmonic that we want to generate, $K = \frac{k_2}{k_1}$ and the average is performed over the longitudinal coordinate ζ. If we change the integration variable from p to $p' = p - \tilde{h}\zeta$ and then we perform the average respect to the ζ variable as reported in [65] we find that the integral does not vanish only if a satisfies the relation:

$$a = \frac{n + mK(1 + \tilde{h}B_1)}{1 + \tilde{h}B}. \tag{3.130}$$

After these steps, we integrate Eq. 3.128 and the EEHG bunching factor for a linearly chirped electron beam results:

$$b_{n,m} = \left| J_m\left(\frac{n + mK(1+\tilde{h}B_1)}{1+\tilde{h}B} A_2 B_2 \right) J_n\left(\frac{A_1(nB + mKB_2)}{1+\tilde{h}B} \right) e^{\frac{(nB+mKB_2)^2}{2(1+\tilde{h}B)^2}} \right|. \tag{3.131}$$

The behavior of the bunching respect to the linear chirp h is represented in Fig. 3.32 [65]. Where we notice that with a positive chirp h the bunching degrades faster respect to a negative chirp. If we focus on the behavior of the bunching for a beam with no chirp, with $\tilde{h} = -0.015$ and $\tilde{h} = 0.015$, we see that by optimizing the second chicane dispersion, also when $\tilde{h} \neq 0$ it is possible to achieve the maximum bunching that we have in the case of no chirp. In particular, if we look at Fig. 3.33 if we have a negative chirp $\tilde{h} < 0$ we have to increase in modulus the second chicane dispersion, and for positive chirp $\tilde{h} > 0$ we should decrease the second chicane dispersion respect to the value that maximized the case with no chirp [65].

If we assume to have a linear chirp that satisfies $|h| \ll 1$ we can expand in Taylor series a defined in Eq. 3.130 and we set $n = -1$, for which we have the

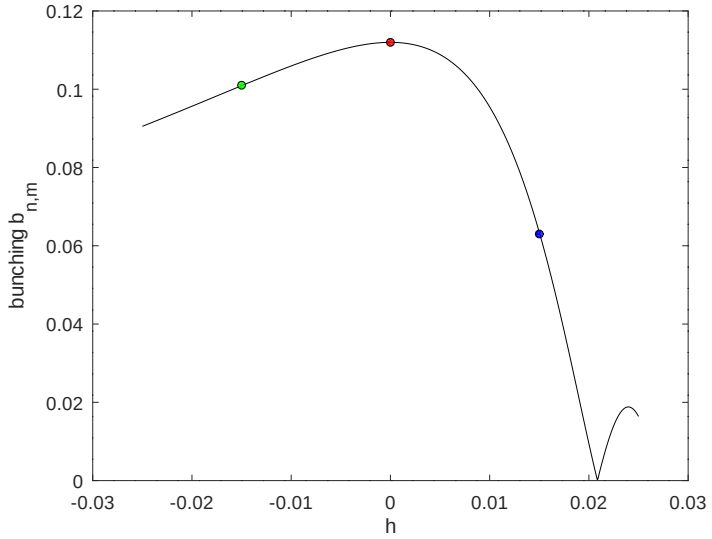

Figure (3.32) EEHG bunching from Eq. 3.131 as a function of the linear energy chirp of the electron beam. The red dot is the bunching value for an electron beam without chirp $\tilde{h} = 0$ and the green and blue dots indicate the bunching value for a linear chirp $\tilde{h} = -0.015$ and $\tilde{h} = 0.015$ respectively.

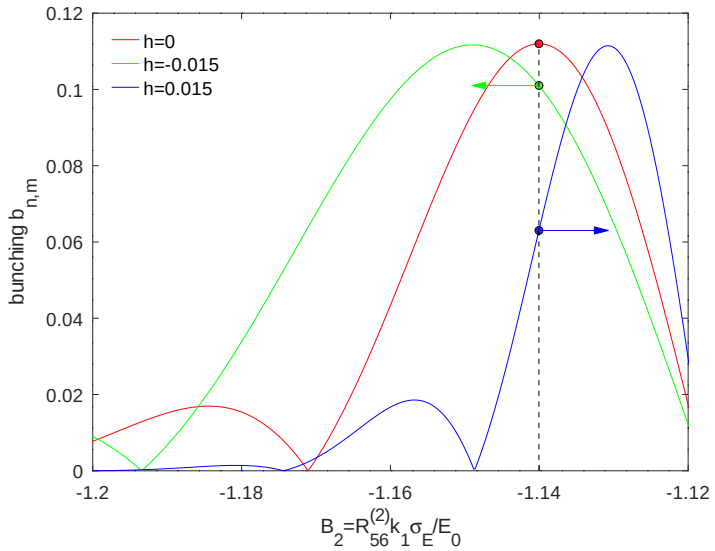

Figure (3.33) EEHG bunching for three different cases: electron beam with no chirp $\tilde{h} = 0$, with negative chirp $\tilde{h} = -0.015$ and with positive chirp $\tilde{h} = 0.015$. By adapting the second chicane dispersion, also for EEHG lasing with a linearly chirped electron beam, it is possible to achieve the maximum bunching that we have with an unchirped electron beam.

maximum bunching for EEHG, we get:

$$a \approx mK - 1 + (B - mKB_2)h. \tag{3.132}$$

The first part of this equation $mK-1$ is the harmonic number that we would have with a beam with no chirp $\tilde{h} = 0$ and the second part $(B-mKB_2)h$ appears only in presence of a linear chirp, however this factor is very small because $mKB_2 \sim B_1$ and so the term $(B - mKB_2)\tilde{h} \propto B_2\tilde{h} \ll 1$. As a result, the wavelength shift induced by a linearly chirped electron beam is almost negligible in EEHG. In Figure 3.34 we show the wavelength shift for EEHG in comparison with the wavelength shift for HGHG. The wavelength shift is defined as:

$$ws_{EEHG/HGHG} = \frac{\lambda'_{EEHG/HGHG}}{\lambda_{EEHG/HGHG}} \tag{3.133}$$

where $\lambda'_{EEHG/HGHG}$ is the FEL wavelength resulting by the use of a linearly chirped electron beam for either the EEHG:

$$\lambda'_{EEHG} = \frac{1 + \tilde{h}B}{\left[\frac{n}{\lambda_{s1}} + (1 + \tilde{h}B_1)\frac{m}{\lambda_{s2}}\right]} \tag{3.134}$$

or the HGHG scheme $\lambda'_{HGHG} = (1+\tilde{h}B)\lambda_{HGHG}$ and $\lambda_{EEHG,HGHG}$ is the expected FEL wavelength when the electron beam has no energy chirp, that for EEHG is:

$$\lambda_{EEHG} = \frac{1}{\frac{n}{\lambda_{s1}} + \frac{m}{\lambda_{s2}}} \tag{3.135}$$

and for HGHG was simply $\lambda_{HGHG} = \frac{\lambda_s}{a}$ where now a is the harmonic number. Figure 3.34 shows that in HGHG we have a visible wavelength shift, while in EEHG the effect of having a linear energy chirp in the electron beam is almost negligible.

Non-linear energy chirp

It might happen that the electron beam arriving from the linac has non-linear energy chirp. In this case, the FEL wavelength is shifted as in the case of having a linear energy chirp, in addition the FEL bandwidth widthens [57]. Compared to

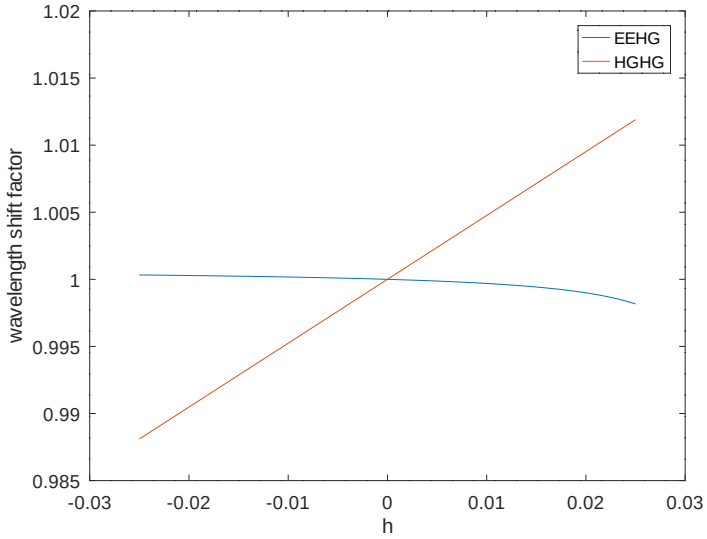

Figure (3.34) Wavelength shift induced by a linear energy chirp in EEHG and HGHG. The plot remarks that the EEHG wavelength is negligiby affected by a linear chirp, while the HGHG FEL wavelength is shifted with a linear trend [57].

the bandwidth widthening of HGHG in case of lasing with a non-linearly chirped electron beam, the EEHG bandwidth grows with a lower rate as shown in [57]. This suggests that with EEHG is easier to keep the FEL pulses close to the transform limit.

3.2.3 Degrading effects affecting EEHG

The EEHG scheme is extremely sensitive to diffusion in energy effects which can smear out the fine-structures in the longitudinal phase space distribution. In c) in Figure 3.23 it is observable that the spacing between the energy bands varies with p. In fact, in the centre the energy bands have an higher density. Nevertheless, the order of magnitude of the energy band separation is [66]:

$$\Delta E_B = \left(\frac{\pi}{B_1}\right)\sigma_E. \tag{3.136}$$

The quantum fluctuations in the Inchoerent Synchrotron Radiation (ISR) are the driver for the growth of the uncorrelated energy spread. This might smear out the EEHG energy bands if the added spread approaches Eq. 3.136. ISR happens

in dipoles and undulator structures. Ergo, it is suggested to estimate its effects before performing experiments. In [67] it is given a formula to estimate the ISR in a dipole:

$$\Delta\sigma_E^2|_{ISR} = \frac{55e^2\hbar c}{48\sqrt{3}}\frac{L}{R^3}\gamma^7 \tag{3.137}$$

where R is its bending radius, L is the dipole length, $E = \gamma mc^2$. Therefore, having a chicane with a high bending radius is beneficial to reduce the ISR effect. An estimate of the quantum diffusion in a planar undulator can be found in [68]:

$$(\Delta\gamma)^2 = \frac{7}{15}\frac{\hbar}{mc}L_w r_e \gamma^4 k_w^3 K^2 F(K) \tag{3.138}$$

where r_e is the classical electron radius, K is the undulator strength and $F(K) \approx 1.42K$. Quantum diffusion matters in the second modulator, because in the first one the structures are not there yet. ISR in the undulator is enhanced for high energy electron beams and long undulators. It is advantageous to increase the period length of the second modulator to help suppressing ISR.

The EEHG scheme is not significantly affected from the perturbations affecting the electron beam in the linac up to the first EEHG modulator [69]. On the other side, energy and density perturbation arising along the EEHG setup might have a significant impact. The arise of microbunching instabilty and the emission of coherent synchrotron radiation are the main drivers of the electron beam unwanted features in this region.

The microbunching instability happens when an electron beam is arriving at the EEHG setup with a modulated current profile:

$$I(z) = I_0(1 + 2b_0\cos(k_0 z)). \tag{3.139}$$

$\omega_0 = k_0 c$ is the frequency of the density modulation and it is assumed that $I(z)$ has a small amplitude, hence $b_0 \ll 1$. The electrons near the density peaks repulse due to the longitudinal space charge force (LSC) along the drifts. The EEHG beamline behaves like an LSC-amplifier (LSCA) [70], where the first modulator and chicane act similarly to a laser heater by washing out part of the energy modulation [71].

As a consequence, the initial density modulation is converted into energy modulation. This process can happen in the first modulator, in parallel with the interaction with the first seed laser. Eventually the first chicane can convert the LSC-induced energy modulation into density modulation again and be further

amplified. Finally, again, in the second modulator the LSC forces convert the density modulation into energy modulation. In order to prevent the microbunching instability to affect the EEHG bunching factor, it is necessary to keep b_0 low in Eq. 3.139 [69].

The coherent synchrotron radiation (CSR) can be generated along a chicane at a wavelength greater than the electron beam length σ_z. As a consequence, the electron beam develops density modulation at wavelengths smaller than σ_z [72]. CSR is particularly aggressive with the EEHG scheme because it acts along the chicanes where the electron beam is shaping its phase space distribution. However, with a proper chicane design is possible to minimize its effects. In [69] it is derived a constrain on the first chicane dispersion strength:

$$R^{(1)}_{(56)} \leq \left[\frac{\sigma_z}{6} \left(1 + \frac{3L_D}{2L_m} \right) \left(\frac{I_A \gamma}{|n| I_0 k_1} \right)^3 \right]^{1/4} \tag{3.140}$$

where L_D is the drift length between the first and second dipole, L_m is the dipole length, I_A is the Alfven current, $|n|$ is the EEHG parameter, I_0 is the electron beam current and k_1 is the wave number of the first seed laser. In order to reduce the CSR effect, chicanes with $L_D/L_m \gg 1$ are favoured.
In [21] it is mentioned that resistive wall wakefields in the radiator section might degrade the spectral purity of the EEHG pulse. So, in the design process of an EEHG beamline it is necessary estimate the tolerances for this effect.

Seeding at sFLASH

Chapter 4

Seeding at sFLASH

sFLASH is the seeding experiment installed at FLASH the Free-electron LASer in Hamburg. The first section of this chapter is giving an overview of the FLASH facility. The rest of the chapter focuses on the seeding experiment at FLASH (sFLASH). sFLASH is exploited to learn external seeding techniques as HGHG, and first steps towards EEHG are on-going. With the consolidated scheme of HGHG seeding is possible to run two different experiments: THz streaking of the FEL pulse and XUV pulse shaper. The THz streaking is a powerful diagnostics technique that permits to reconstruct the full temporal information of the FEL pulse in terms of duration and frequency of the electric field. We are going to focus on the THz streaking in the next sections and benchmark the experimental results with simulations.

4.1 The FLASH FEL

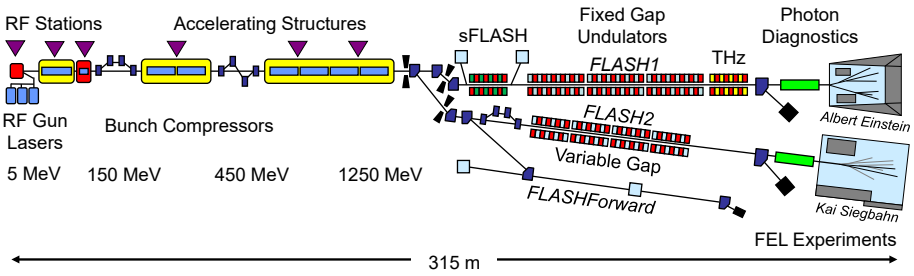

Figure (4.1) Layout of the FLASH facility.

Parameter	**FLASH**1	**FLASH**2
Electron beam energy	$0.35 - 1.25\,\mathrm{GeV}$	$0.4 - 1.25\,\mathrm{GeV}$
Normalised emittance at 1 nC	$1.4\,\mathrm{mm\,mrad}$	$1.4\,\mathrm{mm\,mrad}$
Energy spread	$200\,\mathrm{keV}$	$500\,\mathrm{keV}$
Electron bunch charge	$0.1 - 1.2\,\mathrm{nC}$	$0.02 - 1\,\mathrm{nC}$
Peak current	$1 - 2.5\,\mathrm{kA}$	$1 - 2.5\,\mathrm{kA}$
Electron bunches per second (typ./max)	300/5000	300/5000
Photon energy (fundamental)	$24 - 295\,\mathrm{eV}$	$14 - 310\,\mathrm{eV}$
Photon wavelength (fundamental)	$51 - 4.2\,\mathrm{nm}$	$90 - 4.2\,\mathrm{nm}$
Photon pulse duration (FWHM)	$\leq 30 - 200\,\mathrm{fs}$	$\leq 10 - 200\,\mathrm{fs}$
Peak Power (from av.)	$1 - 5\,\mathrm{GW}$	$1 - 5\,\mathrm{GW}$
Single photon pulse energy (average)	$1 - 500\,\mu\mathrm{J}$	$1 - 1000\,\mu\mathrm{J}$
Spectral width (FWHM)	$0.7 - 2\%$	$0.5 - 2\%$
Photons per pulse	$10^{11} - 10^{14}$	$10^{11} - 10^{14}$
Peak Brilliance	$10^{28} - 10^{31}$ B	$10^{28} - 10^{31}$ B

Table (4.1) Main parameters for FLASH FEL.

FLASH is the free-electron laser user facility in Hamburg. A superconducting linear accelerator that enables high repetition rate operation, up to 1 MHz, drives the FEL. FLASH was initially known as Tesla Test Facility (TTF), that achieved saturation at 109 nm in 2001 [73]. Since than, the radiation is generated using the SASE principle.

After the LINAC upgrade between 2009 and 2010, it was possible to achieve an electron beam energy of 1.25 GeV. As a consequence, FLASH achieved lasing down to 4.12 nm in 2010 [74].

Table 4.1 reports FLASH parameters used for SASE operation in the two beamlines FLASH1 and FLASH2. The requirements regarding electron beam energy, charge and peak current are different for SASE operation in FLASH1 or FLASH2 undulator beamlines and seeding in sFLASH. In the section dedicated to seeding, we are going to present the parameters used routinely at sFLASH.

At FLASH the electrons are produced by a laser-driven photo-injector and then accelerated in a 130 m long linear accelerator. The electron beam is compressed in two stages along the linear accelerator to achieve the wanted peak current. Finally, it is collimated and send to the two undulator beamlines using a combination of fast kicker and septum.

In the next subsections, we are going to give more details on the main parts of the machine: photoinjector, linear accelerator and beamlines.

4.1.1 Photoinjector

The injector at FLASH has been designed to achieve high bunch charge (up to 2 nC) and rapid acceleration to relativistic energies to avoid electron beam disruption due to space charge forces. A UV laser, generated with mode-locking in a solid-state laser system and synchronized to the 1.3 GHz RF of the linac, hits the cathode [75]. The cathode is made by molybdenum and covered by a thin layer of caesium-telluride (Cs_2Te). It achieves quantum efficiencies around 5% and it is placed inside a gun, a 1.5-cell normal conductive radio-frequency cavity, operated at 1.3 GHz with an accelerating voltage of $50 - 53\,\mathrm{MV\,m^{-1}}$. A solenoid surrounds the gun cavity and it is generating a focusing field to keep a small (μm range) electron beam cross-section. The generated electrons are accelerated, and they achieve an energy of about 5.5 MeV at the end of the RF-gun. The electron beam initial current is up to 50 A, and its duration is few picoseconds to avoid space charge effects. For seeding, we typically use a bunch charge of 0.4 nC.

4.1.2 Linear accelerator

The FLASH linac total length is 130 m. Seven superconducting modules each 12 m long are occupying the highest portion of this space. Each module contains eight 1 metre nine-cell standing wave TESLA-type cavities operated with RF power at 1.3 GHz (L-band) with gradients that typically span between $20\,\mathrm{MV\,m^{-1}}$ and $25\,\mathrm{MV\,m^{-1}}$. The power is generated by modulator driven klystrons; the high power electromagnetic RF wave is transported to the cavities by RF waveguides. The cavities are made by ultra-pure niobium, and the temperature is kept at 2 K by a helium cooling system.

Thanks to the extremely low RF energy losses in the superconducting accelerating cavities, an RF duty cycle and thus a beam duty cycle of up to 100%, in other words continous operation, could in principle be achieved. A cw operation upgrade would demand for a higher cryogenic capability, installation of new RF power sources Inductive Output Tubes (IOT), upgrade of the accelerator modules with higher gradient and a new gun concept would be necessary [76]. While the RF duty cycle of the superconducting modules in FLASH is 1.4%, 600 µs fill-time plus 800 µs flat top, with pulse repetition frequency of 10 Hz, the beam duty cycle

at FLASH is currently limited by 0.8% (800 µs flat top duration at 10 Hz). For SASE operation, trains of up to 800 bunches per RF pulse can be accelerated. For seeding experiments, on the other hand, we operate with single bunches at 10 Hz, i.e. one bunch per RF pulse. However, for FLASH2020+ we are aiming at seeding at 100 kHz bursts with 10 Hz.

ACC1 is the first module, and it is accelerating the electron beam up to 165 MeV. ACC1, accelerates the electron beam off-crest respect to the RF voltage, as shown in Fig. 2.2 (left plot). The electrons in front of the beam (in red) gain less energy compared to the trailing electrons (in blue). Hence, the particle position within the bunch becomes correlated with its energy. As a result, the electron beam has an energy chirp h, defined in Eq. 3.82, where E_0 is the reference energy of the electron at the exit of the module.

The module ACC39 follows ACC1. ACC39 operates in deceleration mode (the phase has a 180° shift compared to ACC1) at the third harmonic of the acceleration frequency (3.9 GHz) [56]. ACC39 compensates the energy curvature on the electron bunch introduced by the ACC1 voltage. Afterwards, the energy-chirped electron bunch encounters the first bunch compressor (BC2), where compression will happen. As the Lorentz force depends on the particle momentum

$$p_z[GeV/c] = 0.2998 \cdot B[T] \cdot R[m] \tag{4.1}$$

the radius of curvature R is going to be different for electrons with different energies. After the first compression stage, the electron bunch is accelerated up to 450 MeV by the following two modules ACC23 and compressed a second time in the bunch compressor (BC3). The design of BC2 and BC3 are described in [77]. The electron beam achieves its final energy after the accelerating modules ACC45 and ACC67. The maximum achievable energy is 1.25 GeV. During seeding operation, the module ACC67 is not in operation. Nevertheless, it can be activated to add chirp on the electron beam. After each bunch compressor, the beam arrival monitors (BAM) can be used to determinate the on-crest phases of the accelerating cavities if the nominal energies at the entrance of the bunch compressors correspond to the values showed also in Fig. 4.1 [78]. The sFLASH hardware is designed to operate at ~ 700 MeV, for higher energies we would need to upgrade chicanes, vacuum pipes and undulators. The compression for seeding is mainly performed in the first bunch compressor (BC2) in order to minimize the microbunching gain, following the experimental evidence observed at FERMI FEL [14].

4.1.3 Beamlines: FLASH1 and FLASH2

FLASH has two undulator beamlines: FLASH1 and FLASH2. Simultaneous operation of the two beamlines is possible [79]. When only FLASH1 is in operation the bunch trains are accelerated in up to 800 µs RF flat tops. The repetition rate of the RF-pulses is 10 Hz. Spacing between bunches and bunch charge can be chosen. The representation of the timing for FLASH1 is shown in the top image of Fig. 4.2. During sFLASH operation, the RF-pulse is filled by only one bunch. When FLASH1 and FLASH2 are operated in parallel, two bunch trains are ac-

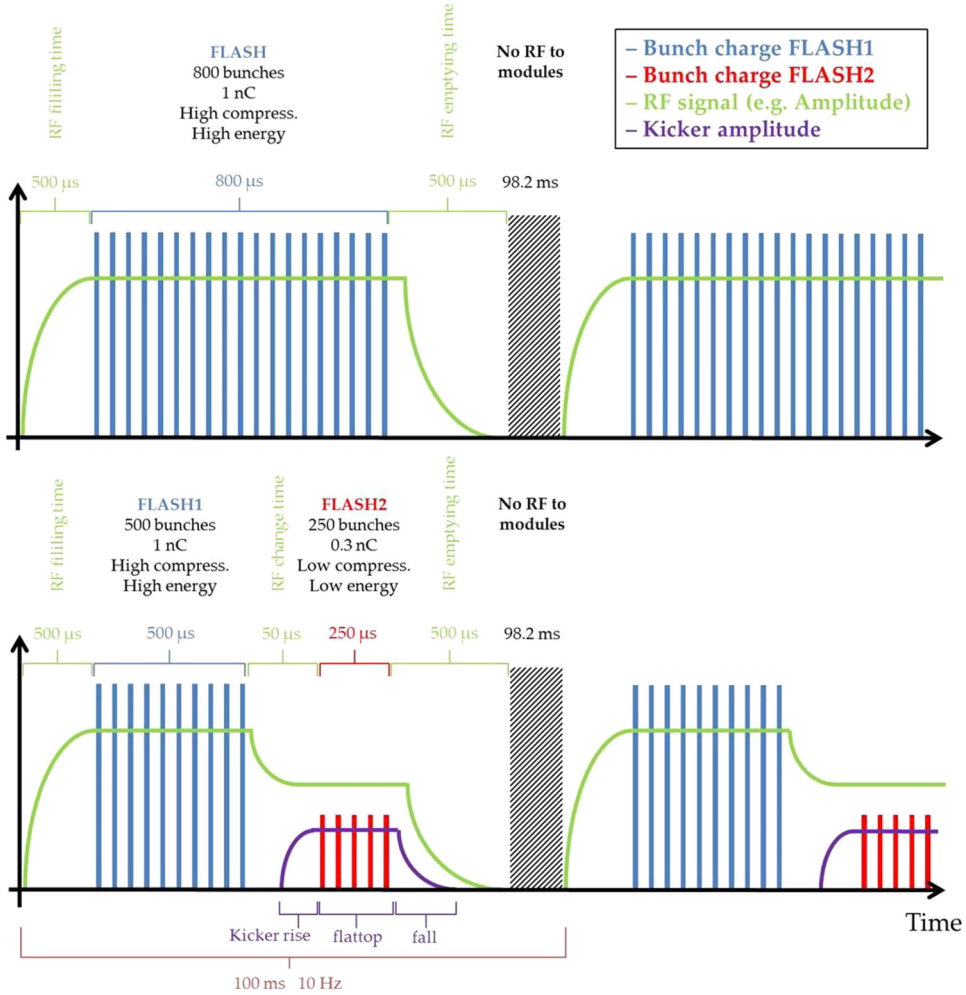

Figure (4.2) Top: timing for FLASH. Bottom: timing for simultaneous operation of FLASH1 and FLASH2. Figure from [79].

celerated in the same RF-pulse. The two trains are generated by two distinct injector lasers. Hence, the charge and the separation of the bunches within the

two different bunch trains is controlled independently. The bunch train designated for FLASH2 is separated by 50 µs gap from the bunch train going in the direction of FLASH1, to permit the ramping up of the fast kicker current in front of FLASH2. The combination of the fast kicker with a septum selects the bunch train for FLASH2. This is shown schematically in the bottom image of Fig. 4.2. A transverse collimator is located between ACC67 and the kicker-septum system for for beam seperation. Both FEL beamlines start with magnetic structures that provide closed disperson bumps that allow for energy collimation. In the case of FLASH2 this is the so-called extraction arc, while for FLASH1 a dogleg serves this purpose. The sFLASH experiment is placed immediately behind the dogleg, and it is described in the next section.

Downstream sFLASH's FEL extraction chicane, there is a vertically transverse deflecting RF structure, LOLA, that together with a horizontally deflecting dipole (D9SMATCH) is used to reconstruct the longitudinal phase space distribution of the electron beam [80]. A matching section follows LOLA before the FLASH1 main undulator, where FEL radiation is generated with the SASE process for photon user experiments. The FLASH1 undulator consists of six undulator module each 4.5 m long. These are made by iron pole shoes with NdFeB permanent magnets in between. Their gap is fixed to 12 mm, the period length λ_u is 27.3 mm and the peak magnetic field at the undulator centre is $B_0 = 0.48\,\mathrm{T}$, so the undulator period can be estimated as:

$$K = \frac{eB_0\lambda_u}{2\pi m_e c} = 0.934 \cdot B_0[T] \cdot \lambda_u[cm] = 1.224 \tag{4.2}$$

The disadvantage in having fixed gap undulators is that in order to change the FEL wavelength it is necessary to change the electron beam energy.

Beyond the FLASH1 undulator section the electron beam is deflected into the beam dump by a bending magnet, while the FEL radiation passes through a diagnostics section and then to the experiments. The tools available in the diagnostics sections are a Ce:YAG screen to image the transverse beam profile, a gas monitor detector (GMD) [81] a micro-channel plate (MCP) [82] both used to quantify the pulse intensity and a grating spectrometer to get information about the spectrum [83].

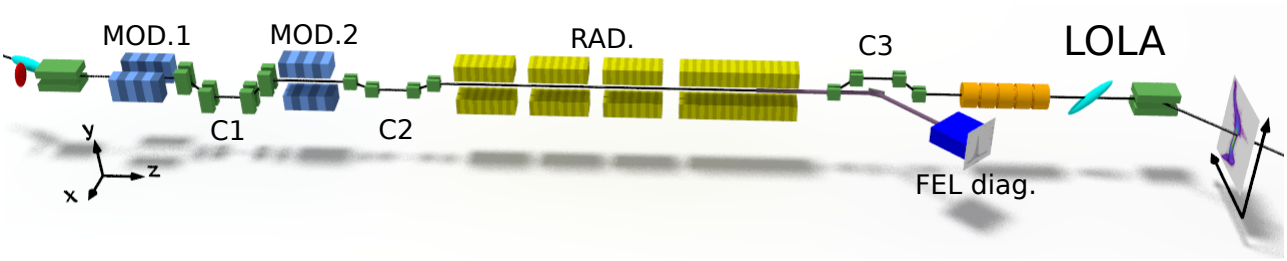

Figure (4.3) sFLASH layout

4.1.4 sFLASH

At DESY, an experimental setup for seeding developments has been installed upstream of the FLASH1 main SASE undulator in 2010 [84]. After successful demonstration of direct-HHG seeding at 38 nm in 2012 [44], the focus of the seeding R&D at FLASH has turned to high-gain harmonic generation (HGHG) and echo-enabled harmonic generation (EEHG) [85]. In the following we describe the sFLASH experimental setup.

Experimental setup

Figure 4.3 shows the schematic layout of the sFLASH experiment. At the exit of the energy collimator, the sFLASH section starts with two electromagnetic undulators (MOD1 and MOD2 in Fig. 4.3) with 5 full periods of period length $\lambda_u = 0.2\,\mathrm{m}$ and orthogonal polarization [86],each followed by a magnetic chicane (labelled as C1 and C2). The seed laser for seeding is injected in the beamline before MOD1.

The seed laser The 267 nm seed is obtained from the third-harmonic generation (THG) of a 800 nm near-infrared (NIR) Ti:sapphire laser. Downstream the THG setup it is placed a thin film polarizer (TFP) able to modify the polarization of the seed laser pulses in order to optimize the interaction in the two modulators (MOD1, MOD2) with different orientation of the field. The maximum energy of these UV seed pulses at the entrance of the vacuum transport beamline to the modulator undulator is 500 µJ. A significant part of the energy is lost during the

transport of the seed laser to the electron vacuum pipe. That consists of an initial part that transports the laser pulses from the optical table down in a pit and from here they enter the FLASH tunnel. At the entrance of the FLASH tunnel, they pass through two boxes, which contain mirrors and diagnostics. Finally, the seed laser is sent to the electron beamline with an angle.
The Rayleigh length of the UV beam is between 1.5 and 3 m, corresponding to a waist of $w_0 = 357\,\mu m$ and $505\,\mu m$ respectively. The waist position is located within the modulator where it happens the interaction with the electron beam. It is possible to optimize the waist position during operation by changing the NIR focusing into the THG setup.
A single-shot cross-correlator for NIR and UV pulses in the laser laboratory enables to measure the UV pulse duration, that is typically between 250 and 280 fs FWHM. The NIR pulse duration is simultaneously measured with a single-shot auto-correlator and it is about 50 fs FWHM. A X-FROG setup for single-shot measurements of the duration of UV pulses is under development. Up and downstream MOD2, the seed beam position and size are measured using Ce:YAG fluorescence screens. Recently Ce:YAG screens have been added before and after MOD1 and are currently under commissioning. These new screens will help the overlap procedure in the first modulator during the EEHG beamtimes.

Radiator section sFLASH has 10 m effective length of radiator, which is composed by four variable gap undulator modules (labeled RAD in Fig. 4.3)) [87, 88]. These undulators are hybrid structures build with NdFeB magnets and Vanadium Permandur poles. The first three undulators have period length of $\lambda_u = 31.4\,mm$, number of periods $N_u = 60$ resulting in a module length of $L_u = 2\,m$. Their minimum gap is 9 mm correspondent to an undulator strength of $K = 2.72$. The last undulator has a slightly higher gap 9.8 mm which corresponds to $K = 3.03$ and it has also a longer period $\lambda_u = 33\,mm$ and number of periods $N_u = 120$. The total length of the fourth undulator is 4 m.
Between any adjacent two of these four undulator modules there is an intersection of 700 mm length which is occupied by a quadrupole, diagnostics components, an vacuum pump and a phase shifter.
Downstream of the sFLASH radiator, the electron beam is guided around the radiation extraction mirrors by chicane C3 and it enters into the LOLA transverse-deflecting structure (TDS). The TDS is followed by a dispersive dipole spectrom-

eter that deflects the electron bunch into a beam dump. An observation screen is installed in the dispersive section between the dipole spectrometer and the beam dump on which the longitudinal phase space distribution of the electron bunch can be observed.
The parameters of the electron bunch such as current and slice emittance can be obtained from the data from LOLA [89].
When operated with uncompressed electron bunches (in order to exclude FEL gain), the uncorrelated energy spread of the electron bunch can be extracted by analysing coherent harmonic generation (CHG) emission at several harmonics [90]. The energy resolution of this technique significantly surpasses that of the TDS setup.

FEL diagnostics The seeded FEL pulses are transported to an in-tunnel photon diagnostics section, where different detectors are available: fluorescence screens for transverse beam diagnostics, a photon energy monitor based on a microchannel plate, and a high-resolution spectrometer for wavelengths from 40 to 4 nm [91]. A second, non-invasive method to obtain the power profile of the photon pulses is to extract this information from longitudinal phase space distributions of the electron bunch [89].

Experiments at sFLASH The FEL pulse instead of being guided to the in-tunnel photon diagnostics, can be transported to the photon laboratory where two experiments are located: the THz streaking and the XUV pulse shaper. More information about the XUV pulse shaper can be found in the thesis [92]. In the next section we are going to explain more in detail the THz streaking experiment.

4.2 HGHG at sFLASH

sFLASH is operated since 2015 with the HGHG seeding scheme. MOD2 (Figure 4.3) is usually set to resonance with the seed laser wavelength ($\lambda = 267\,\mathrm{nm}$), so that the energy exchange with the electron beam is possible. Chicane C2 is

Table (4.2) sFLASH experimental parameters.

	parameter	value
modulator	period length	0.2 cm
	total length	1.2 m
	peak K	10.8
radiator	period length	31.4 mm
	total length	10 m
	peak K	2.7
chicanes	R_{56} C1	not used
	R_{56} C2	$50 - 200$ µm
	R_{56} C3	190 µm
electron beam	energy	$680 - 700$ MeV
	peak current	$500 - 700$ A
	charge	0.4 nC
	bunch duration	> 500 fs (FWHM)
seed beam	wavelength	267 nm
	pulse energy	< 280 µJ
	UV pulse length	$\sim 250 - 280$ fs (FWHM)
	UV Rayleigh length	1.6 m
	NIR pulse length	~ 50 fs (FWHM)

exploited as bunching chicane, which converts the energy modulation imprinted on the electron beam in MOD2 into density modulation and therefore bunching. MOD1 and chicane C1 are not used for standard HGHG operation. Table 4.2 summarizes the parameters of the sFLASH hardware and the typical properties set for the electron beam and the seed laser pulse.

To maximize the energy exchange between seed and electrons, the seed laser should be focused in MOD2 and overlapped longitudinally and transversely with the electron beam. The transverse overlap is performed with two Ce:YAG screens placed before and after MOD2. On these screens a region of interest (ROI) indicates the golden trajectory for the seed laser and for the electron beam. The golden trajectory has been established based on: avoid that the seed laser reflects against the vacuum pipe and the electron beam trajectory is loss-free. The seed laser is moved on the ROIs using the motors of four mirrors placed in the injection beamline. The electron beam is carried at the same position using two horizontal and two vertical steerers iteratively. Once the transverse overlap is achieved, the orbit feedback on the electron beam trajectory is activated to keep the electron beam trajectory within MOD2.

Then, the longitudinal overlap has to be found. This is usually done in two steps, first we find the coarse overlap, and then we fine tune by driving the seed laser on

the electron beam. For the coarse overlap, we use a photo-multiplicator (PMT) linked to an oscilloscope. We sent the OTR radiation coming from the electron beam passing through an OTR screen inserted in C1 to the PMT, which than gives a signal on the oscilloscope and we mark the rising edge of the signal. Afterwards, we observe at the visible light generated from the seed laser passing through a Ce:YAG screen inserted in C1. Hence a second signal on the oscilloscope appears and we can calculate the time separation between the two pulses. The OTR and visible radiation is transported by a mirror in the diagnostic section placed on the optical table located under C1, where is located the PMT. The oscilloscope is mounted in the laser laboratory, outside the tunnel [93]. At this point, the temporal displacement between electron beam and seed laser can be reduced down to 10 ps, using the vector modulator controlling the seed laser phase respect to the master laser oscillator (MLO) which is also controlling the injector laser. Once the screen is taken out, the fine tuning for the longitudinal overlap is achieved by looking at the longitudinal phase space distribution of the electron beam from LOLA. The vector modulator phase is scanned in tiny steps of 0.5 ps until the signature of the modulation from the seed laser is observed on the electron beam phase space. All these steps are usually performed with uncompressed electron beam because the beam is longer respect to the uncompressed case, ergo it is easier to find the overlap. In Figure 4.4 we show how it should look the longitudinal phase space distribution of the electron beam (uncompressed) when successfull longitudinal overlap has been achieved: the typical energy deviation signature left by the seed laser is highlighted by a red circle. This LOLA measurement is performed with radiator off. From the LOLA measurement it is possible to extract the energy modulation imprinted on the electron beam by the seed laser, as shown in Fig. 4.4 and explained in detail in [94]. The maximum modulation amplitude achievable experimentally was found to be (350 ± 50) keV [94]. Afterwards, we compress the electron beam and we set the radiator modules to resonance to the harmonic of interest, mostly the seventh and the eight harmonic. To do so, for each radiator a gap scan within an interval selected by the operator is performed: the gap of the radiator is set to the lowest value of the interval, after a selected number of signals collected by the MCP, the gap is changed to the next value and the procedure is repeated until the highest value of the interval is reached. The first interval is chosen to be coarse so one can see where the radiator is resonant, and the next interval is close to one of the resonances. If we do not see a resonance, it means that the system is not properly optimized, hence further tuning is nec-

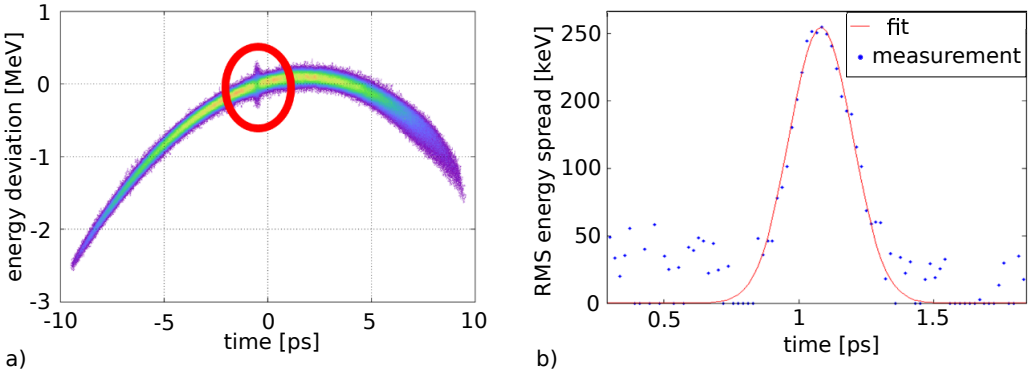

Figure (4.4) Extraction of modulation amplitude from longitudinal phase-space distribution: (a) Measured longitudinal phase space distribution of an uncompressed electron beam and radiator off. Energy-modulated region is highlighted with a red circle. (b) Extracted rms energy spread along the electron bunch from the measurement shown in (a).

essary (electron beam trajectory, overlap between electron beam and seed laser, optics,...). The gap scan is performed for each radiator and finally we expect to see a FEL signal. This we can observe from LOLA, that remarks the region where the electron beam has lased with a significant variation of the electron beam energy deviation, as shown in Fig. 4.5. Figure 4.6 shows consecutive single-shot spectra

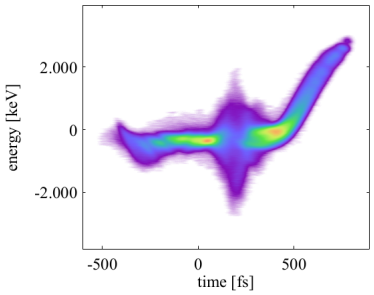

Figure (4.5) Longitudinal phase-space distribution measured after the seeding setup. The region with increased slice energy spread is the signature of the successful laser-electron interaction.

of the FEL at the eighth harmonic. The central wavelength is $\lambda_8 = 33.47\,\text{nm}$ and the spectral width is $\frac{\Delta\lambda}{\lambda_8} = 3.02 \times 10^{-4}$ FWHM. The corresponding FEL pulse energies are presented in the histogram in Fig. 4.7. The average seeded FEL pulse energy is $(26.2 \pm 6.5)\mu\text{J}$. At the seventh harmonic the typical spectral width is $\frac{\Delta\lambda}{\lambda_7} \leq 1.4 \times 10^{-3}$, the seeded FEL pulse energy is $\sim 50\,\mu\text{J}$ and the gain length was measured to be between 0.6 and 0.9 m depending on the initial modulation amplitude [95, 96].

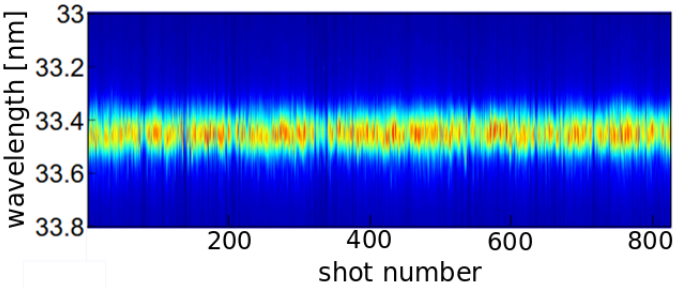

Figure (4.6) Series of consecutive single-shot FEL spectra taken in HGHG operation at the 8^{th} harmonic.

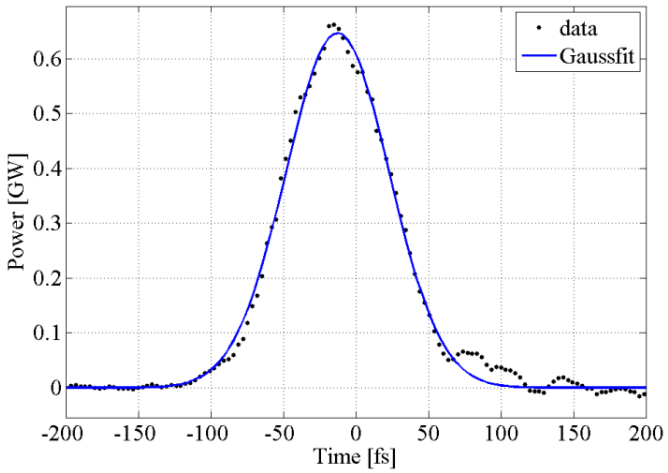

Figure (4.7) FEL power profile at the seventh harmonic extracted from LOLA TDS measurement.

4.2.1 Control of duration and phase of FEL pulses: benchmark between simulation and THz streaking experiment

Characterizing the FEL pulse duration is a well known issue at FEL facilities, and many techniques have been already developed and tested. These methods might be indirect, thus the FEL pulse information are extracted from machine parameters, as the longitudinal phase space of the electron beam [97, 98, 89], the fluctuations of the radiated spectrum [99] or the number of observed spikes in SASE FELs [100]. While direct measurements of the FEL pulse are either based on auto or cross-correlation with an external laser of the FEL pulse in the solid state or in the gas phase. The THz streaking technique is classified as direct method for FEL pulse duration measurement.

THz streaking is an experiment which characterizes the single-shot FEL temporal

profile in terms of duration and phase of the electric field [101]. In particular, it is possible to extract the amount of chirp in the electric field phase, so how much the radiation phase is varying respect to time.
At sFLASH a THz streaking setup is located in the FEL extraction hutch and a description of it can be found in Fig Fig. 4.8 [102].
Simulations of the seeded FEL can help to understand deeper the experimental

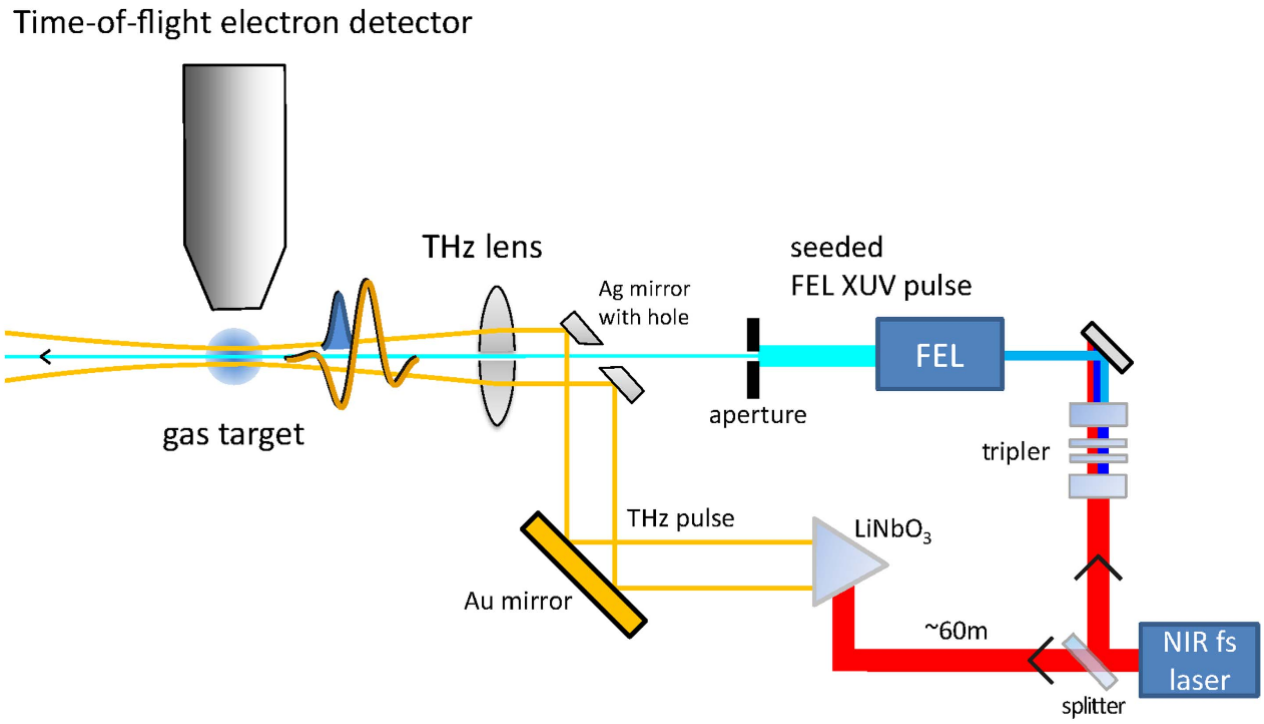

Figure (4.8) THz streaking setup at sFLASH. From right the NIR seed laser is split in two pulses, one part is send first to a tripler (THG), were is produced UV light and then is sent to the FLASH tunnel were it interacts with the electrons that than are going to produce FEL light. The seeded FEL pulse enters the time of flight (TOF) detector through an aperture. The other portion of NIR pulse is sent to a LiNbO3 crystal that converts it into THz wavelength, than through a system of mirrors and lenses is sent to the TOF. The TOF is collecting electrons from the gas target which have been ionized by the energy exchange from the sum of the FEL pulse and the THz pulse, that might be overlapped at different positions during a measurement set.

parameters even if it is necessary to do some assumptions to simplify the real process. For example, seed and FEL pulses are assumed to be perfect Gaussians. In this thesis we have tried to gain more knowledge on the seed laser chirp. This method takes as a reference the final FEL pulse duration measured with the

THz streaking and with the simulation we can estimate which was the duration of the seed laser. Assuming that the pulses are Gaussian, the retrieved seed laser duration is used to calculate the amount of chirp using the time-bandwidth product given in Eq. 3.73. The chirp, usually is expressed in terms of $\alpha = a/2\sigma_{tcI}^2$ where σ_{tcI} is the RMS duration of the chirped seed laser, that can be derived using the relation for Transform-limited pulses Eq 3.73.
This technique might overestimate the seed laser chirp and duration because the FEL chirp and duration depends not only on the seed laser chirp, but also on the electron beam energy chirp and on the FEL process itself [103]. In the following, we assume that the chirp introduced by the FEL amplification process has a negligible effect because of the short radiator (10 m). Similarly, we neglect the contribution from the electron beam energy chirp. To quantify the impact of the electron beam chirp in the experiment we compare the simulated seed laser duration and chirp with the measured ones.
In the following section, we present the simulations based on the data collected during the THz streaking beamtime of March 2017 [102].

Seed laser characterization

The sFLASH seed laser pulses are not transform-limited, because the dispersive media in the optical setup have non negligible GVD and therefore a chirp rises in the temporal phase. Dispersion is also present in the two vacuum windows, which separate the laser laboratory from the accelerator beampipe. Two windows are necessary because the system is passing from the atmospheric pressure of the laser laboratory to the ultra-high vacuum of the accelerator. The first is a 3 mm thick quartz window that separates the laser laboratory atmosphere from the high-vacuum beam tube ($10 - 6$ mbar) containing mirrors to transport the seed into the FEL tunnel. The second is a 1 mm fused-silica window and it permits the passage of the seed pulses into machine vacuum.
The current setup does not allow to measure the chirp directly at the modulator. Nevertheless, we can characterize the spectrum and duration of the seed laser pulses immediately after the THG setup in the laboratory using a commercial spectrometer (Ocean Optics HR4000) with 1 nm-resolution and a cross-correlation measurement. A bandwidth of $\Delta\lambda = (1.3 \pm 0.5)$nm FWHM (corresponding to a

RMS spectral width of $\sigma_\omega = (14.7 \pm 0.3)$THz was estimated averaging over several UV spectrum measurements. Additionally, a pulse duration of $\sigma_t = (140 \pm 10)$fs RMS was obtained from the cross-correlation measurement. If we calculate the RMS duration of the transfomed-limited pulse exploiting Eq. 3.73 with $a = 0$, taking the spectral bandwidth $\Delta\lambda = (1.3 \pm 0.5)$nm, we get $\sigma_{tI} = 34\,$fs (RMS duration). Hence, the laser beam have a chirp already before passing through the vacuum windows. It is not clear from where this initial chirp originates. However, it is possible that the chirp is coming from the THG process or from damages in the optical elements as mentioned in [102]. From Eq. 3.73 we can also estimate the initial amount of chirp of the seed laser:

$$a = \pm 4.004. \tag{4.3}$$

In the laser laboratory there is neither a FROG nor a SPIDER setup, therefore we cannot measure the phase chirp of the seed laser to compare with the calculated value in Eq. 4.3. From estimation that have been done by taking into consideration the whole seed laser system setup it was concluded that the seed laser is compatible with both a negative and a positive chirp, as explained in [102].

THz streaking experiment

The FEL pulse during the experiment has been fully characterized by the THz streaking experiment at sFLASH. The measured FEL duration was

$$\sigma_{t,FEL} = (58 \pm 7.5)\text{fs} \tag{4.4}$$

and the chirp

$$\alpha_{FEL} = (970 \pm 400)\text{THz/ps} \tag{4.5}$$

In the paper [102], the chirp is defined as $c = -2\alpha$.

Simulations

The simulation of the seeded FEL is conducted in two sequential runs of the code GENESIS1.3 v.2 [104].

Table (4.3) Electron beam parameters for the THz streaking experiment at sFLASH.

Parameter	**sFLASH**
Electron beam energy	685 MeV
Normalised emittance	1 mm mrad
Energy spread	50 keV [94]
Electron bunch charge	0.4 nC
Peak current	500 A

Genesis simulation: part one In the first run, the laser-electron interaction in the six-period modulator is simulated. The parameters used for the electron beam are presented in table 4.3, the bunch is assumed to have a Gaussian profile. The transverse size of electron beam is chosen to be completely covered by the seed laser transverse profile.
For the seed laser, in the simulations, we assume a pure TEM00 mode and a Gaussian power profile for the seed laser:

$$P_{seed}(t) = P_0 \exp\left(-\frac{(t-t_0)^2}{2\sigma^2_{t,seed}}\right) \tag{4.6}$$

where $P_0 = E_{seed}/(\sqrt{2\pi}\sigma_{t,seed})$ is the peak power of the seed laser given by the total pulse energy E_{seed} that was set to a value of 16.5 µJ. The temporal phase of the seed laser pulse is

$$\phi_{seed}(t) = \frac{\alpha}{2}(t-t_0)^2 + \omega_0(t-t_0) + \phi_0 \tag{4.7}$$

where α is the chirp and it is related with a through the relation given in Eq. 3.74. We can derive the equivalent α for the seed laser used during the experiment using Eq. 4.3 and that the duration of the seed laser was $\sigma_{tcI} = 140$ fs:

$$\alpha_{seed} = 102.14\,\text{rad} \cdot \frac{\text{THz}}{\text{ps}}. \tag{4.8}$$

In GENESIS, the linear term of the phase $\omega_0(t-t_0)+\phi_0$ is already implemented, only the quadratic term $\alpha/2(t-t_0)^2$ needs to be specified. In order to do so, we have described the seed laser using the radiation description file for GENESIS1.3 v.2. Here the variables: ZPOS, PRAD0, ZRAYL, ZWAIST and PHASE are defined. ZPOS indicates the longitudinal position and for each value of ZPOS corresponds a value for the PHASE and for PRAD0. PRAD0 describes the power

and PHASE describes the quadratic term of the phase profile:

$$PHASE = -\frac{CHIRP}{2\sigma_t^2}\frac{(ZPOS - \bar{Z})^2}{c^2}, \tag{4.9}$$

where $CHIRP = \alpha\sigma_{tcI}^2$, $\bar{Z}$ is the location of the maximum seed laser power and c is the speed of light. ZRAYL is the Rayleigh length and ZWAIST is the position of the waist, which are constant along ZPOS.
In Fig. 4.9, we show PRAD0 and PHASE versus ZPOS for the seed laser defined with zero chirp in the GENESIS radiation description file. This pulse carries an energy of 16.5 µJ. The seed laser duration is derived from Eq. 3.73 knowing the spectral bandwidth $\Delta\lambda = (1.3 \pm 0.5)$nm, it results $\sigma_t = 34$ fs. Here we can use the measured spectral bandwidth, even if the seed laser pulse was chirped, because the added chirp through dispersive media does not affect the spectral domain but only the temporal.

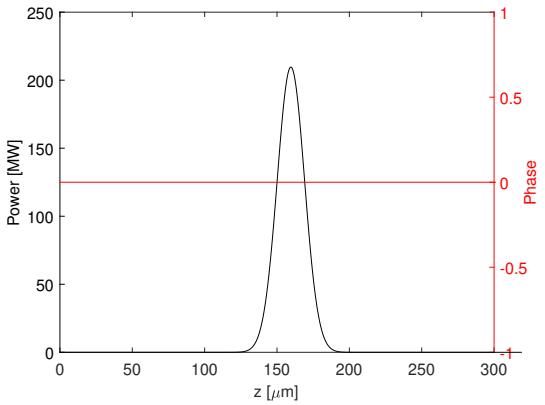

Figure (4.9) Power and phase profile for the seed laser without chirp.

Fig. 4.10 shows the analytical curve describing the dependence of the chirp α on the GDD:

$$\alpha(GDD, \sigma_{tI}) = \frac{GDD}{(2\sigma_{tI}^2)^2 + GDD^2} \tag{4.10}$$

where σ_{tI} is the RMS duration of the unchirped seed laser pulse [105]. The point with zero GDD and zero chirp is the case of the Fourier-transform-limited pulse showed in Fig. 4.9. Knowing that the seed laser is passing through the two vacuum windows, we can estimate the added GDD and find the chirp of the seed laser at the entrance of the modulator, where it interacts with the electron beam. The two vacuum windows are made by fused silica and their total length is $l = 4$ mm.

From [106] we get the group velocity dispersion (GVD) of the fused silica:

$$GVD_{fusedsilica} = 57.54 \frac{\text{fs}^2}{\text{mm}}. \tag{4.11}$$

From $GVD_{fusedsilica}$ we derive the GDD, by multiplication with the total length that the light passes through the vacuum windows:

$$GDD_{vw} = GVD_{fusedsilica} \cdot l = 230.16\,\text{fs}^2. \tag{4.12}$$

Now, Figure 4.10 tell us that the initial GDD of the seed laser in the laser laboratory before passing through the vacuum windows is:

$$GDD_{init} = 9776\,\text{fs}^2. \tag{4.13}$$

The effect of a laser pulse passing through a linear passive optical device, as our vacuum windows, corresponds of the multiplication of the laser field in the frequency domain with a transfer function:

$$E_{out}(\omega) = VW(\omega)E_{in}(\omega) \tag{4.14}$$

where $VW(\omega) \propto \exp\left[-i\phi_H(\omega)\right]$ and $E_{in}(\omega) \propto \exp -i\phi(\omega)$. As a result, the spectral phase of the output light is:

$$\phi_{out}(\omega) = \phi_{VW}(\omega) + \phi_{in}(\omega). \tag{4.15}$$

Hence, the second order phase term of the seed laser after the vacuum windows, which is the final GDD is:

$$GDD_{final} = GDD_{vw} + GDD_{init} = 10\,006\,\text{fs}^2. \tag{4.16}$$

Genesis simulation: part two In the second GENESIS run, the electron bunch goes through the magnetic chicane and afterwards it radiates inside the sFLASH radiator section. For this study the radiator was tuned to the eight harmonic of the seed laser. The FEL optimization is aiming at achieving the electron beam bunching (see Eq. 3.13) giving the FEL saturation at the end of

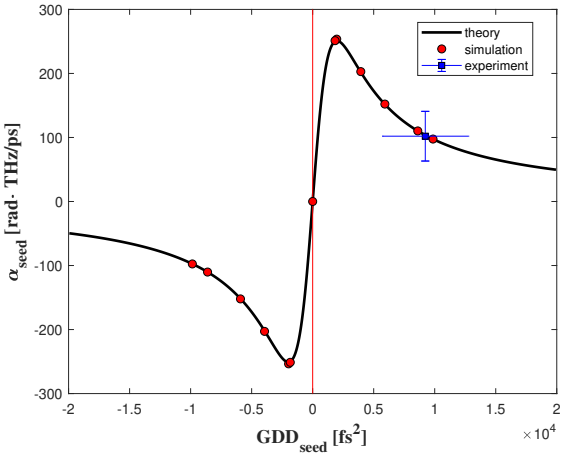

Figure (4.10) Chirp of the seed laser α_{seed} as a function of the group delay dispersion of the seed GDD_{seed}. The red dots indicates the selected working points for the simulation where both α_{seed} and GDD_{seed} are set at the entrance of the modulator and the blue spot indicates the experimental measurements after the THG setup in the laser laboratory, which has the chirp calculated in Eq. 4.8. Thus, the additional 4 mm of vacuum glass windows is not considered.

the radiator. If the FEL saturation happens before the end of the radiator, it results in the deterioration of the FEL Gaussian time profile, which is a problem for the THz-Streaking experiment. The knobs controlling the bunching factor are: the seed laser power and the chicane dispersion. The first determines the energy modulation on the electron beam: $A = \Delta\gamma/\sigma_\gamma$. In this case, we do not change the properties of the seed laser pulse, because they are under study. Therefore, the chicane dispersion R_{56} has been scanned and the value giving the best FEL performance has been selected for the final simulation.

The final simulation results contain information on the power profile and the spectrum of the FEL radiation. We have extracted the RMS pulse duration of these pulses from Gaussian fits to the temporal power profiles. The extracted RMS pulse duration has been compared with the values measured during the THz streaking experiment [102] and the theoretical expectation [50]. The theoretical expectation was presented in Eq. (3.35).

The calculated FEL RMS pulse duration $\sigma_{t;FEL}$ are reported in Fig. 4.11 as a function of the initial GDD of the seed laser GDD_{seed}. In the same plot, the two theoretical curves Eqs. (3.35) and (3.36) confine the region in which the simulated points are expected. Finally, the cyan and green regions represent the temporal duration of the FEL pulses measured in the THz streaking experiment within the measurement error. According to this analysis, GDD_{seed} during the experiment

was:

$$GDD_{seed} = (8.3 \pm 3.2) \times 10^3 \text{fs}^2. \tag{4.17}$$

This value is compatible with the estimation given in Eq. 4.14. This is a significant achievement because when we know the GDD of the seed laser we can retrieve its chirp. The GDD of the seed resulting from simulations and theory is compatible with the value estimated using the measurements done in the laser laboratory and the estimation of the added GDD by the vacuum windows. As a result, for upcoming experiments we can trust our calculation of the GDD from the experimental data collected in the laser laboratory.
According to Fig. 4.10 results that the chirp α_{seed} was (127 ± 43)THz/ps. Accordingly with simulations, the sign of the seed laser pulse chirp is kept during the FEL process, thus the green region in Fig. 4.11 describes the seed laser (because the measured chirp of the FEL is positive). The points $\sigma_{t;FEL}$ indicated with triangular marker that are greater compared to the behavior foreseen from 3.35 represent the cases in which the electron bunch was slightly overbunched. While the points that are smaller represent cases in which the bunching was not fully optimized. To correct the overbunching it would be necessary to set a lower dispersion parameter.

Analysis of the FEL properties The FEL performance with a chirped seed is presented in this paragraph. We show the resultant FEL pulse coming from the HGHG process where it was used a seed without chirp 4.12 and two FEL pulses resulting from the HGHG process where it was used a chirped seed, with chirp $a = \pm 4.2$ in Fig.4.13 and 4.14. The FEL pulse generated with a seed with no chirp has a smoother power profile compared with the chirped cases, as expected from [54]. It is interesting to observe that in the two chirped cases presented the spectrum looks different depending on the sign of the chirp. If we have a positive chirp, Fig. 4.13, the spectral intensity is higher and also the pulse has a Gaussian looking-shape, in case of negative chirp instead, Fig. 4.14 the spectrum has a lower peak intensity and the peak is more subject to degradation. This behavior is observed also for the other cases with lower seed laser a, that we do not show here. From this observation we can state that a negative chirp is affecting more the spectral quality of the seeded FEL spectrum. We notice that the chirp sign is conserved: modulating the electrons with a positive chirped seed laser lead to the generation of seeded FEL radiation with positive chirp as well. This means

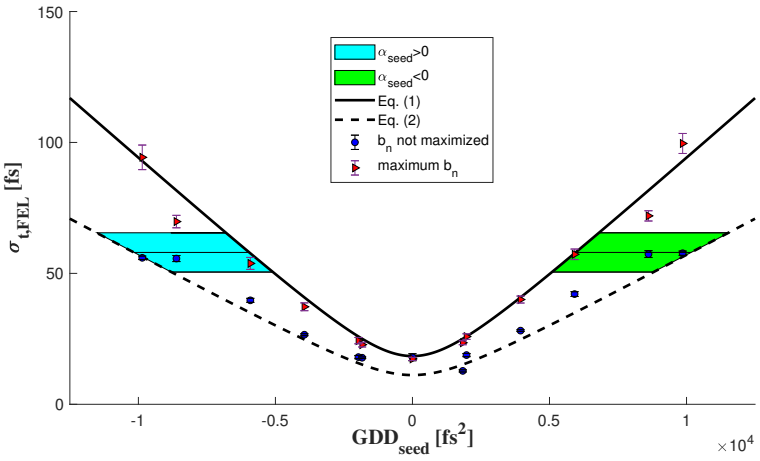

Figure (4.11) Duration of the seeded FEL pulses $\sigma_{t;FEL}$ as a function of the GDD of the seed laser pulse GDD_{seed}. The color-filled boxes represent the regions where the experimental point was measured from the THz streaking experiment. These boxes are limited vertically from error bars given by the experimental uncertainty and the horizontally from the two theoretical curves. The measured time duration of the FEL pulse permits to retrieve the initial GDD of the seed laser pulse at the beginning of the modulator. The markers represent the FEL performance foreseen from the simulations: red triangles show the case of optimized bunching and the blue circles show the case with small dispersion, so low bunching factor.

that the chirp induced by the FEL process itself is not enough to compensate the chirp or to change the sign of the chirp. In Fig. 4.15 we show the FEL RMS

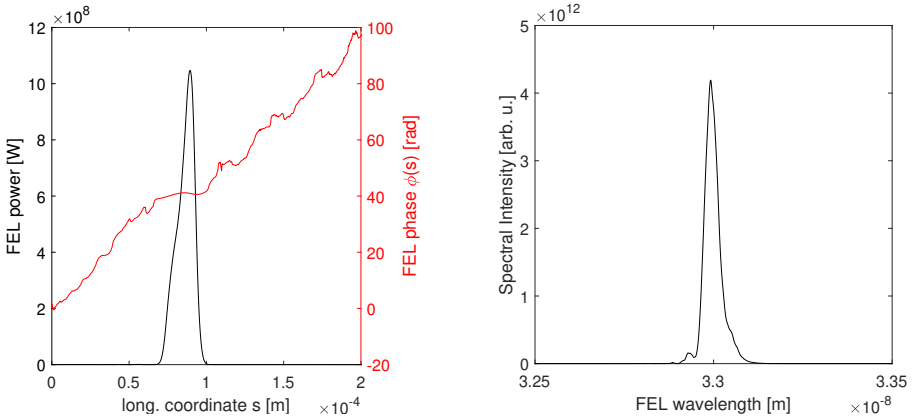

Figure (4.12) Power and phase profile of the FEL pulse at the end of the sFLASH section (left) and corresponding spectrum profile (right). This FEL pulse has been generated from a seed laser without initial temporal chirp.

duration σ_{tcI} and RMS bandwidth σ_ω for the pulse at the end of the sFLASH radiator that we have calculated from the simulation results. This plot shows that

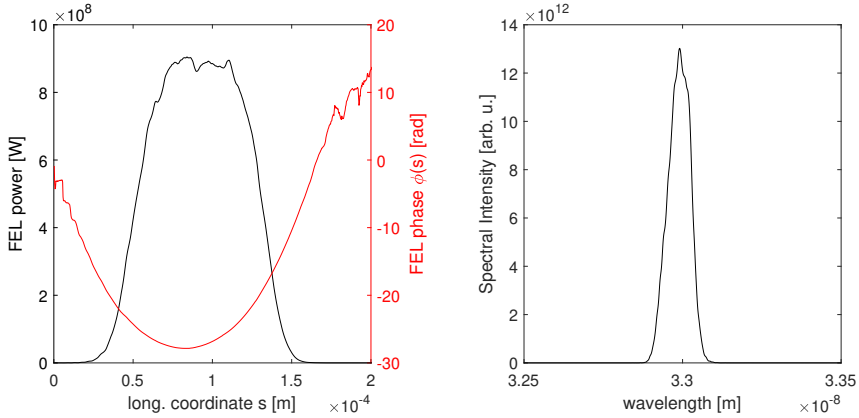

Figure (4.13) Power and phase profile of the FEL pulse at the end of the sFLASH section (left) and corresponding spectrum profile (right). This FEL pulse has been generated from a seed laser with initial temporal chirp, with $a \simeq 4.2$ which correspond to $\alpha = 100\text{THz/ps}$.

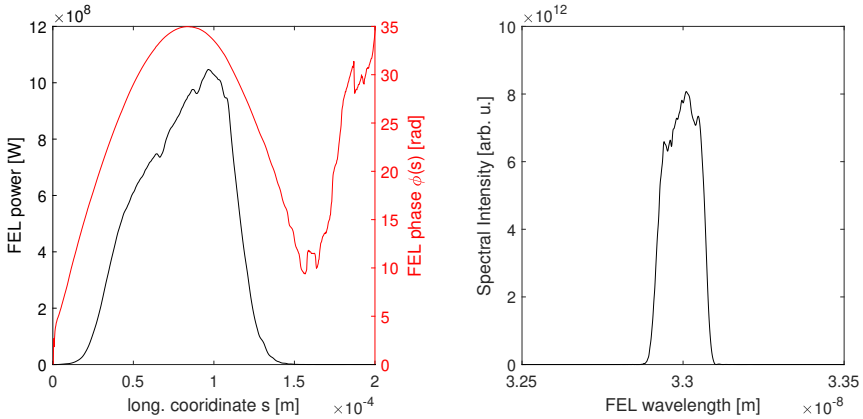

Figure (4.14) Power and phase profile of the FEL pulse at the end of the sFLASH section (left) and corresponding spectrum profile (right). This FEL pulse has been generated from a seed laser with initial temporal chirp, with $a \simeq -4.2$ which correspond to $\alpha = -100\text{THz/ps}$.

the duration of the FEL pulse grows as we add some chirp to the seed laser, this is true for both positive and negative chirp. The FEL spectrum bandwidth is not at its minimum for the case using a zero-chirp seed laser. Instead we observe a bandwidth shrinking at $a_{seed} \sim +1$ and then it grows again for $a_{seed} > -1$. For $a_{seed} < 0$, σ_ω grows significantly up to $a_{seed} \sim -1$, than it continues to grow with a reduced rate up to $a_{seed} \sim -4$. This behavior might explain why with negative chirp we have a worst FEL spectrum at the end: the bandwidth of the spectrum grows, as a consequence the peak spectral intensity is reduced, compared to the positive chirp case.

From the simulation results we have been able to calculate $\sigma_{tcI,FEL}$ and σ_ω.

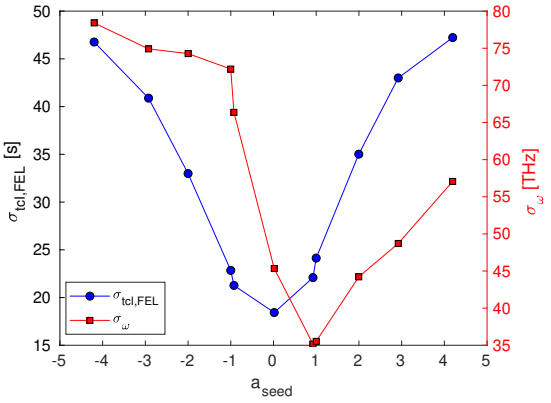

Figure (4.15) RMS duration $\sigma_{tcI,FEL}$ and bandwidth $\sigma_{\omega,FEL}$ of the FEL pulse at the end of the sFLASH undulator vs. the seed chirp a_{seed} from Eq. 3.48.

From these values we can calculate the time bandwidth product (TBP) given in Eq. 3.73 and derive the chirp parameter a. Then from Eq. 3.68 we calculate the chirp α. At this point, we can estimate the dispersion (GDD) that the FEL is carrying. We can find an equation for the GDD using Eq. 3.68 and Eq. 3.71 by inverting them in segments [52]:

$$GDD(\alpha, \sigma_{tcI}) = \frac{\sigma_{tcI}^4 \cdot \alpha}{\frac{1}{4} + \alpha^2 \cdot \sigma_{tcI}^4}. \tag{4.18}$$

Using this equation we have retrieved the GDD carried by the simulated FEL pulses. In Figure 4.16 we show the calculated GDD versus the amount of chirp a_{seed} that was added to the seed laser pulse. We notice that the FEL pulse generated in the HGHG process using an un-chirped seed laser develops a dispersion corresponding to $GDD = 327.3\,\mathrm{fs}^2$. This means that the FEL process is adding positive dispersion and in order to compensate this GDD we need to start with a seed laser with a tiny negative chirp $a_{seed} = -0.4855$ which is indicated in Fig. 4.16 with a cyan-star marker. This correspond to start with a seed laser chirp with a duration of 37.8 fs, a chirp $\alpha = -169.8\mathrm{THz/ps}$ and a GDD of $-1123.4\,\mathrm{fs}^2$, derived from Eq. 4.18.

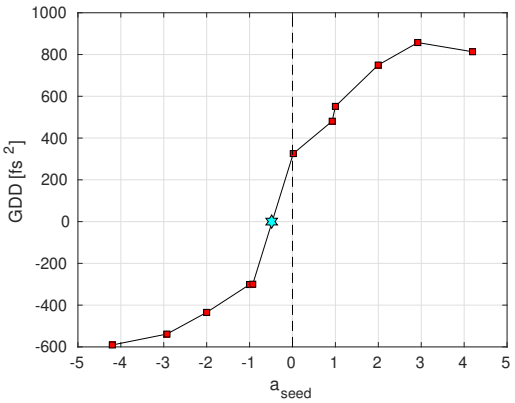

Figure (4.16) GDD of the FEL pulse at the end of the sFLASH undulator vs. the seed chirp a_{seed}. The cyan-star marker shows the FEL pulse with no chirp at the end of the radiator.

4.3 EEHG

Current accelerator research and development at sFLASH is dedicated to show EEHG seeding. The main elements are already installed: two modulators followed by two chicanes and a final radiator. At sFLASH there is only one injection point for the seed laser before the first modulator, here the two seed lasers are introduced together. The first seed laser is focused in the first modulator and is prepared with vertical polarization, the same direction of the field of the electromagnetic modulator. The second seed laser is focused in the second modulator and is perpendicularly polarized respect to the first seed laser. The polarization of the seed lasers is controlled by a thin-film polarizer (TFP) placed in the optical table of the laser laboratory after the THG setup. The focus of the seeds is controlled using telescopes consisting of two lenses. Telescopes are placed in the laser laboratory as well, and this is a great advantage because they are accessible in every moment for laser focus adjustments.

4.3.1 Tolerances for sFLASH

For a successful EEHG experiment, we need to chose carefully the working point by taking into consideration all the possible limitations coming from the sFLASH

setup: chicane strengths, optimal radiator parameter, seed laser power, ...
Figure 4.18 shows the maximum dispersion achievable at specific energy for both chicanes. The chosen energy range corresponds to the possible electron beam energies at FLASH ($0.6 - 1.25\,\mathrm{GeV}$). The dispersion R_{56} of the chicane has been estimated by taking into consideration the chicane geometry, that it is described in Fig. 4.17. The chicane parameters for sFLASH chicanes C1 and C2 are given

Table (4.4) sFLASH chicanes geometrical parameters.

	$1^{\mathbf{st}}$ **chicane**	2^{nd} **chicane**
L_{12}	330 mm	745 mm
L_{23}	310 mm	300 mm
L_{34}	330 mm	745 mm
$d_{pipe,inner}$	34 mm	34 mm
L_B	300 mm	100 mm
I_1	81 T mm	26 T mm

in table 4.4. Firstly, we have derived the maximum chicane deflection angle at

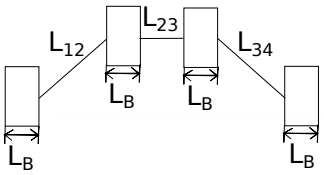

Figure (4.17) Chicane geometric properties.

different electron beam energies:

$$\alpha[\mathrm{mrad}] = \frac{03 I_1[\mathrm{Tmm}]}{E_0[\mathrm{GeV}]} \tag{4.19}$$

where I_1 is the first field integral of the chicane dipole. In this case, I_1 has been approximated to the product of the maximum magnetic field of the dipole and the length of the dipole. Finally the R_{56} can be derived as follows:

$$R_{56} = 2\left(L_{12} + \frac{2L_B}{3}\right)\alpha^2 + o(\alpha^4) \tag{4.20}$$

where L_{12} is the distance between outer and inner dipoles and L_B is the width of a chicane magnet, as shown in Fig. 4.17. At the top of Fig. 4.18 it is shown the maximum available R_{56} for energies from 0.6 to 1.25 GeV. The indaco-shaded region shows the area inaccessible due to the vacuum pipe, this limits the R_{56} to 800 µm to energies in the range 600 and 900 MeV. The achievable dispersion in

the second chicane is shown at the bottom of Fig. 4.18. Here, at low energies (up to 800 GeV) the achievable R_{56} is higher that 150 µm, which it is a value that is not exceeded at low EEHG harmonics. For higher energies, the maximum available dispersion might be insufficient to get enough EEHG bunching for lasing. For the studies that will follow in the next sections we are going to consider a working point using an electron beam with energy $E_0 = 700$ MeV, in this case the maximum chicane strengths result: $R_{56}^{(1)} = 800$ µm and $R_{56}^{(1)} = 200$ µm.

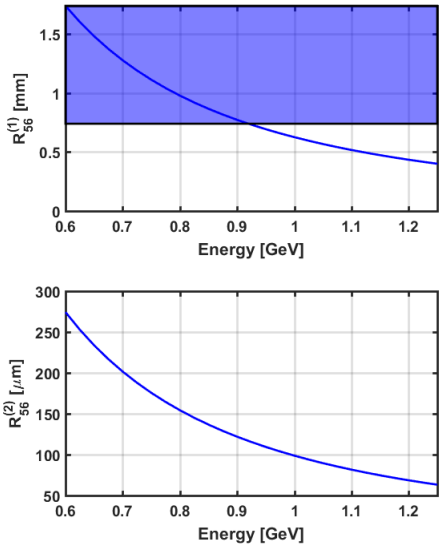

Figure (4.18) Maximum chicane dispersion R_{56} as a function of the electron beam energy. Top figure: first chicane, bottom figure: second chicane.

Figure 4.19 shows the possible harmonics of the seed laser that can be generated at for different electron beam energies using an undulator parameter K for the radiator included in the range 1 to 2.7. This range has been chosen because if the K is smaller than one, the undulator field intensity might be too weak, but on the other side, if the K is too big, the brightness decreases. For the electron beam energy $E_0 = 700$ MeV the harmonics of the seed laser wavelength that can be generated with optimal undulator parameter K, are from the sixth to the eighteenth.

Knowing the harmonics allowed by the radiator, we can take into consideration the chicane limitations and see which are the possible harmonics that we can effectively reproduce if we work with an electron beam energy of 700 MeV. The

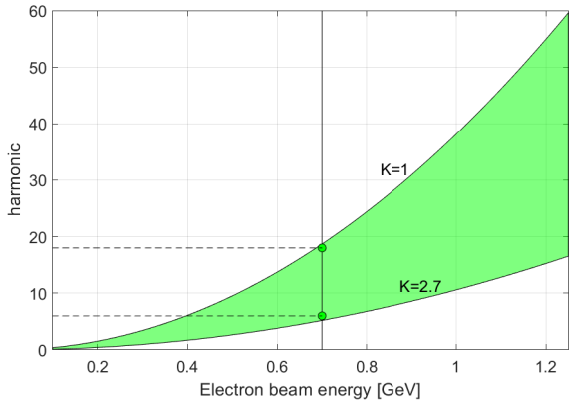

Figure (4.19) Assuming that the optimal performance of the radiator undulators is achieved when the K parameter is in the range 1 to 2.7, the green area shows where the K parameter lies between these two values and the harmonics that can be achieved at a certain electron beam energy. For example, at 700 MeV K is in this interval from the 6^{th} to the 18^{th} harmonic

combination of the maximum chicane dispersion and the radiator parameter are limiting factors for the highest harmonic possible at sFLASH. Another limiting factor is given by the seed laser power. The seed laser power determines the electron beam energy modulation in the two modulators, which in the EEHG theory is the A parameter:

$$A_{1,2} = \frac{\Delta E_{1,2}}{\sigma_E}. \tag{4.21}$$

The typical energy modulation imprinted by the sFLASH seed laser was measured to be (350 ± 50)keV [94]. This measurement was performed during an HGHG beamtime where all the seed laser power was sent into the modulator. This is not the case when it is on-going the THz-Streaking experiments, which requires part of the NIR seed laser to generate the THz pulse, as mentioned in the previous section. During the same beamtime it was measured an uncorrelated electron beam energy spread of $\sim 70\,\mathrm{keV}$, which gives:

$$A_{HGHG} = \frac{350\,\mathrm{keV}}{62\,\mathrm{keV}} = 5. \tag{4.22}$$

Knowing that the total energy spread for HGHG is given by:

$$\sigma_{E,tot} = \sigma_E \cdot \sqrt{1 + \frac{A_{HGHG}^2}{2}} \tag{4.23}$$

and for EEHG is:

$$\sigma_{E,tot} = \sigma_E \cdot \sqrt{1 + \frac{A_1^2}{2} + \frac{A_2^2}{2}} \tag{4.24}$$

we get:

$$A_{HGHG} = \sqrt{A_1^2 + A_2^2} \tag{4.25}$$

which gives the possible maximum $A_{1,2}$ parameters for the EEHG experiment. For example, if $A_1 = 4$ then the maximum value that A_2 can assume is 3. In order to find possible EEHG working points within these set of As and Bs parameters fixed from the sFLASH hardware possibilities we need to calculate the EEHG bunching factor and see the allowed regions. Given the limited dispersion of the first sFLASH chicane, we need to average the bunching over the phase ϕ between the footprint of the modulation density generated in the first modulator-chicane combination and the light field of the laser field in the second modulator. Hence, ϕ represents the relative phase between the two seed lasers and it takes into account also possible offsets between the two Gaussians. As a consequence, there is not a working point based on a specific n, m combination, but all of them are contributing at the bunching at the wished harmonic as follows [107, 62]. The definition of bunching b_a at the $a-th$ harmonic was given in Eq. 3.106. We are going to indicate the bunching averaged over the all possible phases distributed in the range $[0, 2\pi]$ as $\langle b_a \rangle_\phi$ and the expected variation of the bunching at the harmonic a for fluctuation in the phase ϕ as $\sigma_\phi(b_a)$. In the performance of the EEHG experiment, it is possible to control the phase between the two seed laser by the installation of a piezo-linear-precision-positioner in correspondence of the delay which introduce the needed delay between the two seed lasers to be overlapped on the same electron beam region down and upstream the first chicane. A model like $P-620.1-P-629.1$ PIHera from the Physik Instrumente (PI) [108] company enable travel ranges from 50 to 1800 µm.

In the next paragraphs, we present the bunching maps that we have calculated from harmonic 6 to harmonic 18 of the sFLASH 267 nm seed laser. For each harmonic we show the bunching averaged on 100 possible phases equally spaced in the interval $[0, 2\pi]$. For each harmonic, we present four bunching maps calculated for different $A_1 - A_2$ combinations, possible with the estimated sFLASH seed laser power, estimated with Eq. 4.25. The possible $A_1 - A_2$ combinations are much more, but here we select only few cases. For the choice of the working point during an experiment, one can set the observed energy modulations on the electron beam and calculate the bunching map for the actual parameters.

4.3.2 EEHG lasing at harmonic 12

After having evaluated the bunching maps presented in the Appendix B.1, we have decided to evaluate the working point at the twelfth harmonic, where from Fig. B.32. In this way, the bunching coming from the HGHG is excluded from the parameters that we need to set to get EEHG lasing. Figure 4.20 represents the bunching map calculated from the parameters selected in the previous section: twelfth harmonic, $A_1 = 4$, $A_2 = 3$ and by averaging over hundred phase values equally spaced in the interval $[0, 2\pi]$. Here we have marked the chosen working point with a red star.

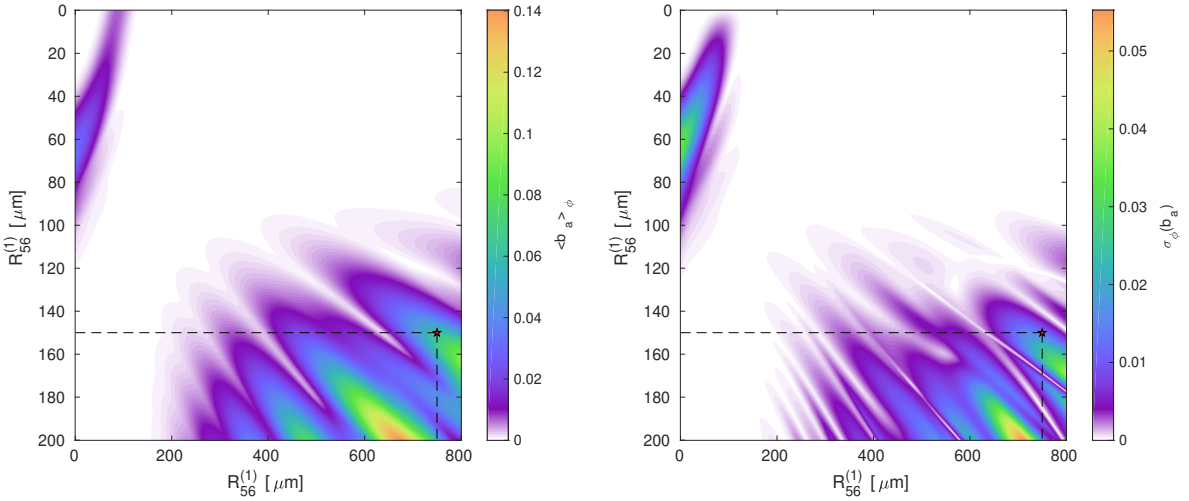

Figure (4.20) EEHG bunching map at the twefth harmonic, where we have averaged the bunching on the phase ϕ. The left plot shows the modulus of the bunching and the right plot shows the standard deviation of the bunching calculated respect to the phase ϕ.

From the presented bunching map, we have chosen to operate with the dispersive strengths: $R_{56}^{(1)} = 750\,\mu\text{m}$ and $R_{56}^{(2)} = 150\,\mu\text{m}$. The performance given from these set of parameters has been studied using the GENESIS1.3 v.4 code, in the one4one configuration, which enables to perform simulations with the real number of particle (see appendix A). The simulated bunching at the twelfth harmonic is shown in Fig. 4.21 and it has a peak at ~ 0.06, which is in agreement with the prevision given in the bunching map in Fig. 4.20. From this bunching factor, we can calculate the expected performance for a pre-bunched electron beam [33].

The calculated gain length is $L_G = 0.913\,\mathrm{m}$ and the saturation power results $P_S = 518\,\mathrm{MW}$ (not achieved in the radiator) as shown in Fig. 4.22.

The FEL energy gain curve derived from the simulation is presented in Fig. 4.23.

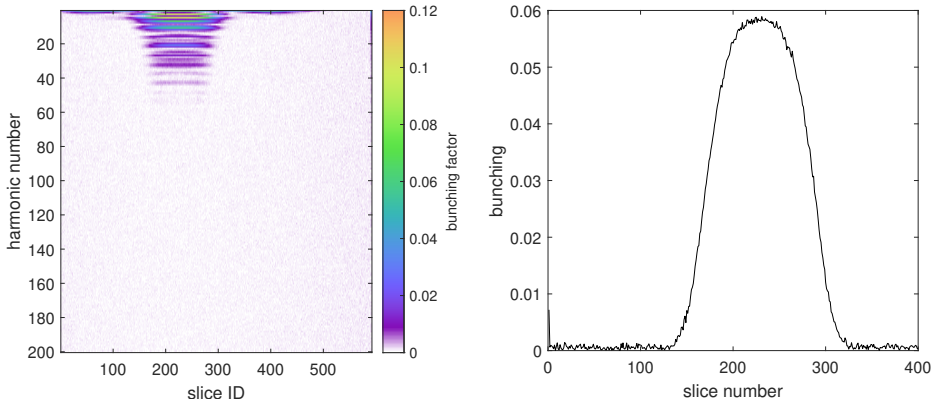

Figure (4.21) Bunching at the 12^{th} harmonic of the 267 nm seed.

Here, the intersections between the radiator modules are not shown. The final FEL energy is 50 µJ. The FEL power profile and the spectra at the end of the sFLASH radiator section are presented in Figure 4.24. The FEL pulse shows a peak in front, which is induced due to superradiance, this prevent us to consider it as a Gaussian. The RMS duration of this pulse is $\sigma_t = 37.2\,\mathrm{fs}$. The FEL spectrum shows a clear single peak, as expected from seeding. The spectrum has an RMS bandwidth of $\sigma_\nu = 5.048\,\mathrm{THz}$.

We have performed simulations with only the first seed and only the second

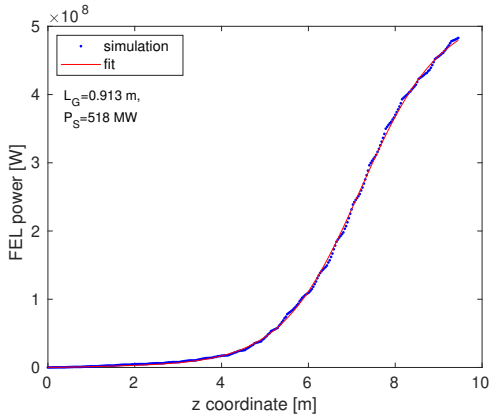

Figure (4.22) FEL power gain curve at the twelfth harmonic with EEHG. From the fit we have estimated a gain length $L_G = 0.913\,\mathrm{m}$ and a saturation power $P_S = 518\,\mathrm{MW}$.

seed to study the contribution to the EEHG signal from HGHG coming from each

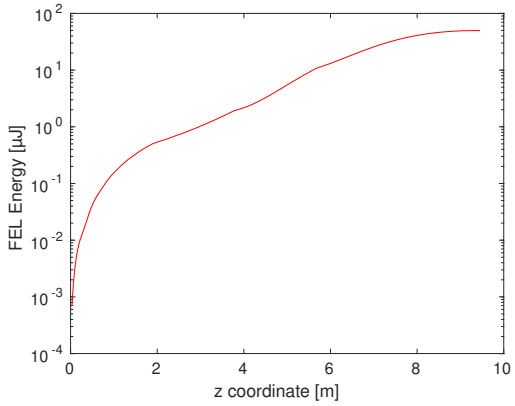

Figure (4.23) Gain curve of the FEL. Here we show the energy growth in logarithmic scale along the radiator. At the end of the sFLASH radiator the FEL pulse achieves an energy of 50 µJ.

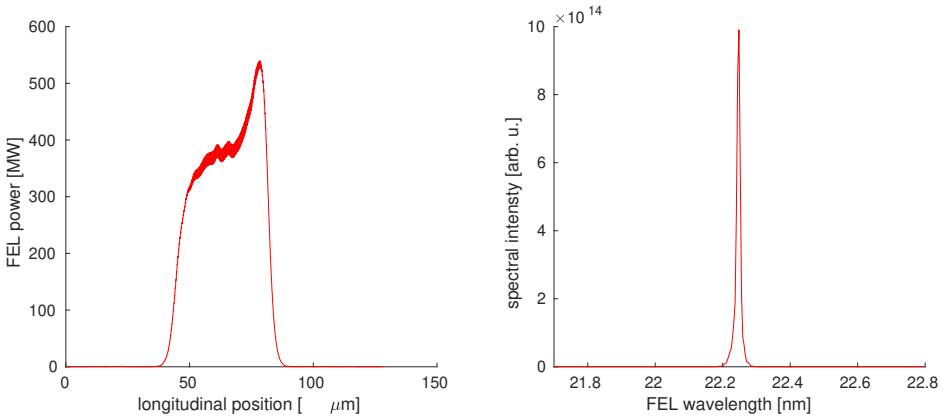

Figure (4.24) FEL power profile (left) and spectra (right) at the end of the sFLASH radiator section.

laser.

The bunching content for the first case, Fig. 4.25, present no bunching at the harmonic of interest. When operating only with the second seed on (HGHG signal from the second seed) we get a tiny bunching at the twelfth harmonic $b_{12} =\sim 0.003$, as shown in Fig. 4.25. In Fig. 4.27 it is reported in logarithmic scale the power (left) and the spectrum (right) at the end of the radiator for EEHG, HGHG from the first and from the second laser and SASE. We observe a not-negligible contribution from the HGHG signal coming from the second seed.

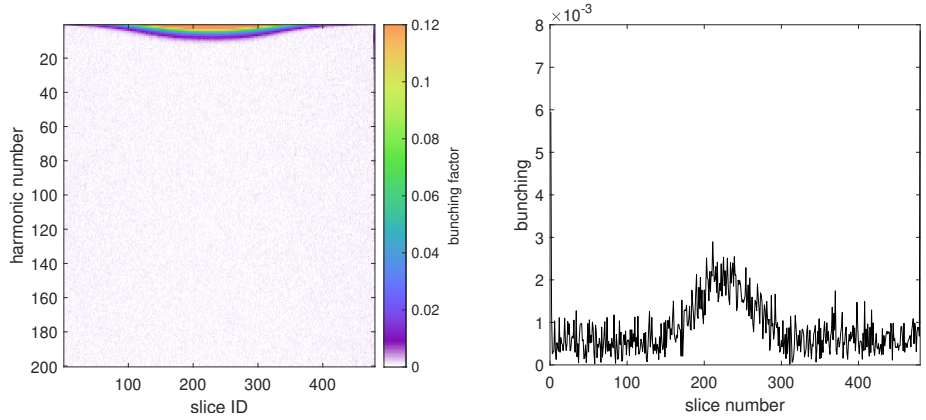

Figure (4.25) HGHG bunching from the first seed, while the second seed laser is off.

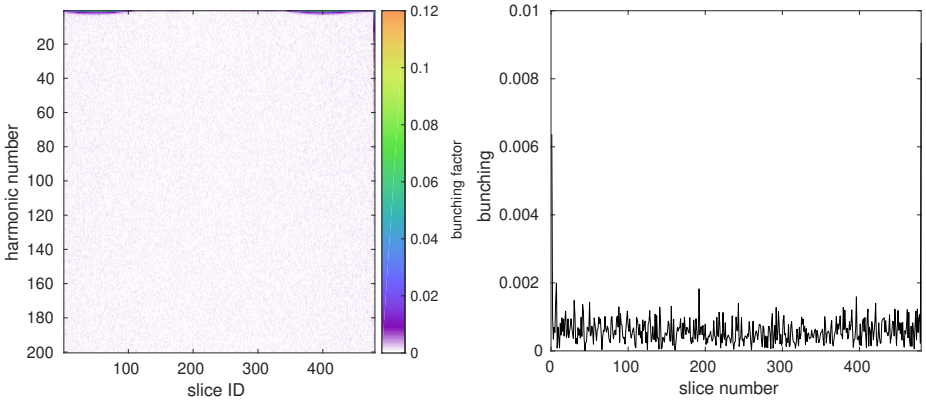

Figure (4.26) Bunching at the 12^{th} harmonic of the 267 nm seed. In this case, the first seed is off, so we see the HGHG bunching from the second seed laser.

4.3.3 EEHG seeding with two different seeds

Even if not possible with the currently installed setup, we have looked at the performance of the EEHG scheme at sFLASH using two different wavelengths for the seed lasers. For these studies, we assume a stronger first chicane, in this way we can calculate the bunching without taking into consideration the phase effect. As we are going to describe in the following paragraphs, using two different seed laser wavelengths might improve the contrast between HGHG signal and EEHG signal. We focus on two configurations. In one case, we look at EEHG using a first seed laser wavelength of $\lambda_1 = 534\,\text{nm}$ and as second seed laser wavelength $\lambda_2 = 267\,\text{nm}$. We name this case down-conversion. In the other case, up-conversion, we use as first seed laser wavelength $\lambda_1 = 267\,\text{nm}$ and as second one $\lambda_2 = 534\,\text{nm}$.

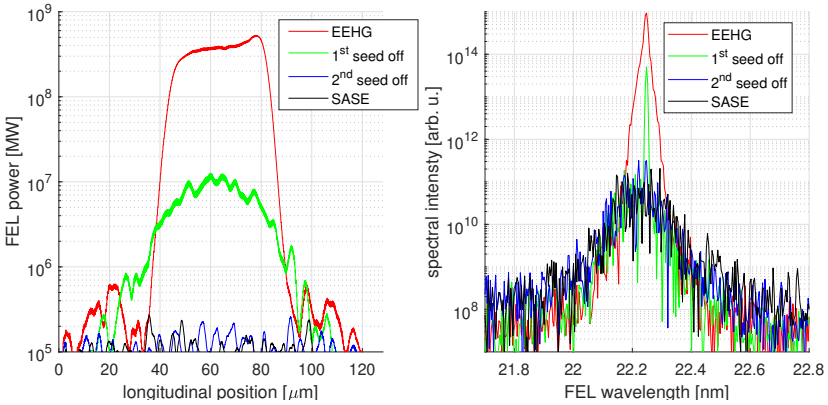

Figure (4.27) FEL power and spectra at the end of the radiator section. Four different cases are presented here: green and blue curves are respectively with first and second seed off, while the red curve is EEHG (both seeds on) and the black curve is SASE (both seeds off).

Once fixed the seed laser peak power, the chicane strengths needed can be derived from the Stupakov bunching formulas. Where the $K = \frac{k_2}{k_1}$ is different from 1, as we are using seed lasers with different wavelengths.

Up-conversion Now we study the EEHG performance achieved by using a first seed laser with a wavelength of $\lambda_1 = 267\,\text{nm} = \lambda$ and a second seed laser with a wavelength of $\lambda_2 = 534\,\text{nm} = 2\lambda$. This corresponds to a $K = \frac{k_2}{k_1} = \frac{1}{2}$. The a, n and m parameters which are linked through the relation 3.104, can be determined from the expression which defines the wavenumber of the EEHG radiation [66]:

$$k_E = nk_1 + mk_2 \tag{4.26}$$

as we want to generate the twelfth harmonic of the 267 nm seed, we reformulate the expression as:

$$12 \cdot \frac{2\pi}{\lambda} = n \cdot \frac{2\pi}{\lambda} + m \cdot \frac{2\pi}{2\lambda} \tag{4.27}$$

which simplifies as:

$$12 = n + \frac{1}{2}m \tag{4.28}$$

that corresponds to Eq. 3.104. For the following study, we operate for $n = -2$, which gives $m = 28$. After fixing the A_1 and A_2 parameters we can calculate the bunching map, which it enables the choice of the proper chicane strengths.
The induced energy modulations on the electron beam by the two lasers are for

the first $A_1 = 4$ and $A_2 = 3.8$. Using an electron beam energy of 700 MeV and an uncorrelated energy spread of 70 keV, the Stupakov formulas give the maximum bunching for the working point at $n = -2$ and $m = 28$ for $R_{56}^{(1)} = 1.545$ mm and $R_{56}^{(2)} \sim 284$ µm. The longitudinal phase space distribution of the electron beam

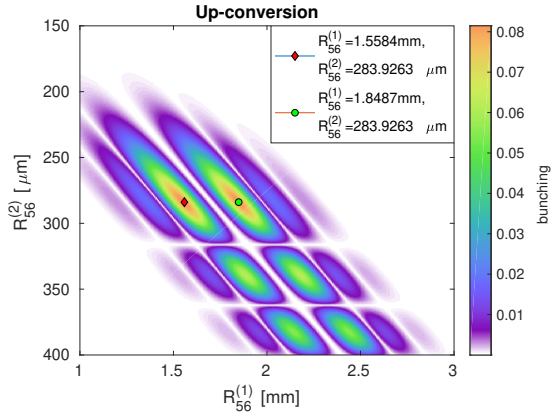

Figure (4.28) Bunching map for the up-conversion case, calculated for $n = -2$, $m = 28$, $K = 1/2$.

after the second chicane, together with the current profile is shown in Fig. 4.29. The corresponding harmonic content of this electron bunch is reported in Fig. 4.30. Here, we show on the right the bunching profile for the 24^{th} harmonic of the 534 nm seed laser, which correspond to the target FEL wavelength of 22.25 nm. The FEL

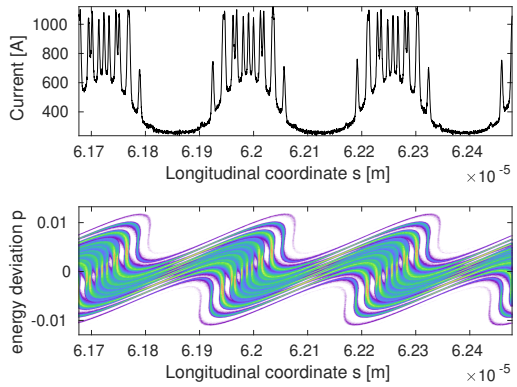

Figure (4.29) Upper plot: current profile. Bottom plot: three slices after the second chicane taken from from the central region of the electron bunch, where the seed laser is sitting.

power evolution along the radiator behaves following Eq. 2.108, which describes the radiation amplified from pre-bunched beams. We have fitted Eq. 2.108 to the power gain curve from Fig. 4.31. The fit gives as a result a power gain length

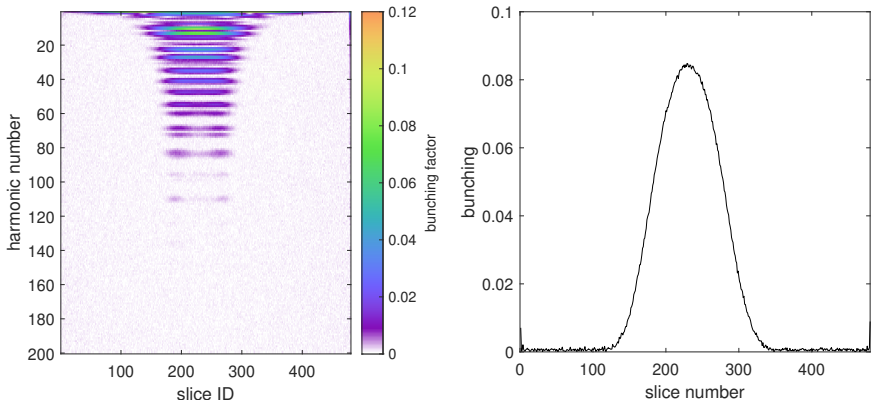

Figure (4.30) Left:Harmonic content of the electron beam in terms of bunching. Right: bunching at the 24^{th}-harmonic of the $\lambda_2 = 534\,\text{nm}$ seed laser

$L_G = 0.957\,\text{m}$ and a saturation power $P_S = 540\,\text{MW}$, which is not achieved within the radiator.

The FEL power profile achieved at the end of the radiator section, has duration

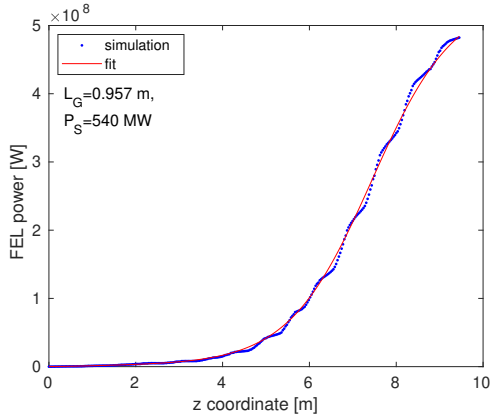

Figure (4.31) Power gain curve of the FEL with the EEHG process.

$\sigma_t \simeq 34.77\,\text{fs}$ and the spectrum has a bandwidth of $\sigma_\nu = \sigma_\omega/(2\pi) = 2.56\,\text{THz}$. The time-bandwidth product is therefore $TBP = \sigma_t \cdot \sigma_\omega = 0.5594$ which is close to the expected TBP for Gaussian pulses, which is $TBP = 0.5$. From the TBP we can derive the amount of chirp α developed due to the FEL process with the following equation:

$$\sigma_t \cdot \sigma_\omega = 0.5\sqrt{1 + (2\sigma_t^2\alpha)^2}. \tag{4.29}$$

From this equation we calculate $\alpha = 207.46\,\text{rad} \cdot \frac{\text{THz}}{\text{ps}}$. If we calculate the duration of the transform limited pulse we can derive the group delay dispersion corresponding to this chirp α. The duration of the transform limited pulse is

$\sigma_{t,TL} = 0.5/\sigma_\omega = 31.08\,\text{fs}$. To derive the GDD β we use the relation given in [52]:

$$\sigma_t = \sigma_{t,TL}\sqrt{1 + \left(\frac{\beta}{2\sigma_{t,TL}^2}\right)^2} \tag{4.30}$$

and we get $\beta = 969.2\,\text{fs}^2$. This group delay dispersion is equivalent to the dispersion that a $\sim 5\,\text{mm}$ length fused silica glass ($GVD = 195.96\,\text{fs}^2/mm$) adds to a laser pulse with wavelength of 267 nm. The spectrum and the power profile of the EEHG FEL is shown in Fig. 4.32.

The EEHG pulse at the end of the radiator is compared with the corresponding

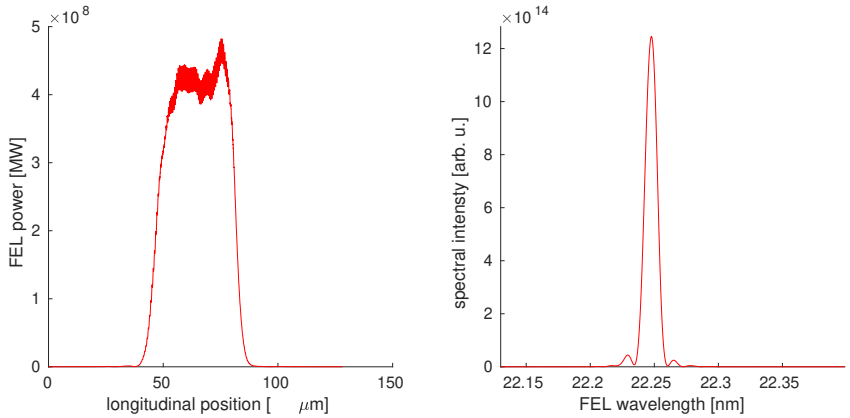

Figure (4.32) Power profile (left) and spectrum (right) of the EEHG FEL signal at the end of the radiator section.

performance when one of the two seed lasers is off (HGHG signals) and when both seeds are off (SASE) in Fig. 4.33. The plot on the left shows the FEL power profile and the plot on the right the spectra profile. The plots are done in a logarithmic scale to show that the signals coming from the HGHG process (when we have either only the first seed on or only the second seed on) are on the same order of magnitude of the SASE signal (both seeds off). Here we see a clear suppression of the HGHG signal, which was not observed when using two seed lasers with the same wavelength $\lambda_1 = \lambda_2 = 267\,\text{nm}$ (Fig. 4.27). This findings can be foreseen by looking at the bunching content for the electron beam when only the second seed in on 4.34 or when only the first seed is on 4.35: there is no bunching at the harmonic of interest. To our understanding, we use as first laser $\lambda = 267\,\text{nm}$ and as second laser $2\lambda = 534\,\text{nm}$. We say that we want to amplify the wavelength 22.25 nm.

When we look at the HGHG signal, 22.25 nm corresponds to the twelfth harmonic

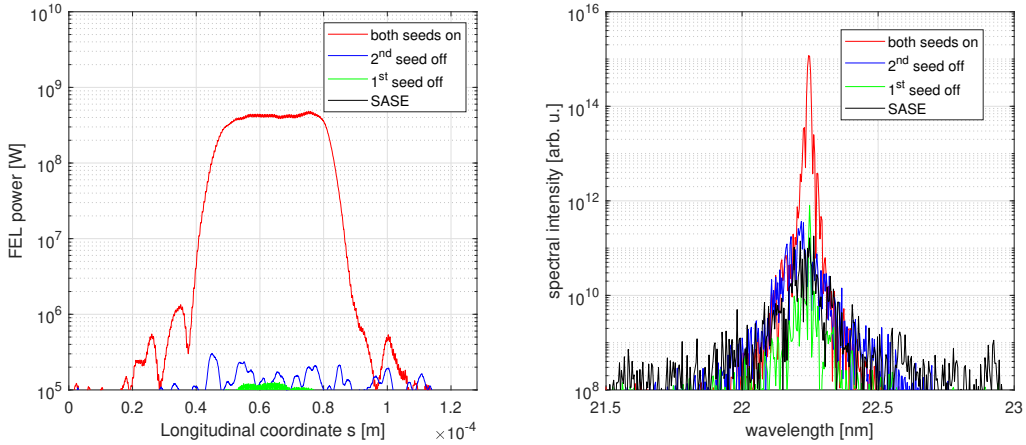

Figure (4.33) Left: FEL power. Right: FEL spectra. Both at the end of the sFLASH radiator. This FEL pulse is generated using two different seed laser wavelengths: $\lambda_1 = 267\,\text{nm}$ and $\lambda_2 = 534\,\text{nm}$. In both plots we present also the signals that we get from only one of the two seeds and from both seeds off (SASE signal).

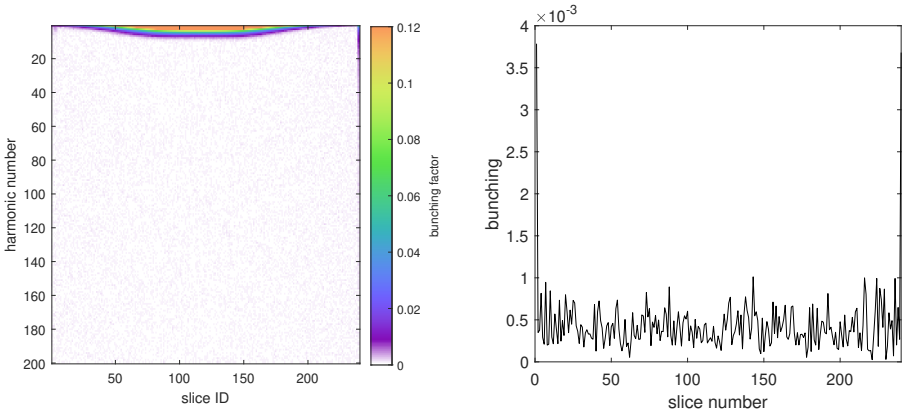

Figure (4.34) Here the first seed laser is off. Hence, we look at the signal of the second seed laser. Left:Harmonic content of the electron beam in terms of bunching. Right: bunching at the 24^{th}-harmonic of the $\lambda_2 = 534\,\text{nm}$ seed laser.

for $\lambda = 267\,\text{nm}$. In this case we don't see any signal because the electron beam is over-sheared along through the first chicane after the seed laser modulation. In the case of the HGHG signal from the second seed laser $2\lambda = 534\,\text{nm}$, amplifying the 22.25 nm corresponds to look at the HGHG signal from the twenty-fourth harmonic. In this case we don't see a signal because we have very low modulation from the seed laser on the beam $A \sim 4$, where we would need to have at least $A \sim 24$. Even if we would have such great energy modulation, the signal along the radiator would be suppressed because of the relative energy spread being beyond

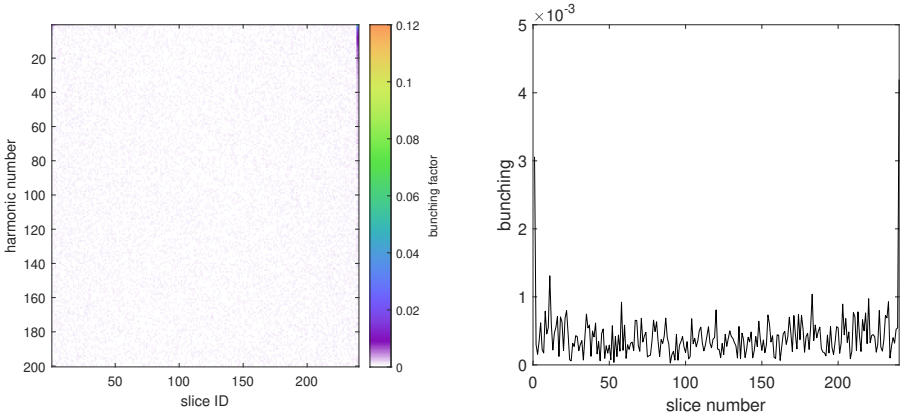

Figure (4.35) Here the second seed laser is off. So we look at the HGHG signal from the first seed laser. Left:Harmonic content of the electron beam in terms of bunching. Right: bunching at the 24^{th}-harmonic of the $\lambda_2 = 534\,\text{nm}$ seed laser.

the bandwidth accepted by the undulator.
So, we conclude that using two different seed laser wavelengths for the EEHG scheme, can be helpful to suppress the HGHG signal when amplifying low harmonics. One have to make sure that the modulators are appropriate for the amplification of the chosen wavelengths.

Down-conversion For the down-conversion we have used a laser with a wavelength of $\lambda_1 = 534\,\text{nm} = 2\lambda$ as first seed, of $\lambda_2 = 267\,\text{nm} = \lambda$ as second seed. In this case, if we take again Eq. 4.26, if we want to get the twelfth harmonic of λ we get:

$$12 \cdot \frac{2\pi}{\lambda} = n\frac{2\pi}{2\lambda} + m\frac{2\pi}{\lambda} \tag{4.31}$$

which becomes

$$24 = n + 2m \tag{4.32}$$

and finally gives $a = 24$, $K = \frac{k_2}{k_1} = 2$ and if we fix $n = -2$, we get $m = 13$. We can estimate the required chicane strengths to maximize the bunching to get FEL lasing by using the bunching equation given in Eq. 3.105. We are still considering an electron beam with an energy of 700 MeV and an uncorrelated energy spread of 70 keV. If we set $A_1 = 4$ and $A_2 = 3.6$ we get from Eq. 3.111 and 3.107: $R_{56}^{(1)} = 1.471\,\text{mm}$ and $R_{56}^{(2)} = 147\,\mu\text{m}$. In the simulation we have set the second chicane strength to $R_{56}^{(2)} = 132\,\mu\text{m}$ to avoid over-bunching and by taking into consideration the added undulator dispersion. With these parameters the

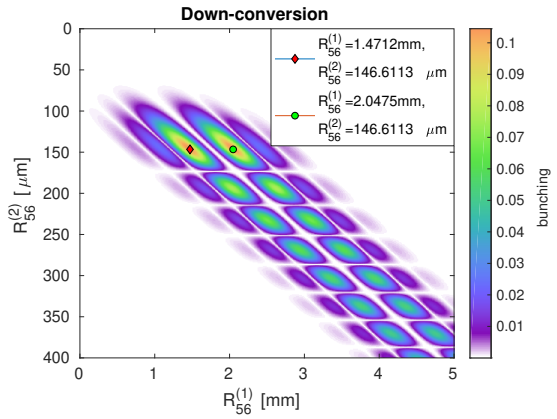

Figure (4.36) Bunching map for the down-conversion case, calculated for $n = -1$, $m = 13$, $K = 2$.

longitudinal phase space distribution and the current profile of the electron beam after the second chicane are shown in Fig. 4.37. The harmonic content of the

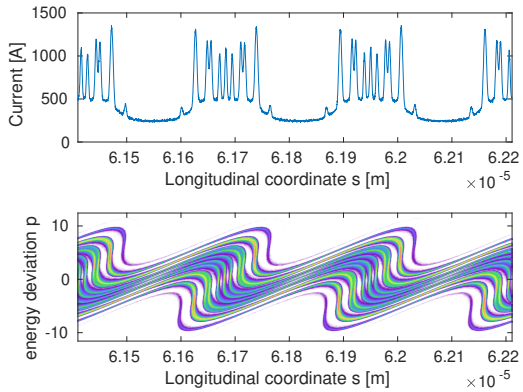

Figure (4.37) Upper plot: current profile. Bottom plot: two slices from the central region where the laser is sitting after the second chicane.

so manipulated electron beam is presented in Fig. 4.38. Here we observe that the bunching at the twelfth harmonic of the 267 nm laser is ~ 0.12. Which is compatible with the amount of bunching foreseen from the bunching map.

The gain curve of the emitted FEL power, Fig. 4.39 is fitted with the expression given in Eq. 2.108.

From the fit we have derived a gain length of $L_G = 0.950\,\mathrm{m}$ and a saturation power of $P_S = 487\,\mathrm{MeV}$, which is achieved within the radiator.

The final FEL pulse and spectrum are shown in Fig. 4.40. The energy within the final pulse is 56 µJ. The RMS duration of the FEL power pulse is $\sigma_t = 48\,\mathrm{fs}$ and the spectral bandwidth is $\sigma_\nu = 2.276\,\mathrm{THz}$. The calculated TBP is 0.6874,

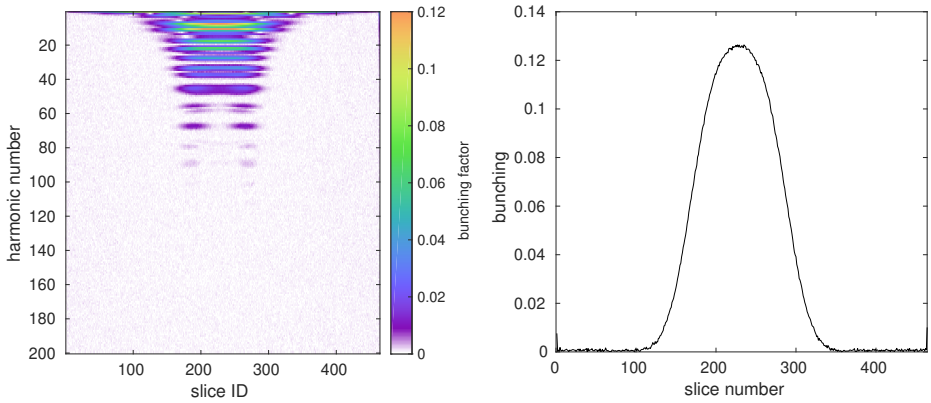

Figure (4.38) Left:Harmonic content of the electron beam in terms of bunching. Right: bunching at the 12^{th}-harmonic of the $\lambda_2 = 267\,\text{nm}$ seed laser

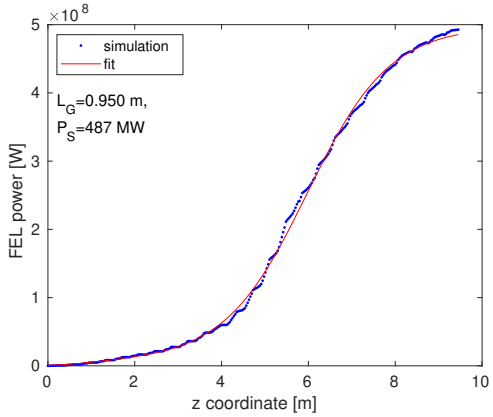

Figure (4.39) FEL power gain curve for the down-conversion case. The fit shows a gain length of $L_G = 0.950\,\text{m}$ and a saturation power $P_S = 487\,\text{MeV}$. Saturation is achieved in the radiator.

from this we derive that the duration of the transform limited pulse is 35 fs and the chirp is $\alpha = 204.18\,\text{rad} \cdot \frac{\text{THz}}{\text{ps}}$. The corresponding group delay dispersion is $\beta = 2306.1\,\text{fs}^2$, which is equivalent to the dispersion added to a 267 nm laser pulse passing through $\sim 12\,\text{mm}$ of fused silica glass.

In Fig. 4.41 we show the FEL power profile (left) and the FEL spectrum (right) for four different cases: EEHG (red), HGHG from the second seed (green), HGHG from the first seed (blue) and SASE. We notice that the signal from the HGHG from the first seed laser is on the same level of the SASE signal, which have more than two order of magnitude difference from the EEHG signal. In this case the signal from HGHG from the second seed laser is not negligible, as there is only one order of magnitude difference. So this scheme does not show an evident advantage

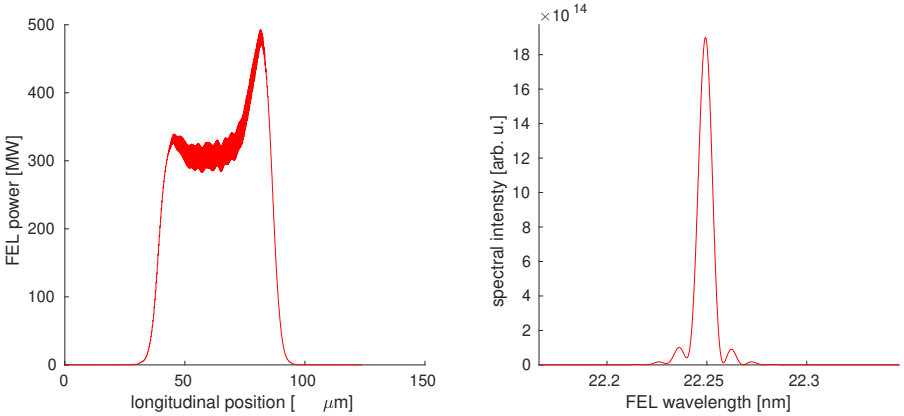

Figure (4.40) FEL power profile (left) and spectrum (right) at the end of the radiator section. The final FEL pulse shows a superradiant peak at the head.

compared to the use of two seeds with the same wavelength. As expected, the

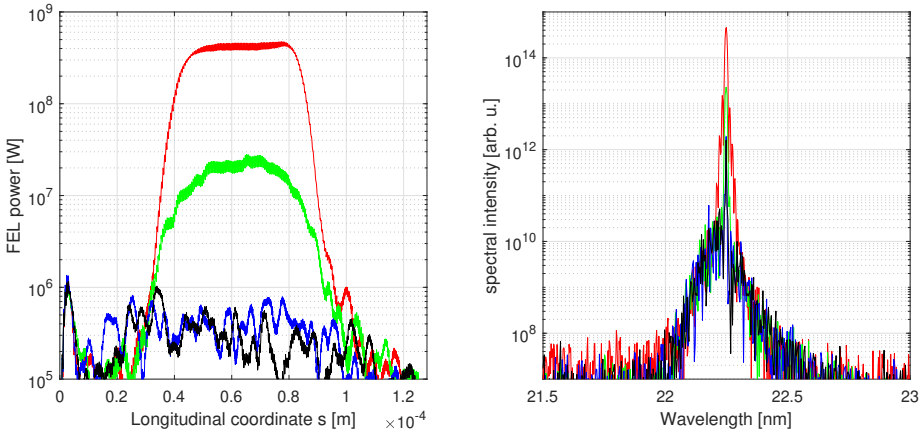

Figure (4.41) Left: FEL power. Right: FEL spectra. Both at the end of the sFLASH radiator. This FEL pulse is generated using two different seed laser wavelengths: $\lambda_1 = 534\,\text{nm}$ and $\lambda_2 = 267\,\text{nm}$. In both plots we present also the signals that we get from only one of the two seeds and from both seeds off (SASE signal).

bunching factor at the twelfth harmonic calculated from the simulation for the HGHG with the second seed, Fig. 4.42, shows the presence of bunching at the ‰ level. While we observe no bunching from the beam seeded from only the first seed laser, Fig. 4.43.

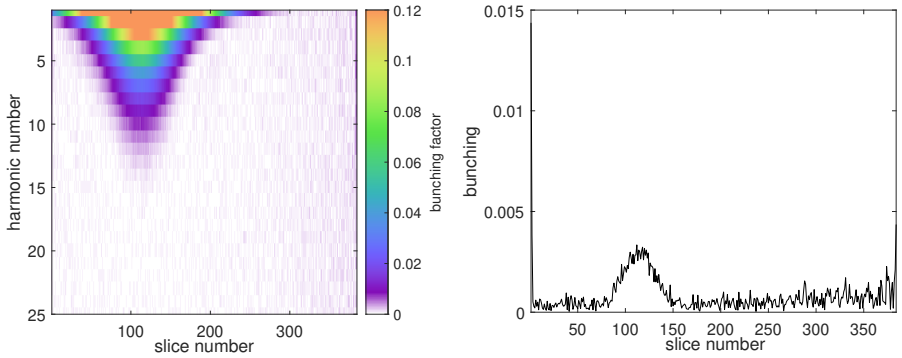

Figure (4.42) HGHG bunching content when the first seed laser is off. Left:Harmonic content of the electron beam in terms of bunching. Right: bunching at the 12^{th}-harmonic of the $\lambda_2 = 267\,\text{nm}$ seed laser

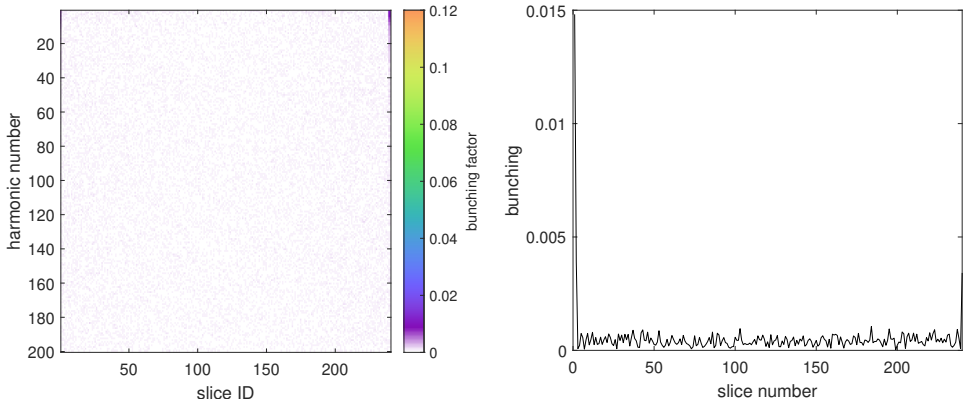

Figure (4.43) HGHG bunching content when the second seed laser is off. Left:Harmonic content of the electron beam in terms of bunching. Right: bunching at the 24^{th}-harmonic of the $\lambda_1 = 534\,\text{nm}$ seed laser

4.3.4 Experimental limitations

The challenge of establishing EEHG operation at sFLASH is mainly due to the constrain of low harmonic operation, where it is difficult discriminating between EEHG and residual HGHG signal. The main limitation is given by both the first and second chicane maximum dispersion and the relative vacuum pipes. As it was discussed in the previous subsection **Tolerances for sFLASH**. Another substantial complication of the EEHG experiment at sFLASH is that the injection beamline for the seed laser is the same for both the sources. So to guarantee the interaction with the first seed laser in the first modulator and the second seed in the second modulator, we should have full control of the focus of the seed laser.

Recently this issue has been addressed by building up a "virtual undulator" that extract the seed laser pulse in the seed laser laboratory and simulates the path that the seed performs until it achieves the modulators in the accelerator tunnel. The real challenge for the optimization of the interaction between the seed laser and the electron beam in the sFLASH electromagnetic modulators, one vertically polarized and one horizontally polarized, is setting the correct polarization to the seed laser. The seed polarization should be orthogonal respect to the polarization of the modulator where the interaction should happen, and it is controlled by a thin-film polarizer (TFP). The only way to optimize the polarization is the experimental scan of the TFP while the seed laser is interacting with the electron beam. This procedure requests a significant amount of time because the scan should be performed for each of the two modulators while the other modulator is off (as a side note: a modulator takes approximately twenty minutes to be closed). The challenge that adds up the difficulty to this task is that we do not have a complete diagnostics for the transverse overlap for the first modulator. The advantage is that there is already a screen station before and after the modulator, and this soon is going to be equipped with UV-sensitive screens to enable the view of the UV seed laser.
Form this experience, we a significant simplification for the implementation of the EEHG scheme would be to have two distinct injection beamlines for the two lasers. Also, extraction of the seed laser after each modulator would be better to avoid interaction between the electron beam and the same seed laser in both modulators.

4.3.5 Planned Upgrades

In [26] is proposed an upgrade of both the first and the second chicane. The chicane length should remain the same for space limitations. So, for the first chicane, it was first considered to reduce the gap of the current dipoles. But, the maximum magnetic field possible with this gap was not achieved due to saturation in the return yokes. Therefore, a new magnet with bigger return yokes was designed. The final upgraded chicane would allow a $R_{56} = 6.5\,\mathrm{mm}$. The second chicane is going to be replaced with the first chicane current dipoles. This upgrade would allow the achievement of harmonics up to the 40^{th}. This upgrade is needed to

facilitate the performance of the EEHG feasibility at FLASH.
Later, is planned an upgrade of the FLASH FEL, where the FLASH1 beamline is going to be completely renewed, and it will be dedicated to EEHG and HGHG seeding. First considerations about the future FLASH1 seeded beamline are described in chapter 6.

EEHG experiment at FERMI

Chapter 5

EEHG experiment at FERMI

FERMI is the VUV-Soft X-ray FEL user facility based on a 1.5 GeV normal conducting linac in operation at Trieste, Italy [109].
Being the first FEL user facility relying on external seeding to produce fully coherent and stable FEL pulses [110, 111], FERMI has attracted a lot of interest for its unique capabilities and new kind of experiments have recently started taking advantage of the coherence of FERMI pulses [112, 113, 6]. Moreover, thanks to the flexible layout of the machine and the possibility to take advantage of the seed laser to tailor the FEL properties, several studies aiming at developing new possibilities have been performed at FERMI [55, 114, 115, 116]. The most recent development study done at FERMI has been focused on confirming the promises of Echo-Enabled Harmonic Generation [66] in terms of extending the harmonic efficiency and improving the FEL properties [21, 69, 63].
In this chapter we are going to report on the latest EEHG results at FERMI [60] where I have contributed to the data analysis and the study of the parameters needed for the simulations that have help a deeper understanding of the experimental data. After a description of the FERMI facility, we present the setup modifications performed for the EEHG experiment. We will characterize EEHG with the experimental data and simulations.

5.1 FERMI FEL

The FERMI FEL entered in operation at the beginning of 2011. The general properties of the FERMI FEL are reported in table 5.1.

Table (5.1) Main electron beam and radiation parameters of the FERMI FEL [109, 110, 111].

Parameter	$FEL1$	$FEL2$	Units
Energy	$1.0 - 1.5$	$1.0 - 1.5$	GeV
Charge	0.7	0.7	nC
Emittance	~ 4 (projected)	~ 1 (normalized transverse)	mm rad
Slice e-spread (r.m.s.)	$100 - 150$	$100 - 150$	keV
Peak current	~ 700	~ 700	A
Bunch length, rms	~ 1	$1 - 1.2$	ps
Output wavelength	$100 - 20$	$20 - 4$	nm
Output pulse length, rms	≤ 100	≤ 100	fs
Energy per pulse	~ 100	Up to 100 ($\sim$ 10@4 nm)	μJ
Polarization	Variable	Variable	
Shot to shot stability (r.m.s.)	~ 10	25 ($\sim$ 40@4 nm)	%
Typical relative bandwidth (r.m.s.)	≤ 0.05	~ 0.03 ($\sim$ 0.07@4 nm)	%
Rep. rate	$10 - 50$	$10 - 50$	Hz

FERMI electrons are generated in a copper photo-cathode with a typical charge of 0.7 nC [117]. Space charge effects are minimized by immediately accelerating the electron bunch to relativistic energies using the L0 section of the LINAC shown in Fig. 5.1. The electron beam encounters now the laser heater [118], that mitigates the microbunching of the electron beam. The device is based on a C-type chicane, an undulator is installed between the second and third dipole. In the undulator the electron beam is energy modulated with a IR-laser, which is resonant to the undulator. The R_{51} and the R_{52} transport elements are smearing out the energy modulation on the electron beam, while it is going through the chicane. As a

final result, the uncorrelated energy spread of the electron beam is heated up respect to the initial value, allowing to mitigate the microbunching instability. Then, the electron beam is further accelerated in the module L1 up to 320 MeV and an energy chirp is introduced to enable the compression in the following bunch compressor BC1. A typical value for the peak current after compression is 700 A. In this accelerating section it is present a X-band cavity that compensates the curvature of the electron beam energy profile to optimize the compression. Finally, the electron beam is accelerated along the next accelerating modules L2, L3 and L4. An additional bunch compressor is located between L3 and L4, but this is not used during routine operation because it has shown to enhance the microbunching instability. Figure 5.1 shows the FERMI linac.
A wall is separating the linac hall from the undulator hall. A transport line (transfer line to spreader, TLS) guides the electrons to the two undulator lines of FERMI: FEL1 and FEL2. The electron beam can either be directed to FEL1 or FEL2 through the spreader. At the end of the TLS it is placed the diagnostic beam dump (DBD), where it is possible to reconstruct the longitudinal phase space distribution using a dipole and a transverse deflecting structure. At the end of the two undulator lines the electron are dumped in the main beam dump (MBD). Here is possible to diagnose the energy profile of the electron beam.
In the next section we describe in more detail the two undulator lines.

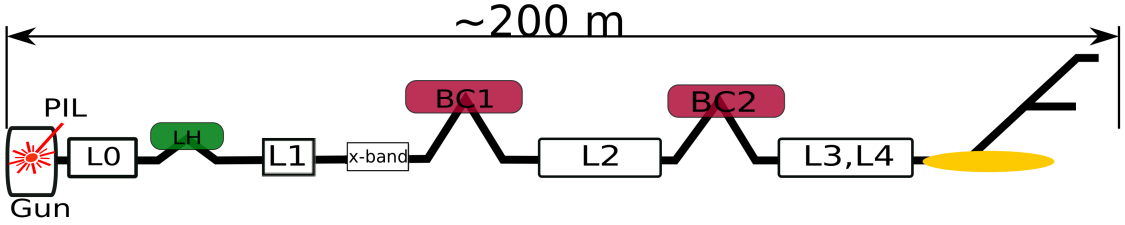

Figure (5.1) Schematic representation of the FERMI injector and LINAC.

5.1.1 FEL1 and FEL2

The two FERMI undulator lines are FEL1 and FEL2. FEL1 [15] is operated with the HGHG scheme [46], it has a planar undulator used as modulator, a bunching chicane and six variable polarization undulators that are used as radiator modules. Up to the 13th harmonic is generated starting from the 260 nm seed laser. FEL1 can deliver wavelengths from 100 nm down to 20 nm.

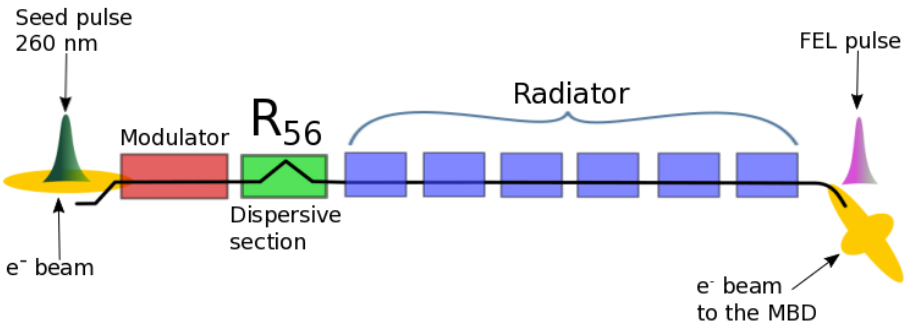

Figure (5.2) FEL 1 undulator line.

The wavelength range from 20 nm to 4 nm is covered by the FEL2 undulator line [119]. Here the setup required for fresh-bunch HGHG (FB-HGHG), also known as cascaded HGHG, is installed [46, 120]. A representation of FEL2 is given in Fig. 5.3 a). Downstream the spreader the electron beam encounters a typical HGHG setup: a modulator (M1) tuned to resonance to the seed laser wavelength of 260 nm, a bunching chicane (DS1 in Fig. 5.3) and three radiator modules (R1) tuned to harmonics in the range $5-13$ of the seed laser. So, radiation in the range $65-20$ nm is generated in the first stage. This radiation is used as a seed for the second stage. This consists first in a delay line, that is used to delay the electron beam respect to the FEL radiation. Hence the radiation produced by the first stage will sit near the head of the electron beam, in a region that was not interacting with the seed in the first stage. At this point, the HGHG process happens again but the seed source has shorter wavelength, thus the final FEL radiation has a shorter wavelength. This scheme is very challenging, because the electron beam should have uniform properties over a long portion of the beam. Moreover, the setup is space demanding and the operation at very short wavelengths make the system very sensitive to small electron beam imperfections coming from possible collective effects developing along the linac and in the chicanes [69].
The FEL2 at FERMI has been exploited for an experiment aiming at comparing the performances in this spectral range between EEHG and HGHG. In order to be able to test EEHG few changes to the layout have been necessary. This lead to have FEL2 modified as requested for EEHG and not optimized for cascaded HGHG for a period of about six months. The modifications that have been applied to the FEL2 beamline, are described in the section 5.2.

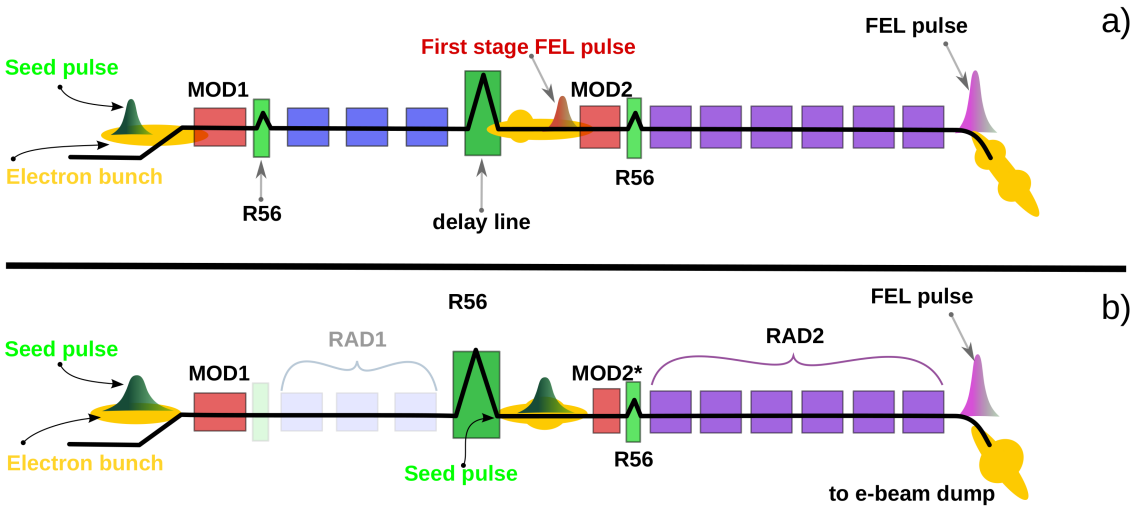

Figure (5.3) FEL 2 undulator line. a) FEL2-setup for cascaded HGHG, b) FEL2-setup adapted for EEHG seeding.

5.1.2 Photon transport at FERMI

Downstream the FELs beamlines there are two identical photon transport beamlines denominated PADReS [121], which stays for Photon Analysis Delivery and REduction System, that transport the photon beam to the FERMI photon science end stations: EIS [122], DiProi [123], LDM [124] and MagneDYN [125]. During the photon transport, it is also possible to characterize the radiation properties like intensity, spectral distribution, position and coherence. The PADReS beamlines are schematically shown in Fig. 5.4.

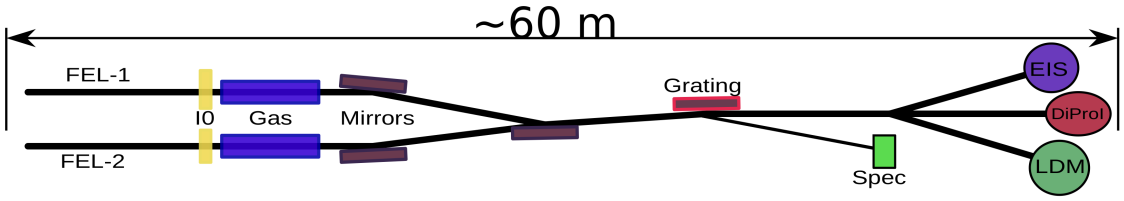

Figure (5.4) Schematic representation of the Photon Analysis Delivery and REduction System (PADReS) at FERMI.

5.2 Setup modifications for the EEHG experiment

The FERMI-FEL2 undulator line has been exploited to perform the EEHG experiment. The setup installed for cascaded-HGHG differs from the one required from EEHG. In fact some modifications has been performed to the beamline upstream the experiment, as we can observe in Fig. 5.3 b).
As first EEHG modulator has been used the modulator of the first stage of the cascaded HGHG, which has 30 periods and a period length of 10 cm. The first chicane was off and the three radiators of the first stage has been kept open during the whole experiment. The delay line between the first and the second stage has been used as first EEHG chicane. In order to increase the maximum dispersion $R_{56}^{(1)}$ of this chicane, the nominal distance between the first and the second and between the third and fourth dipole has been increased. The second laser injection hardware and additional beam diagnostics has been placed in the small drift between the central dipoles. In order to increase the dispersive strength of the chicane, and therefore the maximum peak current achievable by the single dipole, the power supply was upgraded. In this way it was possible to achieve a maximum disepersion of 2.4 mm for e-beam energies of ~ 1.3 GeV. The nominal second modulator of the second stage is inappropriate to be resonant at a UV seed laser wavelength in the GeV range for the electron beam energy. So this was exchanged with a spear undulator of the Elettra synchrotron. This modulator is 1.5 m long, it has a period $\lambda_u = 113$ mm, a number of periods $N_u = 13$ and a maximum K of 12, corresponding to a peak field of 1.2 T. The chicane of the second stage has been used as EEHG bunching chicane without modifications. The seed laser interacting in the first modulator was the same as the one also used for cascaded-HGHG. While a new seed laser has been prepared for the second modulator. For this task it has been used the IR Ti:Sapphire that is sent to the users end-stations during normal operation. For the experiment, this laser was brought at the optical table placed near the first big EEHG chicane, where is converted to UV radiation. The final wavelength of this seed is 264 nm, the pulse length 110 fs and a maximum energy of 50 µJ. The FEL radiation was produced in the final six radiator modules which have 68 periods each with a period length of 3.5 cm that can be operated in both linear and circular polarization.

5.3 EEHG beamtime organization

Once the FERMI FEL2 beamline has been re-organized for the purpose of showing and perform more advanced EEHG experiments, five periods, each lasting one week, of machine studies has been dedicated to this aim. The time span was limited because of the necessity to re-establish the cascaded HGHG setup to continue with user operation afterwards. Between the different periods, the operation of FERMI for users has been based on FEL delivery from FEL1 only.
During the different periods, the electron beam energy has been progressively increased in order to allow starting the EEHG operations at longer wavelengths (lower harmonics) and conclude at short wavelengths. In order to reach the maximal electron beam energy at FERMI in the last period the repetition rate of the accelerator had to be reduced from 50 Hz to 10 Hz. Table 5.3 shows the electron beam energy and the repetition rate exploited for each period, the electron beam current and charge have been set to the FERMI nominal values presented in table 5.1.

Table (5.2) Electron beam energy and machine repetition rate for each period.

PERIOD	Energy [GeV]	Frequency [Hz]
1	0.9	50
2	1.1	50
3	1.3	50
4	1.3	50
5	1.5	10

First attempt of operating FERMI in EEHG occurred in May 2018. After few shifts of commissioning of the new dedicated hardware, it has been immediately possible to show evidence of an EEHG signal at harmonic 12, corresponding to a FEL wavelength of 22 nm. During the same period shorter wavelengths as well have been achieved. In particular, we report in Fig 5.5 the spectrum of the 18th harmonic of the seed laser. The lasing was achieved after HGHG optimization

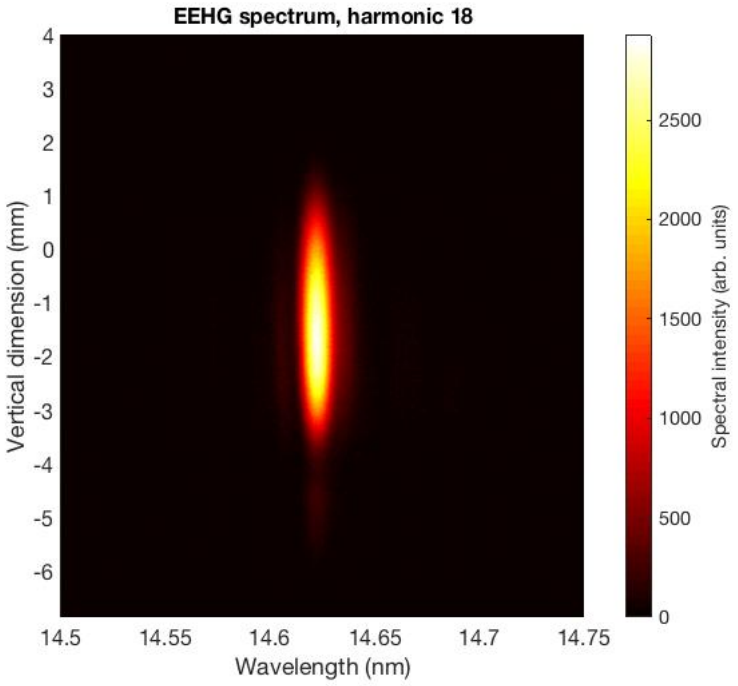

Figure (5.5) Spectrum of the 18th harmonic of the UV seed laser recorded during the first period of EEHG experiments.

in the second stage of FEL2. To show if the signal was authentic EEHG, it was performed a scan of the second chicane dispersion and a minimum in the FEL signal was found for $\sim |n|R_{56}^{(1)}/h$. This confirmed the authenticity of EEHG. Figure 5.6 shows the typical behavior of the FEL spectrum as the dispersive strength is scanned: plot A) shows it for HGHG and B) shows it for EEHG where it is scanned the second chicane dispersive strength. The measurement shown in plot B) was taken during the first EEHG beamtime when the FEL was tuned for generating EEHG at the 18^{th} harmonic at the working point $n = -2$, here we have set $A_1 = 1.5$ and $A_2 = 0.84$, the first chicane dispersion was $R_{56}^{(1)} = 2\,\text{mm}$. As expected the minimum of the EEHG normalized FEL intensity has been observed at $R_{56}^{(2)} = 222\,\mu\text{m}$ which satisfies the previsions from formula $|n|R_{56}^{(1)}/h = 2 \times \frac{2000\,\mu\text{m}}{18} = 222\,\mu\text{m}$.

After the first evidence of EEHG lasing at the harmonic 12, we have focused on the optimization of all the parameters of the machine that determine the EEHG performance. For example, the alignment of the seed lasers on the electron beam within the two modulators, the electron beam trajectory all along the machine and the electron beam optics. This optimization campaign has been fundamental

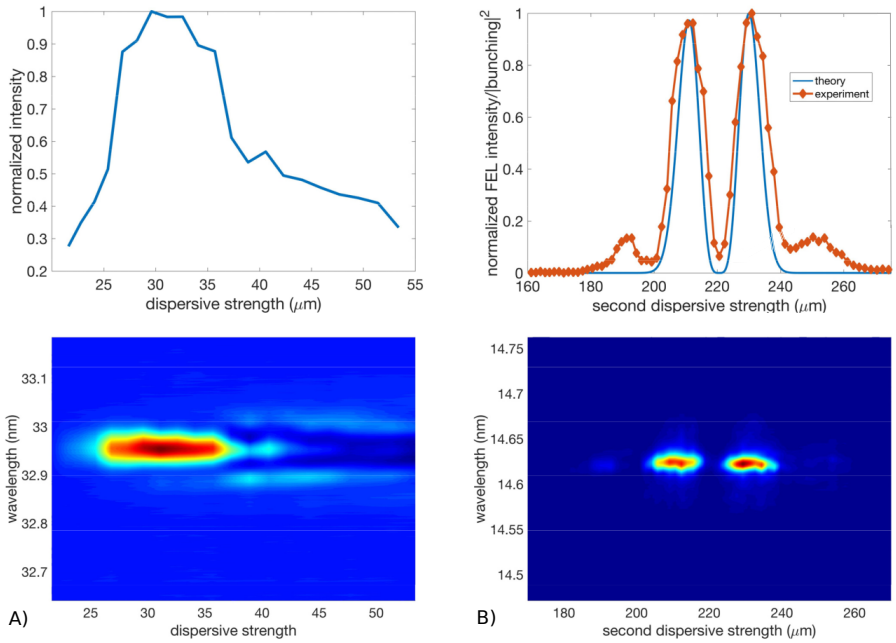

Figure (5.6) FEL intensity and spectra as a function of the (second) dispersive strength: A) shows how the spectra and the intensity is expected to variate for HGHG as the chicane strength is scanned around the optimal point, B) shows the variation of the FEL intesity and spectral signal as the second dispersive strength is scanned [126].

to guarantee a stable and reproducible FEL for the two successive periods, which have enabled to perfom a fully characterization at higher harmonics. In fact in the next sections we are going to focus of the results achieved at the 36^{th} harmonic of the seed laser.

5.4 Selected working points

The detailed analysis of EEHG has been performed for the harmonic 36 of the UV seed laser, corresponding to $\lambda = 7.3\,\text{nm}$. The experimental conditions (seed laser power and R_{56} strength) have enabled the establishment of EEHG at the working points $n = -1$ and $n = -2$. In the following we present the data collected for the $n = -1$ working point, which have shown better spectral quality. For this working point, the first chicane dispersion was 2.38 mm and the second one was 62 µm. The electron beam has been accelerated in the FERMI LINAC up to 1.31 GeV.

The curvature is corrected before compression happens by a fourth-harmonic RF cavity. However, a residual energy-curvature was present on the e-beam due to wakefields effects occurring in the last part of the linac. The measured slice normalized transverse emittances was 1 mm·mrad. While the RMS uncorrelated energy spread at the LINAC end was 150 keV. In Fig. 5.7 we show the measured longitudinal phase space distribution of the electron beam at the end of the linac, in the same plot we show also the current profile. The current profile is uniform along the region where the seed laser is going to sit, which is the central region of the electron bunch while the electron beam energy profile shows a not-negligible quadratic chirp, the effect of having a quadratic chirp in seeding was analyzed in chapter 3. The detailed analysis of EEHG has been performed for the harmonic 36 of the UV seed laser, correspondent to $\lambda = 7.3\,\mathrm{nm}$. For this harmonic the EEHG n parameter was *-1*, the first chicane dispersion was 2.38 mm and the second one was 62 µm. The electron beam has been accelerated in the FERMI LINAC up to 1.31 GeV. The curvature is corrected before compression happens by a fourth-harmonic RF cavity. However, a residual energy-curvature was present on the e-beam due to wakefields effects occurring in the last part of the linac. The measured slice normalized transverse emittances was 1 mm·mrad. While the RMS uncorrelated energy spread at the LINAC end was 150 keV. In Fig. 5.7 we show the measured longitudinal phase space distribution of the electron beam at the end of the linac, in the same plot we show also the current profile. The current profile is uniform along the region where the seed laser is going to sit, which is the central region of the electron bunch while the electron beam energy profile shows a not-negligible quadratic chirp, the effect of having a quadratic chirp in seeding was analyzed in chapter 3.

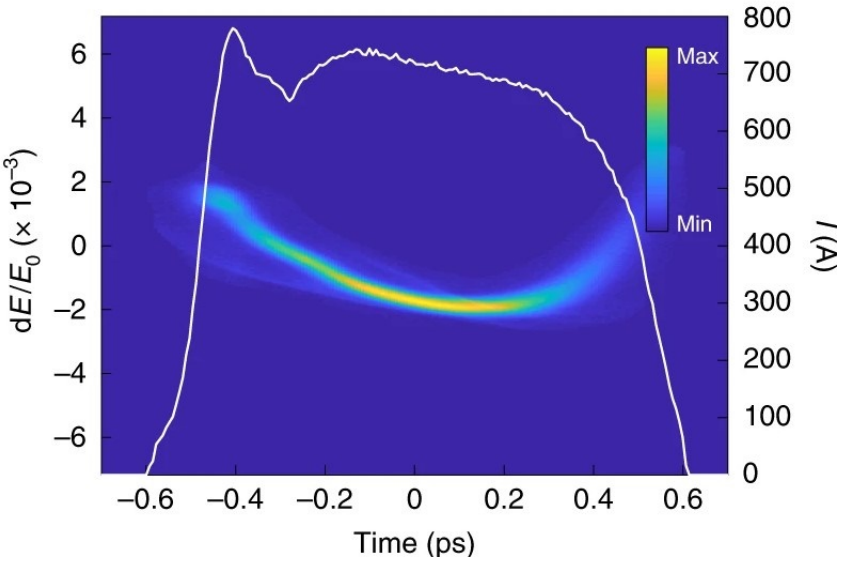

Figure (5.7) Measured electron beam during the experiment. Longitudinal phase space distribution and corresponding current profile (white curve).

5.5 Characterization of the Gain Length curve

During the EEHG beamtime several gain curves have been measured for the different runs. This is usually done by measuring the signal from an instrument able to detect the FEL radiation energy or FEL spectral properties every time one radiator is set on resonance. During the experiment we had different diagnostic instrumentation to detect the signal. To record the FEL spectrum, the FERMI spectrometer was exploited [127]. The single shot spectra for FEL pulse energies above the microjoules was measured with a combined system. First, the FEL radiation encounters a planar variable-spacing grating which focuses the first order of diffraction mode onto a yttrium aluminium garnet (YAG) screen. The generated florescence radiation was imaged by a charge-coupled device (CCD). Estimation of the absolute FEL flux has been done using a photodiode previously calibrated on a synchrotron beam line in Elettra. An useful measure of the relative FEL intensity has been obtained from the measure of the photocurrent drain produced by the FEL on the first mirror (PM2A).

In order to reliably characterize the exponential gain of the EEHG signal and

derive an estimate of the gain length, it has been necessary to do a careful optimization of all the parameters that are known to possibly influence the measurement: tapering, optics, trajectory, laser-electron alignment,... . During this optimization phase we have measured gain curves to remark possible issues as off-resonance undulators, electrons off from the designed trajectory, etc. . For most of these optimization measurements was registered only the FEL intensity and not the spectral information. These measurements have enabled further optimization of the machine. At this point, we have collected the gain curve measurement for the final characterization of the selected EEHG configuration. All these measurements are reliable when there is a relevant FEL gain, therefore the gain curves have been measured up to harmonic 45.

The gain curve acquisition routine is based in the code REALTA available at FERMI [128]. Starting from the condition with all the undulators set on resonance with the desired FEL wavelength, the main FEL parameters (spectra and intensity) are measured. The acquisition is repeated as the number of the on resonance undulator is reduced by opening the gap of the downstream ones. Thanks to the real time capabilities of the structure, relevant electron beam parameters (charge, trajectory,energy,...) are aquired at the same time and can be used for data filtering. The routine is also collecting useful data for background subtraction, for example it is measuring the machine parameters for the case in which the modulator is set off resonance.

For the harmonic 36 of the seed laser we have chosen a scan that was measured using an electron beam with an energy of 1.31 GeV and longitudinal phase space distribution as shown in Fig. 5.7. The EEHG parameters for this measurement were $n = -1$, $A_1 \simeq A_2 = 3$ and $R_{56}^{(1)} = 2.38\,\mathrm{mm}$ (corresponding to a chicane current of $I = 740\,\mathrm{A}$) $R_{56}^{(2)} = 62\,\mu\mathrm{m}$ (corresponding to a current of 85.8 A).

For each iteration of the gain curve measurement 50 FEL spectra are registered. In the post-processing phase of the data, it is possible to select the best spectra by applying the filters based on suitable machine parameters. The filtering procedure enables to keep only the spectra that were recorded for optimal electron beam properties. It is possible to select the filters to apply by observing at the correlation plots between the FEL signal e.g. the PM2A signal versus the readings from the machine diagnostics hardware (pyro-detectors, BPMs, BAMs,...), as shown in Figure 5.8.

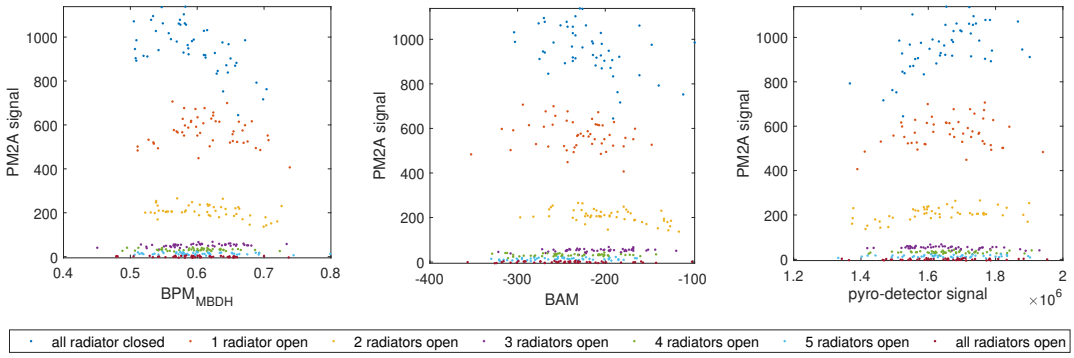

Figure (5.8) Correlation plots between the machine hardware readings and the FEL signal from the PM2A. The first subplot shows the correlation between the FEL signal from the PM2A and the horizontal position in the BPM in the main beam dump, which gives the information about the energy stability of the electron beam (providing information on the sensitivity to the relative timing between the seed and the electron beam). The second subplot shows the correlation between beam arrival monitor (BAM) signal and the PM2A signal. The last subplots represents the correlation plot between FEL signal and the pyro-detector signal. The correlation behavior is different for the different undulator configurations.

From these, a filtering is done based on the pyro signal, on the beam arrival monitor (BAMs) and on three different beam position monitors (BPMs). The pyro-detector measures the length of the electro beam downstream BC1 (see Fig. 5.1). The used BPMs are: one is the horizontal BPM of the main beam dump(BPM_{MBDH}), which signal is proportional to the electron beam energy, the second one is the horizontal BPM located in the radiator section (BPM_{FEL3H}), and the third is a vertical BPM located in the transfer line spreader (BPM_{SCL2V}), these two last BPMs are accounting for the trajectory fluctuations of the electron beam. The resultant percentage of filtered out data varies between 50 and 78% depending on the configuration of the undulators.

The remaining spectra are then averaged for each iteration and the final result is shown in Fig. 5.9. Here the first left subplot represents the condition where all the radiator are closed, while the last subplot is when all the radiator are open, this last subplot can be used as reference for background. So in Fig. 5.10 the spectra with background subtraction are shown. Here we present the cases from all radiator closed to only one radiator closed. If we sum along the vertical coordinate of Fig. 5.10, we obtain the spectra profiles shown in Fig. 5.11.

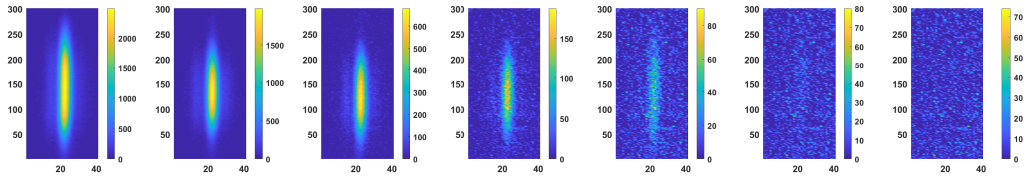

Figure (5.9) Average of the remaining FEL spectra shots after applying the cuts for each loop. From left to right: all radiator closed to all radiator open. The units are not calibrated yet, but horizontally there is the FEL wavelength.

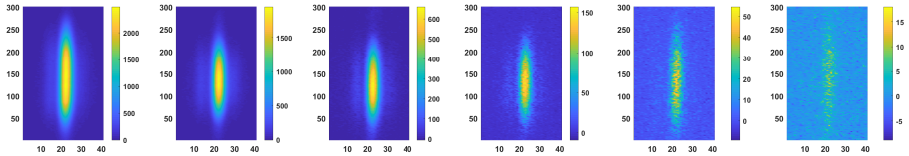

Figure (5.10) FEL spectra averaged with noise subtraction. The noise is obtained from the last plot of Fig. 5.9. From left to right: all radiator closed to only one radiator closed.

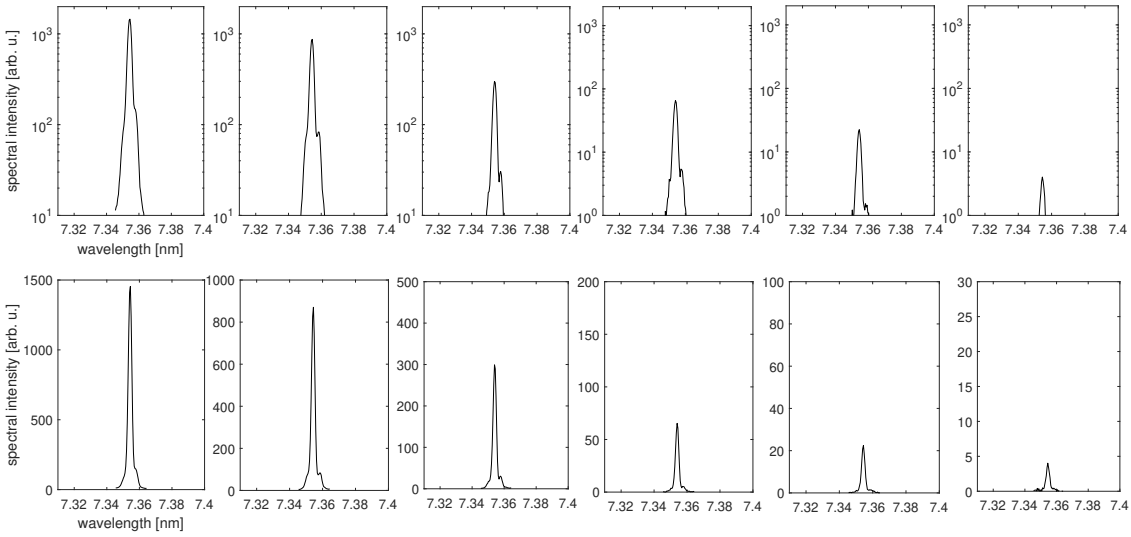

Figure (5.11) FEL spectra averaged with noise subtraction and summed over the y axis of Fig. 5.10. From left to right: all radiator closed to only one radiator closed. The top plots are in logarithmic scale and the bottom plots are in linear scale, in this case the y-axis are not the same for all the subplots.

In this Figure, the horizontal axis has been converted from pixel to nanometer scale, this operation is performed only in the region where there is a significant signal, which is the region of interest (ROI). The calibration of the spectrometer is based on the procedure reported in [127]. A measure proportional to the FEL intensity is obtained by summing the FEL spectra presented in Fig. 5.11 along the

wavelength axis. The error on this value is calculated by calculating the standard deviation on the FEL intensity obtained from the spectra selected. The final FEL curve is obtained by plotting the integrated FEL intensity against the number of closed undulators and it gives a gain length of $L_G = 1.9\,\mathrm{m}$, Fig. 5.12. Simulations done with GENESIS1.3 v.4 [104], that reproduce the electron beam parameters from Fig. 5.7 and table 5.3, agree with the calculated gain length. In Fig. 5.12 we report the measured gain curve in arbitrary units and the simulation result.

In order to give an estimate of the FEL energy we used a calibrated photodiode,

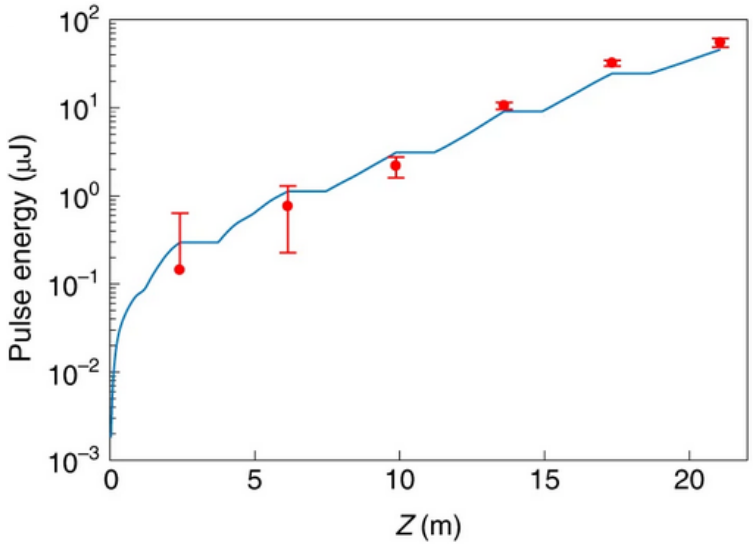

Figure (5.12) Gain curve of the EEHG FEL at 7.37 nm. The experimental data are compared with the simulation result that foresees a gain length of 1.9 nm.

because the spectra cannot give an absolute measure, but only relative. From the photodiode it was estimated a FEL peak power of 420 MW which corresponds to an energy of 25 µJ for an estimated pulse duration of 60 fs. The simulation is overestimating the measured FEL power due to possible losses of energy in the photon transport of the FEL radiation to the photodiode, but one possible reason could also be that the simulation is overestimating the expected power due to saturation effects [60]. The pulse duration obtained from simulation is in reasonable good agreement with the one obtained from the Fourier transform of the FEL spectra assuming Fourier limited pulses.

5.6 EEHG spectral characterization

Besides the characterization of the FEL in terms of gain length we have also focused on the measurement of the EEHG FEL spectral quality for the two lowest wavelengths for which high gain was observed: $\lambda = 7.3\,\text{nm}$ and $\lambda = 5.9\,\text{nm}$, which corresponds to the harmonic 45 of the seed laser. Multiple single-shot spectral profiles for the two cases are reported in Fig. 5.13. For both wavelengths we observe a Gaussian-like shape for the FEL spectrum. The relative central wavelength stability is $\sim 7 \times 10^{-5}$ and the root mean square intensity fluctuations increase

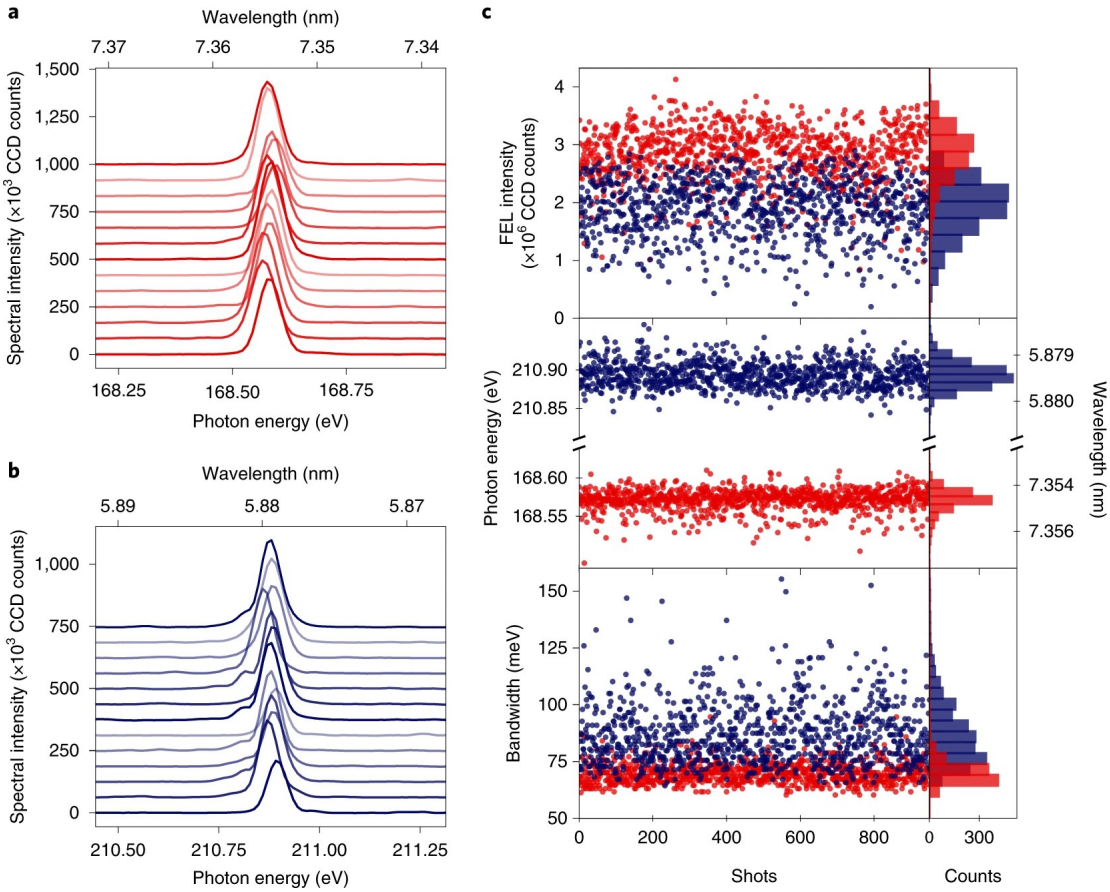

Figure (5.13) Single-shot spectra randomly chosen in a sequence of 1000 consecutive shots at $\lambda = 7.3\,\text{nm}$ ($\sim 160\,\text{eV}$; **a**) and $\lambda = 5.9\,\text{nm}$ ($\sim 211\,\text{eV}$; **b**) in the $n = -1$ EEHG working point. **c**, Data for 7.3 nm and 5.9 nm are shown in red and blue respectively. FEL intensity (top), central wavelength/average photon energy (middle) and $\sigma_{76\%}$ spectral width for the 1000 consecutive shots and the corresponding histograms.

as the wavelength shortens, for $\lambda = 7.3\,\text{nm}$ we have 16% and for $\lambda = 5.9\,\text{nm}$ 25%. The spectral width is indicated with $\sigma_{76\%}$ and it represents the minimum width containing the 76% of the pulse energy which corresponds to the full-width half maximum ($FWHM = \frac{\sigma}{2\sqrt{2ln2}}$, where σ is the standard deviation of the distribution) for a Gaussian. However, $\sigma_{76\%}$ is more sensitive to the tails of the spectrum compared to the FWHM. The spectrum tails can be caused from electron beam imperfections and laser-phase errors. For the wavelength $\lambda = 7.3\,\text{nm}$ we have measured $\sigma_{76\%} = 3.0 \times 10^{-3}$nm, giving a relative bandwidth of 4×10^{-4} [60]. From the theory presented in paragraph 3.1.1 and using the EEHG spectral bunching distribution of Eq. 3.126 it is derived that the expected $\sigma_{76\%}$ is 1.5 times smaller than the one obtain experimentally, this could be related to a residual frequency chirp on the second seed laser, non-zero spectrometer resolution and a possible spectral broadening due to electron beam instabilities [60]. At $\lambda = 5.9\,\text{nm}$ the measured average $\sigma_{76\%}$ is 2.4×10^{-3}nm, giving a relative bandwidth of 4×10^{-4}. The $\sigma_{76\%}$ calculated from theory is 1.8 times smaller. The reason why this value is higher compared to the higher wavelength is is visible from Fig. 5.13 where the selected spectra for $\lambda = 5.9\,\text{nm}$ have visible side-bands. The possible reason for the increase in bandwidth is related to the increase in sensitivity of the bunching phase in Eq. 3.126 on electron-beam imperfections. In addition, we have observed that the side-bands are correlated to the electron beam arrival time, meaning that the effect is induced depending on the portion of electron beam "seen" by the seed laser.

Harmonic 45 has been the largest one allowing FEL to be strongly amplified in the radiator with the available parameters at FERMI during the experiment. At shorter wavelength, the undulator parameters were not optimal for supporting a large gain with the available electron beam energy. Nevertheless, during the EEHG experiment at FERMI, we have observed coherent emission at very high harmonics. Here, we are going to present performances at the harmonic 84 (3.1 nm), that is the highest harmonic where it was possible to acquire single-shot spectra and at the harmoni 101 (2.6 nm), which is the highest harmonic that was achieved at FERMI during the whole EEHG experiment. For the harmonic 101 case, due to the limited dispersion of the first chicane and seed laser power it was necessary to operate at the EEHG working point $n = -4$ at the electron beam energy $E_0 = 1.5\,\text{GeV}$. With such high $|n|$ the EEHG bunching is low, also the FEL gain was low due to a small undulator parameter, a small FEL parameter. As a result, the observed FEL signal was proportional to the bunching squared,

that, as mentioned, was very small Fig. 5.14. In Figure 5.14, we observe that the coherent emission at the harmonic 101 happens in a tiny portion of the electron beam ($\sim 10\,\text{fs}$) and it overlaps with the inchoerent emission taking place all over the beam ($\sim 1\,\text{ps}$).

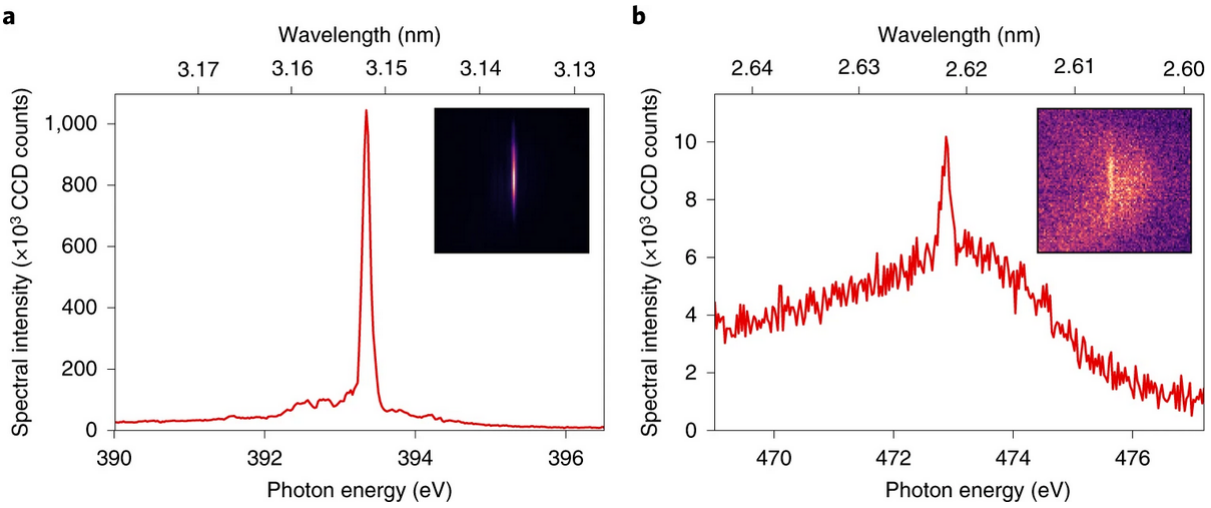

Figure (5.14) **a.** Coherent emission spectra at $\lambda = 3.1\,\text{nm}(\sim 394\,\text{eV})$ and **b.** $\lambda = 2.6\,\text{nm}(\sim 474\,\text{eV})$. Insets show the raw CDD images.

5.7 Comparison between EEHG and cascaded HGHG performances

EEHG [66] and cascaded HGHG [46] are both schemes which enable the generation of seeded radiation at extremely short wavelengths. Considering as an example the FERMI seeded FEL, cascaded HGHG is exploited routinely to generate powerful FEL pulses in the wavelength range between 20 and 4 nm starting from a UV seed laser. While with EEHG we observed coherent emission at wavelengths as short as 3.1 nm and 2.6 nm corresponding respectively to harmonic 84 and 101 of the seed laser (Fig. 5.14).

In terms of continuity of tunability EEHG is preferred because it can cover all the harmonics $a = n + Km$, where a is the target harmonic, and n and m are two integer numbers that are fixed depending on how the EEHG parameters (chicane strengths, seed laser modulations) are set. On the other side, cascaded HGHG

can only produce the harmonics $a = n \cdot m$ where n is the harmonic generated in the first stage and m is the harmonic generated in the second stage.
In order to verify the previsions that were derived in [69] related to the superiority of EEHG respect to cascaded HGHG, regarding stability respect to the electron beam instabilities arising in the linac, we compare in the following the EEHG with the cascaded HGHG performances.
Seeding schemes are highly demanding on the electron beam quality. Electron beams should hold uniform properties (energy,energy spread, emittance,beamsize,...) along the region where the laser is supposed to be overlapped. The electron beam instablities along the linac and the seeding section lead to imperfections that should be minimized. This is challenging for schemes as cascaded HGHG where the electron beam needs to be substantially long (see table 5.1) compared to single stage HGHG and EEHG, to accommodate the seed of the second stage in a "fresh" region. Therefore, it is necessary to have uniform properties over a longer segment, and this is more challenging.
To compare the EEHG and cascaded HGHG stability, we have chosen to operate at the FEL wavelength of 8.8 nm ($\sim$ 141 eV) corresponding to the harmonic 30 of the UV seed laser, this working point has been established with an electron beam with an energy of 1.1 GeV. The electron beam was having the typical length used for cascaded HGHG 5.1 and the remaining parameters were as for the gain length curve measurement (see Fig. 5.7). The same beam was used for both EEHG and cascaded HGHG.
For the measurement the seed (or seeds for EEHG) laser arrival time has been scanned respect to the electron beam in an interal of 500 fs and the FEL spectra have been measured at each step. Figure 5.15 shows the result of the measurement. It is immediately evident that cascaded HGHG shows a wavelength shift, while this is not observed with the EEHG scheme, which shows a better stability respect to the non-uniformities of the electron beam properties. The wavelength shift is caused by a chirp in the electron beam energy profile. In fact for EEHG, the variation of the beam energy profile causes a phase variation of the EEHG bunching factor given by [63]:

$$\Delta\psi \approx -k_E \left(R_{56}^{(2)} + \frac{n}{a} R_{56}^{(1)} \right) \frac{\Delta E}{E_0}, \tag{5.1}$$

where ΔE is the deviation from the nominal energy of the electron beam E_0. If the electron beam has a varying local linear energy chirp $\frac{dE(t)}{dt}$ along its longitudinal

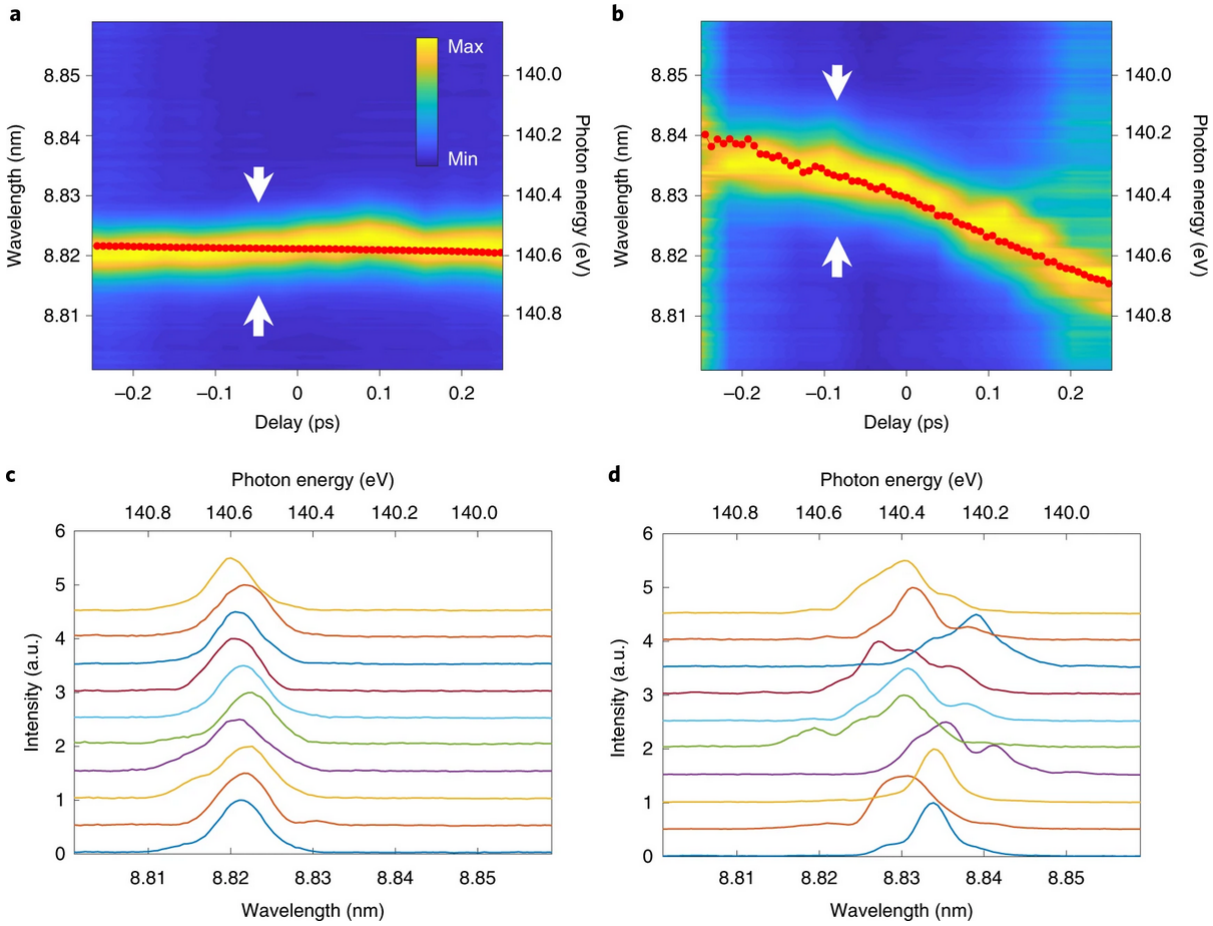

Figure (5.15) **a,b** Averaged and normalized FEL spectra as a function of the delay between electron beam and the seeds for EEHG (**a**) and cascaded HGHG (**b**). The red dots show the calculated central FEL wavelength using the electron beam local energy chirp. **c,d** Consecutive normalized single-shot spectra for EEHG **c** and for cascaded HGHG **d** taken at the maximum intensity, which is indicated with the white arrows in **a** and **b**.

coordinate t, this gives a relative shift of the central wavelength:

$$\frac{d\lambda(\tau)}{\lambda} \approx -\frac{1}{E}\left((R_{56}^{(2)} + \frac{n}{a}R_{56}^{(1)}\right)\frac{dE(\tau)}{cdt} \tag{5.2}$$

which depends on the position τ of the seed (that corresponds to the delay in Fig. 5.15) with respect to the to the electron beam. When EEHG is optimized is valid the condition:

$$R_{56}^{(2)} = \frac{|n|}{a}R_{56}^{(1)} \tag{5.3}$$

therefore the wavelength shift of Eq. 5.2 is not present.
For single stage HGHG the same formula 5.2 is valid with $R_{56}^{(1)} = 0$, therefore there is always a wavelength shift. Finally for cascaded HGHG the same formula valid for HGHG should be applied twice, by taking into consideration the chicane dispersion of the two HGHG stages and the dispersion added from the delay line. In figure 5.15 the red dots represent the location of the central wavelength calculated by taking into consideration Eq. 5.2 and the modified version for cascaded HGHG, which show to be in agreement with the experimental data.

5.8 Simulations

In this section, we are going to present the EEHG simulations based on the FERMI setup. In particular, we are going to focus on few FEL wavelengths: 7.37 nm, which is the one used to extract the gain curve from the experimental data. 4 nm, corresponding to harmonic 66 of the seed laser. For this wavelength we are going to consider two EEHG working points: one at n=-2, that is the one feasible with the setup used for the EEHG experiment at FERMI, and n=-1, which would need an upgrade of the first EEHG chicane. Finally we present simulation result also for the 10 nm case, corresponding approximately to harmonic 26 of the seed laser. These two last cases are of our interest, because in the next chapter we are going to compare the performances between the FERMI setup and the expected performances of the FLASH2020+ upgrade.

5.8.1 FEL lasing at 4 nm

Before setting up the simulation, we have estimated the Pierce parameter, from which we can get the expected saturation power and the necessary saturation length. For this calculation the formulas for pre-bunched beam presented in the initial theory chapter have been used. In table 5.3 we report the electron beam parameters used for this simulation.

In table 5.4 are indicated the parameters set for the radiator modules.

Table (5.3) Electron beam parameters.

Nominal energy	1.5 GeV
Slice energy spread	150 keV
Slice transverse emittance	1.0 µm
Peak current	700 A

Table (5.4) Radiator parameters.

Length/module	2.415 m
Undulator period	35 mm
Number of period/module	69
Undulator type	helical
Undulator strength ($a_w = K$)	0.9846
Number of undulator modules	6

The estimated Pierce parameter results $\rho \simeq 1 \times 10^{-3}$. We should check if the energy spread of the electron beam normalized to the total energy is lower than the Pierce parameter, otherwise FEL lasing is suppressed. As we are modulating twice the electron beam, in the first modulator setting $A_1 = \Delta\gamma_1/\sigma_\gamma = 3$ and in the second modulator $A_2 = \Delta\gamma_2/\sigma_\gamma = 5$. The energy spread of the electron beam upstream the radiator is:

$$\frac{\sigma\gamma^{TOT}}{\gamma_0} = \sigma_\gamma \cdot \sqrt{\frac{A_1^2}{2} + \frac{A_2^2}{2} + 1} \simeq 4 \times 10^{-4} \tag{5.4}$$

Thus we do not expect FEL suppression because $\rho > \sigma\gamma^{TOT}/\gamma_0$.
We consider two cases for lasing at 4 nm within the FERMI-FEL2 setup. One is EEHG lasing with n=-2, that is possible with the current first EEHG chicane (equivalent to the FEL-2 delay line), and n=-1, which would need an upgrade of the delay line. For both cases we keep $A_1 = 3$ and $A_2 = 5$. With the Stupakov EEHG formulas we can estimate the needed dispersion strength for both cases. For the n=-1 case the first chicane is set to $R_{56}^{(1)} = 2.6$ mm and the second chicane has $R_{56}^{(2)} = 80$ µm, the dispersion strength calculated from the Stupakov formulas is tenths of micrometers higher. In the simulation it is necessary to lower down the value estimated using Stupakov formulas because also the undulator has a

dispersive effect.
For n=-2 we set the first chicane to $R_{56}^{(1)} = 1.3\,\text{mm}$ and the second dispersive strength to $R_{56}^{(2)} = 96.8\,\mu\text{m}$. In the simulation the effective $R_{56}^{(2)} = 83.8\,\mu\text{m}$ was found after a scan of $R_{56}^{(2)}$ considering that the second undulator contributes with $\sim 8\,\mu\text{m}$ and velocity bunching happens in the drift space between the modulator and the chicane. The added dispersion from the first modulator is negligible.

The resultant FEL peak power and spectra at the end of the six FERMI radiator modules is shown in Fig. 5.16. The achieved peak power is 150 MW for the n=-1 case, and 50 MW for the n=-2 case. We expect this behavior from the EEHG theory. In fact if the n parameter increases in modulus, the achievable bunching is smaller, as it is shown in Fig. 5.17 from the simulation results.

The Ming-Xie formulas adapted for pre-bunched beam are giving a gain length of $L_G = 2.1\,\text{m}$ and a saturation power of $P_{sat} = 790\,\text{MW}$. Exploiting the formulas presented in [33] (in the chapter: Seeding and Harmonic Generation in Free-Electron Lasers) it is possible to characterize the behavior of the power growth along the radiator for the two cases n=-1 and n=-2. The behavior is going to be different, as they are starting from a different initial bunching. In fact for the n=-1 case, the saturation is achieved at $\sim$ 10 gain lengths, that correspond to a total active length of 21 m. While for the n=-2 case, the saturation power is achieved at11.21 gain lengths, corresponding to a total active length of 23.5 m. Having six undulator gives 14.5 m active length, and the peak power results from the simulation are compatible with the calculated power behavior, as shown in Fig. 5.19.
The simulation results downstream the six radiator modules is showing a good contrast between seeded signal and SASE background in Fig. 5.16 and the spectra are also clean and centered at the target wavelength of 4 nm as shown in Fig. 5.18.

5.8.2 FEL lasing at 7.33 nm

The 36^{th} harmonic of the seed laser has been tuned to achieve lasing at 7.33 nm. The electron beam energy for this working point was 1.31 GeV, therefore the

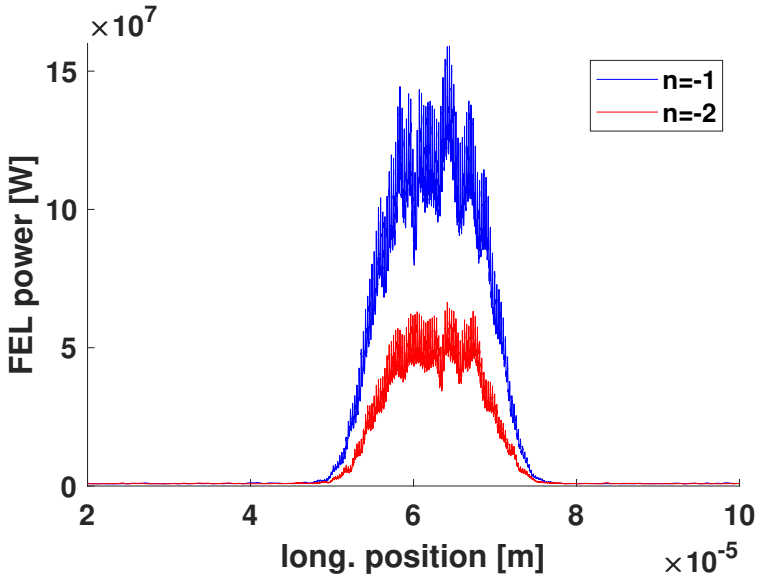

Figure (5.16) Power profiles of the FEL at 4 nm at the end of the six radiators. Two EEHG working points have been considered: n=-1 and n=-2.

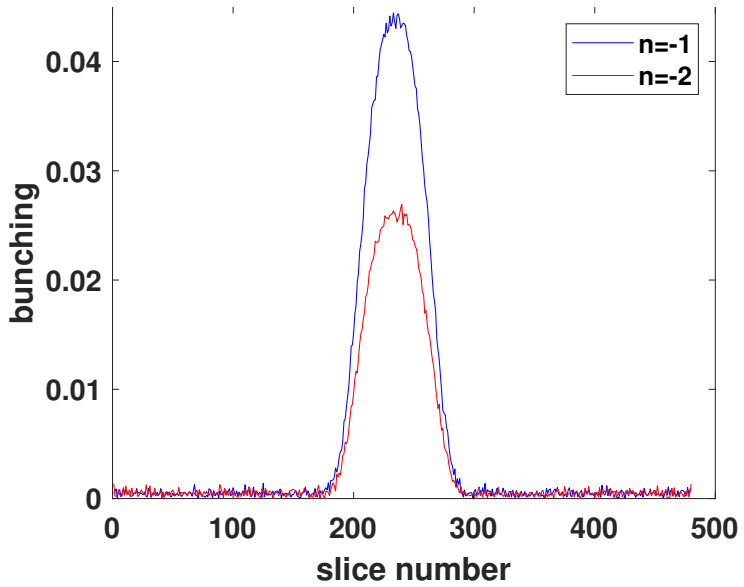

Figure (5.17) Bunching factor for EEHG lasing at 4 nm for the different working points: n=-1 (blue) and n=-2 (red).

undulator strength is set to 1.324 for the resonance condition. The chosen EEHG working point is for n=-1 as was implemented during the experiment. The chicane strengths that set in the simulation are $R_{56}^{(1)} = 2.3\,\text{mm}$ and $R_{56}^{(2)} = 67\,\mu\text{m}$, these values was estimated using the Stupakov EEHG optimization formulas. Also for this case, the energy modulation from the seed laser corresponds to $3\sigma_e$ for the

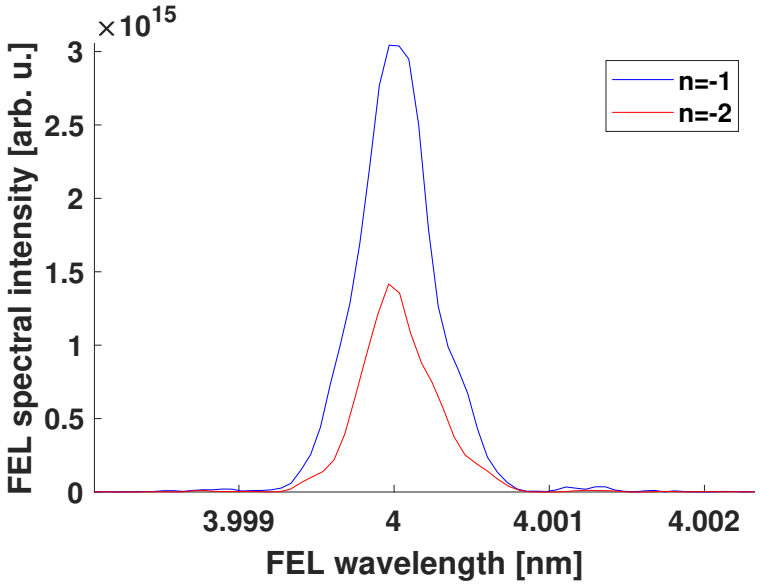

Figure (5.18) Spectra profiles of the FEL at 4 nm at the end of the six radiators.

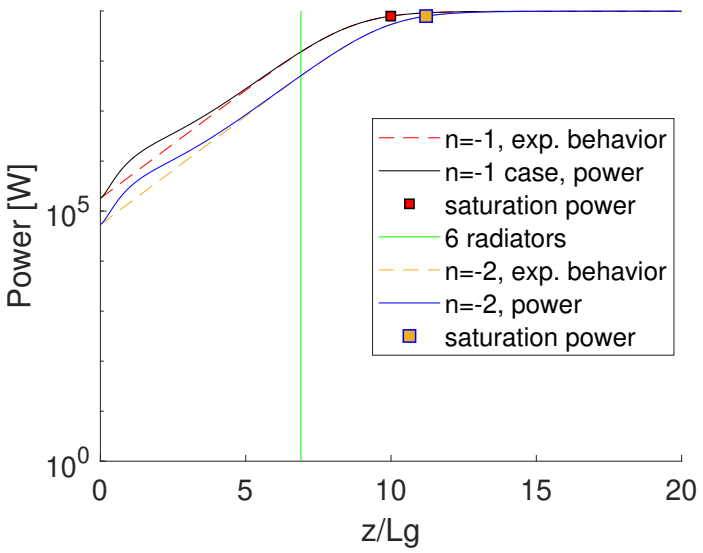

Figure (5.19) Power evolution for a pre-bunched beam in the EEHG n=-1 case (black curve) and in the n=-2 case (blue curve). A dashed line indicates the exponential growth region for both cases. The saturation power value is the same, but is achieved at different undulator lengths. The peak power results from the simulations are in agreement with the here calculated power evolution downstream the six undulator modules.

first modulator and $5\sigma_e$ for the second modulator.

With these parameters it was estimated a FEL parameter $\rho = 0.0014$ and a gain length of $L_G = 1.432\,\mathrm{m}$. Starting with a bunching of 6.7% the saturation power

is achieved at 13.3 m and it equals 1.36 GW.
The simulation has shown that with all the radiators closed to the gap giving an undulator strength of 1.324, there was no exponential growth in the sixth radiator module Fig. 5.20. By tapering the last radiator module, setting its strength to 1.320 the exponential growth can continue also in the last radiator module. This is an improvement in terms of peak power of the pulse at the end of the radiator section. In fact, the peak power doubles once the radiator is tapered compared to the untapered case and it reaches a peak power of ∼1.5 GW Fig. 5.21. In terms of spectral properties, there are not observable changes.

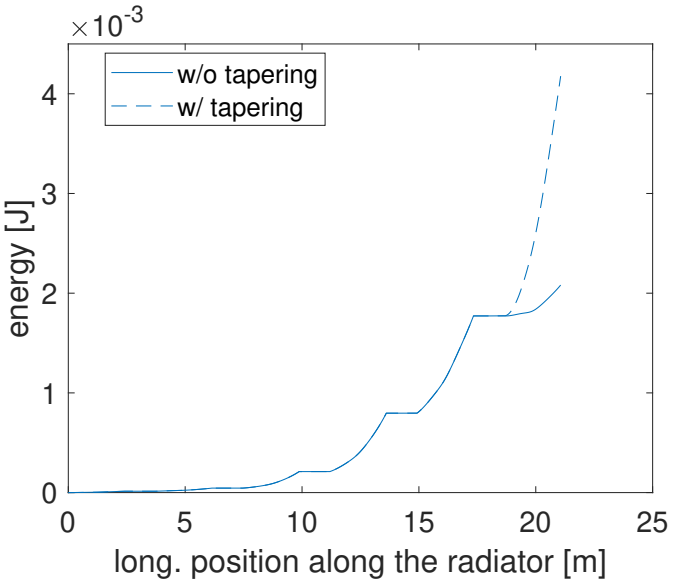

Figure (5.20) Gain curve for FEL lasing at 7.33 nm with tapering in the last radiator module and without. Tapering helps the electrons to be on resonance when they start to loose energy due to the FEL process.

5.8.3 FEL lasing at 10 nm

In this section it is presented the FEL lasing with the EEHG scheme at 10 nm that corresponds to the 26^{th} harmonic of the seed laser. The chosen EEHG working point was for n=-1 and the energy modulation from the seed laser in the first and in the second modulator was respectively: $3\sigma_e$ and $5\sigma_e$. The first chicane dispersion is set to $R_{56}^{(1)} = 2$ mm and the second one to $R_{56}^{(2)} = 68.2$ µm. With these parameters the peak value of the bunching factor at the entrance

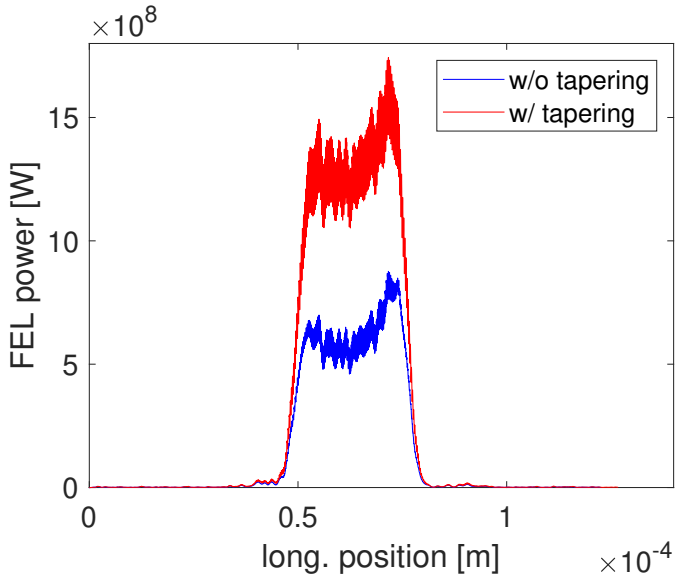

Figure (5.21) Power profiles for FEL lasing at 7.33 nm with tapering in the last radiator module (red curve) and without (blue curve). The pulses are shown at the end of the six radiator modules. Tapering doubles the output peak power.

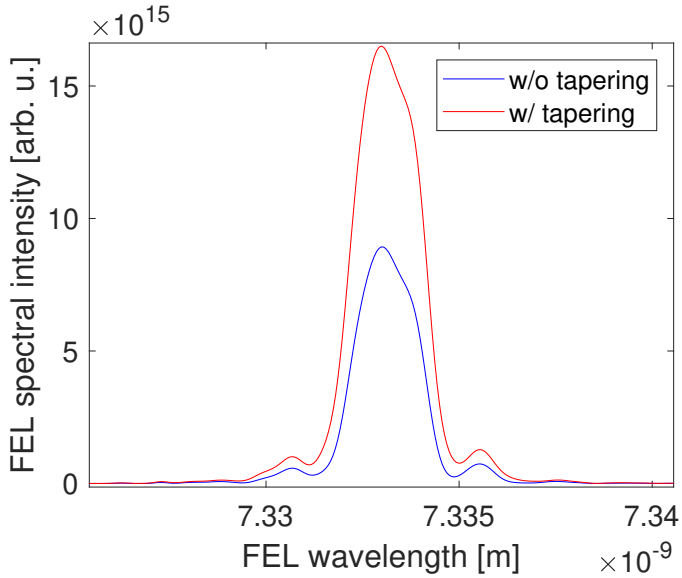

Figure (5.22) Spectra profiles for FEL lasing at 7.33 nm with tapering in the last radiator module (red curve) and without (blue curve). The pulses are shown at the end of the six radiator modules. Tapering does not affect the shape of the spectrum.

of the radiator section is 7.8%. The resonance of the undulator is satisfied for $K = 1.6773$. If all the radiator modules are set to this value, the exponential growth stops downstream the third module. Therefore, after trying out a tapering

scheme, where the fifth undulator is set to $K = 1.6733$ and the sixth module to $K = 1.6703$, it is possible to keep the exponential growth Fig. 5.23. Thanks to the tapering it is possible to achieve higher peak power (up to 3 GW) and improve the final pulse shape, as shown in Fig. 5.24. These power profiles are taken at the end of the sixth radiator. The spectra are not visibly affected from the tapering. For this working point it has been estimated a FEL parameter of $\rho = 0.0016$ and a gain length $L_G = 1.18$ m. From the estimations the saturation is foreseen between the forth and the fifth undulator and the saturation power is 1.67 GW. Therefore the plot of Fig. 5.24 shows the FEL pulse when saturation is already happened. In this case the tapering enables to extract more power out of the electron beam, respect what it is expected from the Ming-Xie estimations.

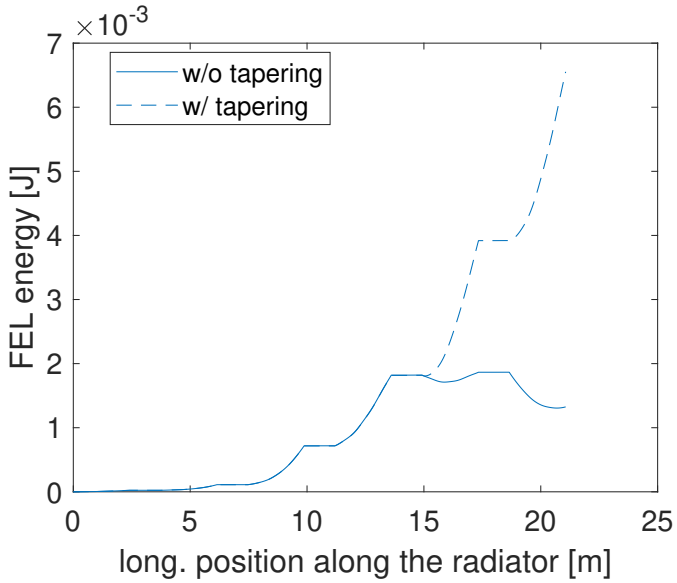

Figure (5.23) Energy gain curve for the FEL lasing at 10 nm. The dashed curve is with tapering and the solid line indicates no tapering. For this case the tapering has been applied for the fifth and sixth radiator modules. Tapering keeps the exponential growth.

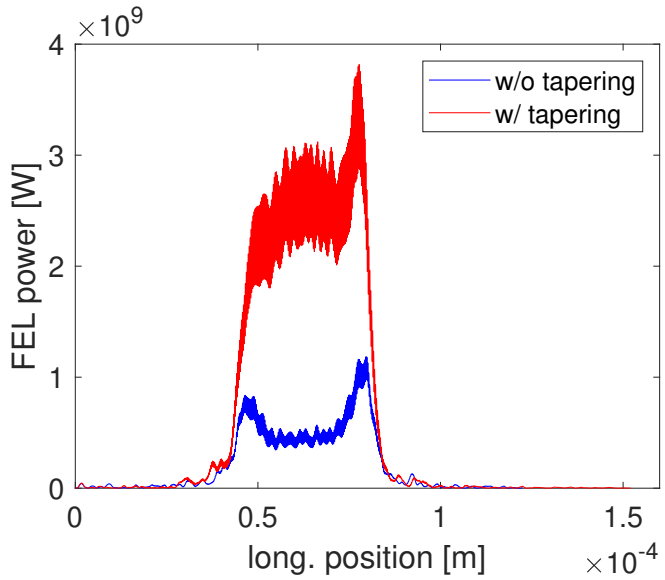

Figure (5.24) FEL power profiles downstream the sixth radiator module. The tapered case shows a profile with two peaks at the head and at the tail with an averaged peak power that is less than 1 GeV. While in the tapered case there is only a peak at the head of the pulse and the averaged peak power approaches the 3 GeV. Also in this case, tapering is beneficial.

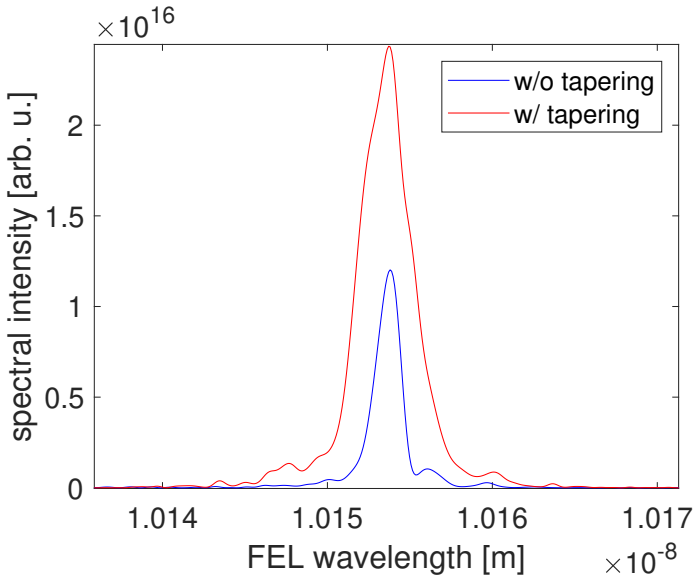

Figure (5.25) FEL spectra profiles at the end of the radiator section. The shape of the spectrum is not changing significantly in the two different cases: tapered and untapered.

Seeding upgrade at FLASH

Chapter 6

Seeding upgrade at FLASH

The existing sFLASH activity at FLASH has focused on proof of principle and studies of seeded FEL schemes as HGHG and EEHG and experiments with the generated FEL radiation (THz-streaking, XUV pulse shaper). However, the current setup is not optimized for 24/7 operation as user-facility. The insights from the sFLASH studies were exploited in the new design of the FLASH2020+ upgrade project [129], where FLASH1 will become the seeded beamline. The initial upgrade plan was presented in the framework of the DESY2030 strategy program [130], and a conceptual design report was completed in March 2019 [129]. In Fig. 6.1 the layout of the FLASH upgrade is shown.

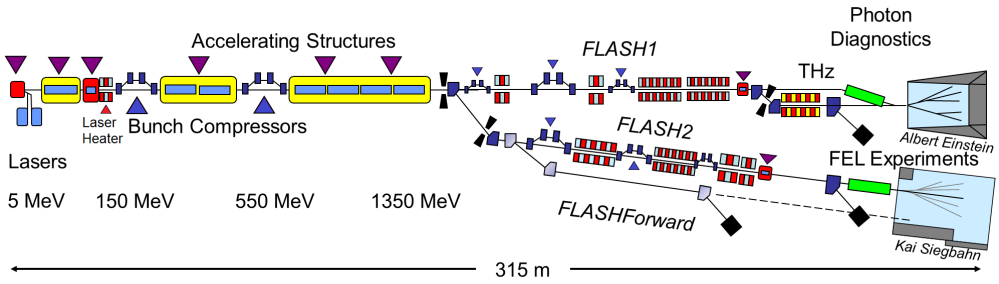

Figure (6.1) Layout for the FLASH upgrade

The modifications in the FLASH linear accelerator are targeting to an energy increase from the current 1.25 GeV to 1.35 GeV, by substituting two accelerator

modules with refurbished ones, to permit the FEL lasing at shorter wavelengths. Upstream FLASH linear accelerator a laser heater (LH) will be installed to mitigate the microbunching instability affecting the electron beam. The present first bunch compressor is going to be moved downstream to make space for the LH. The matching section downstream the first bunch compressor will be modified and shortened to allow moving the chicane while keeping its geometry. The geometry of the second bunch compressor chicane will be modified from Z-chicane to C-chicane and shortened. The section downstream the second chicane will be modified for designated quadrupole scans. Two modulators followed by one chicane are going to be installed in FLASH1 beamline to allow seeding. Also, the radiator section where now are installed fixed gap undulators will be replaced by APPLE III undulators. More details on FLASH1 beamline and the FEL wavelength range of operation is described in the next sections of this chapter. FLASH2 beamline upgrade has as target wavelengths the interval from 18 to 1.8 nm that will be achieved utilizing novel lasing schemes, for more details we suggest consulting the article [131].

6.1 Working points for FLASH1 seeded

Two working points for electron beam energy are considered for the FLASH upgrade, one at low energy and one at high energy, respectively 0.75 GeV and 1.35 GeV. FLASH1 beamline will deliver seeded FEL radiation in the wavelength range from 60 to 4 nm. The choice of the seed laser wavelength is still pending. The options under consideration are an ultraviolet (UV), and a visible (VIS) seed laser. Both are based on Optical Parameteric Chirped-Pulse Amplification (OPCPA) technology [132]. The technology under consideration for the UV option is both cascaded sum frequency generation (SFG), which would allow wavelength tunability in the range from 328 nm to 294 nm and third harmonic generation (THG), which would allow wavelengths from 300 nm to 230 nm (for a full description of these laser schemes see [129] at page 63). The VIS option enables wavelengths from 480.3 nm to 413.2 nm. The next sections aim is to understand which is the best seed laser option.

In the FLASH2020+ CDR, a HGHG scheme up to the fifteenth harmonic of the seed laser and with the EEHG scheme for higher harmonics is suggested. This

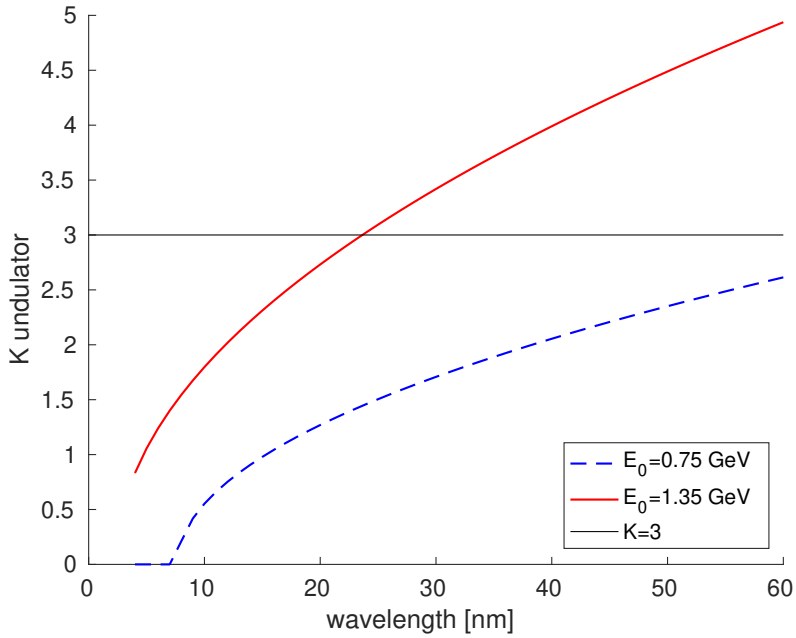

Figure (6.2) Undulator strength for the two energies considered as working point. In black the line indicating the higher K allowed.

choice follows from the physics of the two schemes, that was presented in Chapter 2 and the experience in HGHG operation for user operation gained from the HGHG-based FERMI FEL-1 beamline [14].

The energy to use at the different harmonics should be evaluated carefully by taking into consideration the undulator strength K, period length λ_u and the diameter of the vacuum pipe. The undulator strength can be estimated by the resonance condition for the helical undulator: $\lambda_{FEL} = \lambda_u \frac{1+K^2}{2\gamma^2}$ from which we derive $K(\lambda_{FEL}) = \sqrt{2\gamma^2 \frac{\lambda_{FEL}}{\lambda_u} - 1}$. Figure 6.2 shows the undulator strength as a function of the FEL wavelength for the two energy working points. In order to have an undulator and not a wiggler we want to keep the K lower than 3, so the wavelengths from 24 to 60 nm will be delivered with an electron beam with 0.75 GeV. On the other hand, K should not be too low. Otherwise, the undulator field is not strong enough, so we exclude to operate at 0.75 GeV from 9 nm to lower wavelengths. We can use the 1.35 GeV working point to produce radiation in the range between 4 nm and 23 nm.

6.2 Design for FLASH1 seeded

The additional diagnostics for seeding respect to a SASE FEL is primarily related to the setup and the stability preservation of the overlap, both longitudinal and transverse, between the electron beam and seed laser, or lasers. Figure 6.3 shows a schematic view of the FLASH1 upgraded beamline with the designed diagnostics. For the transverse overlap, screen boxes with Ce:YAG, OTR screens are going to be placed up and downstream each modulator to localize the seed and electron beams. The steering of the seed laser beams will be performed using motorized mirrors installed in the seed laser beamline, if necessary the electron beam will be steered with dipole steerers on the wished position recognized by the BPM. At this point, it is necessary to measure the position of the electron beam respect to the seed laser in time: the seed laser radiation is extracted using a movable mirror in a chicane and detecting the signal using a photo-multiplier linked with an oscilloscope. From the same mirror, it is also possible to extract the electron beam signal coming from OTR radiation inserting in the chicane an OTR screen. Once the two pulses have been observed on the oscilloscope and the positions have been marked, it is possible to move the seed laser closer to the electron beam by using the vector modulator controlling its phase. At this point, the seed laser beam and electron beam are within a few hundredths of picoseconds. The fine overlap is achieved by closing the first modulator at resonance with the seed laser wavelength. Afterwards, the seed laser is moved in small steps ($0.5 - 1\,\mathrm{ps}$) until the energy modulation signature appears on the electron beam. A transverse deflecting cavity, followed by a dipole and an imaging screen, placed after the radiator, enables the reconstruction of the longitudinal phase space distribution of the electron beam, hence the comparison energy modulation signature.
Screen boxes and BPMs will be installed between the radiator modules as well, to reconstruct the beam size of the electron beam and the seed laser. Quadrupoles between the radiator modules will enable operation with an electron beam matched to a FODO lattice. The modulator for seeding is chosen to satisfy resonance for both UV and VIS options. It currently under discussion the possibility of starting from a simpler seed laser setup the VIS providing more laser power and then upgrade the system to UV. For this reason, we have proposed a modulator period of $\lambda_u = 82.6\,\mathrm{mm}$. The minimum modulator gap is 12 mm; this value is established by the beampipe diameter of the nearby diagnostics, typically 10 mm.

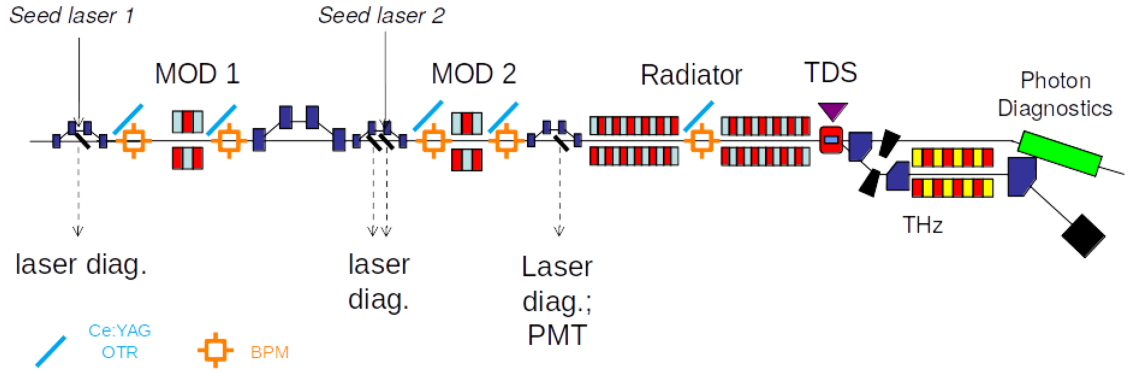

Figure (6.3) Detail of the FLASH1 upgraded beamline with diagnostics. The radiator modules shown are only two to allow to see the whole beamline, but the number of radiator modules effectively used in the simulation studies were ten in total.

With these parameters, our modulator can offer tunability in the range of wavelengths $228-487\,\text{nm}$ with an undulator strength spacing in the range $6.12-9.003$ for an electron beam energy of $1.35\,\text{GeV}$ and $3.293-4.939$ for an electron beam energy of $0.75\,\text{GeV}$. These values have been derived assuming a planar Vanadium Permandur undulator using *params.xlsx*, a tool developed by B. Faatz, described in appendix B. To decide the modulator length, we take into consideration collective effects and the needed seed laser power. In the next sections, we are going to analyze which is the optimal modulator length.

6.3 Choice of working point for EEHG

The FLASH1 beamline will produce wavelengths down to $4\,\text{nm}$. For such short wavelength, the requirements on first chicane dispersion and second seed laser power might be a limiting factor. So, in this section, we are going to present a possible method to follow for EEHG tuning.
To start with, we fix the energy spread of the electron beam to $150\,\text{keV}$. This energy spread value is a pessimistic assumption, compared to the expected one of $70\,\text{keV}$ achieved in [133]. We optimize for this energy spread for EEHG parameters such that $n=-1$, $A_1=3$ and $A_2=5$ corresponding respectively to $\Delta E_1=450.6\,\text{keV}$ and $\Delta E_2=751\,\text{keV}$. The choice of A_1 is aiming at maximizing the EEHG bunching, by keeping a moderate energy modulation on the electron

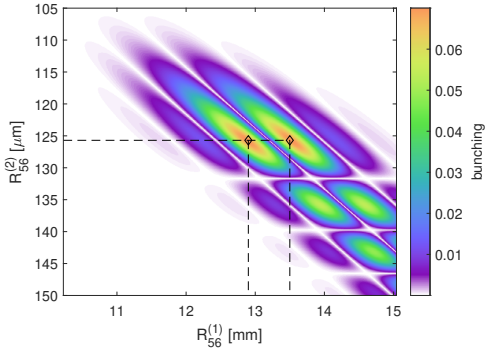

Figure (6.4) EEHG bunching map calculated for VIS seed laser with $\lambda = 420\,\text{nm}$. The target harmonic is 4 nm, that corresponds to the 105 harmonic of the VIS seed. The chosen EEHG parameters are $A_1 = 3$, $A_2 = 5$. The electron beam has an energy of 1.35 GeV and an uncorrelated energy spread of 150 keV. The dispersion strengths giving the maximum bunching are $R_{56}^{(1)} = 12.9\,\text{mm}$ or $13.5\,\text{mm}$ for the first chicane and $R_{56}^{(2)} = 125.8\,\mu\text{m}$ for the second chicane and the contribution from the second undulator.

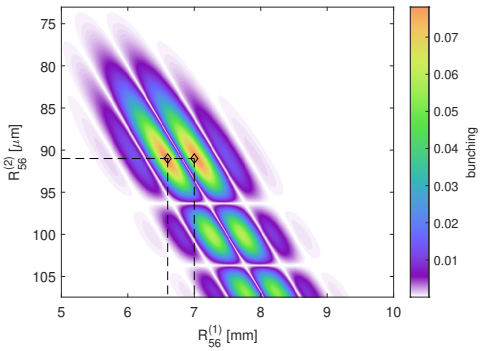

Figure (6.5) EEHG bunching map calculated for UV seed laser with $\lambda = 300\,\text{nm}$. The target harmonic is 4 nm, that corresponds to the 75 harmonic of the UV seed. The chosen EEHG parameters are $A_1 = 3$, $A_2 = 5$. The electron beam has an energy of 1.35 GeV and an uncorrelated energy spread of 150 keV. The dispersion strengths giving the maximum bunching are $R_{56}^{(1)} = 6.6\,\text{mm}$ or $7\,\text{mm}$ for the first chicane and $R_{56}^{(2)} = 91\,\mu\text{m}$ for the second chicane and the contribution from the second undulator.

beam. Figure 3.24 shows that the factor depending on A_1 of the EEHG bunching, converges asymptotically to a constant value for $A_1 \geq 3$. We decide to set $A_1 = 3$ because the bunching factor is approaching its maximum and keeping the needed seed laser power low. At this point, we calculate the bunching as a function of the chicane dispersions using the electron beam parameters in table 6.1.

Figure 6.4 shows that the chicane dispersions maximizing the bunching result $R_{56}^{(1)} = 13.5\,\text{mm}$ and $R_{56}^{(2)} = 125.8\,\mu\text{m}$. At this point, we have a complete set of EEHG parameters that are giving a determinate bunching value. Now we are going to show how the bunching is changing if the electron beam energy spread is different, keeping all other physical parameters the same. Form the EEHG bunching formula we can derive a new expression for the bunching as a function of the energy spread:

$$b_{n,m}(\sigma_E) = e^{-\frac{\eta^2\sigma_E^2}{2}} J_n(\Delta E_1 \eta) J_m(\chi) \tag{6.1}$$

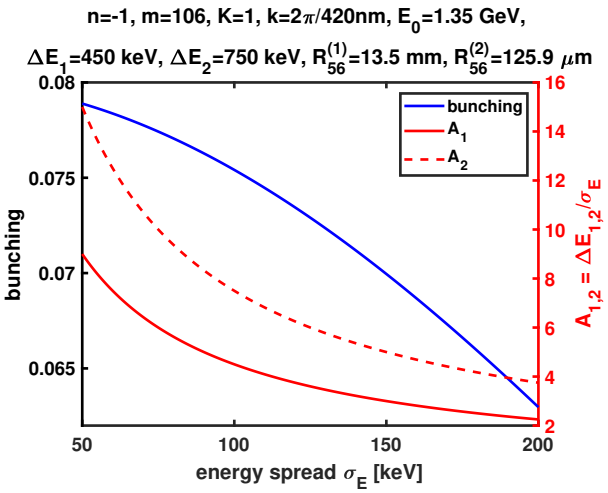

Figure (6.6) EEHG bunching as a function of the energy spread, estimated using the parameters that are optimizing the bunching at 150 keV when the electron beam is modulated with a VIS seed laser.

with $\eta = \left(|n|R_{56}^{(1)} - (Km - |n|)R_{56}^{(2)}\right) \cdot \frac{k}{E_0}$ and $\chi = (Km - |n|)\Delta E_2 \frac{k}{E_0}$. Using the parameters maximizing the bunching for the energy spread of 150 keV, the bunching as a function of the energy spread of the electron beam is presented in Fig. 6.6. This method has been checked with simulations. First, the beam with an energy spread of 150 keV has been optimized to radiate at the harmonic 105 of the VIS seed laser. In the Genesis simulation, we have set the $R_{56}^{(1)} = 13.5$ mm accordingly with theory, and we had to adjust $R_{56}^{(2)} = 111$ µm, smaller compared to the value obtained from theory (125.9 µm), because also the undulator is contributing with additional dispersion. Once this was done, we have repeated the simulation only by lowering the energy spread to 70 keV. The surprising result is that, even without the need to adjust the seed laser powers, we got already a good bunching with a peak value of 0.077. This method is beneficial to fix the requirements for seed laser powers and chicane dispersions for EEHG, without being lost in the multitude of possible working points of the EEHG scheme, that easily might fall in a region which is not allowed by the hardware. The electron beam parameters used for the following considerations are presented in the table 6.1.

The working point for EEHG under evaluation is the one giving the maximum bunching, at $n = -1$. For the two seed laser working points we need to consider a different harmonic number to achieve the 4 nm. If we assume a VIS laser with wavelength $\lambda_{VIS} = 420$ nm the 105^{th} harmonic needs to be achieved, while for a UV seed laser with wavelength $\lambda_{UV} = 300$ nm, we need the 75^{th} harmonic. The

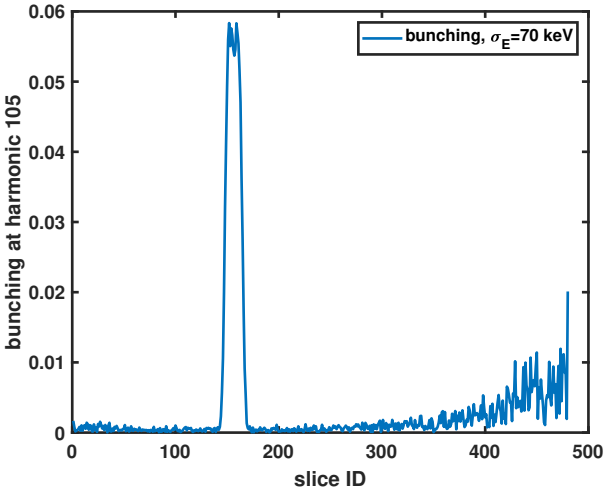

Figure (6.7) Bunching at 4 nm for a beam with energy spread of 70 keV and with EEHG parameters that are optimizing a bunch with 150 keV

Table (6.1) Electron beam parameters.

Bunch charge	400 pC
Nominal energy	1.35 GeV
Slice energy spread	150 keV
Slice transverse emittance	0.6 µm
Peak current	500 A

energy modulation induced by the seed lasers for this study $A_1 = 3$ and $A_2 = 5$ corresponding respectively to $\Delta E_1 = 450\,\text{keV}$ and $\Delta E_2 = 750\,\text{keV}$. Once the energy modulations from the seed lasers and the EEHG n parameter is fixed, it is possible to retrieve the chicane dispersive strengths that are maximizing the bunching using Eqs. (3.107) and (3.111). For the VIS seed case we are using the chicane dispersions maximizing the bunching presented in Fig. 6.4. For the UV case the corresponding bunching map is presented in Fig. 6.5, where we are going to choose as chicane dispersions: $R_{56}^{(1)} = 7\,\text{mm}$ and $R_{56}^{(2)} = 91\,\mu\text{m}$. With the given parameters, the amount of EEHG bunching foreseen from theory (Eq. 3.105) results in 7.8% for the UV seed laser and 7% for the VIS seed laser. The bunching sensibly decreases once we use the VIS seed laser because a higher harmonic is required to reach bunching at 4 nm.

The bunching factor value that we have just presented is achieved only in the case where we have precisely the parameters listed earlier in the text. In the next sections, we investigate the impact of fluctuations in the main EEHG parame-

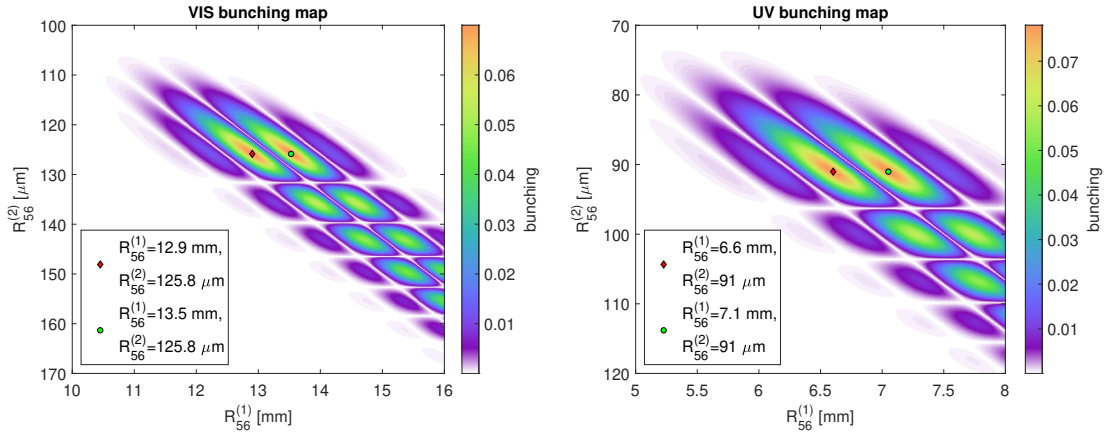

Figure (6.8) Left:EEHG Bunching map at 4 nm for a beam with energy spread of 150 keV and modulated with a UV seed laser. Right: EEHG Bunching map at 4 nm for a beam with energy spread of 150 keV and modulated with a VIS seed laser.

ters: chicane strengths and seed laser peak power. This analysis has the goal to distinguish the advantages of using either a UV or a VIS laser.

6.3.1 Chicanes for EEHG

Chicanes characteristics

For the first chicane is planned to use the so called *TDA* magnets with a magnetic length of 420 mm, maximum field 0.78 T and a gap of 40 mm. The maximum chicane dispersion at 1.35 GeV is 25 mm. The distance between inner and outer dipole is 2.153 m for a whole chicane length of minimum 5.986 m. This chicane has enough dispersion for both the UV and VIS case, which in the EEHG working point at $n = -1$ requires respectively 7 mm and 13.5 mm of R_{56}.
While the *TDB*-type magnets are going to be used for the second chicane. The TDB magnets are characterized by: magnetic length 220 mm, maximum field 0.51 T and gap of 40 mm. The maximum chicane dispersion at 1.35 GeV is 1.153 mm, corresponding to an angle of 1.43 degrees. The distance between inner and outer dipole is 780 mm for a whole chicane length of minimum 2.44 m. Also, in this case, the needed R_{56} is achieved, as we foresee a maximum dispersion below 300 µm for both the EEHG and HGHG schemes.

Tolerances on chicane dispersion

The main task of this section is to understand how the bunching is affected by chicane strength drifts from the optimal value, based on what has been studied in [63].

Usually, we estimate the needed chicane strengths using the Stupakov formulas presented in Eq. 3.111 and Fig. 6.5, from which we can derive the R_{56}s. However, these dispersion accounts not only the chicane, but also the contributions from the undulator and the drift spaces. A useful formula which gives an estimate for the contribution of the undulator R_{56} is given by [134]:

$$R_{56}^{[u]}[\mu\text{m}] = 2.61 \cdot 10^{-1} \frac{N_u \lambda_u[\text{m}]}{E^2[\text{GeV}^2]} + 3.41 \cdot 10^3 \frac{N_u \lambda_u^3[\text{m}^3] B_0^2[\text{T}^2]}{E^2[\text{GeV}^2]} \tag{6.2}$$

where N_u and λ_u are respectively the number of periods and the period length of the undulator, B_0 is the magnetic field of the undulator and E is the electron beam energy. $R_{56}^{[u]}$ should be subtracted from the Stupakov dispersion to get the needed chicane strength.

For the FLASH2020+ modulator tuned to the UV seed laser $\lambda = 300\,\text{nm}$: $N_u = 30$, $\lambda_u = 82.6\,\text{mm}$, $B_0 = 1.2923\,\text{T}$ for an electron beam energy of $1.35\,\text{GeV}$ we get $R_{56}^{[u]} = 53.2\,\mu\text{m}$. From experience from simulation, we have noticed that this amount of $R_{56}^{[u]}$ does not affect the first chicane dispersion for EEHG, as it is usually in the order of the millimeters. While, it is crucial to take into consideration $R_{56}^{[u]}$ for the second chicane, the typical value of which is $\sim 100\,\mu\text{m}$. Hence, the tolerances for the second chicane are tighter respect to the first chicane.

If we assume that the energy modulation from the seed laser is fixed at the chosen working point $A_1 = 3$, $A_2 = 5$ and we calculate the EEHG bunching for varying chicane dispersions $R_{56}^{(1),(2)}$ we obtain the bunching maps represented in Fig. 6.8. In both bunching maps, we estimate a variation in dispersion of several hundreds of micrometres for the bunching to go to zero for the first chicane dispersion while for the second dispersion strength less than ten micrometres lead to bunching suppression.

A more precise estimation on how the bunching is affected from chicane strengths variations can be derived by Taylor expanding the bunching factor for a small variation of each dispersion strength at one time [63]. By doing this, we get a

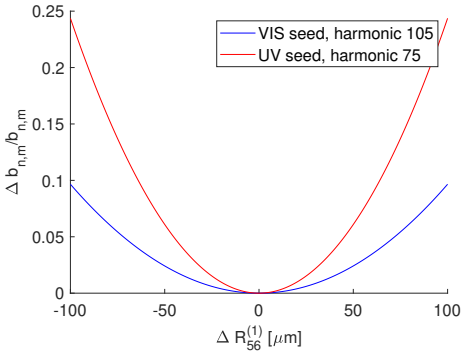

Figure (6.9) Sensitivity of the EEHG bunching on a variation of the first chicane strength.

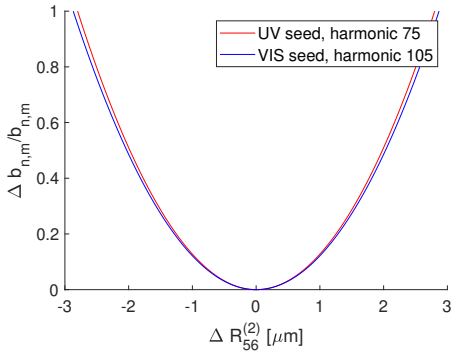

Figure (6.10) Sensitivity of the EEHG bunching on a variation of the second chicane strength.

bunching variation formula for the first chicane dispersion:

$$\frac{\Delta\bar{b}_{n,m}}{\bar{b}_{n,m}} = -\frac{(\Delta B_1)^2}{2B_1^2}\left(\frac{nB_1}{\xi_E}\right)^2 [\xi_E^2(A_1^2+\xi_E^2+2)-n^2] \tag{6.3}$$

where ξ_E is the EEHG scaling factor and it is defined as [63]:

$$\xi_E = aB - mKB_1 = nB_1 + aB_2 \tag{6.4}$$

where $B = B_1 + B_2$ and a is the harmonic number. In Fig. 6.9 is represented the impact of the variation of the first chicane strength on the bunching factor anticipated in Eq. 6.3 for the working points under consideration at 4 nm. The plot shows that the bunching is more sensitive on the first chicane dispersion when the UV seed is used. On the other side, if the second chicane dispersion is changing in some range from the value that is maximizing the bunching, Taylor expanding the bunching factor leads to the formula:

$$\frac{\Delta\bar{b}_{n,m}}{\bar{b}_{n,m}} \simeq -\frac{(\Delta B_2)^2}{2B_2^2}\left[\left(j'_{m,1}\frac{A_1}{A_2}\right)^2 [1-n^2/(j'_{n,1})^2] + [(j_{m,1})^2 - m^2]\right] \tag{6.5}$$

From the study of Eq. 6.5, for the different working points, we get a similar behaviour as the one of Eq. 6.3. Figure 6.10 shows that the bunching is extremely sensitive on how it is set the second chicane strength. If the R_{56} is 3 µm different from the optimal value, the bunching is suppressed, for both the UV and VIS case.

Degrading effects in the EEHG chicanes

In section 3.2.3 we already mentioned the degrading effects that can affect the EEHG scheme. In the chicane, the electron beam emits coherent (CSR), incoherent synchrotron radiation (ISR), and it is subject of space charge (SC) effects. These effects are heating the energy spread of the electron beam or induce distortions in the longitudinal phase space distribution. Energy spread increase might lead to smear out the typical EEHG structures in the longitudinal phase space. In preparing the electron beam for EEHG, one should watch out to maximize the energy separation between the energy bands shaped after the first chicane. The spacing is quantified by Eq. 3.136. In order to have big spacing (between energy bands), it is necessary to use a low value for the first chicane dispersion[135]. To reduce the first chicane dispersion, we have used $A_2 = 5$ that is a quite high energy modulation.
Assuming an electron beam with $\sigma_E = 150\,\mathrm{keV}$, we have estimated a spacing between energy bands for the UV case of about 28.7 keV and the VIS case 21 keV. The quantum diffusion in the bending magnets of the first chicane has been estimated using the formula presented in Eq. 3.137. That can be simplified by expressing it by [136]:

$$\Delta\sigma_E = 6.4\,\mathrm{keV}\sqrt{\frac{L[m]}{\rho[m]^3}}\,(E[GeV])^{7/2}\,. \tag{6.6}$$

Where $\rho[\mathrm{m}] = 10/2.998\beta E[\mathrm{GeV}]/B[\mathrm{T}]$ is the bending radius of the chicane. Using a chicane with dipole width $l_b = 420\,\mathrm{mm}$, projected distance between inner and outer dipoles of $l_d = 2.153\,\mathrm{m}$ and total length of $L = 6.146\,\mathrm{m}$, we got a energy spread increase in the bends equivalent to 1.285 keV for the UV case with an $R_{56} = 7.1\,\mathrm{mm}$ and 2.102 keV for the VIS case with an $R_{56} = 13.5\,\mathrm{mm}$. The effect of ISR on the energy spread smearing is negligible, this also thanks to the quite long distance between chicane dipoles, so the the bending radius increases. While for the second chicane the energy spread increase due to ISR is negligible.

In the paper [69], it has been done an analytical study, including CSR. Here the author concludes that the CSR in the first two dipoles in the first EEHG chicane is not relevant for EEHG, because the longitudinal phase space distribution has

not yet developed the energy bands (that are originating from the strong chicane dispersion). Therefore, it is enough to study the effect of CSR in only the two last dipoles. In Eq. 3.140 it is given the maximum R_{56} allowed for a definite chicane geometry to prevent CSR. Assuming a bunch with a Gaussian current profile peaked at 500 A, with a bunch length (RMS) $\sigma_z = 95.7\,\mu$m which gives a total bunch charge of 0.4 nC. Assuming the chicane design used so far: $L_D = 2.153$ m and $L_m = 420$ mm. Taking the electron beam with energy $E = 1.35$ GeV, we estimate for the VIS case $\lambda_{seed} = 420$ nm: $R^{(1)}_{56,MAX} = 2.3$ mm. While for the UV case $\lambda_{seed} = 300$ nm, $R^{(1)}_{56,MAX} = 1.8$ mm. $R^{(1)}_{56,MAX}$ is below the needed chicane strengths: $R^{(1)}_{56} = 13.5$ mm for the VIS case and $R^{(1)}_{56} = 7$ mm for the UV case. The needed dispersions are beyond the maximum allowed value calculated. However the formula for $R^{(1)}_{56,MAX}$ given in Eq. 3.140 is calculated for a beam which satisfies the following condition:

$$\frac{R}{\gamma^3} \ll \sigma_z \ll \frac{R\theta^3}{24} \tag{6.7}$$

where R is the bending radius and θ is the bending angle. For the UV case (VIS case) we get $R/\gamma^3 \sim 6$ Å ($R/\gamma^3 \sim 4$ Å) and $R\theta^3/24 \sim 5$ nm ($R\theta^3/24 \sim 9$ nm), so a $\sigma_z = 95.7\,\mu$m does not satisfies the given relation. We conclude that numerical simulations are necessary to prove the feasibility of the 4 nm case at the n=-1 point.

6.3.2 Tolerances on seed lasers

The seed lasers can affect the EEHG process in many aspects. The seed laser itself is a complex system consisting of a high power pump laser and nonlinear frequency conversion setups in order to provide powerful and wavelength tunable ultra-short laser pules in the relevant spectral range. In addition, the laser beam transport to the modulator as well as the in-coupling to the accelerator vacuum drives to energy losses up to 50%. Moreover, there might be sources of instabilities for the seed laser that can lead to power fluctuations. The seed laser quality in terms of the transverse and longitudinal profile as well as the energy and wavelength stability are of determinant importance for the EEHG performance. These issues are addressed to the next subsections.

Fluctuation in seed laser power

To analyze the effect of seed laser power fluctuations on the electron beam bunching, we follow the treatment of [63].
For this study we recall the definition of the EEHG parameter A:

$$A_{1,2} = \frac{\Delta E_{1,2}}{\sigma_E} \tag{6.8}$$

where σ_E is the uncorrelated energy spread of the electron beam and $\Delta E_{1,2}$ is the resulting energy modulation imprinted on the electron beam at the end of the modulator from either the first or the second EEHG seed laser. If the EEHG bunching factor (defined previously in Eq. 3.105) is Taylor expanded for a small variation of A_1 parameter, we get the following equation:

$$\frac{\Delta \bar{b}_{n,m}}{\bar{b}_{n,m}} = \xi_E^2 \frac{\Delta A_1}{A_1} - \frac{(\Delta A_1)^2}{2A_1^2}[\xi_E^2(1 + A_1^2) - n^2] \tag{6.9}$$

Considering that around the maximum of the EEHG bunching $|\xi_E \sim 1/2|$, in our case we have for the VIS case $|\xi_E| = 0.48$ and for the UV case $|\xi_E| = 0.41$, so we can neglect the terms multiplied by $|\xi_E|$ squared. As a result, we observe that the bunching deviation depends on the n parameter and, neither on the specific seed laser wavelength nor to the target FEL harmonic. In particular, by increasing the n parameter, the bunching is more sensitive to variations of A_1.
In EEHG, the first seed laser does not influence the bunching and the FEL properties because its modulation is smeared out in the first chicane. While the second seed laser affects the electron beam and the FEL properties. Ergo, we are going to focus on the effects caused by fluctuations on the second seed laser parameters. For the second seed laser, we have a similar equation like Eq. 6.9:

$$\frac{\Delta \bar{b}_{n,m}}{\bar{b}_{n,m}} = -\frac{(\Delta A_2)^2}{2A_2^2}[(j_{m,1} - m^2)] \tag{6.10}$$

For this tolerance study, we start from the parameter set giving the maximum bunching with the wished A_2 parameter. Then, we scan the A_2 parameter by changing the second seed laser power, keeping all the other parameters unchanged. In Fig. 6.11, the two seed lasers performances are compared: the UV case at the top and the VIS case at the bottom. Here, the bunching variation is represented as a function of the A_2 parameter variation from the optimal value $A_2 = 5$:

$\Delta A_2 = 5 - A_2$. The bunching $\tilde{b_{n,m}}$ and $b_{n,m}$ are the bunching value at the longitudinal position of the electron beam where we have the maximum energy spread at the radiator entrance. The black parabola is the representation of Eq. 6.10: as expected, the parabola for the UV case is wider compared to the VIS case because of the lower target harmonic. The simulation points overestimate this theory curve in both UV and VIS cases. As a result, in order to quantify the sensitivity of the bunching to A_2 variation in the two different cases, we focus on the region where $\Delta A_2/A_2 \leq 0$ and we have fit with a line (red curve): $\frac{\Delta b_{n,m}}{b_{n,m}} = c_1 \frac{\Delta A_2}{A_2} + c_2$. For $\Delta A_2/A_2 \geq 0$ the seed laser power is too high, and the generated FEL results in a double horn power profile shown in Fig. 6.12 (third plot on the right). Thus, we do not consider these points for the fit.

The outcome of the linear fit gives a steepness of $c_1 = (8.7 \pm 0.8)$ for the UV case and $c_1 = (10.3 \pm 0.8)$ for the VIS case. Accordingly, the VIS fluctuation in A_2 parameter - so in second seed laser power - affects slightly more the bunching compared to the UV case. As a result, from this study we conclude that the UV seed does not significantly improve the stability.

Figure 6.12 shows in the top plots the FEL power and in the bottom plot the corresponding spectra both are taken at the position into the radiator were the signal to noise ratio is maximized for three different working points of the tolerance scan: $A_2 = 4.75$, 5 and 5.25. Theoretical considerations [63] show that the bunching deviation induced by deviation from the chosen A_2 parameter depends on the harmonic number m. Therefore, it could be a selection criterion for the seed laser wavelength to use in our design.

The simulations have shown consistency with the theory: the VIS case is slightly more sensitive on bunching due to seed laser power variations in the second modulator, compared to the UV case. Fluctuations in the bunching factor are transferred to FEL power fluctuations.

This study is not sufficient to make a final decision on the seed laser wavelength to use.

Though, at higher harmonics, the physics of EEHG becomes more challenging. In fact, with a VIS seed laser, we need to go down to higher harmonics compared to UV to achieve the same FEL wavelength. Nevertheless, from the laser technology point of view, the VIS seed laser is more stable and more comfortable to control compared to the UV. Thus, it would be easier to keep the power stability.

In conclusion, further studies with a realistic seed laser pulse are foreseen to evaluate the impact of transverse imperfection in the beam.

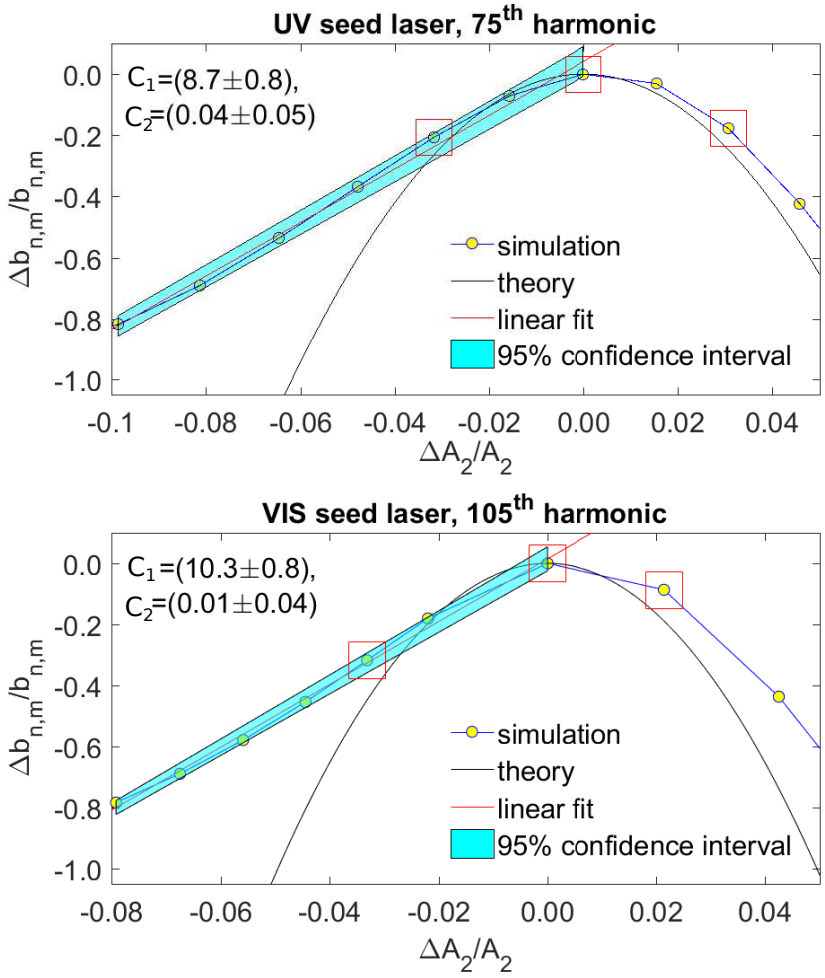

Figure (6.11) Comparison of relative bunching deviation as a function of the relative deviation in A_2 factor between VIS and UV seed laser. The red boxes indicated the simulation points selected for Fig. 6.12.

6.3.3 Considerations on issues affecting EEHG

The fine structures in the longitudinal phase space distribution of the electron beam are determining the current distribution of the electrons and thus the amount of bunching at the different harmonics. So it is crucial to keep these structures in the passage of the electron bunch trough the different sections of the EEHG scheme. The possible effects that might be an issue are the incoherent synchrotron radiation (ISR) coming from modulator and chicane dipoles. Coherent synchrotron radiation (CSR) in the chicanes should also be taken into considera-

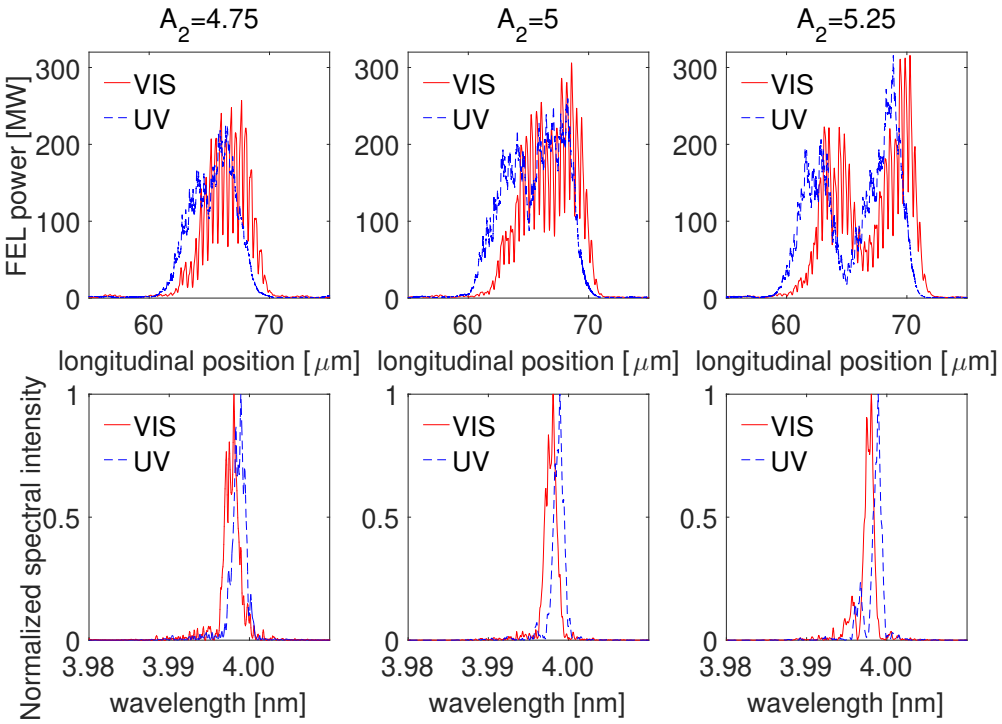

Figure (6.12) Performance of FEL power as seed laser power is changed for both UV and VIS seed lasers.

tion.

Quantum diffusion

Quantum diffusion refers to the ISR that the electron beam radiates as it passes through both undulators and dipoles. The energy of the emitted synchrotron radiation changes randomly leading to an increase of the energy spread of the electron beam. ISR might become an issue for the fine structures that are generated on the longitudinal phase space distribution of the electron beam after passing through the first chicane. So in the following, we are going to estimate the energy spread increase due to ISR from the second modulator [137].

The energy spread increase given from the second planar modulator can be estimated with [138]:

$$(\Delta\gamma)^2 = \frac{7}{15}\frac{\hbar}{m_0 c} L_u r_e \gamma^4 \kappa_u^3 K F(K) \tag{6.11}$$

where $\lambda\!\!\!^{-}_c = \frac{\hbar}{m_0 c}$ is the reduced Compton wavelength, L_u is the undulator length that is our case is 2.478 m, r_e is the classical radius of the electron, γ is the electron beam energy, $\kappa_u = 2\pi/\lambda_u$ and λ_u is the undulator period, that we assumed to be 82.6 mm, K is the undulator parameter and $F(K)$ is a function that can be approximated to $F(K) \approx 1.42K$ for $K >> 1$. In the UV case we have $K = 9.970$ and for the VIS $K = 11.830$. The energy modulation induced by the ISR from the modulator is 0.997 keV for the UV case and 1.183 keV for the VIS case. In both cases, the increase in energy spread is not significant for the overall process. With the GENESIS simulations, it is possible to take ISR into account by exploiting the list *sponrad*, which enables the electrons to lose energy and consequently increase their energy spread. We checked for significant effects between a simulation where this list was enabled and where it was not enabled. No significant energy spread increase has been noticed after the comparison of the simulation outcomes.

6.3.4 Start to end simulations

The start-to-end simulation was performed in collaboration with J. Zemella, who has performed the LINAC simulation part with the tracking code Xtrack [139] by taking into consideration the collective effects and instabilities as coherent synchrotron radiation (CSR), incoherent synchrotron radiation (ISR) and wakefields. In the following, we present the EEHG FEL radiation generated using the beam from J. Zemella along the beamline designed for FLASH1 within the FLASH2020+ project.

Beam used for simulation

In Figs. 6.13 to 6.15 we show the main properties of the beam that we get at the end of the LINAC. These properties are reported in Table 6.2.

From Figure 6.13 we can estimate the electron beam energy chirp:

$$h = \frac{1}{E_0}\frac{\Delta E}{\Delta z} = -37\,\mathrm{m}^{-1} \tag{6.12}$$

Table (6.2) Electron beam parameters.

Bunch charge	250 pC
Nominal energy	1.35 GeV
Slice energy spread	70 keV
Slice transverse emittance	0.6 µm
Peak current	500 A

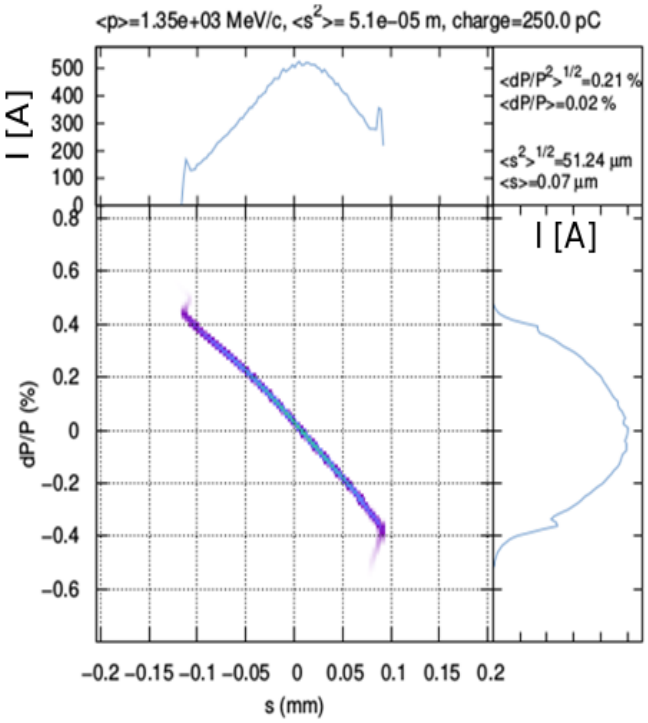

Figure (6.13) Longitudinal phase space of the electron beam. On top is shown the current profile with a peak current of 500 A. The energy distribution is shown on the right. The phase space shows a visible energy chirp on the electron beam.

We have loaded this beam to GENESIS4 and, a one-for-one simulation has been performed. As an initial proof of principle, we have tuned the FEL in EEHG mode at 10 nm as working with a realistic chirped beam is more challenging as we are going to explain in the next sections.

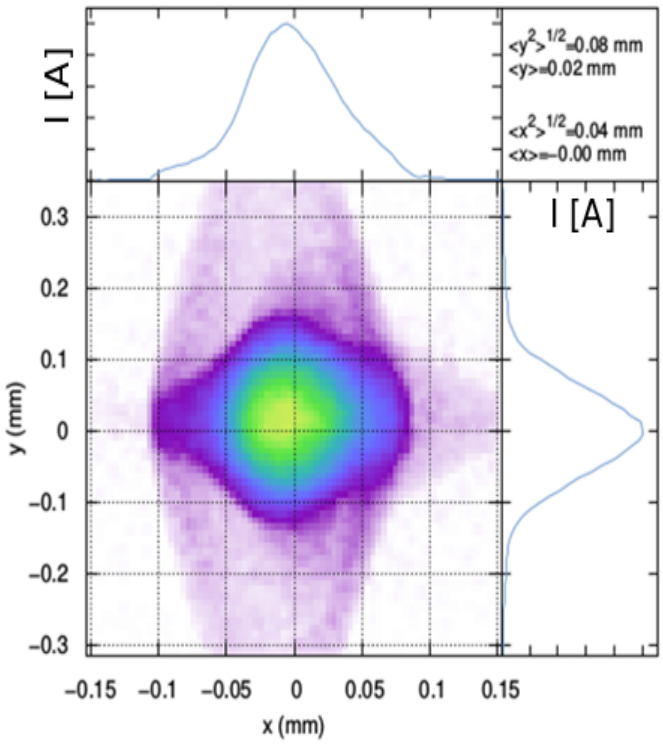

Figure (6.14) Transverse beamsize of the electron beam, how we would see the electron beam on a screen.

EEHG at 10 nm with a S2E beam

The aim of performing a FEL simulation with an electron beam simulated from the FLASH linac was to demonstrate the EEHG lasing with a more realistic beam. We have performed an optimization for the two cases considered so far: UV and VIS seed laser.

The EEHG parameters chosen for the seed laser modulation are the same for the two cases: $A_1 = 3$, $A_2 = 5$. For the UV case we have maximized the bunching at the $n = -1$ working point, so the dispersion used are: $R_{56}^{(1)} = 5.1\,\text{mm}$ and $R_{56}^{(2)} = 183\,\mu\text{m}$. Once optimized for these parameters, we have achieved bunching at a slightly higher harmonic of the seed laser (32). Nevertheless, the peak power achieved in the UV case at the saturation length is comparable with the one predicted with Ming-Xie estimation adapted for pre-bunched beams [33].

In the Figs. Figs. 6.16 to 6.18 the simulation with the S2E beam is compared with the one done by using a beam internally generated by GENESIS, denoted as ideal beam for the UV case. These results are in agreement. For the VIS seed case

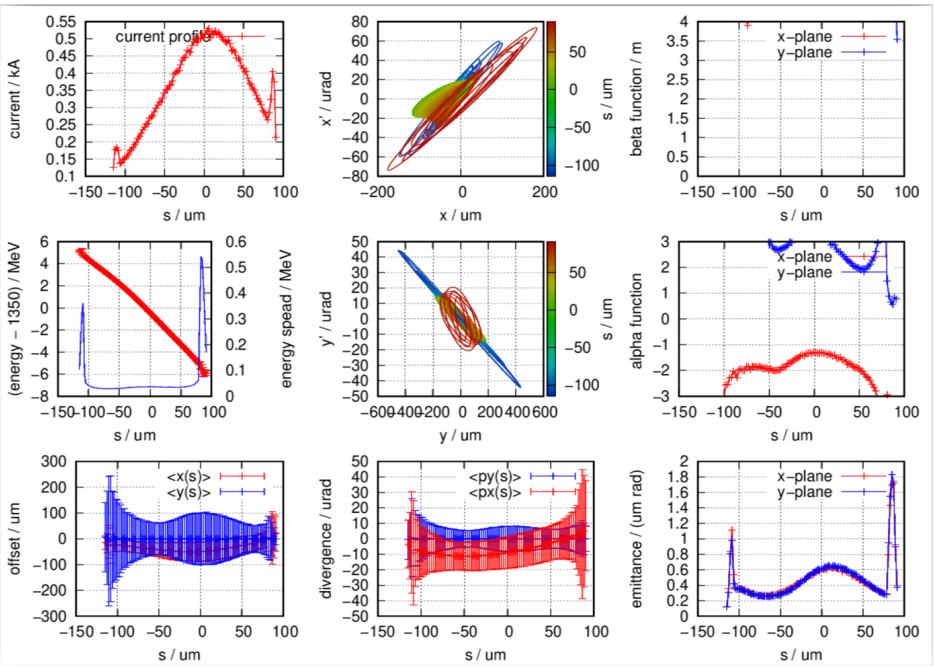

Figure (6.15) Main properties of the electron beam are shown here. Of particular interest are: current profile (top left), energy spread and energy profile (centre left), transverse phase spaces (middle up plots) and emittance profile (bottom right).

initially we have tuned for the $n = -1$ case, where the foreseen chicane dispersions where: $R_{56}^{(1)} = 9.7\,\text{mm}$ and $R_{56}^{(2)} = 251\,\mu\text{m}$. However, as the electron beam has an energy chirp, the high dispersion of the first chicane compresses it significantly. Thus the seed laser modulation is not effective; as a result, the bunching is not achieved. The unsuccessful tuning of EEHG with the VIS seed laser already for lasing at 10 nm drives us to suggest the UV seed laser as preferred option. Taking also into consideration the deep interest of the scientific community to achieve wavelength of the order of 4 nm and below.

The use of a UV seed laser is advantageous respect the use of a VIS seed laser also because the needed harmonic and the chicane strength needed for the fist chicane are lower.

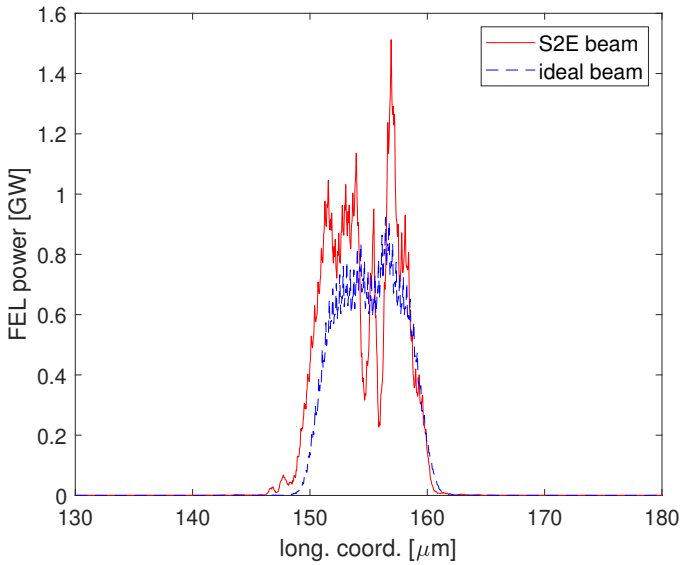

Figure (6.16) FEL power profile after 10 m from the start of the radiator section.

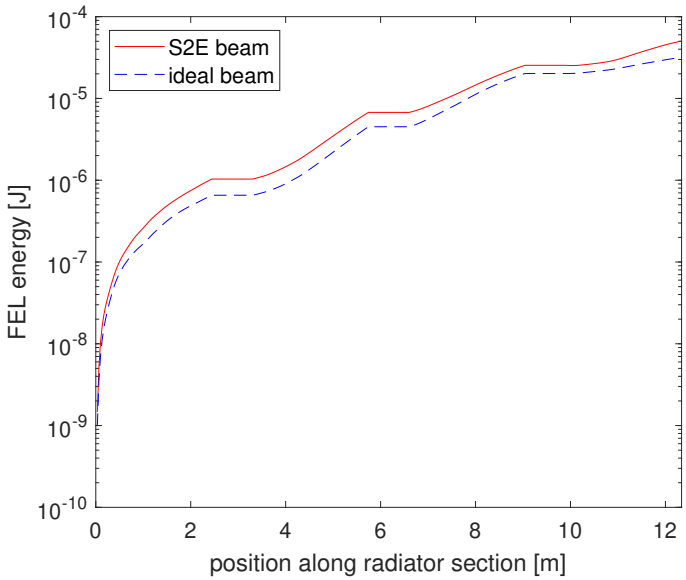

Figure (6.17) FEL gain curve along the radiator in logarithmic scale for ideal beam and the S2E simulations are shown.

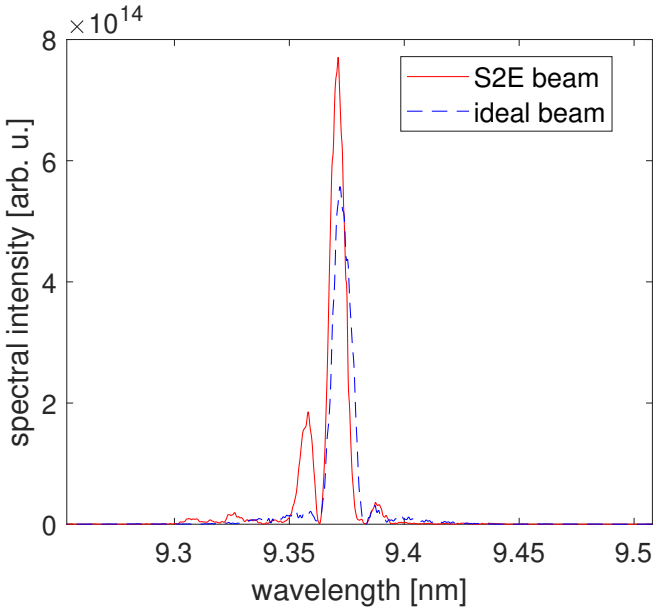

Figure (6.18) FEL spectrum profile after 10 m from the start of the radiator section.

6.4 Consideration on undulator used as modulator for seeding

So far, we were doing all the considerations using as a first and second modulator an undulator with a number of periods $N_u = 30$ and undulator period length $\lambda_u = 82.6\,\text{mm}$, corresponding to a total length of $L_u = N_u\lambda_u = 2.478\,\text{mm}$.
Taking a minimum gap for the modulator of 12 mm, we can estimate the tunability range of the modulator with the FEL Excel tool from B. Faatz (described in Appendix A). For the estimation, we have used a planar undulator hybrid with Vanadium Permandur, with a field factor of 1 and a minimum gap of 12 mm. In table 6.3 we present the outcome.
This modulator is tunable in the wavelength range, including both the seed laser options.

We want a long undulator to reduce the needed seed laser power and a high undulator strength K to maximize the energy exchange from the seed laser to the electrons, which is approximately following the relation presented in Eq. 3.3. At the same time, we want a short undulator to minimize the space charge (SC)

Table (6.3) Considerations about modulator parameters.

λ_u[mm]	82.6
N_u	30
L_u[m]	2.478
$K_{750\,\mathrm{MeV}}$	3.293-4.939
$K_{1.35\,\mathrm{GeV}}$	6.12-9.003
λ_{seed}[nm]	228-487

Table (6.4) Electron beam parameters.

λ_{seed} [nm]	s_L[µm]	s_L[fs]
300	9	30
420	12.6	42
480	14.4	48

effects and a short undulator period to reduce the ISR (see Eq. 3.138). SC and ISR can affect the EEHG phase space in particular in the second modulator, but they are not an issue in the first modulator where the phase space distribution has not fine structures yet. For this reason, it is advisable to shorten the length of the second modulator and reduce the number of undulator periods. In this way, also the slippage length is kept low. For the FLASH2020+ design, we suggest to keep the undulator presented in table 6.3 as first EEHG modulator. With these parameters, we can estimate the slippage length $s_L = N_u\lambda_{seed}$ of the seed laser respect to the electron beam. In Table 6.4 we report the calculation outcome. Here we see that using a VIS laser is a limitation in terms of slippage length, which then, impose a limit also in the minimum duration of the FEL pulse.

6.5 Comparison between EEHG and frequency doubling for the most critical point at 4 nm

Frequency doubling is an advantageous scheme for SASE when aiming at short wavelengths [140]. It consists of tuning the first undulator modules to a particular

wavelength λ and the remaining undulators to $\lambda/2$. Along the first section, the electron beam develops bunching at $\lambda/2$, without entering into the saturation regime. So, this bunching is used in the second section to lase, and the final signal at $\lambda/2$ is higher compared to the signal that we would expect if we would close the whole undulator to $\lambda/2$.

EEHG is not the same as SASE because the electron beam enters the radiator with already a bunched structure. Figure 6.19 shows the bunching map for $\lambda \approx 8\,\text{nm}$, the black diamonds in the figure show the optimized chicane parameters that we should use to maximize the bunching. We observe that the parameters that optimize the λ at the working point $n = -1$ (Fig. 6.19), are optimizing the frequency-doubled harmonic $\lambda/2 \approx 4\,\text{nm}$ at the working point $n = -2$, as shown in Fig. 6.20. Therefore, in the case of EEHG, optimizing first for λ to get $\lambda/2$ corresponds to optimize directly $\lambda/2$ for the $n = -2$ EEHG working point, which gives a lower bunching value compared to directly optimize for $\lambda/2$ at the $n = -1$ working point.

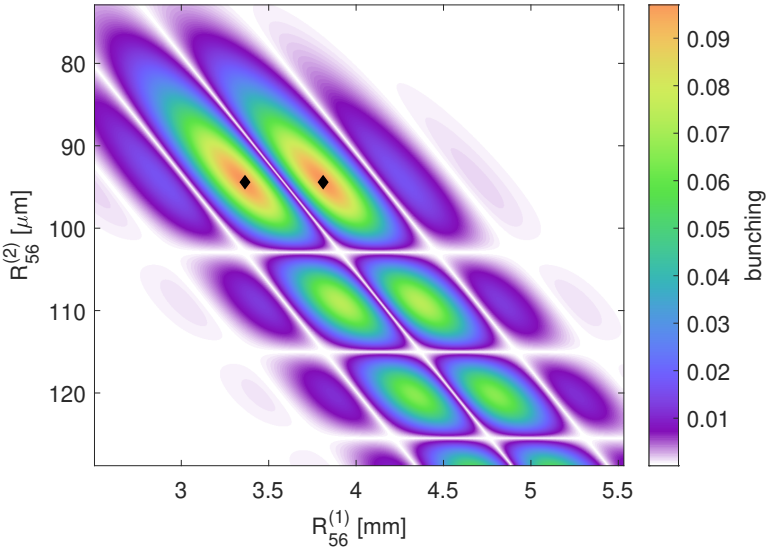

Figure (6.19) Bunching map at $n = -1$ for the harmonic 38 of the 300 nm seed laser, corresponding to a FEL wavelength of 7.89 nm. The electron beam energy is 1.35 GeV and its energy spread is 150 keV. The EEHG parameters are $A_1 = 3$ and $A_2 = 5$. The optimal dispersions of the first and second section result respectively: 3.36 mm or 3.81 mm and 94 µm.

In the following subsection, we are going to present the results achieved with

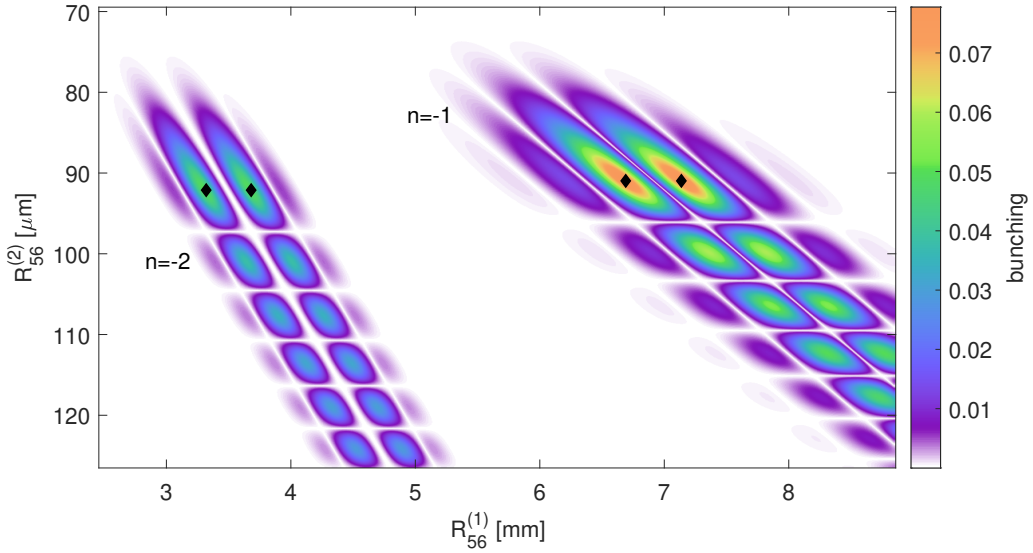

Figure (6.20) Bunching maps at the $n = -1$ and $n = -2$ for the harmonic 76 of the 300 nm seed laser, corresponding to a FEL wavelength of 3.95 nm. The electron beam parameters and $A_{1,2}$ are the same as Fig. 6.19. The parameters that are optimizing the $n = -2$ working point are 3.36 mm or 3.81 mm for the first dispersion section and 94 µm for the second dispersion section.

the frequency doubling. We compare the results obtained by the use of the two considered seed laser wavelengths: 300 nm (UV) and 420 nm (VIS). With these simulations we want to show that exploiting frequency doubling is not an advantage in the case of an EEHG FEL. Therefore, we have decided to tune the final FEL wavelength to 5 nm to take advantage of the simulations already tuned for proper EEHG at 10 nm presented in the previous sections in this chapter.
The bunching maps referring to the simulation cases are shown in Figs. 6.21 to 6.24. To achieve FEL lasing using the UV seed laser we have first to tune EEHG to the 30^{th} harmonic. Choosing the EEHG parameters $n = -1$, $m = 31$, $A_1 = 3$ and $A_2 = 5$, we get the bunching map shown in Fig. 6.21, which shows that the bunching is maximized for $R_{56}^{(1)} = 2.65$ mm or 3.1 mm and $R_{56}^{(2)} = 96$ µm. The maximum bunching $b_{m=31,n=-1} =\sim 0.1$. The expected bunching at 5 nm, hence the 60^{th} harmonic, is ~ 0.03 at the beginning of the radiator section as shown in Fig. 6.22. In fact, the chicane parameters chosen to generate the 30^{th} harmonic are lying within the higher lobes for the $n = -2$ point of the 60^{th} harmonic. The optimal $R_{56}^{(1,2)}$ indicated in the legend are not matching exactly between the cases: $n = -1$, 30^{th} harmonic and $n = -2$, 60^{th} harmonic, because the formula used to estimate them is only an approximation.

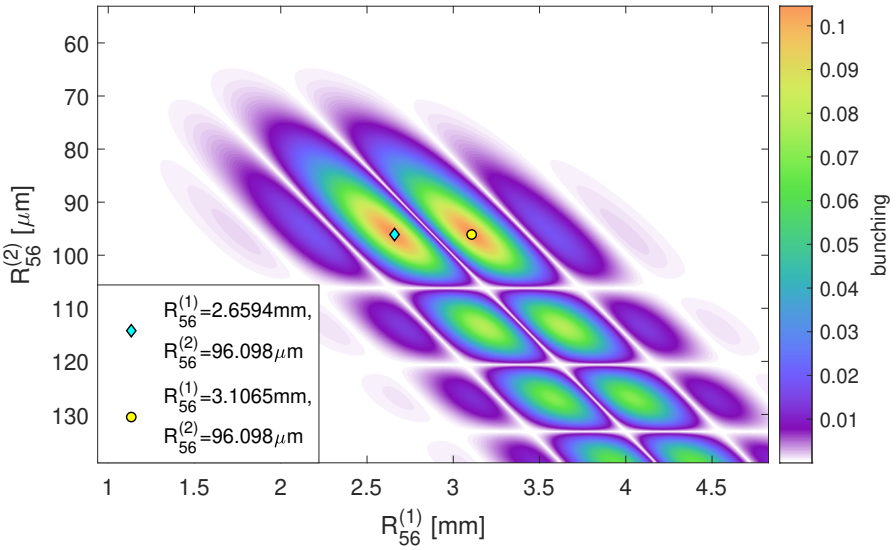

Figure (6.21) Bunching map at $n = -1$ for the harmonic 30 of the 300 nm seed laser (UV), corresponding to a FEL wavelength of 10 nm. The electron beam energy is 1.35 GeV and its energy spread is 150 keV. The EEHG parameters are $A_1 = 3$ and $A_2 = 5$. The optimal dispersions of the first and second section result respectively: 2.65 mm or 3.1 mm and 96 µm.

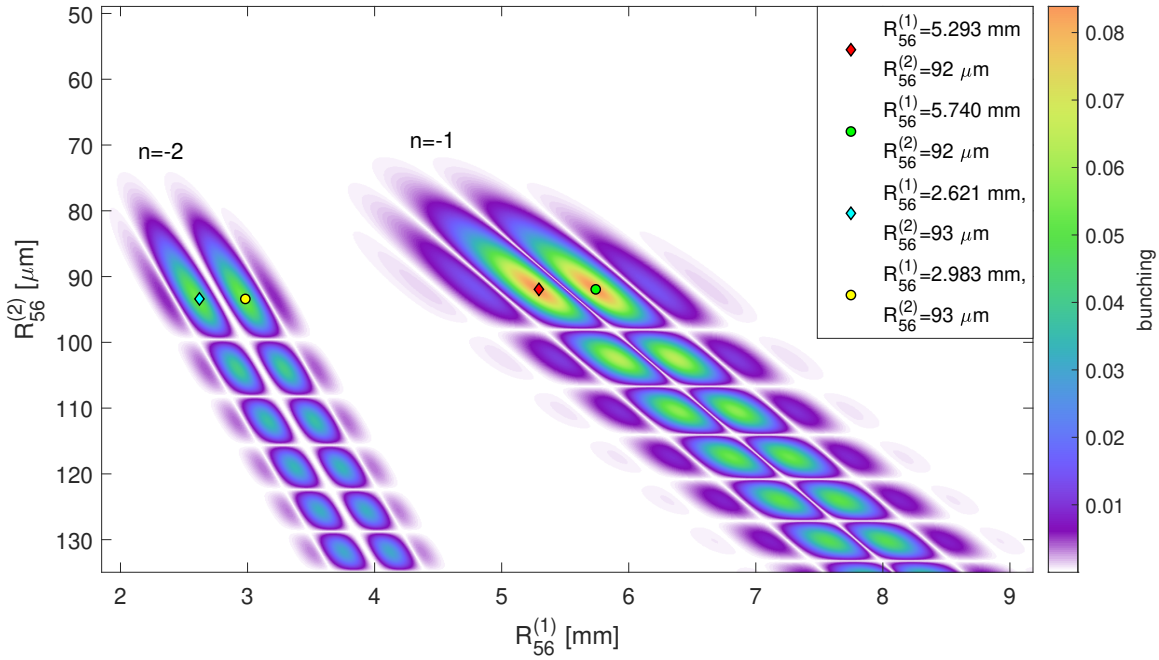

Figure (6.22) Bunching maps at the $n = -1$ and $n = -2$ for the harmonic 60 of the 300 nm seed laser (UV), corresponding to a FEL wavelength of 5 nm. The electron beam parameters and $A_{1,2}$ are the same as Fig. 6.21. The parameters that are optimizing the $n = -2$ working point are 2.62 mm or 2.98 mm for the first dispersion section and 93 µm for the second dispersion section.

Similarly, we present the working point chosen for the case in which a VIS seed laser is used. In this case, we need to tune to the 42^{nd} harmonic first to get the 10 nm FEL radiation. The EEHG parameters chosen to find the optimal chicane diseprsion are: $n = -1$, $m = 43$, $A_1 = 3$ and $A_2 = 5$. Figure 6.23 shows the resulting bunching map. Here the bunching is maximized for $R_{56}^{(1)} = 5.2$ mm or 5.8 mm and $R_{56}^{(2)} = 131$ µm. With these parameters, the expected bunching of the frequency doubled wavelength (harmoni 84) at the entrance of the radiator is shown in Fig. 6.24. Also in this case, we have bunching for the frequency doubled harmonic at the EEHG $n = -2$ working point and the bunching value is ~ 0.02.

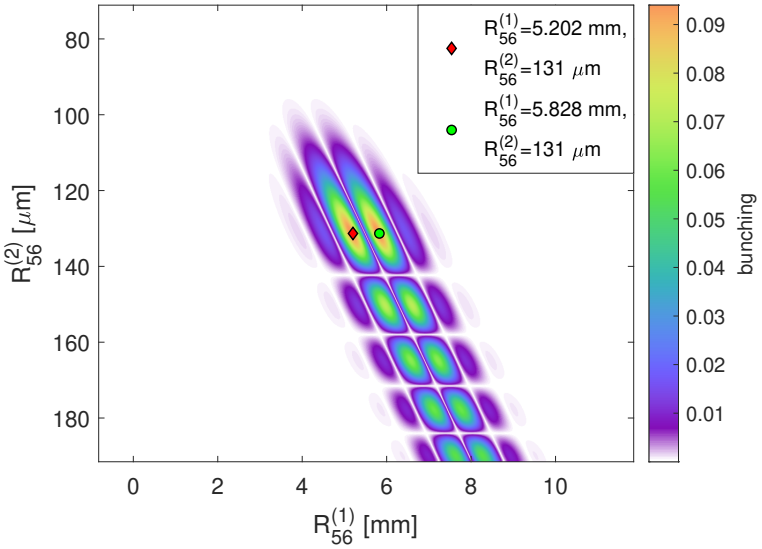

Figure (6.23) Bunching map at $n = -1$ for the harmonic 42 of the 420 nm seed laser (VIS), corresponding to a FEL wavelength of 10 nm. The electron beam energy is 1.35 GeV and its energy spread is 150 keV. The EEHG parameters are $A_1 = 3$ and $A_2 = 5$. The optimal dispersions of the first and second section result respectively: 5.2 mm or 5.8 mm and 131 µm.

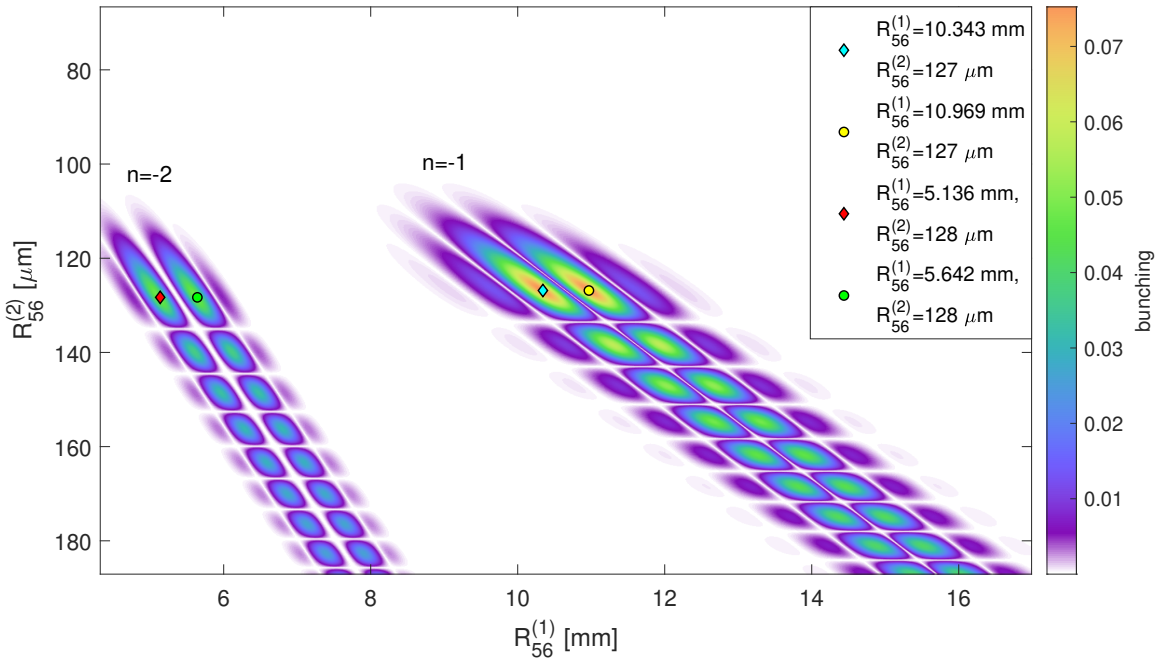

Figure (6.24) Bunching maps at the $n = -1$ and $n = -2$ for the harmonic 84 of the 420 nm seed laser (VIS), corresponding to a FEL wavelength of 5 nm. The electron beam parameters and $A_{1,2}$ are the same as Fig. 6.23. The parameters that are optimizing the $n = -2$ working point are 5.1 mm or 5.6 mm for the first dispersion section and 128 µm for the second dispersion section.

6.5.1 Simulation outcomes

After proper tuning of the chicanes to the parameters calculated from the bunching maps, we have verified if the bunching achieved in the simulations is in agreement with the bunching calculated using theory formulas. Figure 6.25 shows the bunching content of the electron beam energy-modulated by the UV seed laser. We observe the presence of bunching at the harmonics of our interest 30 and 60 and also bunching at higher harmonic. To get a better insight into the harmonics of interest, in Fig. 6.26 we show the bunching profiles for the 30^{th} and the 60^{th} harmonic. The bunching at the 30^{th} is ~ 0.09 and the bunching at the 60^{th} harmonic is ~ 0.03, these values are fairly reproducing the expected theory values shown in Figs. 6.21 and 6.22.

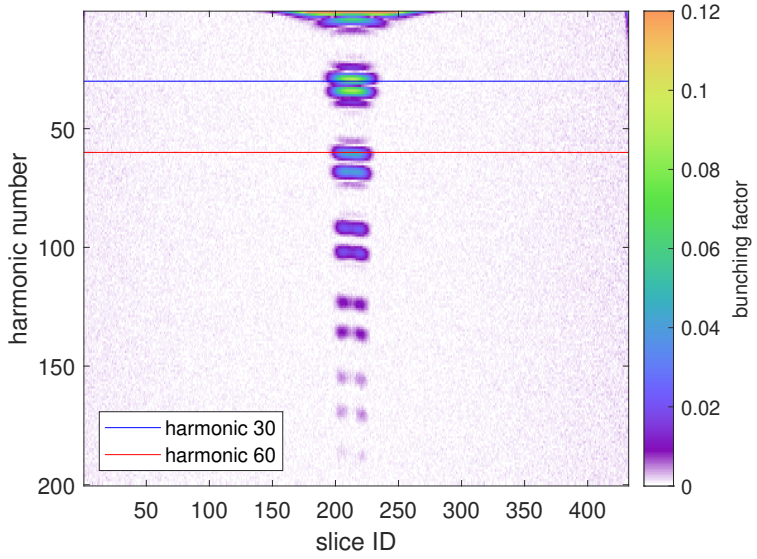

Figure (6.25) Harmonic content of the electron beam downstream the radiator. Bunching is present at both the 30^{th} and 60^{th} harmonic of the UV seed laser.

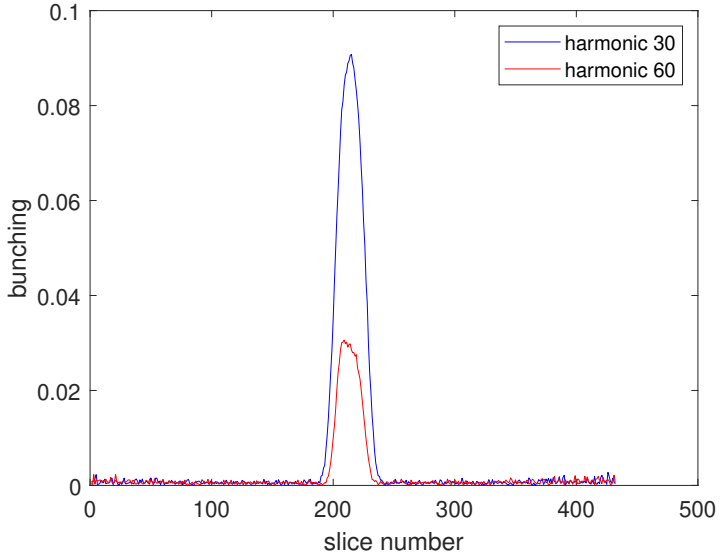

Figure (6.26) Bunching profiles of the electron beam at the 30^{th} and 60^{th} harmonic of the UV seed laser. The peak values of both profiles are in agreement with the foreseen value from the bunching map shown in Fig. 6.22.

When the electron beam is energy-modulated by the VIS seed laser, we get a bunching content shown in Fig. 6.27 and Fig. 6.28 shows the bunching profiles

at the harmonics of interest. The bunching at the 42$^{\text{nd}}$ harmonic is ~ 0.09 and ~ 0.02 at the 84$^{\text{th}}$ harmonic. Another time the theory is confirmed.

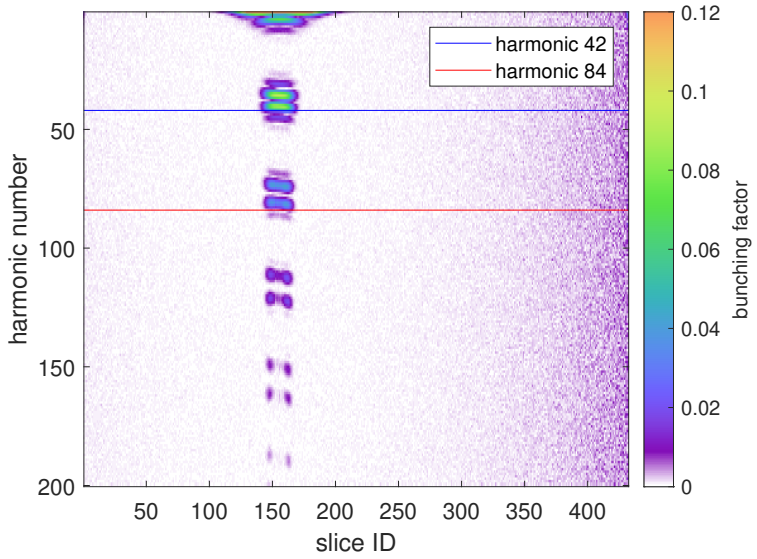

Figure (6.27) Harmonic content of the electron beam downstream the radiator. Bunching is present at both the 42$^{\text{nd}}$ and 84$^{\text{th}}$ harmonic of the VIS seed laser.

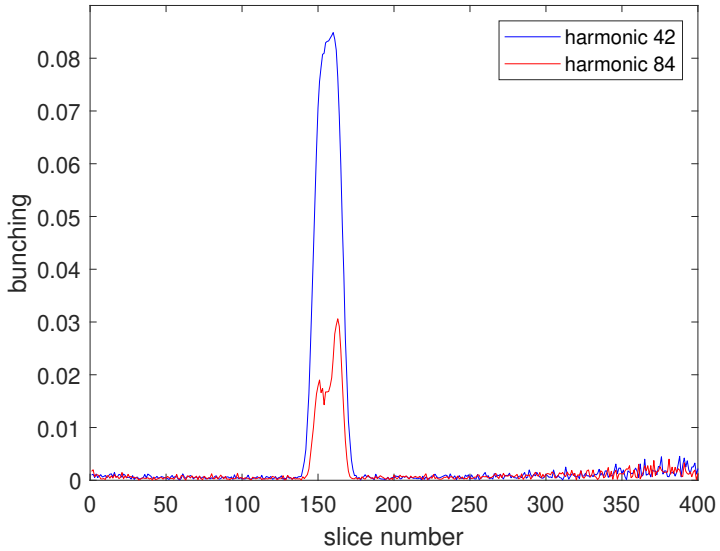

Figure (6.28) Bunching profiles of the electron beam at the 42$^{\text{nd}}$ and 84$^{\text{th}}$ harmonic of the VIS seed laser. The peak values of both profiles are in agreement with the foreseen value from the bunching map shown in Fig. 6.24.

After having achieved reliable bunching, we have tuned the radiator. For both

cases (UV and VIS seed), we have tuned the first four radiator modules to 10 nm and the last six undulators to 5 nm.
For the UV case we have found that the optimal FEL signal is achieved by opening the three last undulator modules. In Fig. 6.29 we show in Fig. 6.29a the FEL power profile and the corresponding spectrum in Fig. 6.29b. In the FEL power profile we notice relevant SASE background and the spectra is noisy as well. The peak power achieved is just ~ 200 MW.

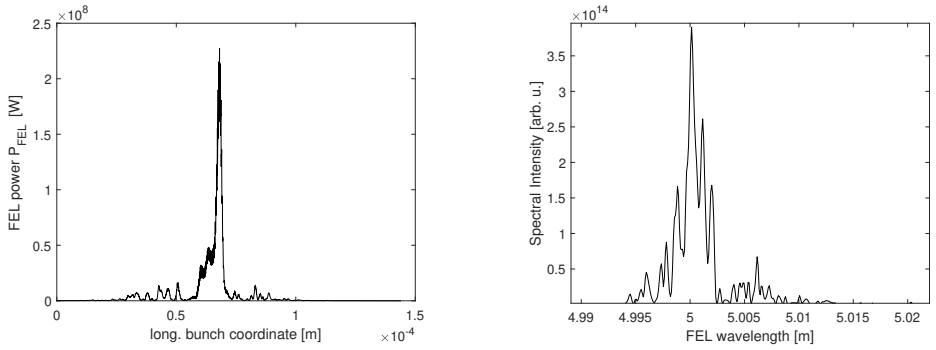

(a) FEL power profile. (b) FEL spectrum.

Figure (6.29) Power and spectra profiles of the FEL radiation generated at 5 nm from the UV seed laser, shown after the first three radiators tuned to be resonant with 5 nm.

For the electron beam modulated from a VIS seed laser the result is not better. In this case, it was necessary to look at the signal at the very end of the radiator section to achieve a reasonable high power, as a consequence the SASE background it is prominent. In Figure 6.30a we show the FEL profile and in Fig. 6.30b the corresponding spectra. We can observe that the high SASE background deteriorates the quality of the spectrum. As a result, the advantages of seeding are lost.

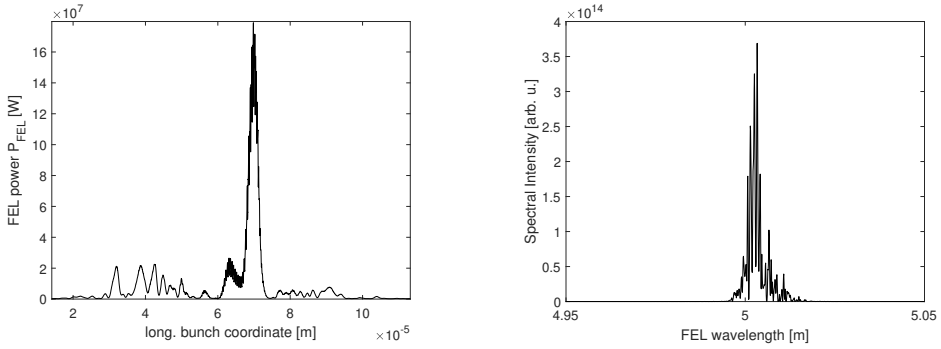

(a) FEL power profile. (b) FEL spectrum.

Figure (6.30) Power and spectra profiles of the FEL radiation generated at 5 nm from the VIS seed laser, shown at the very end of the radiator.

From these preliminary results, we have the impression that the freuency doubling is not advantageous when operating with the EEHG scheme. However, further studies, where also phase shifters between the radiator modules are adjusted are interesting to either confirm our impressions or to fine a fundamental knob which might lead to the optimization of the frequency doubling in an EEHG senario.

Conclusions and outlook

Chapter 7

Conclusions and outlook

In this work, we have shown the potentialities of the existing seeding infrastructure present at FLASH: sFLASH. With it, we can perform extended studies to characterize the properties of the seed laser and the final FEL radiation, thanks to a unique THz streaking setup installed in the experimental station at the end of the sFLASH beamline.

Simulations performed with the GENESIS1.3 code are a powerful tool that helps the understanding of the results achieved experimentally and to foresee the outcomes of schemes that have not been tested yet, for example, EEHG. With these simulations, we have proved the feasibility of the twelfth harmonic at sFLASH, even if we are at the limits of the parameters achievable with the currently installed setup. Because of upcoming upgrades to the sFLASH chicane and diagnostics, we have also studied more exotic EEHG configurations using two different seed laser wavelengths. This scheme has remarked an increased purity in the EEHG signal when we use a seed laser with longer wavelength as the second EEHG seed laser. Using a second seed laser with longer wavelength is an advantage in particular when the target harmonics are low, and they would be possible also exploiting the HGHG scheme.

We have presented the first successful experimental demonstration of the use of the EEHG scheme to generate FEL radiation in the XUV range. The experiment was performed at the FERMI FEL in Trieste, Italy. Exponential amplification

has been shown down to 5.9 nm and coherent emission down to 2.6 nm. The promising finding is that the EEHG FEL radiation is extremely sensitive to the quality of the electron beam properties, but it seems to show stability respect to seed laser phase errors. The experiment at FERMI was performed by adapting the FEL-2 beamline, hence also a comparison between the cascaded HGHG and EEHG was possible. This comparison has shown the superiority of the EEHG scheme compared to the cascaded HGHG. At FERMI, the colleagues are planning an upgrade for the FEL-1 beamline to enable the EEHG scheme. The aim is to explore further the EEHG scheme and understand its behaviour deeply with different experimental conditions.

The successful experimental EEHG results shown at FERMI have attracted the interest of the whole seeding community. In particular, at DESY, within the upcoming FLASH2020+ upgrade, we are designing a beamline to dedicate completely for seeding. We are going to upgrade the FLASH1 beamline for this aim. In this thesis, we have presented initial considerations and concepts that have to be considered during the development of a technical design report. In particular, we have contextualized the possible seed laser options under consideration, and we have analyzed the advantages and disadvantages. It results that, even if the technology for UV seeds at high-repetition-rate is extremely challenging, it opens more possibilities to achieve wavelengths of the order of 4 nm successfully. We have also considered frequency doubling as an option to achieve the 4 nm to reduce the constraints of EEHG, but, from the EEHG theory and simulations, we have proven that it does not represent an advantage compared to achieve the 4 nm with a pure EEHG scheme.

As an outlook, we are planning to continue the studies of the FLASH2020+ upgrade and complete a technical design report based on the experience gained from sFLASH and FERMI. Already, the needed hardware for the upgrade is under development and extended shutdowns at FLASH to start with the installation are planned for the upcoming year.

Appendices

The FEL simulation code Genesis1.3 version 4

Appendix A

Simulation code: Genesis1.3 version 4

The simulations presented in this thesis in the theory chapter, the FERMI chapter and the FLASH2020+ chapter are using this new simulation code. This code is an upgrade from GENESIS1,3 v.2 [141] (that was written in Fortran) and it is written in C++. The code GENESIS1.3 v.2 has been used in the chapter dedicated to the seeding at sFLASH for the chirp study, while for the EEHG simulations for sFLASH the newer code was used.

Genesis1.3 version 4 is a time-dependent, 3D code to simulate the amplification process of a Free-electron Laser that is under development. Genesis v.4 should be run on a parallel computer network. If this is large enough, there it is the possibility to keep the entire electron beam and radiation field in memory to enable features that was not possible with the previous versions.

GENESIS v.2 was based on the simulation of a number of macroparticles **npart** per slice. The macroparticles are loaded in the slice though the quiet loading: they are mirrored and evenly distributed in longitudinal position to completely cancel out completely any Fourier component for a given wavelength. In addition, a controlled random offset is applied to the particle to give the correct statistics in the bunching factor [34]. Each slice is long one radiation wavelength and the macroparticles cannot move outside the initial slice where they are collocated. If this would happen, the bunching would be enhanced in an unphysical way [34].

This prevent from the proper simulation of FEL schemes which includes high dispersion chicanes, for example the first chicane of the EEHG scheme. As explained in the theory chapter, the first EEHG chicane is thought to let the particles travel though several radiations wavelengths to generate the characteristic energy bands in the longitudinal phase space distribution. In the new GENESIS version (4) it is possible to do a single particle simulation (**one4one**) instead of using macroparticles and the particles can move freely between slices because they are all kept in memory during the simulation process. Moreover, with one4one simulations is not necessary without mirroring particles [34]. As the old version, GENESIS1.3 v.4 bases its algorithm on the slowly varying envelope approximation (SVEA), where the equations of motions are averaged over one undulator period. Therefore, the integration step can be more than one undulator period, to reduce the simulation time of the radiator section for seeding [34].

A tool for the evaluation of fundamental FEL parameters: params

Appendix B

params: the excel tool

Params is an excel tool developed by B. Faatz and it is useful to get a pratical estimation of the main FEL parameters based on the main hardware elements involved. The document is subdivided different excel sheets:

- Parms
- Phase-shifter
- Chicanes
- HHG-Divergence
- Harmonics
- HGHG
- Cascaded Harmonics
- Phasing.

Here we focus on two sheets: parms and chicanes. Parms is a sheet that helps with the undulator design based on the wished FEL performances. Figure B.1 shows the excel sheet. The FEL performances are estimated following the M. Xie model [39]. As **input undulator** parameter we can either set the undulator gap or the RMS undulator parameter K_{rms}. In the first case, the gap width given as an input in column G is taken as starting value in column H, as we see in Fig.B.1. In the second case, the K_{rms} defined in column G is taken as a constant.
As optics we can define it either using the Twiss parameter beta and assuming a thin lens optics or we can give the quadupole gradients. **Input radiation** set the reference value from which the tool have to scan the other parameters, and it can either be the electron beam energy or the target FEL wavelength. Once we have defined these quantities, we can set the **scan step**, that defines how much the scanned variable in column H is increased each step. The **Field Factor** depends on the undulator selected in column F: for planar undulators it should be set to 1, while for helical undulators this factor depend on the particular geometry assumed by the undulator to give a specific polarization. On column F and G we define the electron beam, undulator (together with the electron beam optics) and co-propagating radiation properties.
As already mentioned, in column H we decide the parameter that we want to scan, and this can be:

- undulator gap
- undulator period
- Twiss parameter beta
- electron beam energy
- electron beam peak current
- electron beam charge
- normalized emittance
- energy spread
- seed power

and in column I we can choose another parameter, that can give to us information about the undulator parameters (K_{rms}, peak field), the generated FEL radiation (wavelength, energy) and the electron beam properties (beam power, beamsize, rms bunch length, beta function). The remaining colums (J, K, L, M and N) calculate parameters useful to understand the FEL performance in dependence of the variable that is scanned: Saturation length, output power, FEL parameter, photons per bunch, peak brilliance, ..

The chicanes sheet is shown in Figure B.2 and it is useful to estimate a proper

R19

	A	F	G	H	I	J	K	L	M	N
1	**Model**	**Version: 2009-04-15**		Gap (mm)	K_rms	Saturation Length (m)	Output Power (GW)	rho_1D	Photons per bunch	gain length (1-D)
2	Xie	**Electron Beam**		***8.000***	2.642	6.941	1.772	0.003	6.76447E+13	0.557
3		Energy (GeV)	1.350	***8.300***	2.496	7.145	1.728	0.003	5.97571E+13	0.578
4	**input undulator**	Peak Current (kA)	0.500	***8.600***	2.358	7.358	1.683	0.003	5.28092E+13	0.601
5	Gap (mm)	Charge (nC)	0.400	***8.900***	2.228	7.581	1.637	0.002	4.66886E+13	0.624
6	**input optics**	Normalized emittance (mm mrad)	1.000	***9.200***	2.105	7.816	1.590	0.002	4.12953E+13	0.648
7	beta (thin lens, m)	Energy Spread (MeV)	0.150	***9.500***	1.989	8.063	1.542	0.002	3.65411E+13	0.673
8	**input radiation**	**Undulator**		***9.800***	1.879	8.322	1.492	0.002	3.23482E+13	0.699
9	Energy (GeV)	APPLE III (circ.)	11	10.100	1.776	8.597	1.442	0.002	2.86477E+13	0.725
10		Period (mm)	33.000	10.400	1.678	8.887	1.390	0.002	2.53792E+13	0.753
11	**Scan step**	Gap (mm)	***8.000***	10.700	1.586	9.195	1.337	0.002	2.24895E+13	0.782
12	0.3	K_rms		11.000	1.499	9.523	1.283	0.002	1.9932E+13	0.812
13		FODO Period (m)	6.600	11.300	1.416	9.873	1.228	0.002	1.76659E+13	0.843
14	**Field Factor**	Quadrupole Length (m)	0.0760	11.600	1.339	10.248	1.172	0.002	1.56555E+13	0.876
15	**1.8**	beta (thin lens, m)	5.000	11.900	1.265	10.650	1.114	0.002	1.38697E+13	0.909
16	**Gain Length Factor**	minimum gap (mm)	10.000	19.000	1.196	11.082	1.056	0.002	1.22817E+13	0.944
17	**1**	Undulator length (m)	26.928	12.500	1.131	11.549	0.997	0.002	1.0868E+13	0.980
18		**Radiation**		12.800	1.069	12.053	0.937	0.001	9.6083E+12	1.018
19		Seed Power (MW)	1.0000	13.100	1.011	12.601	0.877	0.001	8.48513E+12	1.056
20		Seed Pulse length (fs)		13.400	0.955	13.195	0.818	0.001	7.4833E+12	1.097
21		Wavelength (nm)		13.700	0.903	13.841	0.758	0.001	6.58966E+12	1.138
108		Seed Energy (muJ)	#VALUE!	14.000	0.854	14.545	0.700	0.001	5.79279E+12	1.182
109				14.300	0.808	15.312	0.643	0.001	5.08269E+12	1.227
110				14.600	0.764	16.150	0.588	0.001	4.45059E+12	1.273
111				14.900	0.722	17.064	0.534	0.001	3.88871E+12	1.322
112				15.200	0.683	18.062	0.483	0.001	3.3901E+12	1.372
113		Length undulator segment	1.200	15.500	0.646	19.153	0.435	0.001	2.94852E+12	1.424
114		# Periods	36.364	15.800	0.611	20.344	0.389	0.001	2.55831E+12	1.477
115		Magnetic length	34.000	16.100	0.578	21.646	0.347	0.001	2.21433E+12	1.533
116		Number of segments	24.000	16.400	0.547	23.066	0.308	0.001	1.91186E+12	1.591
117		Intersection	0.460	16.700	0.517	24.618	0.272	0.001	1.64659E+12	1.651
118		Total length	39.552	17.000	0.489	26.310	0.239	0.001	1.41457E+12	1.714
119				17.300	0.463	***28.157***	0.150	0.001	8.7221E+11	1.778
120				17.600	0.438	***30.172***	0.082	0.001	4.67615E+11	1.845
121				17.900	0.414	***32.368***	0.047	0.001	2.60859E+11	1.915
122				18.200	0.392	***34.762***	0.027	0.001	1.51291E+11	1.987
123				18.500	0.371	***37.370***	0.017	0.001	91123278568	2.061
124				18.800	0.351	***40.210***	0.011	0.001	56922173863	2.138

Figure (B.1) Parms sheet

chicane geometry to achieve the needed dispersion strength R_{56}. The implemented chicane types are the so called C-shape chicane (Figure B.3), and the S-shape chicane (Figure B.4), thy are modelled following the definitions described in [77]. In the following we consider only the C-shape chicane. From row 5 to 8, we can input the dipole magnet length, the magnetic field and the distance between outer and inner magnets. As an output, we get the arc of radius (l_{arc} in Figure B.3), the deflection angle (α in Figure B.3), the minimum value for the total chicane length, the dispersive parameter R_{56} and the maximum dispersion. As total

A1

	A	B	C	D	E	F
1	Beam Energy (GeV)	1.1				
2						
3						
4						
5	**BC2 chicane (C-shape)**			**BC3 chicane (S-shape)**		
6	Magnet length (mm)	375		Magnet length (mm)	500	
7	Magnet field (T)	0.564		Magnet field (T)	0.185	
8	Distance D12=D34 (mm)	0		Distance D12=D56 (mm)	2380	
9				Distance D34 (mm)	5259	
10	Arc of Radius (mm)	6501		Arc of Radius (mm)	19820	
11	Deflection Angle (mrad)	57.7	3.31	Deflection Angle (mrad)	25.2	1.45
12	Total Length Chicane (m)	> 1.5		Total Length Chicane (m)	> 13.019	
13	R56 (mm)	1.669		R56 (mm)	7.019	
14	Max. D (mm)	21.685		Max. D (mm)	-72.699	
15				Exit D (mm)	0.019	
16						
17						
18	Approx. R56 (mm)	2.498		Approx. R56 (mm)		
19						
20	Length difference (mm)	0.833045908		Length difference (mm)	3.50956	
21	Length difference (ps)	2.778764827		Length difference (ps)	11.7067	
22	Length difference (degr.)	1.300451305		Length difference (degr.)	5.4787	
23						

Figure (B.2) Chicanes sheet

chicane length is given a minimum value which refers to the length of the chicane in the case of no drift between the two inner dipoles. From row 27 to 39 and columns from A to J, there is a list of magnets types and their properties that are exploited at the FLASH accelerator. *sFLASH bunching maps*

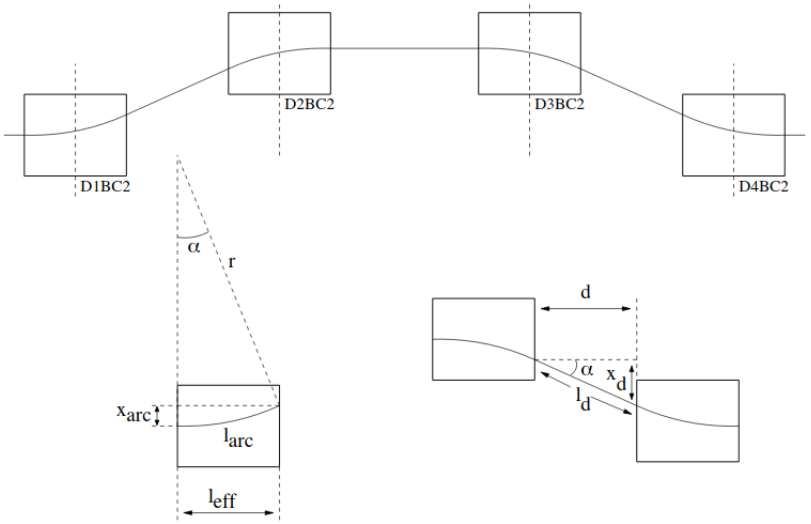

Figure (B.3) C-shape chicane [77].

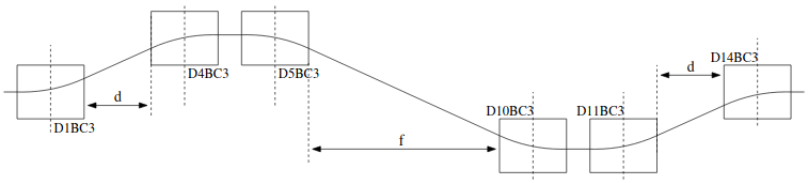

Figure (B.4) S-shape chicane [77].

from the 6^{th} *to the* 18^{th} *harmonic*

B.1 Working points for the 6^{th} harmonic

For the bunching maps presented in Figs. B.5 and B.6 it is hard to distinguish between HGHG and EEHG bunching. Instead, in Fig. Figs. B.7 and B.8 where the A_2 parameter is reduced, compared to the two earlier maps, the EEHG bunching is clearly distinguishable. In these figures, the HGHG bunching is present in the region where $R_{56}^{(1)} < 100\,\mu\text{m}$ and $R_{56}^{(2)} < 100\,\mu\text{m}$ and the EEHG bunching is present for $R_{56}^{(1)} > 50\,\mu\text{m}$ and $R_{56}^{(2)} > 80\,\mu\text{m}$. For the working point shown in Fig. B.7 we get the maximum EEHG bunching for the cases under consideration, that is greater than 0.3.

Choosing a EEHG working point at the 6^{th} or at the 7^{th} harmonic might be challenging because of the high signal coming from the HGHG scheme. Based on the information that we got from the bunching maps, one way to increase the EEHG signal is to increase the first seed laser to the maximum possible and maximize the first chicane dispersive strength.

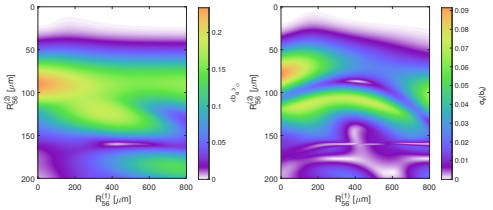

Figure (B.5) Bunching map at the 6^{th} harmonic with $A_1 = 1$ and $A_2 = 4.9$. Left plot: bunching averaged on the phase ϕ. Right plot: RMS bunching fluctuations respect to the phase ϕ.

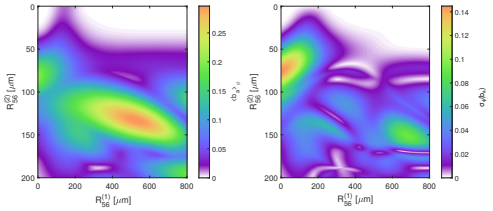

Figure (B.6) Bunching map at the 6^{th} harmonic with $A_1 = 2$ and $A_2 = 4.6$. Left plot: bunching averaged on the phase ϕ. Right plot: RMS bunching fluctuations respect to the phase ϕ.

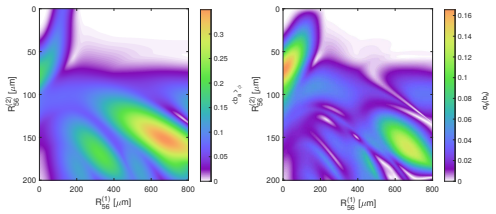

Figure (B.7) Bunching map at the 6^{th} harmonic with $A_1 = 3$ and $A_2 = 4$. Left plot: bunching averaged on the phase ϕ. Right plot: RMS bunching fluctuations respect to the phase ϕ.

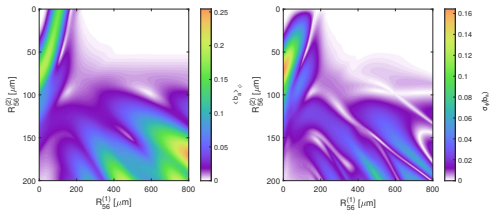

Figure (B.8) Bunching map at the 6^{th} harmonic with $A_1 = 4$ and $A_2 = 3$. Left plot: bunching averaged on the phase ϕ. Right plot: RMS bunching fluctuations respect to the phase ϕ.

B.2 Working points for the 7^{th} harmonic

At the 7th harmonic, we obtain a similar behavior to the 6^{th} harmonic.

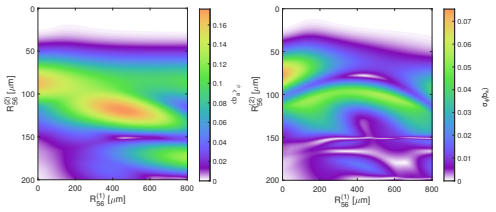

Figure (B.9) Bunching map at the 7^{th} harmonic with $A_1 = 1$ and $A_2 = 4.9$. Left plot: bunching averaged on the phase ϕ. Right plot: RMS bunching fluctuations respect to the phase ϕ.

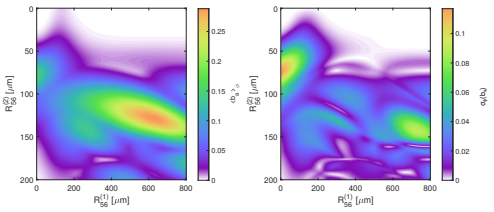

Figure (B.10) Bunching map at the 7^{th} harmonic with $A_1 = 2$ and $A_2 = 4.6$. Left plot: bunching averaged on the phase ϕ. Right plot: RMS bunching fluctuations respect to the phase ϕ.

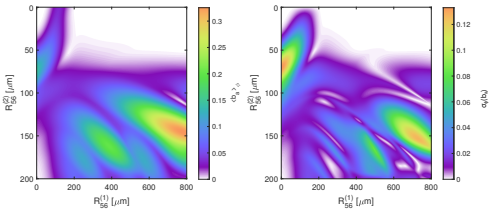

Figure (B.11) Bunching map at the 7^{th} harmonic with $A_1 = 3$ and $A_2 = 4$. Left plot: bunching averaged on the phase ϕ. Right plot: RMS bunching fluctuations respect to the phase ϕ.

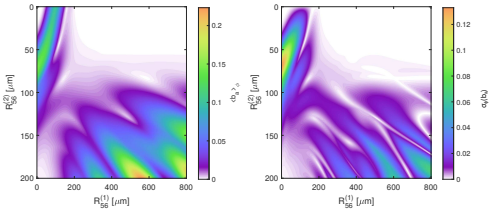

Figure (B.12) Bunching map at the 7^{th} harmonic with $A_1 = 4$ and $A_2 = 3$. Left plot: bunching averaged on the phase ϕ. Right plot: RMS bunching fluctuations respect to the phase ϕ.

B.3 Working points for the 8^{th} harmonic

At the 8^{th} harmonic, we are already able to distinguish between EEHG and HGHG bunching when $A_1 = 2$ and $A_2 = 4.6$. The HGHG bunching stands in the region delimited by $R_{56}^{(1)} < 200\,\mu\text{m}$ and $R_{56}^{(2)} < 100\,\mu\text{m}$, while the EEHG bunching lies in the area where $R_{56}^{(1)} > 200\,\mu\text{m}$ and $R_{56}^{(2)} > 70\,\mu\text{m}$. The maximum EEHG bunching is below 0.3, that was observed for the 6^{th} and 7^{th} harmonic. In Figs. B.15 and B.16 is even clearer the distinction between HGHG and EEHG bunching.

We observe that as the A_2 parameter decreases, the EEHG bunching features are moving in regions with higher $R_{56}^{(1)}$, hence we have to compensate with higher first chicane dispersion.

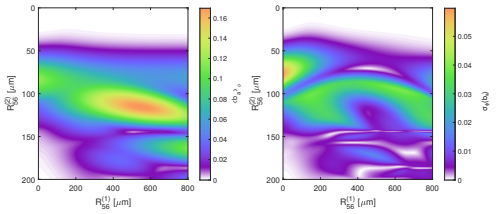

Figure (B.13) Bunching map at the 8^{th} harmonic with $A_1 = 1$ and $A_2 = 4.9$. Left plot: bunching averaged on the phase ϕ. Right plot: RMS bunching fluctuations respect to the phase ϕ.

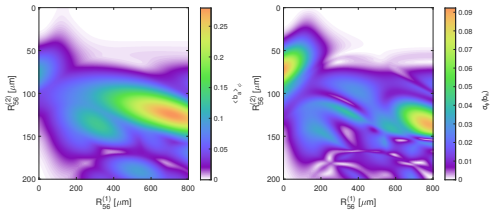

Figure (B.14) Bunching map at the 8^{th} harmonic with $A_1 = 2$ and $A_2 = 4.6$. Left plot: bunching averaged on the phase ϕ. Right plot: RMS bunching fluctuations respect to the phase ϕ.

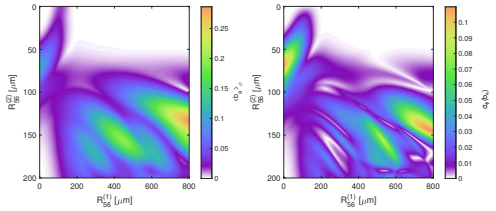

Figure (B.15) Bunching map at the 8^{th} harmonic with $A_1 = 3$ and $A_2 = 4$. Left plot: bunching averaged on the phase ϕ. Right plot: RMS bunching fluctuations respect to the phase ϕ.

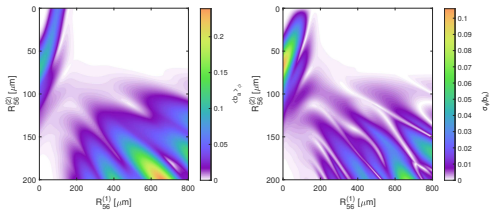

Figure (B.16) Bunching map at the 8^{th} harmonic with $A_1 = 4$ and $A_2 = 3$. Left plot: bunching averaged on the phase ϕ. Right plot: RMS bunching fluctuations respect to the phase ϕ.

B.4 Working points for the 9^{th} harmonic

The EEHG bunching behavior at the 9^{th} is similar to what we have observed for the 8^{th} harmonic.

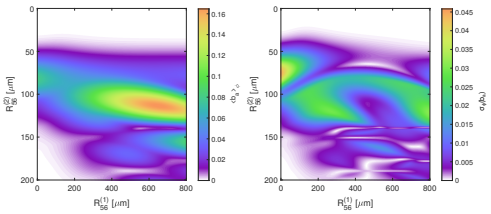

Figure (B.17) Bunching map at the 9^{th} harmonic with $A_1 = 1$ and $A_2 = 4.9$. Left plot: bunching averaged on the phase ϕ. Right plot: RMS bunching fluctuations respect to the phase ϕ.

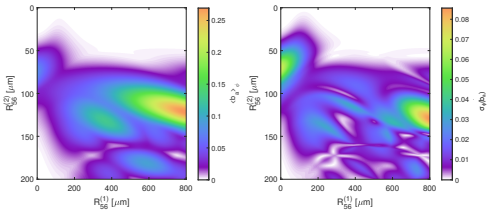

Figure (B.18) Bunching map at the 9^{th} harmonic with $A_1 = 2$ and $A_2 = 4.6$. Left plot: bunching averaged on the phase ϕ. Right plot: RMS bunching fluctuations respect to the phase ϕ.

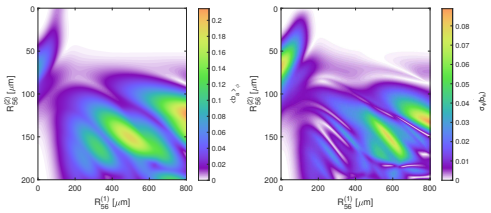

Figure (B.19) Bunching map at the 9^{th} harmonic with $A_1 = 3$ and $A_2 = 4$. Left plot: bunching averaged on the phase ϕ. Right plot: RMS bunching fluctuations respect to the phase ϕ.

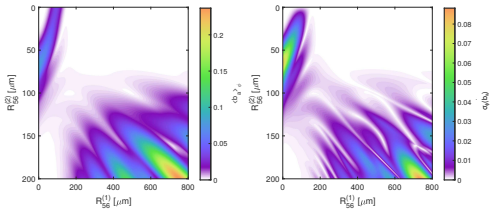

Figure (B.20) Bunching map at the 9^{th} harmonic with $A_1 = 4$ and $A_2 = 3$. Left plot: bunching averaged on the phase ϕ. Right plot: RMS bunching fluctuations respect to the phase ϕ.

B.5 Working points for the 10^{th} harmonic

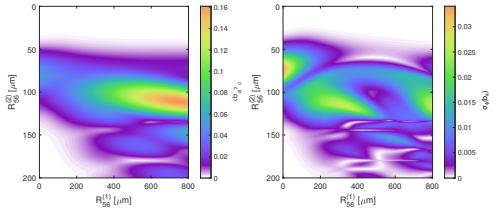

Figure (B.21) Bunching map at the 10^{th} harmonic with $A_1 = 1$ and $A_2 = 4.9$. Left plot: bunching averaged on the phase ϕ. Right plot: RMS bunching fluctuations respect to the phase ϕ.

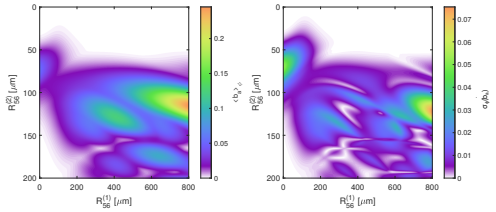

Figure (B.22) Bunching map at the 10^{th} harmonic with $A_1 = 2$ and $A_2 = 4.6$. Left plot: bunching averaged on the phase ϕ. Right plot: RMS bunching fluctuations respect to the phase ϕ.

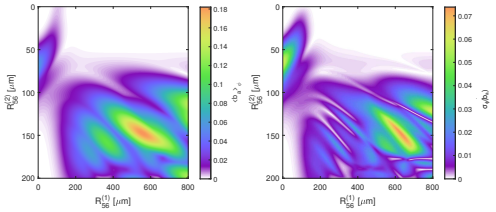

Figure (B.23) Bunching map at the 10^{th} harmonic with $A_1 = 3$ and $A_2 = 4$. Left plot: bunching averaged on the phase ϕ. Right plot: RMS bunching fluctuations respect to the phase ϕ.

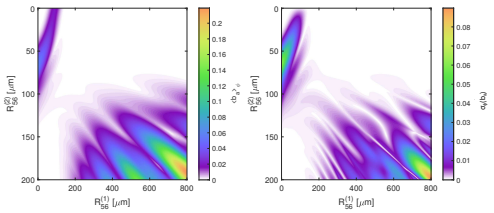

Figure (B.24) Bunching map at the 10^{th} harmonic with $A_1 = 4$ and $A_2 = 3$. Left plot: bunching averaged on the phase ϕ. Right plot: RMS bunching fluctuations respect to the phase ϕ.

B.6 Working points for the 11^{th} harmonic

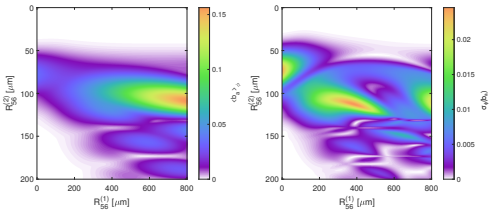

Figure (B.25) Bunching map at the 11^{th} harmonic with $A_1 = 1$ and $A_2 = 4.9$. Left plot: bunching averaged on the phase ϕ. Right plot: RMS bunching fluctuations respect to the phase ϕ.

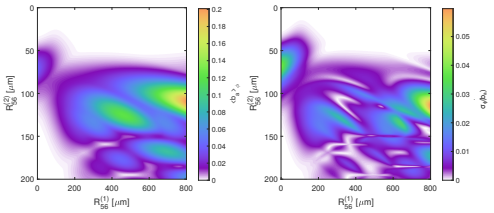

Figure (B.26) Bunching map at the 11^{th} harmonic with $A_1 = 2$ and $A_2 = 4.6$.Left plot: bunching averaged on the phase ϕ. Right plot: RMS bunching fluctuations respect to the phase ϕ.

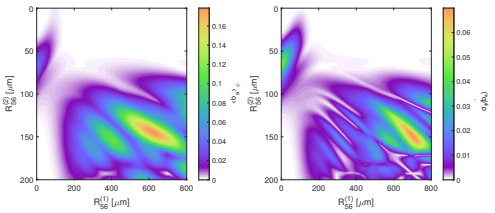

Figure (B.27) Bunching map at the 11^{th} harmonic with $A_1 = 3$ and $A_2 = 4$. Left plot: bunching averaged on the phase ϕ. Right plot: RMS bunching fluctuations respect to the phase ϕ.

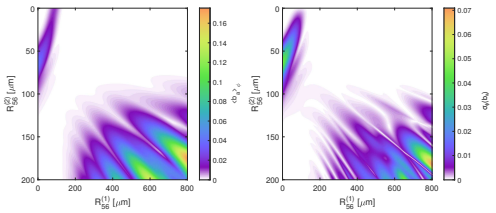

Figure (B.28) Bunching map at the 11$^{\text{th}}$ harmonic with $A_1 = 4$ and $A_2 = 3$. Left plot: bunching averaged on the phase ϕ. Right plot: RMS bunching fluctuations respect to the phase ϕ.

B.7 Working points for the 12$^{\text{th}}$ harmonic

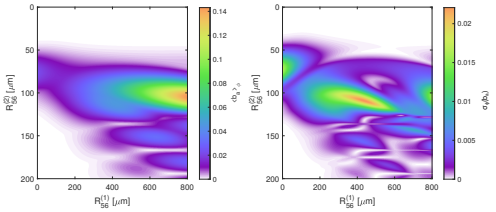

Figure (B.29) Bunching map at the 12$^{\text{th}}$ harmonic with $A_1 = 1$ and $A_2 = 4.9$. Left plot: bunching averaged on the phase ϕ. Right plot: RMS bunching fluctuations respect to the phase ϕ.

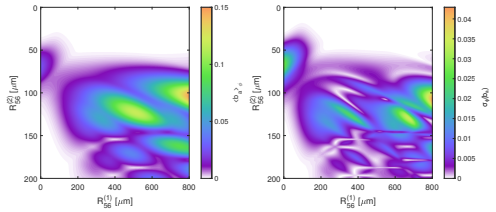

Figure (B.30) Bunching map at the 12$^{\text{th}}$ harmonic with $A_1 = 2$ and $A_2 = 4.6$. Left plot: bunching averaged on the phase ϕ. Right plot: RMS bunching fluctuations respect to the phase ϕ.

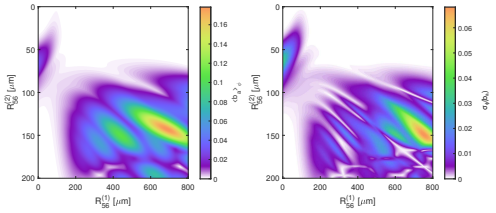

Figure (B.31) Bunching map at the 12$^{\text{th}}$ harmonic with $A_1 = 3$ and $A_2 = 4$. Left plot: bunching averaged on the phase ϕ. Right plot: RMS bunching fluctuations respect to the phase ϕ.

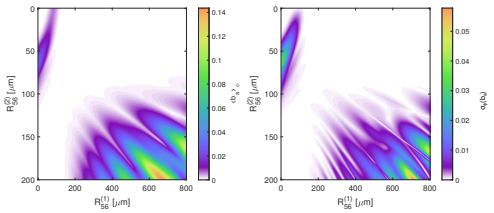

Figure (B.32) Bunching map at the 12$^{\text{th}}$ harmonic with $A_1 = 4$ and $A_2 = 3$. Left plot: bunching averaged on the phase ϕ. Right plot: RMS bunching fluctuations respect to the phase ϕ.

B.8 Working points for the 13$^{\text{th}}$ harmonic

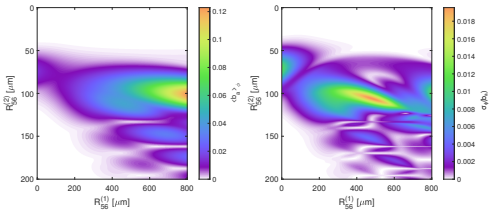

Figure (B.33) Bunching map at the 13$^{\text{th}}$ harmonic with $A_1 = 1$ and $A_2 = 4.9$. Left plot: bunching averaged on the phase ϕ. Right plot: RMS bunching fluctuations respect to the phase ϕ.

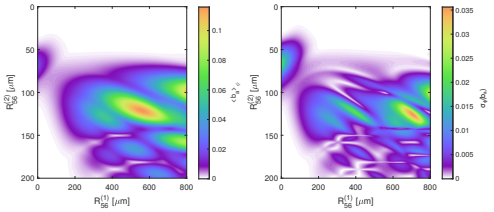

Figure (B.34) Bunching map at the 13$^{\text{th}}$ harmonic with $A_1 = 2$ and $A_2 = 4.6$. Left plot: bunching averaged on the phase ϕ. Right plot: RMS bunching fluctuations respect to the phase ϕ.

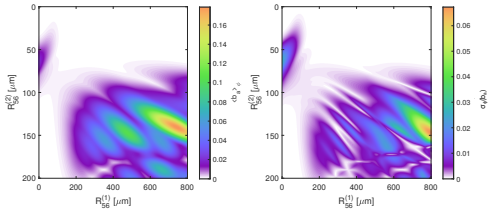

Figure (B.35) Bunching map at the 13$^{\text{th}}$ harmonic with $A_1 = 3$ and $A_2 = 4$. Left plot: bunching averaged on the phase ϕ. Right plot: RMS bunching fluctuations respect to the phase ϕ.

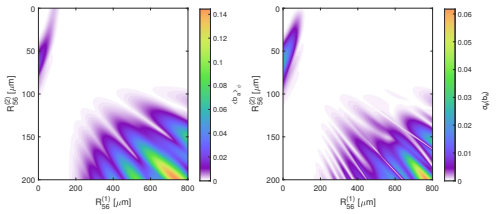

Figure (B.36) Bunching map at the 13$^{\text{th}}$ harmonic with $A_1 = 4$ and $A_2 = 3$. Left plot: bunching averaged on the phase ϕ. Right plot: RMS bunching fluctuations respect to the phase ϕ.

B.9 Working points for the 14$^{\text{th}}$ harmonic

The advantage to operate from harmonic 14$^{\text{th}}$ to harmonic 18$^{\text{th}}$ is that the HGHG bunching is negligible from the first considered working point $A_1 = 1$ and $A_2 = 4.9$. The HGHG bunching is always below 0.01. However, the needed first chicane strength to get a reasonable EEHG bunching is often above the 700 µm, which might be a challenge for the currently installed sFLASH chicane.

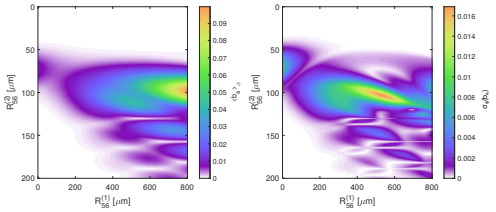

Figure (B.37) Bunching map at the 14$^{\text{th}}$ harmonic with $A_1 = 1$ and $A_2 = 4.9$. Left plot: bunching averaged on the phase ϕ. Right plot: RMS bunching fluctuations respect to the phase ϕ.

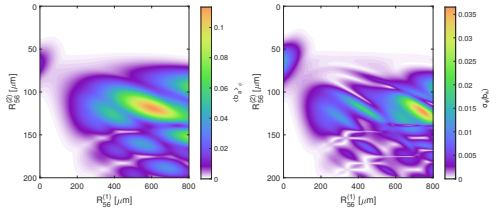

Figure (B.38) Bunching map at the 14$^{\text{th}}$ harmonic with $A_1 = 2$ and $A_2 = 4.6$. Left plot: bunching averaged on the phase ϕ. Right plot: RMS bunching fluctuations respect to the phase ϕ.

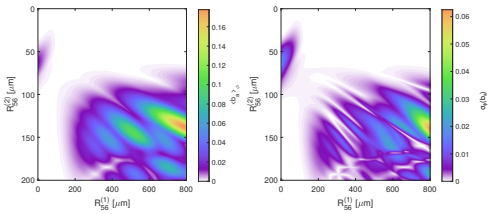

Figure (B.39) Bunching map at the 14^{th} harmonic with $A_1 = 3$ and $A_2 = 4$. Left plot: bunching averaged on the phase ϕ. Right plot: RMS bunching fluctuations respect to the phase ϕ.

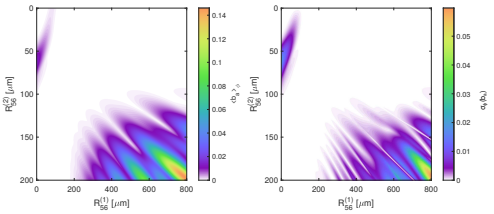

Figure (B.40) Bunching map at the 14^{th} harmonic with $A_1 = 4$ and $A_2 = 3$. Left plot: bunching averaged on the phase ϕ. Right plot: RMS bunching fluctuations respect to the phase ϕ.

B.10 Working points for the 15^{th} harmonic

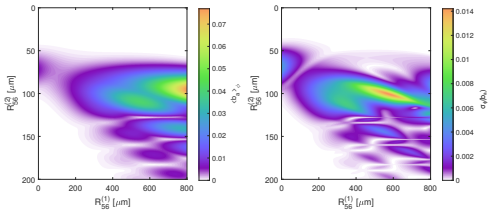

Figure (B.41) Bunching map at the 15^{th} harmonic with $A_1 = 1$ and $A_2 = 4.9$. Left plot: bunching averaged on the phase ϕ. Right plot: RMS bunching fluctuations respect to the phase ϕ.

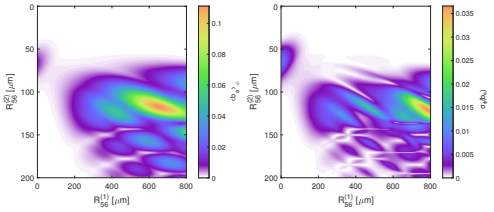

Figure (B.42) Bunching map at the 15^{th} harmonic with $A_1 = 2$ and $A_2 = 4.6$. Left plot: bunching averaged on the phase ϕ. Right plot: RMS bunching fluctuations respect to the phase ϕ.

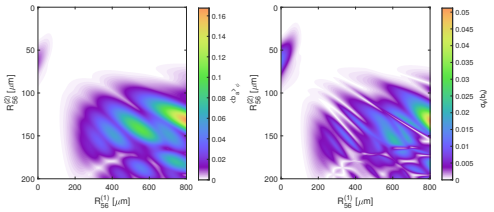

Figure (B.43) Bunching map at the 15$^{\text{th}}$ harmonic with $A_1 = 3$ and $A_2 = 4$. Left plot: bunching averaged on the phase ϕ. Right plot: RMS bunching fluctuations respect to the phase ϕ.

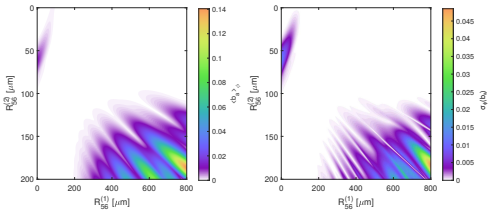

Figure (B.44) Bunching map at the 15$^{\text{th}}$ harmonic with $A_1 = 4$ and $A_2 = 3$. Left plot: bunching averaged on the phase ϕ. Right plot: RMS bunching fluctuations respect to the phase ϕ.

B.11 Working points for the 16$^{\text{th}}$ harmonic

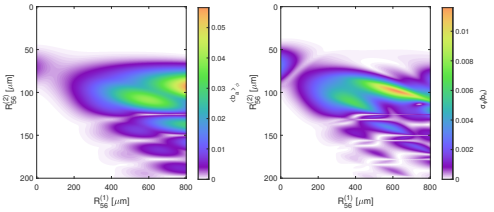

Figure (B.45) Bunching map at the 16$^{\text{th}}$ harmonic with $A_1 = 1$ and $A_2 = 4.9$. Left plot: bunching averaged on the phase ϕ. Right plot: RMS bunching fluctuations respect to the phase ϕ.

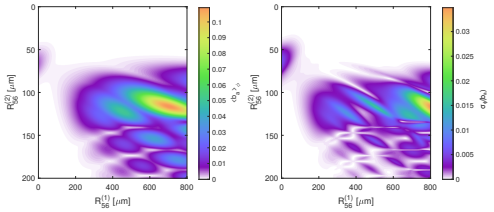

Figure (B.46) Bunching map at the 16$^{\text{th}}$ harmonic with $A_1 = 2$ and $A_2 = 4.6$. Left plot: bunching averaged on the phase ϕ. Right plot: RMS bunching fluctuations respect to the phase ϕ.

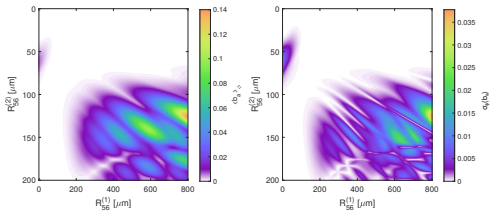

Figure (B.47) Bunching map at the 16$^{\text{th}}$ harmonic with $A_1 = 3$ and $A_2 = 4$. Left plot: bunching averaged on the phase ϕ. Right plot: RMS bunching fluctuations respect to the phase ϕ.

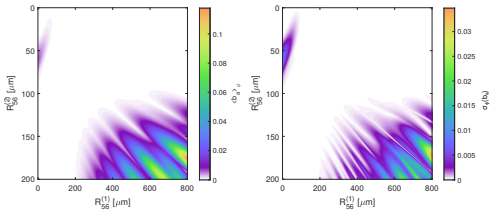

Figure (B.48) Bunching map at the 16$^{\text{th}}$ harmonic with $A_1 = 4$ and $A_2 = 3$. Left plot: bunching averaged on the phase ϕ. Right plot: RMS bunching fluctuations respect to the phase ϕ.

B.12 Working points for the 17$^{\text{th}}$ harmonic

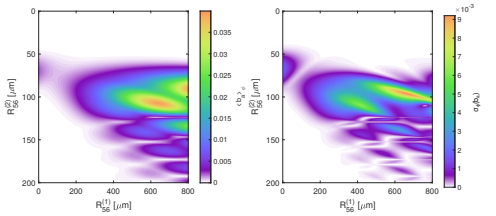

Figure (B.49) Bunching map at the 17$^{\text{th}}$ harmonic with $A_1 = 1$ and $A_2 = 4.9$. Left plot: bunching averaged on the phase ϕ. Right plot: RMS bunching fluctuations respect to the phase ϕ.

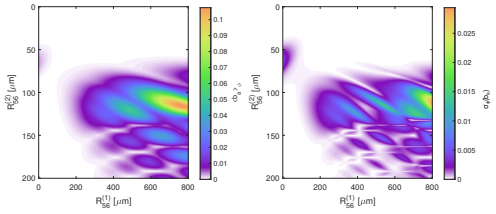

Figure (B.50) Bunching map at the 17$^{\text{th}}$ harmonic with $A_1 = 2$ and $A_2 = 4.6$. Left plot: bunching averaged on the phase ϕ. Right plot: RMS bunching fluctuations respect to the phase ϕ.

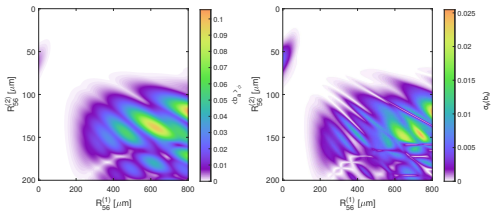

Figure (B.51) Bunching map at the 17$^{\text{th}}$ harmonic with $A_1 = 3$ and $A_2 = 4$. Left plot: bunching averaged on the phase ϕ. Right plot: RMS bunching fluctuations respect to the phase ϕ.

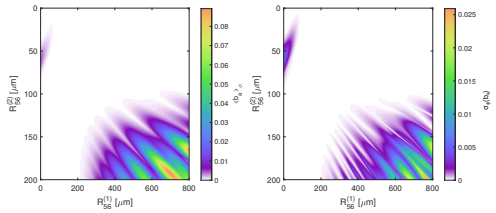

Figure (B.52) Bunching map at the 17$^{\text{th}}$ harmonic with $A_1 = 4$ and $A_2 = 3$. Left plot: bunching averaged on the phase ϕ. Right plot: RMS bunching fluctuations respect to the phase ϕ.

B.13 Working points for the 18$^{\text{th}}$ harmonic

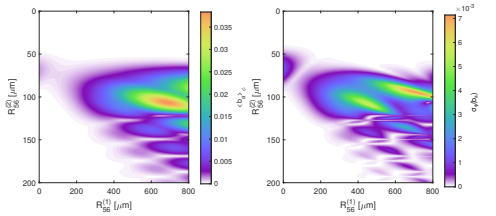

Figure (B.53) Bunching map at the 18$^{\text{th}}$ harmonic with $A_1 = 1$ and $A_2 = 4.9$. Left plot: bunching averaged on the phase ϕ. Right plot: RMS bunching fluctuations respect to the phase ϕ.

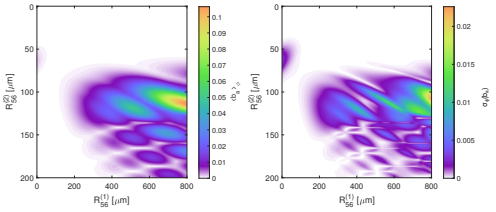

Figure (B.54) Bunching map at the 18$^{\text{th}}$ harmonic with $A_1 = 2$ and $A_2 = 4.6$. Left plot: bunching averaged on the phase ϕ. Right plot: RMS bunching fluctuations respect to the phase ϕ.

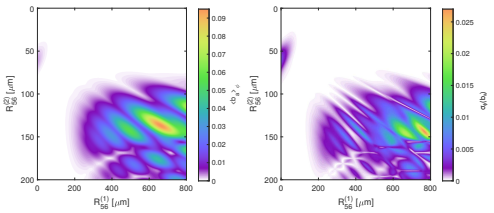

Figure (B.55) Bunching map at the 18^{th} harmonic with $A_1 = 3$ and $A_2 = 4$. Left plot: bunching averaged on the phase ϕ. Right plot: RMS bunching fluctuations respect to the phase ϕ.

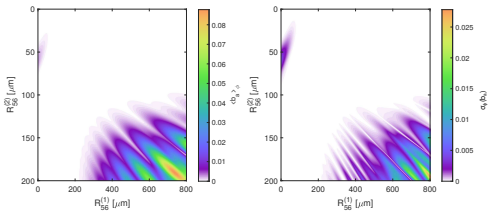

Figure (B.56) Bunching map at the 18^{th} harmonic with $A_1 = 4$ and $A_2 = 3$. Left plot: bunching averaged on the phase ϕ. Right plot: RMS bunching fluctuations respect to the phase ϕ.

Eidesstattliche Versicherung / Declaration on oath

Hiermit versichere ich an Eides statt, die vorliegende Dissertationsschrift selbst verfasst und keine anderen als die angegebenen Hilfsmittel und Quellen benutzt zu haben. Die eingereichte schriftliche Fassung entspricht der auf dem elektronischen Speichermedium. Die Dissertation wurde in der vorgelegten oder einer ähnlichen Form nicht schon einmal in einem früheren Promotionsverfahren angenommen oder als ungenügend beurteilt.

Hamburg, den 11.06.2020

Unterschrift der Doktorandin

Acknowledgments

Acknowledgments

I would like to thank all the people that have supported these three years of doctorate at DESY. I would like to start with my professor Wolfgang Hillert and Ralph Assman whom have been always open for letting me taking part to international conferences and collaborations in order to present my work and share scientific knowledge with the cutting edge experts of the sector. This aspect has been fundamental for the success of my work. I thank them also for supporting my work constantly.
A particular thank goes to Joern Boedewadt and Tim Plath which have been very helpful to introduce me to DESY, the sFLASH experiment, GENESIS simulations and to Hamburg. I would like to thank Hauke Biss for all the useful scientific conversations and the mutual support that we shared during the time of his master thesis. I don't want to forget my first office mate, Christian Henkel, whom is always very friendly and we can share our doctoral experiences. I would like to thank Georgia Paraskaki my current office mate, as a good friend and colleague. Together we have had the possibility to share our knowledge about simulations and FELs, which have made grown together and have matured a positive scientific critical view. Also the shared mutual support has been very important for me. I thank infinitely Bart Faatz for his interest in my simulation work about FLASH2020+ and all the useful scientific discussions that we have had together. His motivation and his determination have motivated me immensely for achieving the end of my doctoral studies. I thank very much Velizar Miltchev for proofreading my thesis and being always open to share his knowledge about FELs

and tuning of sFLASH with me. I thank Christoph Lechner for keeping care of the sFLASH hardware and introducing me to the topic of my doctoral thesis. I would like to thank Mehdi Kazemi for his infinite patience and motivation with the maintenance of our seed laser and his encouragements in particular during the night-shifts. Together with Mehdi I thank Jiian Zahng and Tino Lang for the very useful scientific conversations we had together and for inspiring me with their seriousness and passion that they are dedicating to their job. I thank Armin Azima for maintaining the THz-streaking experiment and explaining very clearly its working principle, that was very useful for me for performing the dedicated FEL simulations. I thank Ingmar Hartl and Joerg Rossbach for their critical view of my work and the very useful questions they have made to me during my presentations that have enabled me to mature as well a critical view of my job.
I would like to remember Wilfired Wurth and acknowledge his passion and dedication to the seeded FELs that drove him to develop the idea of a possible upgrade for FLASH based on a seeded beamline. I would like to thank him for all the useful suggestions he gave to us (the seeding team) to improve and understand better the sFLASH experiment.
I thank the FLASH team: Siggy Schreiber, Katja Honkavaara, Mathias Vogt, Johann Zemella, Juliane Ronsch-S. and Florian Christie and all the FLASH operator that have supported the several beamtimes that I have spend at the FLASH machine during these years and also the DESY techincal groups that are supporting the sFLASH project (MSK, MVS, ZDM1, MCS,...).
I thank the European XFEL theory team: Gianluca Geloni, Takanori Takinawa (now HZDR), Svitozar Serkez and Sergey Tomin (now DESY) for letting me using the xfel nodes in the Maxwell cluster that have been fundamental to complete the FLASH2020+ simulations. I would also like to thank them for the very useful scientific conversations about simulations and the support for the multi-physics simulation code OCELOT.
I thank the FERMI team and all the EEHG collaboration for having enabled me to take part in such great achievement for the whole FEL community. I would like in particular to thank Enrico Allaria whom has proof-read the chapter dedicated to the EEHG experiment at FERMI in my thesis and to be always very open for scientific discussion despite the distance and Luca Giannessi whom has allowed me to participate the the FERMI experiment, both I want to thank for being a great inspiration and reference for my doctoral studies. From the EEHG team I want to thank Primoc Ribic, Bill Fawley, Eleonore Roussel, Eugenio Fer-

rari, Simone Di Mitri, Giuseppe Penco, Erik Hemsing, Giuseppe De Ninno, Mihai Pop, Eduard Prat... thank you for sharing with me the passion for seeded FELs. I thank Sven Reiche for his constant support with the new code GENESIS1.3 v.4 and for the useful scientific discussion we have had during the visit at PSI and during conferences. I would like to thank Simona Bettoni, Laura Monaco, Benedetta Marmiroli and Cecilia Maiano for their encouragements.

Finally I would like to thank my family for the constant support and love, motivation, self-confidence and trust they are giving to me: my grandmother Lucia, my mother Sandra my sister Anna and Andrea P. Fundamental to complete my PhD studies was Andrea B., my love, whom has given to me the stronger support and motivation to complete my PhD and we have shared together this hard route which is the PhD. Thank you.

List of Figures

LIST OF FIGURES

Bibliography

[1] D. Strickland and G. Mourou. "Compression of amplified chirped optical pulses". In: *Optical Communications* 55.6 (1985), pp. 447–449. DOI: 10.1016/0030-4018(85)90151-8. URL: https://doi.org/10.1016/0030-4018(85)90151-8.

[2] A. Roy et al. "Influence of laser pulse duration on extreme ultraviolet and ion emission features from tin plasmas". In: *Physics of Plasmas* 21 (2014), p. 033109. DOI: 10.1063/1.4870092. URL: https://doi.org/10.1063/1.4870092.

[3] A. Barty. "Time-resolved imaging using x-ray free electron lasers". In: *Journal of Physics B: Atomic, Molecular and Optical Physics* 43.194014 (2010), p. 15. DOI: JPhysB/43/19014. URL: stacks.iop.org/JPhysB/43/19014.

[4] John M. J. Madey. "Wilson Prize article: From vacuum tubes to lasers and back again". In: *Phys. Rev. ST Accel. Beams* 17 (2014), p. 074901. DOI: 10.1103/PhysRevSTAB.17.074901. URL: https://doi.org/10.1103/PhysRevSTAB.17.074901.

[5] C. H. Yoon et al. "Conformation sequence recovery of a non-periodic object from a diffraction-before-destruction experiment". In: *Optics Express* 22.7 (2014), pp. 8085–8093. DOI: 10.1364/OE.22.008085. URL: https://doi.org/10.1364/OE.22.008085.

[6] O. Gorobtsovet et al. “Seeded X-ray free-electron laser generating radiation with laser statistical properties”. In: *Nature Communications* 9 (2018), p. 4498. DOI: 10.1038/s41467-018-06743-8. URL: https://doi.org/10.1038/s41467-018-06743-8.

[7] L. Müller et al. “Ultrafast Dynamics of Magnetic Domain Structures Probed by Coherent Free-Electron Laser Light”. In: *Synchrotron Radiation News* 26.6 (2010), pp. 27–32. DOI: 10.1080/08940886.2013.850384. URL: https://doi.org/10.1080/08940886.2013.850384.

[8] R. J. Glauber. “The quantum theory of optical coherence”. In: *Phys. Rev.* 130 (1963), pp. 2529–2539. DOI: 10.1103/PhysRev.130.2529. URL: https://doi.org/10.1103/PhysRev.130.2529.

[9] J. Frisch. *Synchrotron Radiation Sources and Free Electron Lasers*. URL: http://stanford.edu/~melkor/X_ray_tutorial_UXSS_11.pdf.

[10] G. Margaritondo. *Elements Of Synchrotron Light: For Biology, Chemistry, and Medical Research (Physics)*. Oxford University, UK: OXFORD, 2002.

[11] P. Fromme S. Boutet and M. S. Hunter. *X-ray Free Electron Lasers*. Gewerbestrasse 11,6330 Cham, Switzerland: Springer, Cham, 2018.

[12] R. Paschotta. *High Harmonic Generation*. URL: https://www.rp-photonics.com/high_harmonic_generation.html (visited on 05/27/2020).

[13] Z. Zhentang et al. “Shanghai Soft X-Ray Free-Electron Laser Facility”. In: *Chinese Journal of Lasers* 46 (1 Jan. 2019), p. 100004. DOI: 10.3788/CJL201946.0100004. URL: https://doi.org/I:10.3788/CJL201946.0100004.

[14] E. Allaria et al. “Highly coherent and stable pulses from the FERMI seeded free-electron laser in the extreme ultraviolet”. In: *Nat. Phot.* 6 (Sept. 2012), p. 699. DOI: 10.1038/nphoton.2012.233. URL: https://doi.org/10.1038/nphoton.2012.233.

[15] E. Allaria et al. “Highly coherent and stable pulses from the FERMI seeded free-electron laser in the extreme ultraviolet”. In: *Nature Photonics* 6 (10 Oct. 2012), pp. 699–704. DOI: 10.1038/nphoton.2012.233. URL: https://doi.org/10.1038/nphoton.2012.233.

[16] E. Amann et al. “Demonstration of self-seeding in a hard-X-ray free-electron laser”. In: *Nature Photonics* 6 (10 Oct. 2012), pp. 693–698. DOI: 10.1038/nphoton.2012.180. URL: https://doi.org/10.1038/nphoton.2012.180.

[17] T. Inagaki et al. “Stable Generation of High Power Self-seeded XFEL at SACLA”. In: *5th International Particle Accelerator Conference*. July 2014, THPRO016. DOI: 10.18429/JACoW-IPAC2014-THPRO016.

[18] C.-K. Min et al. “Hard X-ray self-seeding commissioning at PAL-XFEL”. In: *Journal of Synchrotron Radiation* 26.4 (July 2019), pp. 1101–1109. DOI: 10.1107/S1600577519005460. URL: https://doi.org/10.1107/S1600577519005460.

[19] S. Liu. *First results of the Hard X-Ray Self-Seeding Commissioning at the European XFEL*. May 2020.

[20] E. Prat and S. Reiche. In: *Proc. FEL'13* (New York, NY, USA). Free Electron Laser Conference. JACoW Publishing, Geneva, Switzerland, 2013, pp. 618–622. ISBN: ISBN 978-3-95450-126-7.

[21] E. Hemsing et al. “Soft x-ray seeding studies for the SLAC Linac Coherent Light Source II”. In: *Phys. Rev. Accel. and Beams* 22 (Nov. 2019), p. 110701. DOI: 10.1103/PhysRevAccelBeams.22.110701. URL: https://doi.org/I:10.1103/PhysRevAccelBeams.22.110701.

[22] K. Wille. *The Physics of Particle Accelerators*. Oxford, Great Britain: Oxford University Press, 2000.

[23] F. Hinterberger. *Physik der Teilchenbeschleuniger und Ionenoptik*. Universität Bonn, Helmholtz-Institut für Strahlen- und Kernphysik Nußallee, Bonn, Germany: Springer, 2009.

[24] K. L. Brown. “A First- and Second-Order Matrix Theory for the Design of Beam Transport Systems and Charged Particle Spectrometers”. In: *Adv. Part. Phys.* 1 (1968), pp. 71–134.

[25] A. Wolski. *Beam Dynamics in High Energy Particle Accelerators*. University of Liverpool, UK: Imperial College Press, 2014.

[26] H. Biss. “Conceptual Design of a Chicane Upgrade for EEHG Seeding at sFLASH”. Master thesis. Universität Hamburg, Jan. 2019.

[27] P. Schmueser, M. Dohlus, and J. Rossbach. *Ultraviolet and Soft X-ray Free Electron Lasers*. Berlin, Heidelberg: Springer, 2009.

[28] J. Rossbach. *Free-Electron Lasers in the Ultraviolet and X-Ray Regime*. Heldelberg, Germany: Springer, 2008.

[29] R. Walker. "Insertion devices: Undulators and wigglers". In: *Cern Accelerator School (CAS) proceedings* Synchrotron Radiation and Free Electron Lasers (1998), p. 129.

[30] Centre Laser Infrarouge d'Orsay. *Undulator Radiation*. 2012. URL: http://old.clio.lcp.u-psud.fr/clio_eng/FELrad.html (visited on 03/04/2020).

[31] Y. Shvyd'ko K.-J. Kim and S. Reiche. "A Proposal for an X-Ray Free-Electron Laser Oscillator with an Energy-Recovery Linac". In: *Phys. Rev. Lett.* 100 (24 June 2008), p. 244802. DOI: 10.1103/PhysRevLett.100.244802. URL: https://link.aps.org/doi/10.1103/PhysRevLett.100.244802.

[32] S. Di Mitri and M. Cornacchia. "Electron beam brightness in LINAC drivers for free-electron-lasers". In: *Physics Reports* 539 (1 June 2014), pp. 1–48. DOI: j.physrep.2014.01.005. URL: https://doi.org/10.1016/j.physrep.2014.01.005.

[33] J.R. Schneider E.J. Jaeschke S. Khan and J.B. Hastings. *Synchrotron light sources and free-electron lasers: Accelerator physics, instrumentation and science applications*. Jan. 2016, pp. 1–1840. DOI: 10.1007/978-3-319-14394-1.

[34] S. Reiche. "Update on the code GENESIS 1.3". In: *Porceedings of the FEL 2014, Basel, Switzerland* TUP019 (2014), pp. 403–407.

[35] P.-L. Morton N.-M. Kroll and M.-N. Rosenbluth. "Free-Electron Lasers with Variable Parameter Wigglers". In: *Journal of Quantum Electronics* 17 (8 1981).

[36] L. Giannessi et al. "Self-Amplified Spontaneous Emission Free-Electron Laser with an Energy-Chirped Electron Beam and Undulator Tapering". In: *Phys. Rev. Lett.* 106 (Apr. 2011), p. 144801. DOI: 10.1103/PHYSREVLETT.106.144801. URL: https://link.aps.org/doi/10.1103/PHYSREVLETT.106.144801.

[37] Z. Huan S. Huang Y. Ding and J. Qiang. "Generation of Stable Subfemtosecond Hard X-ray Pulses with Optimised Non-linear Bunch Compression". In: *Phys. Rev. ST Accel. Beams* 17 (Nov. 2014), p. 120703. DOI: 10.1103/PhysRevSTAB.17.120703. URL: https://link.aps.org/doi/10.1103/PhysRevSTAB.17.120703.

[38] J. Rossbach. "FLASH: The First Superconducting X-Ray Free-Electron Laser". In: (2016), pp. 303–328. DOI: 10.1007/978-3-319-14394-1_10.

[39] M. Xie. "Design optimization for an X-ray free-electron laser driven by SLAC LINAC." In: *Proceedings of the Particle Accelerator Conference* 1 (May 1995), pp. 183–185.

[40] N. Piovella R. Bonifacio and W. J. McNeil. "Superradiant evolution of radiation pulses in a free-electron laser". In: *Phys. Rev. A* 44.6 (1991), R3441. DOI: https://doi.org/10.1103/PhysRevA.44.R3441.

[41] T. Watanabe et al. "Experimental characterization of superradiance in a single-pass high-gain laser-seeded free-electron laser". In: *Phys. Rev. Lett.* 98 (2007), p. 038402. DOI: https://doi.org/10.1103/PhysRevLett.98.034802.

[42] N.S. Mirian, L. Giannessi, and S. Spampinati. "FEL Pulse Shortening by Superradiance at FERMI". In: *Proc. of International Free Electron Laser Conference (FEL'17), Santa Fe, NM, USA, August 20-25, 2017* (Santa Fe, NM, USA). International Free Electron Laser Conference 38. https://doi.org/10.18429/JACoW-FEL2017-MOP005. Geneva, Switzerland: JACoW, Feb. 2018, pp. 38–41. ISBN: 978-3-95450-179-3. DOI: https://doi.org/10.18429/JACoW-FEL2017-MOP005. URL: http://jacow.org/fel2017/papers/mop005.pdf.

[43] G. Lambert et al. "Injection of harmonics generated in gas in a free-electron laser providing intense and coherent extreme-ultraviolet light". In: *Nature Physics* 4 (4 Apr. 2008), pp. 296–300. DOI: 10.1038/nphys889. URL: https://doi.org/10.1038/nphys889.

[44] S. Ackermann et al. "Generation of coherent 19-and 38 nm radiation at a free-electron laser directly seeded at 38 nm". In: *Phys. Rev. Lett.* 111 (11 2013), p. 114801.

[45] M.-E. Couprie and L. Giannessi. "Seeding Free Electron Lasers with High Order Harmonics Generated in Gas". In: *In: Canova F., Poletto L. (eds) Optical Technologies for Extreme-Ultraviolet and Soft X-ray Coherent Sources*. Springer Series in Optical Sciences 197. Springer, Berlin, Heidelberg, 2015, pp. 79–113. ISBN: 978-3-662-47443-3. DOI: 10.1007/978-3-662-47443-3_5. URL: https://doi.org/10.1007/978-3-662-47443-3_5.

[46] L. H. Yu. "Generation of intense uv radiation by subharmonically seeded single-pass free-electron lasers". In: *Phys. Rev. A* 44 (8 Oct. 1991), p. 5178. DOI: 10.1103/PhysRevA.44.5178. URL: https://doi.org/10.1103/PhysRevA.44.5178.

[47] E. Hemsing et al. "Beam by design: Laser manipulation of electrons in modern accelerators". In: *Reviews of Modern Physics* 86 (June 2014), p. 897. DOI: 10.1103/RevModPhys.86.897. URL: https://doi.org/10.1103/RevModPhys.86.897.

[48] Gennady Stupakov. "Effect of Finite Pulse Length and Laser Frequency Chirp on HGHG and EEHG Seeding". In: (Jan. 2011). DOI: 10.2172/1029478.

[49] R. Bonifacio et al. "Physics of the High-Gain FEL and Superradiance." In: *Rivista del Nuovo Cimento (1978-1999)* 13 (9 Sept. 1990), pp. 1–69. DOI: 10.1007/BF02770850. URL: https://doi.org/10.1007/BF02770850.

[50] P. Finetti et al. "Pulse Duration of Seeded Free-Electron Lasers". In: *Physical Review X* 7 (June 2017), p. 021043. DOI: 10.1103/PhysRevX.7.021043.

[51] C. Rulliere. *Femtosecond Laser Pulses*. Springer Science+Business Media, Inc., 233 Spring Street, New York, NY 10013, USA: Springer, 2009.

[52] A. Azima. *Seeded FEL spectrum, chirp and pulse duration at once -a tutorial-*. June 2017.

[53] S. Serkez et al. S. Tomin. *OCELOT collaboration*. 2012. URL: https://github.com/ocelot-collab (visited on 03/13/2020).

[54] D. Ratner et al. "Laser phase errors in seeded free electron lasers". In: *Phys. Rev. ST Accel. Beams* 15 (3 Mar. 2012), p. 030702. DOI: 10.1103/PhysRevSTAB.15.030702. URL: https://link.aps.org/doi/10.1103/PhysRevSTAB.15.030702.

[55] D. Gauthier et al. “Chirped pulse amplification in an extreme-ultraviolet free-electron laser”. In: *Nature Communications* 7 (Dec. 2016), p. 13688. DOI: 10.1038/ncomms13688. URL: https://doi.org/10.1038/ncomms13688.

[56] E. Vogel et al. “Test and commissioning of the third harmonic RF system for FLASH”. In: *presented at the 1st Int. IPAC Conf.(IPAC’10), Kyoto, Japan* THPD003 (2010), p. 3. URL: http://www.desy.de/~evogel/files/thpd003.pdf.

[57] C. Feng et al. “Study of the Energy Chirp Effects on Seeded FEL Schemes at SDUV-FEL”. In: *Proceedings 3rd International Particle Accelerator Conference (IPAC’12), New Orleans, LA, USA* TUPP056 (May 2012), pp. 1724–1726.

[58] T. Shaftan and L. H. Yu. “High-gain harmonic generation free-electron laser with variable wavelength”. In: *Phys. Rev. E* 71 (2005), p. 046501. DOI: 10.1103/PhysRevE.71.046501. URL: https://doi.org/10.1103/PhysRevE.71.046501.

[59] G. Paraskaki et al. “Study of a Seeded Oscillator-Amplifier FEL”. In: *Proc. FEL’19* (Hamburg, Germany). Free Electron Laser Conference 39. https://doi.org/10.18429/JACoW-FEL2019-TUP077. JACoW Publishing, Geneva, Switzerland, Nov. 2019, pp. 234–237. ISBN: 978-3-95450-210-3. DOI: doi:10.18429/JACoW-FEL2019-TUP077. URL: http://jacow.org/fel2019/papers/tup077.pdf.

[60] P. R. Ribic et al. “Coherent soft X-ray pulses from an echo-enabled harmonic generation free-electron laser”. In: *Nature Photonics* 13 (Aug. 2019), pp. 555–561. DOI: 10.1038/ncomms4762.

[61] D. Xiang and G. Stupakov. “Echo-enabled harmonic generation free electron laser”. In: *Phys. Rev. ST Accel. Beams* 12 (3 Mar. 2009), p. 030702. DOI: 10.1103/PhysRevSTAB.12.030702. URL: https://link.aps.org/doi/10.1103/PhysRevSTAB.12.030702.

[62] J. Boedewadt et al. “Parameter optimization for operation of sFLASH with Echo-Enabled Harmonic Generation”. In: *Proceedings of IPAC2017, Copenhagen, Denmark* (WEPAB015 May 2017), pp. 2592–2595.

[63] Erik Hemsing et al. “Effect of Finite Pulse Length and Laser Frequency Chirp on HGHG and EEHG Seeding”. In: *Phys. Rev. Accel. Beams* 20 (June 2017), p. 060702. DOI: 10.1103/PhysRevAccelBeams.20.060702.

[64] G. Stupakov. "Echo-Enabled Harmonic generation". In: *Proceedings of IPAC2010, Kyoto, Japan* (WEXRA02 May 2010), p. 4.

[65] Z. Huang et al. "Effects of Energy Chirp on Echo-Enabled Harmonic Generation Free-Electron Lasers". In: *31st Free Electron Laser Conference, FEL2009, Liverpool, UK* MOPC45 (2009), pp. 127–129.

[66] G. Stupakov. "Tolerance study for the Echo-Enabled Harmonic generation Free-Electron Laser". In: *Proceedings of PAC2009, Vancouver, BC, Canada* (WE5RFP044 May 2009), p. 3.

[67] A. W. Chao and M. Tigner. *Handbook of Accelerator Physics and Engineering*. Singapore: World Scientific, 2006.

[68] E. Saldin et al. "Calculation of energy diffusion in an electron beam due to quantum fluctuations of undulator radiation". In: *Nucl. Instrum. Meth. A* 381 (2-3 Nov. 1996), p. 545. DOI: 10.1016/S0168-9002(96)00708-5. URL: https://doi.org/10.1016/S0168-9002(96)00708-5.

[69] E. Hemsing. "Bunching phase and constraints on Echo-Enabled Harmonic Generation". In: *Phys. Rev. Accel. and Beams* 21 (May 2018), p. 050702. DOI: 10.1103/PhysRevAccelBeams.21.050702. URL: https://doi.org/10.1103/PhysRevAccelBeams.21.050702.

[70] E. A. Schneidmiller and M. V. Yurkov. "Longitudinal space charge amplifier". In: *Proc. of SPIE* 8779 (May 2013). DOI: 10.1117/12.2017015. URL: https://doi.org/%2010.1117/12.2017015.

[71] E. L. Saldin, E. A. Schneidmiller, and M. V. Yurkov. "Longitudinal space charge-driven microbunching instability in the TESLA Test Facility linac". In: *Nucl. Instr. and Methods in Physics A* 528 (1-2 Aug. 2004), pp. 355–359. DOI: 10.1016/j.nima.2004.04.067. URL: https://doi.org/10.1016/j.nima.2004.04.067.

[72] S. Heifets, G. Stupakov, and S. Krinsky. "Coherent synchrotron radiation in a bunch compressor". In: *Phys. Rev. Accel. and Beams* 5 (June 2002), p. 064401. DOI: 10.1103/PhysRevSTAB.5.064401. URL: https://doi.org/10.1103/PhysRevSTAB.5.064401.

[73] V. Ayvazyan et al. "Generation of GW Radiation Pulses from VUV Free-Electron Laser Operating in the Femtosecond Regime". In: *Phys. Rev. Lett.* 88 (8 Mar. 2002), p. 4. DOI: 10.1103/PhysRevLett.88.104802. URL:

https://journals.aps.org/prl/pdf/10.1103/PhysRevLett.88.104802.

[74] S. Schreiber. "First lasing in the water window with 4.1 nm at FLASH". In: *Proceedings of FEL2011, Shanghai, China* (TUOBI2 Aug. 2011), p. 2.

[75] I. Will et al. "Photoinjector drive laser of the FLASH FEL". In: *Optics Express* 19 (24 Sept. 2011), p. 12. DOI: 10.1364/OE.19.023770. URL: http://www.opticsexpress.org/abstract.cfm?URI=oe-19-24-23770.

[76] J. Sekutowicz R. Brinkmann E.A. Schneidmiller and M.V. Yurkov. "Prospects for CW and LP operation of the European XFEL in hard X-ray regime". In: *Nucl. Instrum. Meth. A* 768 (2014), pp. 20–25. DOI: 10.1016/j.nima.2014.09.039. URL: https://arxiv.org/pdf/1403.0465.pdf.

[77] P. Castro. "Beam trajectory calculations in bunch compressors of TTF2". In: *Tesla Technical Report* (2003), pp. 1–20.

[78] M. K. Bock. "Measuring the Electron Bunch Timing with Femtosecond Resolution at FLASH". Diplomarbeit. Universität Hamburg, Oct. 2012. URL: http://www-library.desy.de/preparch/desy/thesis/desy-thesis-13-008.pdf.

[79] B. Faatz et al. "Simultaneous operation of the two soft x-ray free-electron lasers driven by one linear accelerator". In: *New Journal of Physics* 18.6 (June 2016), p. 062002. DOI: 10.1088/1367-2630/18/6/062002. URL: https://doi.org/10.1088/1367-2630/18/6/062002.

[80] Markus Hüning et al. "Observation of femtosecond bunch length using a transverse deflecting structure". In: (Jan. 2005).

[81] K. Tiedtke et al. "Gas detectors for x-ray lasers". In: *Journal of Applied Physics* 103 (May 2008), p. 094511. DOI: 10.1063/1.2913328. URL: https://doi.org/10.1063/1.2913328.

[82] L. Bittner et al. "MCP-based photon detector with extended wavelength range for sFLASH". In: *presented at the 29th Int. FEL Conf.(FEL'07), Novosibirsk, Russia* WEPPH007 (2007), p. 4.

[83] G. Brenner et al. "First results from the online variable line spacing grating spectrometer at FLASH". In: *Nuclear Instruments and Methods in Physics Research* 635.1 (Apr. 2011), S99–S103. DOI: 10.1016/j.nima.2010.09.134. URL: https://doi.org/10.1016/j.nima.2010.09.134.

[84] A. Azima et al. “sFLASH: An Experiment for Seeding VUV Radiation at FLASH. 2008-08-25 - 2008-08-29”. In: (July 2007).

[85] J. Bödewadt and C. Lechner. “Results and perspectives on the FEL seeding activities at flash”. In: *FEL 2013: Proceedings of the 35th International Free-Electron Laser Conference* (Jan. 2013), pp. 491–495.

[86] G. Angelova et al. “Installation of the optical replica synthesizer in flash”. In: (Jan. 2007), pp. 438–440.

[87] M. Tischer et al. “Undulators of the sFLASH experiment”. In: *presented at the 1st Int. IPAC Conf.(FEL’10), Kyoto, Japan* WEPD014 (2010), p. 3114.

[88] H. Delsim-Hashemi et al. “Status of the sFLASH undulator system”. In: *presented at the 31st Int. FEL Conf.(FEL’09), Liverpool, UK* WEPC04 (2009), p. 500.

[89] T. Plath et al. “Mapping few-femtosecond slices of ultra-relativistic electron bunches”. In: *Scientific Reports* 7 (May 2017). DOI: 10.1038/s41598-017-02184-3.

[90] J. Bödewadt et al. “Determination of the slice energy spread of ultra-relativistic electron beams by scanning seeded coherent undulator radiation”. In: *FEL 2017: Proceedings of the 38th International Free-Electron Laser Conference* (Aug. 2017), pp. 322–324.

[91] F. Curbis et al. “Photon Diagnostics for the Seeding Experiment at FLASH”. In: (July 2007).

[92] Leslie L. Lazzarino. “Design and Commissioning of an XUV and Soft X-Ray FEL Pulse Shaper”. Doctoral thesis. Universität Hamburg, Jan. 2018.

[93] sFLASH team. *sFLASH Setup Tutorial*. Jan. 2019.

[94] T. Plath. “Measurements and Detailed Analysis of Seeded High-Gain Free-Electron Lasers at FLASH”. Diplomarbeit. Universität Hamburg, 2017. URL: http://ediss.sub.uni-hamburg.de/volltexte/2017/8776/.

[95] J. Bödewadt et al. “Experience in Operating sFLASH With High-Gain Harmonic Generation”. In: *Proc. of International Particle Accelerator Conference (IPAC’17), Copenhagen, Denmark, 14-19 May, 2017* (Copenhagen, Denmark). International Particle Accelerator Conference 8. https://doi.org/10.18429/JACoW-IPAC2017-WEPAB016. Geneva, Switzerland: JACoW, May 2017, pp. 2596–2599. ISBN: 978-3-95450-182-3. DOI: https://doi.org/10.18429/JACoW-

IPAC2017-WEPAB016. URL: http://jacow.org/ipac2017/papers/wepab016.pdf.

[96] V. Grattoni et al. "Status of Seeding Development at sFLASH". In: *Proc. of International Free Electron Laser Conference (FEL'17), Santa Fe, NM, USA, August 20-25, 2017* (Santa Fe, NM, USA). International Free Electron Laser Conference 38. https://doi.org/10.18429/JACoW-FEL2017-MOP042. Geneva, Switzerland: JACoW, Feb. 2018, pp. 136–139. ISBN: 978-3-95450-179-3. DOI: https://doi.org/10.18429/JACoW-FEL2017-MOP042. URL: http://jacow.org/fel2017/papers/mop042.pdf.

[97] C. Behrens et al. "Constraints on photon pulse duration from longitudinal electron beamdiagnostics at a soft X-ray free-electron laser". In: *Physical Review Special Topics - Accelerators and Beams* 15 (Jan. 2012), p. 030707. DOI: 10.1103/PhysRevSTAB.15.030707.

[98] C. Behrens et al. "Few-femtosecond time-resolved measurements of X-ray free-electron lasers". In: *Nature communications* 5 (Apr. 2014), p. 3762. DOI: 10.1038/ncomms4762.

[99] A. A. Lutman et al. "Femtosecond X-Ray Free Electron Laser Pulse Duration Measurement from Spectral Correlation Function". In: *Phys. Rev. ST Accel. Beams* 15 (Apr. 2012), p. 030705. DOI: 10.1103/PhysRevSTAB.15.030705.

[100] Y. Inubushi et al. "Determination of the Pulse Duration of an X-Ray Free Electron Laser Using Highly Resolved Single-Shot Spectra". In: *Phys. Rev. Lett.* 109 (Apr. 2012), p. 144801. DOI: 10.1103/PhysRevLett.109.144801. URL: https://doi.org/10.1103/PhysRevLett.109.144801.

[101] U. Frühling et al. "Light-field streaking for FELs". In: *Journal of Physics B: Atomic, Molecular and Optical Physics* 44.24 (Nov. 2011), p. 243001. DOI: 10.1088/0953-4075/44/24/243001. URL: https://doi.org/10.1088/0953-4075/44/24/243001.

[102] A. Azima et al. "Direct measurement of the pulse duration and frequency chirp of seeded XUV free electron laser pulses". In: *New Journal of Physics* 20 (Nov. 2017). DOI: 10.1088/1367-2630/aa9b4c.

[103] J. Wu et al. "Interplay of the chirps and chirped pulse compression in a high-gain seeded free-electron laser". In: *Journal of the Optical Society of*

America B 44.24 (Mar. 2011), p. 243001. DOI: 10.1364/JOSAB.24.000484. URL: http://josab.osa.org/abstract.cfm?URI=josab-24-3-484.

[104] S. Reiche. "GENESIS 1.3: a fully 3D time-dependent FEL simulation code". In: *Nuclear Instruments and Methods in Physics Research Section A: Accelerators, Spectrometers, Detectors and Associated Equipment* 429.1-3 (June 1999), pp. 243–248. DOI: 10.1016/S0168-9002(99)00114-X. URL: https://doi.org/10.1016/S0168-9002(99)00114-X.

[105] J. Diels and W. Rudolph. *Ultrashort Laser Pulse Phenomena*. USA: Elsevier, 2006.

[106] Mikhail N. Polyanskiy. *Refractive index database*. URL: https://refractiveindex.info (visited on 02/07/2020).

[107] K. Hacker and H. Schlarb. "Tolerances for Echo-seeding in the FLASH ORS section". In: *TESLA-FELReport* (May 2011), pp. 1–16. URL: https://bib-pubdb1.desy.de/record/92099.

[108] Physik Instrumente (PI). *P-620.1-P-629.1 PIHera Piezo Linear Precision Positioner*. URL: https://www.pionline.it/it/prodotti/stage-flexure-piezo-per-il-nanoposizionamento/stage-flexure-piezo-lineari/p-6201-p-6291-pihera-piezo-linear-stage-202300/ (visited on 05/18/2020).

[109] E. Allaria et al. "The FERMI free-electron lasers". In: *Journal of Synchrotron Radiation* 22 (Mar. 2015), pp. 485–491. DOI: 10.1107/S1600577515005366. URL: http://dx.doi.org/10.1107/S1600577515005366.

[110] E. Allaria et al. "Highly coherent and stable pulses from the FERMI seeded free-electron laser in the extreme ultraviolet". In: *Nature Photonics* 6 (Oct. 2012), pp. 699–704. DOI: 10.1038/NPHOTON.2012.233.

[111] E. Allaria et al. "Two-stage seeded soft-X-ray free-electron laser". In: *Nature Photonics* 7 (Oct. 2013), pp. 913–918. DOI: 10.1038/NPHOTON.2013.277.

[112] G. De Ninno. "Single-shot spectro-temporal characterization of XUV pulses from a seeded free-electron laser". In: *Nature Communications* 6 (Aug. 2015), p. 8075. DOI: 10.1038/ncomms9075. URL: https://doi.org/10.1038/ncomms9075.

[113] C. Callegari et al. K. C. Prince E. Allaria. "Coherent control with a short-wavelength free-electron laser". In: *Nature Photonics* 10 (Feb. 2016), pp. 176–179. DOI: 10.1038/nphoton.2016.13. URL: https://doi.org/10.1038/nphoton.2016.13.

[114] D. Gauthier et al. "Generation of Phase-Locked Pulses from a Seeded Free-Electron Laser". In: *Physical Review Letters* 116 (Jan. 2016), p. 024801. DOI: 10.1103/PhysRevLett.116.024801. URL: https://doi.org/10.1103/PhysRevLett.116.024801.

[115] E. Roussel et al. "Multicolor High-Gain Free-Electron Laser Driven by Seeded Microbunching Instability". In: *Physical Review Letters* 115 (Nov. 2015), p. 214801. DOI: 10.1103/PhysRevLett.115.214801.

[116] E. Ferrari et al. "Single Shot Polarization Characterization of XUV FEL Pulses from Crossed Polarized Undulators". In: *Scientific Reports* 5.13531 (Aug. 2015). DOI: 10.1038/srep13531. URL: https://doi.org/10.1038/srep13531.

[117] G. Penco et al. "Optimization of a high brightness photoinjector for a seeded FEL facility". In: *Journal of Instrumentation* 8.P05015 (May 2013), pp. 1–24. DOI: 10.1088/1748-0221/8/05/P05015. URL: https://doi.org/10.1088/1748-0221/8/05/P05015.

[118] S. Spampinati et al. "Laser heater commissioning at an externally seeded free-electron laser". In: *Phys. Rev. ST Accel. Beams* 17 (12 Dec. 2014), p. 120705. DOI: 10.1103/PhysRevSTAB.17.120705. URL: https://link.aps.org/doi/10.1103/PhysRevSTAB.17.120705.

[119] E. Allaria et al. "Two-stage seeded soft-X-ray free-electron laser". In: *Nature Photonics* 7 (11 Nov. 2013), pp. 913–918. DOI: 10.1038/nphoton.2013.277. URL: https://doi.org/10.1038/nphoton.2013.277.

[120] L. H. Yu and I. Ben-Zvi. "High-Gain Harmonic Generation of soft X-rays with the "fresh bunch" technique". In: *Nuclear Instruments and Methods in Physics Research Section A: Accelerators, Spectrometers, Detectors and Associated Equipment* 393 (1-3 July 1997), pp. 96–99. DOI: 10.1016/S0168-9002(97)00435-X. URL: https://doi.org/10.1016/S0168-9002(97)00435-X.

[121] M. Zangrando et al. “Recent results of PADReS, the Photon Analysis Delivery and REduction System, from the FERMI FEL commissioning and user operations”. In: *Journal of Synchrotron Radiation* 22.3 (May 2015), pp. 565–570. DOI: 10.1107/S1600577515004580. URL: https://doi.org/10.1107/S1600577515004580.

[122] C. Masciovecchio et al. “EIS: the scattering beamline at FERMI”. In: *Journal of Synchrotron Radiation* 22.3 (May 2015), pp. 553–564. DOI: 10.1107/S1600577515003380. URL: https://doi.org/10.1107/S1600577515003380.

[123] E. Pedersoli et al. “Multipurpose modular experimental station for the DiProI beamline of Fermi at Elettra free electron laser”. In: *Review of Scientific Instruments* 82.4 (2011), p. 043711. DOI: 10.1063/1.3582155.

[124] C. Svetina. “The Low Density Matter (LDM) beamline at FERMI: optical layout and first commissioning”. In: *Journal of Synchrotron Radiation* 22.3 (May 2015), pp. 538–543. DOI: 10.1107/S1600577515005743. URL: https://doi.org/10.1107/S1600577515005743.

[125] M. Malvestuto et al. “MagneDyn: the future beamline for ultrafast magnetodynamical studies at FERMI”. In: *Advances in X-Ray/EUV Optics and Components* 9 (2014).

[126] P. Rebernik Ribič. “Echo-Enabled Harmonic Generation Lasing of the FERMI FEL in the Soft X-Ray Spectral Region”. In: *Proc. FEL’19* (Hamburg, Germany). Free Electron Laser Conference 39. https://doi.org/10.18429/JACoW-FEL2019-TUB01. JACoW Publishing, Geneva, Switzerland, Nov. 2019, pp. 33–37. ISBN: 978-3-95450-210-3. DOI: doi:10.18429/JACoW-FEL2019-TUB01. URL: http://jacow.org/fel2019/papers/tub01.pdf.

[127] C. Svetina et al. “PRESTO, the on-line photon energy spectrometer at FERMI: design, features and commissioning results.” In: *J Synchrotron Radiat.* 23 (1 Jan. 2016), pp. 35–42. DOI: 10.1107/S1600577515021116. URL: https://doi.org/10.1107/S1600577515021116.

[128] E. Allaria, E. Ferrari, E. Roussel, and L. Vidotto. “REALTA and pyDART: A Set of Programs to Perform Real Time Acquisition and On-Line Analysis at the FERMI Free Electron Laser”. In: *Proc. of International Conference on Accelerator and Large Experimental Control Systems (ICALEPCS’17)* (Barcelona, Spain). International Conference on Accelerator and Large Experimental Control Systems 16. https://doi.org/10.18429/JACoW-ICALEPCS2017-

THPHA044. Geneva, Switzerland: JACoW, Jan. 2018, pp. 1460–1464. ISBN: 978-3-95450-193-9. DOI: https://doi.org/10.18429/JACoW-ICALEPCS2017-THPHA044. URL: http://jacow.org/icalepcs2017/papers/thpha044.pdf.

[129] *FLASH2020+, Making FLASH brighter, faster and more flexible (CDR).* Mar. 2020. URL: https://bib-pubdb1.desy.de/record/434950/files/FLASH2020pCDR.pdf.

[130] R. Roehlsberger. "Light Source Upgrades at DESY: PETRAIV and FLASH2020+". In: *Synchrotron Radiation News* 32.1 (2019), pp. 27–31. DOI: 10.1080/08940886.2019.1559605.

[131] E.A. Schneidmiller. "A Concept for Upgrade of FLASH2 Undulator Line". In: *presented at the 10th Int. Particle Accelerator Conf.(IPAC'19), Melbourne, Australia, May 2019* ().

[132] R. Paschotta. *Optical Parametric Chirped-pulse Amplification.* URL: https://www.rp-photonics.com/optical_parametric_chirped_pulse_amplification.html (visited on 05/04/2020).

[133] J. Zemella and M. Vogt. "Optics and Compression Schemes for a Possible FLASH Upgrade". In: *presented at the 10th Int. Particle Accelerator Conf.(IPAC'19), Melbourne, Australia, May 2019* TUPRB026 ().

[134] Robert Molo. "Investigation of Short-Pulse Radiation Sources atDELTA Based on Coherent Harmonic Generation and Echo-Enabled Harmonic Generation". Diplomarbeit. Technische Universität Dortmund, Oct. 2011.

[135] D. Xiang and G. Stupakov. In: *Proc. of PAC09* WE5RFP044 ().

[136] Gennady Stupakov. *Intra-beam scattering and the ultimate seeding wavelength in EEHG.* Dec. 2012.

[137] G. Penn and M. Reinisch. In: *J. of Modern Opt.* (2011).

[138] E. Saldin et al. In: *Nucl. Instrum. Methods A* 381 (1996), pp. 545–547.

[139] M. Dohlus. *Xtrack.* 2017. URL: https://www.desy.de/~dohlus/2017/2017.06.XtrackUG/Xtrack_2017__10_25.pdf (visited on 05/11/2020).

[140] M. Kuhlmann, E.A. Schneidmiller, and M.V. Yurkov. "Frequency doubling mode of operation of free electron laser FLASH2". In: *presented at the 38th Int. FEL Conf.(FEL'17), Santa Fe, NM, USA, August 2017* MOP036 ().

[141] S. Reiche. “GENESIS 1.3: a fully 3D time-dependent FEL simulation code”. In: *Nuclear Instruments and Methods in Physics Research Section A: Accelerators, Spectrometers, Detectors and Associated Equipment* 429.1-3 (1999), pp. 243–248. DOI: 10.1016/S0168-9002(99)00114-X. URL: https://doi.org/10.1016/S0168-9002(99)00114-X.